CHRONOSTRATIGRAPHIC AND GEOCHEMICAL CHARACTERIZATION OF THE CENOMANIAN – TURONIAN EAGLE FORD GROUP IN WEST AND SOUTH TEXAS, USA

A Dissertation

by

ROY AUGUSTINE CONTE

Submitted to the Office of Graduate and Professional Studies of
Texas A&M University
in partial fulfillment of the requirements for the degree of

DOCTOR OF PHILOSOPHY

Chair of Committee,	Michael C. Pope
Committee Members,	Arthur D. Donovan
	Brent V. Miller
	Debbie Thomas
Head of Department,	Ramalingham Saravanan

December 2020

Major Subject: Geology

ABSTRACT

Organic-rich mudstone depositional environments commonly were thought to require low-energy and persistent benthic anoxia for accumulation and preservation of large amounts of organic matter. However, more recent studies indicate that organic-rich, mudstone-dominated successions commonly were deposited in environments at least episodically influenced by more energetic bottom currents (e.g. storms, turbidites, debris flows, contourites). Integrated redox-sensitive trace element (RSTE) geochemistry, mineralogy, organic geochemistry, and thin section petrography from outcrops and cores characterizing the Upper Cretaceous (Cenomanian –Turonian) Eagle Ford Group in west and south Texas (USA) indicate its organic-rich, mudstone-dominated depositional environments were heterogeneous, having different depositional processes simultaneously affecting coeval deposits in different parts of the same basin.

High-precision isotope dilution thermal ionization mass spectrometry (ID-TIMS) uranium – lead (U-Pb) zircon geochronology was used to constrain the outcrop-to-subsurface stratigraphy of the Eagle Ford Group. ID-TIMS analyses of individual zircon grains characterizing sixteen volcanic ash beds from three outcrops and two petroleum industry cores were integrated with regional biostratigraphy to provide a comprehensive outcrop-to-subsurface geochronology for the Eagle Ford Group. The $^{206}Pb/^{238}U$ ages range from 96.45 ± 0.18 Ma near the base of the Eagle Ford Group in west Texas to 88.9 ± 0.12 Ma near the base of the Austin Chalk in Karnes County, Texas. This interval encompasses uppermost Lower Cenomanian, Turonian and upper Lower Coniacian, spanning ~7.5 m.y.

of deposition from the base of the Eagle Ford Group to the base of the Austin Chalk, and provides important age constraints that tie the Eagle Ford Group outcrops in west Texas to subsurface oil-and-gas producing wells in south Texas.

The Ford Group outcrops at Lozier Canyon also contain several volcanic ash deposits with abundant apatite crystals. Over 230 apatite samples characterizing nine volcanic ash beds in the Eagle Ford Group in west Texas were analyzed for trace element concentrations using laser ablation inductively coupled plasma mass spectrometry (LA-ICP-MS). When the apatite trace element concentrations are integrated with U-Pb zircon geochronology, the Cenomanian and Turonian ash beds can be distinguished on the basis of the Eu/Eu* on chondrite-normalized REE plots and on cross-plots using a combination of $(Th/U)_{CN}$, $\sum(La, Ce, Pr, Nd)_{CN}$ and $(Ce/Yb)_{CN}$.

DEDICATION

This dissertation is dedicated to every young girl and boy who dreams of becoming a scientist.

ACKNOWLEDGEMENTS

I want to express my profound gratitude to my committee chair, Dr. Michael C. Pope, for his years of mentorship and support through my M.S. and Ph.D. program at Texas A&M University. I am also thankful to my committee members, Dr. Arthur D. Donovan, Dr. Brent V. Miller and Dr. Debbie Thomas for their guidance, support and constructive criticisms. This research would not have been successful without the very helpful suggestions they provided throughout this project. I also want to thank Dr. Michael M. Tice for guiding me through the inorganic geochemistry aspect of this project.

I would like to thank Pioneer Natural Resources, BP America and Comstock Resources for providing the data set for this research. This research would not have been successful without the financial support of the Crisman Institute for Petroleum Studies, The Berg-Hughes Center for Petroleum and Sedimentary Systems, The American Association of Petroleum Geologists (AAPG) Foundation, and the Society of Exploration Geophysicists (SEG) Foundation. I would like to thank the Director of the Berg-Hughes Center, Dr. Mukul Bhatia, for ensuring that I had the finances to complete this project. I am grateful to the R. Ken Williams '45 Radiogenic Isotope Geosciences Laboratory at Texas A&M University for the CA-ID-TIMS analyses.

I want to thank my loving mother for her prayers and support through the years. I want to thank my elder brother, Firmus, for always believing in me. I am thankful to my loving wife, Nikita, whose love, patience and support carried me to the finish line of this project.

I also want to thank the entire faculty and staff of the Department of Geology & Geophysics for making my time at Texas A&M University a great experience. Specifically, I would like to thank Dawn R. Spencer, Suzanne Rosser, Patricia Fike and Randolph Rozean for their assistance throughout the course of my research. I want to thank my friends and colleagues Hamid Adesokan, Mohamed Moustafa, Kieron Prince and Aris Pramudito for their willingness to support and help me at different times during my time at Texas A&M University. Finally, I want to thank the following undergraduate students Robert Elder, Alden Griffin, Juan Pablo Acevedo, Kristin Moczygemba, Kory Talcott, Eduardo Alvarez, Alex Brown, Samir Jreij, Christopher Garza and Luke Gezovich for doing undergraduate research with me. Their different undergraduate research projects contributed immensely to the overall success of my research and saved me a lot of time.

CONTRIBUTORS AND FUNDING SOURCES

Contributors

This work was supervised by a dissertation committee consisting of Dr. Michael Pope (committee chair), Dr. Arthur Donovan and Dr. Brent Miller of the Department of Geology & Geophysics, and Dr. Debbie Thomas (external committee member) of the Department of Oceanography and Dean of the College of Geosciences. Dr. Michael Tice guided me through the inorganic geochemistry in chapter III.

The data set for this research was provided by Pioneer Natural Resources, BP America and Comstock Resources. XRF data for the BP/SLB Lozier Canyon #1 well was made available to me by my colleague Aris Pramudito. XRF Data set for the Swenson 1H well and wells 1 and 2 were collected with my colleague Matthew Wehner for separate independent research using various elements of interest. I also benefited from organic and inorganic geochemistry data sets from unpublished and published M.S. and Ph.D. theses that were integrated with my original work. All other work conducted for the dissertation was completed by the student independently.

Funding Sources

My graduate study was supported by a fellowship from Crisman Institute for Petroleum Studies and the Berg-Hughes Center for Petroleum and Sedimentary Systems. This work was also made possible in part by AAPG Foundation grant-in-aid, SEG Foundation scholarship, and the Priscilla & Thomas Kelly ’53 Fellowship Award.

NOMENCLATURE

ACM	Antonio Creek Member
AIR	Aryl Isoprenoid Ratio
BI	Bioturbation Index
CA-ID-TIMS	Chemical Abrasion Isotope Dilution Thermal Ionization Mass Spectrometry
cfcf	cubic feet/cubic feet
CP	Comanche Platform
ED-XRF	Element Dispersive X-Ray Fluorescence
EFGOB	Eagle Ford Group Outcrop Belt
Enr.Fac.	Enrichment Factor
Eu	Europium
Eu*	Europium Anomaly
GAPI	Gamma-Ray American Petroleum Industry
GR	Gamma Ray
HO	Highest Occurrence
ICP-MS	Inductively Coupled Plasma Mass Spectrometry
K	Potassium
k.y.	thousand year (duration)
KWIS	Cretaceous Western Interior Seaway
LA-ICP-MS	Laser Ablation Inductively Coupled Plasma Mass Spectrometry
LCM	Lozier Canyon Member

LO	Lowest Occurrence
m.y.	million year (duration)
Ma	Million Year (Age)
MB	Maverick Basin
Mo	Molybdenum
Ni	Nickel
Ohm	Ohm Meter
Pb	Lead
PCA	Principal Component Analysis
Pr/Ph	Pristane/Phytane
RF-I	Redox Facies ICPMS
RF-X	Redox Facies X-RF
RSTE	Redox Sensitive Trace Element
SMA	San Marcos Arch
SRM	Scott Ranch Member
STSP	South Texas Submarine Plateau
Th	Thorium
TOC	Total Organic Carbon
U	Uranium
V	Vanadium
VPDB	Vienna Pee Dee Belemnite
XRD	X-Ray Diffraction

TABLE OF CONTENTS

LIST OF FIGURES

LIST OF TABLES

Page

CHAPTER I

INTRODUCTION

Background

The Upper Cretaceous (Cenomanian – Turonian) Eagle Ford Group is an important unconventional source rock reservoir in the subsurface of south Texas that produces oil, condensate and dry gas from up dip to down dip, and is an integral part of the growth of the United States' unconventional resource plays since 2008 (Cusack et al., 2010). Prior to Mitchel Energy successfully fracturing the Barnett Shale of the Fort Worth Basin in the early 1980s to commercially produce natural gas, mudstone generally was considered uneconomic resource play for major oil companies because its small grain size and extremely low permeability, and was inadequately studied and poorly understood (Ehler and Blatt, 1982; Selley, 1998; Blatt et al., 2006). Consequently, organic-rich, mudstone-dominated successions like the Eagle Ford Group were described as homogeneous and monotonously uniform sedimentary rocks that formed from continuous mud deposition during suspension settling out of the water column (Ehler and Blatt, 1982; Dawson, 2000; Blatt et al., 2006). Following Mitchel Energy's success in the Barnett Shale, several oil and gas companies have successfully explored and exploited organic-rich mudstone as unconventional source rock reservoirs (for example, the Eagle Ford Group in south Texas and the Wolfcamp Formation in the Permian Basin), providing scientists and researchers with valuable data sets to study mudstone. Consequently, scientists are now beginning to understand the complexities in mudstone-dominated successions and the heterogeneities in their associated depositional environments.

In this research, a multi-disciplinary approach was used to study the organic-rich, mudstone-dominated succession of the Eagle Ford Group within its three-dimensional stratigraphic framework. The research aims to better characterize heterogeneities in the Eagle Ford Group's organic-rich, mudstone-dominated succession and their associated depositional environments and expand our current understanding of mudstone complexities for successful oil and gas exploration and exploitation of unconventional source rock reservoirs. First, the study investigates the outcrop to subsurface chronostratigraphy of the Eagle Ford Group by providing a high-precision chronostratigraphic correlation that ties outcrop analogs to subsurface oil- and gas-producing units to understand the Eagle Ford Group's three-dimensional stratigraphic architecture and timing of significant geological events. Second, the research documents the sedimentological and geochemical variations within the Eagle Ford Group depositional settings and provide insights to better understand heterogeneities in organic-rich mudstone depositional environments. Third, the research investigates the use of laser ablation inductively coupled plasma mass spectrometry (LA-ICP-MS) apatite trace element concentrations as a technique that provides a potentially rapid, sensitive, cost-effective and viable way to characterize the Eagle Ford Group's volcanic ashes for stratigraphic correlation across west Texas.

References

Blatt, H., R. Tracy, and B. Owens, 2006, Petrology: Igneous, sedimentary, and metamorphic: New York, W.H. Freeman and Company, 3rd Ed. 530 p.

Cusack, C., J. Beeson, D. Stoneburner, and G. Robertson, 2010, The discovery, reservoir attributes, and significance of the Hawkville Field and Eagle Ford Shale trend, Texas, Gulf Coast Association of Geological Societies, Transactions, v. 60.

Dawson, W. C., 2000, Shale microfacies: Eagle Ford Group (Cenomanian-Turonian) north-central Texas outcrops and subsurface equivalents, Gulf Coast Association of Geological Societies Transactions, v. 50, p. 607-621.

Ehler, E., and H. Blatt, 1982, Petrology: Igneous, sedimentary and metamorphic. San Francisco, WH Freemanand Company, 732 p.

Selley, R., 1998, Elements of petroleum geology: Waltham, Academic Press, 2nd Ed. 470 p.

CHAPTER II

OUTCROP TO SUBSURFACE CHRONOSTRATIGRAPHY OF THE CENOMANIAN – TURONIAN EAGLE FORD GROUP (TEXAS, USA) BASED ON U-PB ASH BED ZIRCON GEOCHRONOLOGY

Overview

Isotope dilution thermal ionization mass spectrometry (ID-TIMS) analyses of individual zircon grains characterizing sixteen volcanic ash beds from three outcrops and two petroleum industry cores were integrated with regional biostratigraphy to provide a comprehensive outcrop-to-subsurface geochronology for the Cenomanian – Turonian Eagle Ford Group, Texas, USA. The geochronology provides constraints for the outcrop-to-subsurface chronostratigraphy and builds on existing Eagle Ford Group age models. The $^{206}Pb/^{238}U$ ages range from 96.45 ± 0.18 Ma near the base of the Eagle Ford Group in west Texas to 88.9 ± 0.12 Ma near the base of the Austin Chalk in Karnes County, Texas. This interval encompasses uppermost Lower Cenomanian, Turonian and upper Lower Coniacian, spanning ~ 7.5 m.y. of deposition from the base of the Eagle Ford Group to the base of the Austin Chalk, and provides important age constraints that tie the Eagle Ford Group outcrops in west Texas to subsurface oil-and-gas producing wells in south Texas. The $^{206}Pb/^{238}U$ age models constrain deposition for the base of the Eagle Ford Group in both west and south Texas to the uppermost Lower Cenomanian. Deposition for the base of the Austin Chalk in west Texas (Terrell County) is constrained to the Upper Turonian, whereas deposition for the base of the Austin Chalk in south Texas (Karnes County) is constrained to the upper Lower Coniacian. The age models are largely consistent with Eagle Ford Group isochore thickness trends, indicating substantial erosion occurred in south Texas (close to the San Marcos Arch) relative to west Texas.

Introduction

The Upper Cretaceous (Cenomanian – Turonian) Eagle Ford Group is an important source rock reservoir in the subsurface of south Texas and is an integral part of the growth of the United States' unconventional resource plays since 2008 (Cusack et al., 2010). The Eagle Ford Group outcrop at Lozier Canyon and others along Highway 90 in west Texas provide excellent exposures that are a natural laboratory to study organic-rich mudstone and are analogs for the subsurface reservoirs in south Texas (figure II.1). Therefore, providing high-precision chronostratigraphic correlation that ties outcrop units to subsurface oil- and gas-producing units is critical to understanding the Eagle Ford Group three-dimensional stratigraphic architecture and timing of significant geological events. The Eagle Ford Group outcrop and subsurface stratigraphy is well documented in the literature (Donovan and Staerker, 2010; Donovan et al., 2012; Gardner et al., 2013; Corbett et al., 2014; Denne et al., 2014; Lowery et al., 2014; Donovan et al., 2015; Eldrett et al., 2015; Denne et al., 2016; Denne and Breyer, 2016; Donovan et al., 2016; Minisini et al., 2017; Lowery and Leckie, 2017b; Alnahwi et al., 2018), and this study builds on existing age models by providing detailed chronostratigraphic correlation based on volcanic ash uranium (U) – lead (Pb) zircon geochronology linking outcrop units to subsurface oil- and gas-producing units.

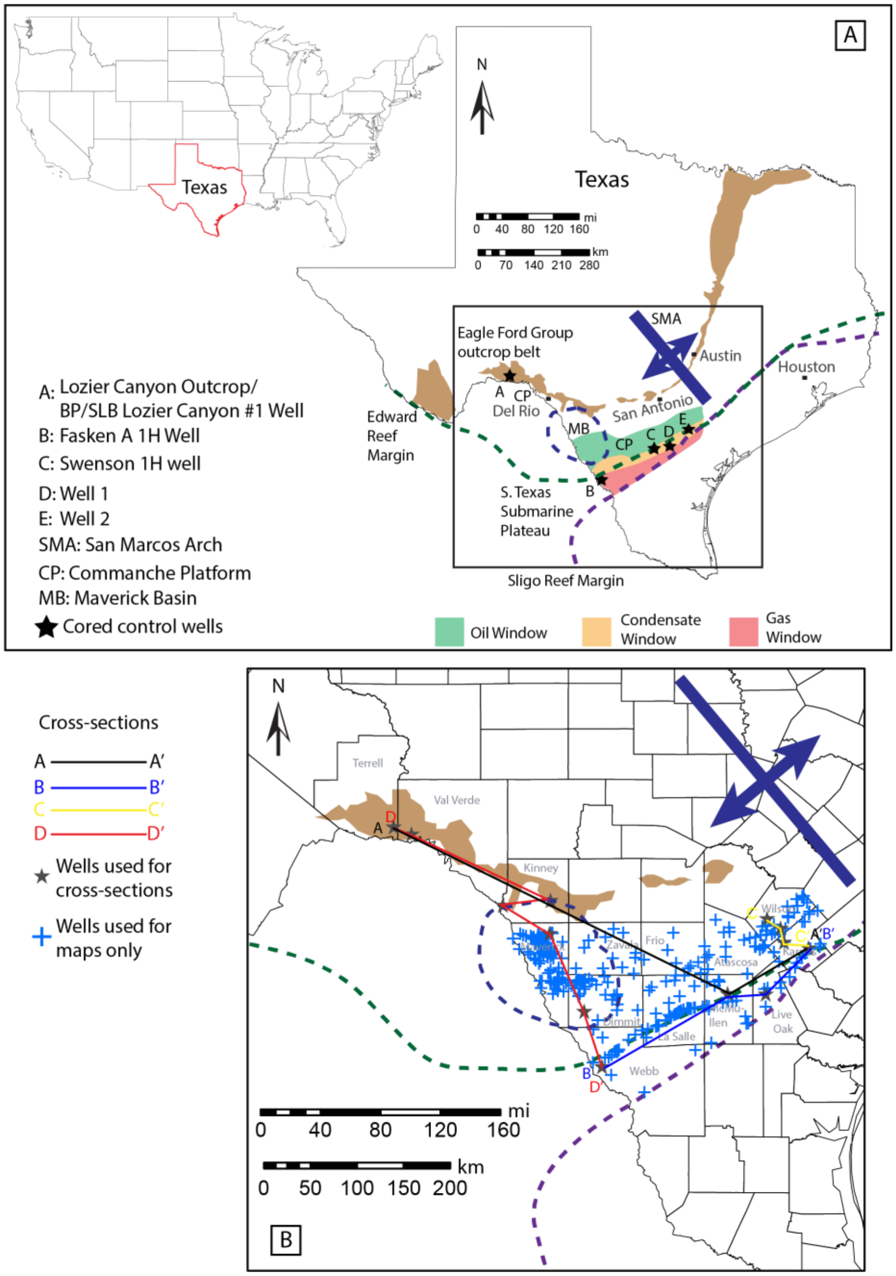

Figure II.1 (A) Location map showing the state of Texas, Eagle Ford Group outcrop belt, major structural and physiographic features, well locations for cored wells with biostratigraphy and/or U-Pb zircon geochronology age, and the Eagle Ford Group play in south Texas. Black polygon highlights zoomed-out area in figure B. (B) Location map showing wells with geophysical well logs used in isochore maps, cross-sections and cored wells. Eagle Ford Group oil and gas window modified from EIA 2010.

The Eagle Ford Group (figure II.2) was deposited in the southern gateway of North America's Cretaceous Western Interior Seaway (KWIS) during a major third-order sea level rise accompanying global greenhouse conditions (Kauffman, 1984; Arthur et al., 1987; Roberts and Kirschbaum, 1995; Donovan et al., 2012; Eldrett et al., 2015). The Lower Cretaceous Sligo (Hauterivian – Barremian) and Edwards (Albian) reef margins created paleo-topographic reliefs that persisted throughout the Upper Cretaceous until Eagle Ford Group deposition (Kauffman, 1984; Phelps et al., 2014), resulting in decreased accommodation along the ancestral reef trends. The greenhouse period that accompanied the global sea level rise was marked by rapid environmental and biotic changes, elevated tectonic activities, eruption of large igneous provinces (LIPs) and widespread burial of large amounts of organic carbon (Schlanger and Jenkyns, 1976; Scholle and Arthur, 1980; Arthur et al., 1987; Lee et al., 2013). In the United States, the Cordilleran orogenic system (figure II.2) contained a zone of extensive volcanic activity that intermittently produced large amounts of volcanic ash that are preserved as bentonites in the KWIS. These volcanic ashes provide regional marker beds for stratigraphic correlation and precise age dating.

The Eagle Ford Group outcrops in west Texas were correlated to subsurface oil- and gas-producing wells in south Texas using hand-held gamma ray logs for outcrops and wireline well logs for both outcrop research wells and oil- and gas-producing wells. This study provides detailed stratigraphic correlation linking the Eagle Ford Group outcrops in west Texas to subsurface oil- and gas-producing wells in south Texas using four cored wells and several wells (~250) with geophysical wireline logs.

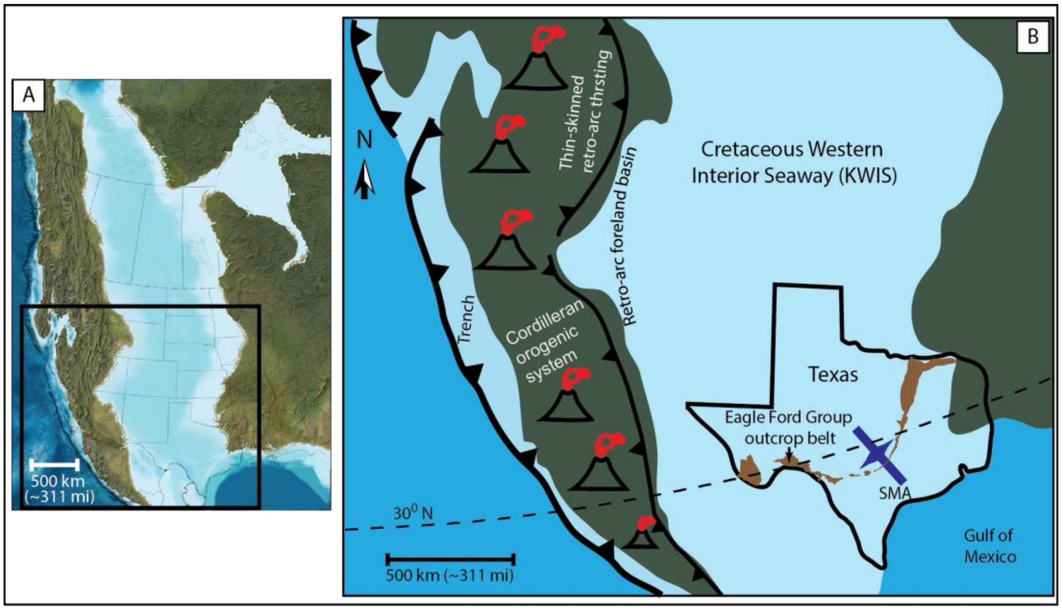

Figure II.2 Upper Cretaceous (92.1 Ma) paleogeographic map of the Cretaceous Western Interior Seaway (KWIS; modified from Blakey, 2011). (A) The Eagle Ford Group was deposited during a major third-order sea level rise. The KWIS extended from the Gulf of Mexico to the Canadian Arctic. The black polygon highlights the zoomed-out section in B. (B) Outline of the Eagle Ford Group outcrop belt in the KWIS. The Cordilleran orogenic system had a zone of extensive volcanic activity that intermittently produced large amounts of ash.

The study area spans ~ 47000 sq km (~18146 sq mi) from Terrell County (west Texas) to Wilson and Karnes County southwest of the San Marcos Arch, a regional structural arch that is the subsurface continuation of the Llano uplift in central Texas (Adkins, 1932). This long distance correlation is constrained by high-precision chemical abrasion isotope dilution thermal ionization mass spectrometry (CA-ID-TIMS) uranium (U) – lead (Pb) zircon geochronology and regional biostratigraphy to establish a comprehensive outcrop to subsurface chronostratigraphy of the Eagle Ford Group in this area.

Stratigraphy

The Eagle Ford Group, also referred to as the Boquillas Formation by some authors (e.g. Udden 1907; Pessagno 1969), is an unconformity-bounded, mudstone-dominated stratigraphic unit between the underlying Woodbine Group (Karnes County area)/ Buda Limestone (west Texas) and the overlying Austin Chalk (figure II.3). The Eagle Ford Group strata in outcrops (west Texas) and in the subsurface (south Texas) comprises two informal units called the Lower and Upper Eagle Ford Formations (Donovan et al., 2012), each comprised of two allostratigraphic members. In the west Texas outcrops, these members are designated as the Lozier Canyon (Lower Member) and Antonio Creek (Upper Member) Members of Lower Eagle Ford Formation and the Scott Ranch (Lower Member) and Langtry (Upper Member) Members of the Upper Eagle Ford Formation (Donovan et al., 2012; Gardner et al., 2013). A similar sub-division also was used for the subsurface in south Texas where the Lower and Upper Eagle Ford Formations are each sub-divided into upper and lower members (Donovan et al., 2012). This work follows the stratigraphic nomenclature of Donovan et al., (2012).

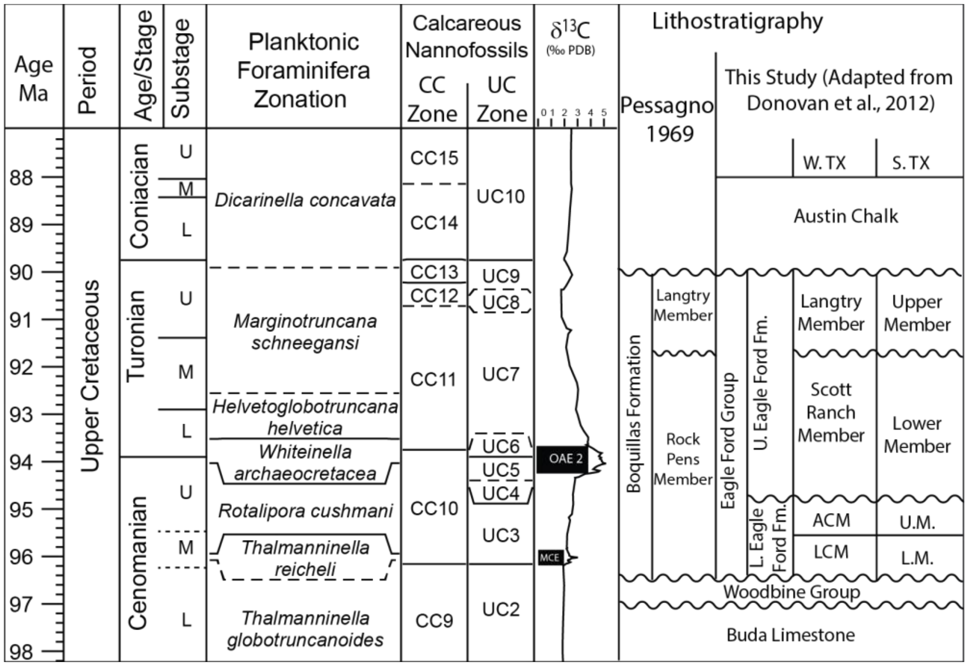

Figure II.3 Chronostratigraphy for the unconformity bounded Cenomanian - Turonian Eagle Ford Group strata. Modified after Donovan et al., 2012. Geologic time scale after Ogg et al. (2016). LCM = Lozier Canyon Member; ACM = Antonio Creek Member; L = lower; M = middle; U = upper; OAE = oceanic anoxic event; MCE = Middle Cenomanian excursion.

Methods and Data

Zircon crystals characterizing sixteen ash beds from Antonio Creek (~ 2.5 mi/4 km south of Lozier Canyon), road cut outcrop along US Highway 90 (~ 12 km/7.5mi north of Lozier Canyon), Osman Canyon (~ 20 km or 12.4 mi NE of Lozier Canyon), well 2 (Karnes County) and Swenson 1H well (McMullen County) were analyzed for $^{206}Pb/^{238}U$ and $^{207}Pb/^{235}U$ isotope ratios using the CA-ID-TIMS method (Mattinson, 2005). The Antonio Creek and US Highway 90 ash beds were correlated to the Lozier Canyon outcrop using high-resolution bed-by-bed stratigraphic correlation between Lozier Canyon and Antonio Creek (Gardner, 2013). CA-ID-TIMS analyses were conducted in the R. Ken

Williams ’45 Radiogenic Isotope Geosciences Laboratory at Texas A&M University (TAMU) on a ThermoScientific Triton thermal ionization mass spectrometer. This instrument is equipped with a retarding-potential-quadrupole (RPQ) energy filter and a modified MassCom secondary electron multiplier (SEM). Zircons with Pb content of about 1 to 100 picogram (pg) were measured by peak-hopping on the SEM, >200 pg Pb were measured with a two-step Faraday/SEM dynamic gain analysis. Uranium was analyzed as the dioxide in static Faraday mode.

Bulk rocks were crushed in a Bico Badger jaw crusher and disaggregated in a Bico disk pulverizer. Fine clays were removed from weakly indurated volcanic ash beds with a combination of sonication, deflocculating with dimethyl sulfoxide (DMSO) and differential gravity settling in water. Dense minerals were concentrated using a Wilfley table followed by heavy liquid separations (bromoform and methyline iodide). Magnetic separations were conducted on a Frantz isodynamic separator. Minerals for ID-TIMS dating were hand-picked under a binocular microscope and photographed. Chemical abrasion and dissolution were both conducted in an eighteen-position Parr-style high pressure dissolution vessel using 200 µl modified Parrish-style teflon capsules.

Sample preparation and separation chemistry for U-Pb dating was conducted in the Class 100 ultra-clean laboratory. U-Pb zircon geochronology protocols largely follow the annealing, chemical abrasion, and thermal-ionization mass spectrometry (CA-TIMS) methods described in (Mattinson, 2005). Concomitant total procedural blanks for U-Pb protocols were on the order of 0.5-0.8 pg. Samples were spiked with the EarthTime ^{205}Pb-^{233}U-^{235}U spike (Condon et al., 2015). CA-ID-TIMS data were reduced using the

“YourLab” algorithms of Schmitz and Schoene (2007). Diagrams were plotted and final ages calculated in IsoPlot (Ludwig, 2003). Final U-Pb age interpretations are given in the form AGE ± X (Y) [Z], where AGE is the weighted mean $^{206}Pb/^{238}U$ age of individual analyses interpreted to be least affected by Pb-loss, or xenocrystic or antecrystic inheritance; X, Y, Z represent the age uncertainty taking into account random and systematic analytical sources (X), those combined with contributions from uncertainty in the ET535 spike (Y) and both of those and including decay constant uncertainties (Z).

Despite the overall success of the chemical abrasion technique (Mattinson, 2005), a small number of analyses in this study reflect residual Pb-loss or other complications such as incorrect Pb_c correction, inheritance or long magmatic residence time; these analyses were excluded from the final age calculation and are indicated as such in appendix A. The final age interpretations were calculated using the weighted mean of the remaining $^{206}Pb/^{238}U$ ages. The stratigraphic position of all the volcanic ash beds (outcrop and subsurface cores) are reported in meters (and feet) above the top of the Buda Limestone.

Biostratigraphic analyses on cores were performed on wells 1 and 2 by biostratigraphic services consultants (Morin Biostratigraphic Studies and BugWare, Inc., respectively) and were correlated with available biostratigraphic data for Lozier Canyon outcrop and Fasken A 1H well (Donovan and Staerker, 2010; Corbett et al., 2014; Lowery et al., 2014; Lowery and Leckie, 2017b). Core samples for wells 1 and 2 and the Swenson 1H well were analyzed for bulk rock inorganic carbonate fraction of $^{13}C/^{12}C$ ($\delta^{13}C_{carb.}$) isotope ratios at ~ 30.5 cm (1 ft.) interval. In wells 1 and 2, selected intervals near the

Lower - Upper Eagle Ford Formation contact anticipated to have the positive carbon isotope excursion (CIE) associated with oceanic anoxic event 2 (OAE 2), a positive 2 to 4 ‰ shift in the $\delta^{13}C$ that occurs close to the Cenomanian – Turonian boundary and is a global secondary marker for this stage boundary (Schlanger and Jenkyns, 1976; Arthur et al., 1987; Kennedy et al., 2005), were further analyzed for organic fraction $^{13}C/^{12}C$ ($\delta^{13}C_{org.}$) isotope ratios at ~ 30.5 cm (1 ft.) interval. All the stable isotope analyses were performed at the Stable Isotope Geosciences Facility (SIGF) at Texas A&M University and the values are reported relative to Vienna Pee Dee Belemnite (VPDB). Carbon stable isotope data for wells 1and 2 and the Swenson 1H also were correlated with carbon isotope data for the Lozier Canyon outcrop and Fasken A 1H core (Donovan et al., 2012; Corbett et al., 2014; Lowery et al., 2014). Geophysical well logs were correlated first for wells with biostratigraphic and/or U-Pb geochronology age control in Webb, McMullen, Live Oak and Karnes County to a composite section of the Lozier Canyon, Antonio Creek and BP/SLB Lozier Canyon #1 well in Terrell County, Texas. The well logs used in the high-resolution stratigraphic correlation are the total gamma ray (GR), spectral gamma ray (SGR – uranium, U; thorium, Th; and potassium, K), and resistivity logs. The regional correlations of the Eagle Ford Group involve more than 250 wells utilizing only geophysical well logs (GR) across multiple counties. Well tops from these wells were used to generate Eagle Ford Group isochore thickness maps in Petrel®.

Results

U-Pb Zircon Geochronology

Population variance in the U-Pb zircon dates varies by individual ash bed (figure II.4). Some ash beds have zircons with broad age range and multiple sample population, reflecting complex processes such as inheritance, long magmatic residence time, and post-eruption reworking of older zircon grains in the sedimentary environment that may potentially degrade the interpretation of the final U-Pb age (Schoene, 2014).

The AC-B10 ash bed is ~ 0.5 m (1.5 ft.) stratigraphically above the top of the Buda Limestone (figure II.5). Seventeen out of the thirty-six analyzed zircon grains were excluded from the final age interpretation because they were inferred to be xenocrysts or extreme outliers due to Pb-loss, incorrect Pb_c correction or unusably imprecise analysis. The weighted mean age of 96.45 ± 0.143 (0.15) [0.18] Ma with mean square of weighted deviates (MSWD) of 2.23 (figure II.4A) for the remaining nineteen analyses was taken as the most robust age interpretation. The AC-B9 ash bed is ~ 2.9 m (9.5 ft.) stratigraphically above the top of the Buda Limestone (figure II.5). Eight zircon grains were analyzed, and one was excluded from the final age interpretation because it was inferred to be a xenocryst. The weighted mean age of 96.42 ± 0.105 (0.12) [0.16] Ma with MSWD of 1.53 for the remaining seven remaining zircon grains (figure II.4B) was taken as the most robust age interpretation. The AC-B8 ash bed is ~ 18 m (59 ft.) stratigraphically above the top of the Buda Limestone (figure II.5).

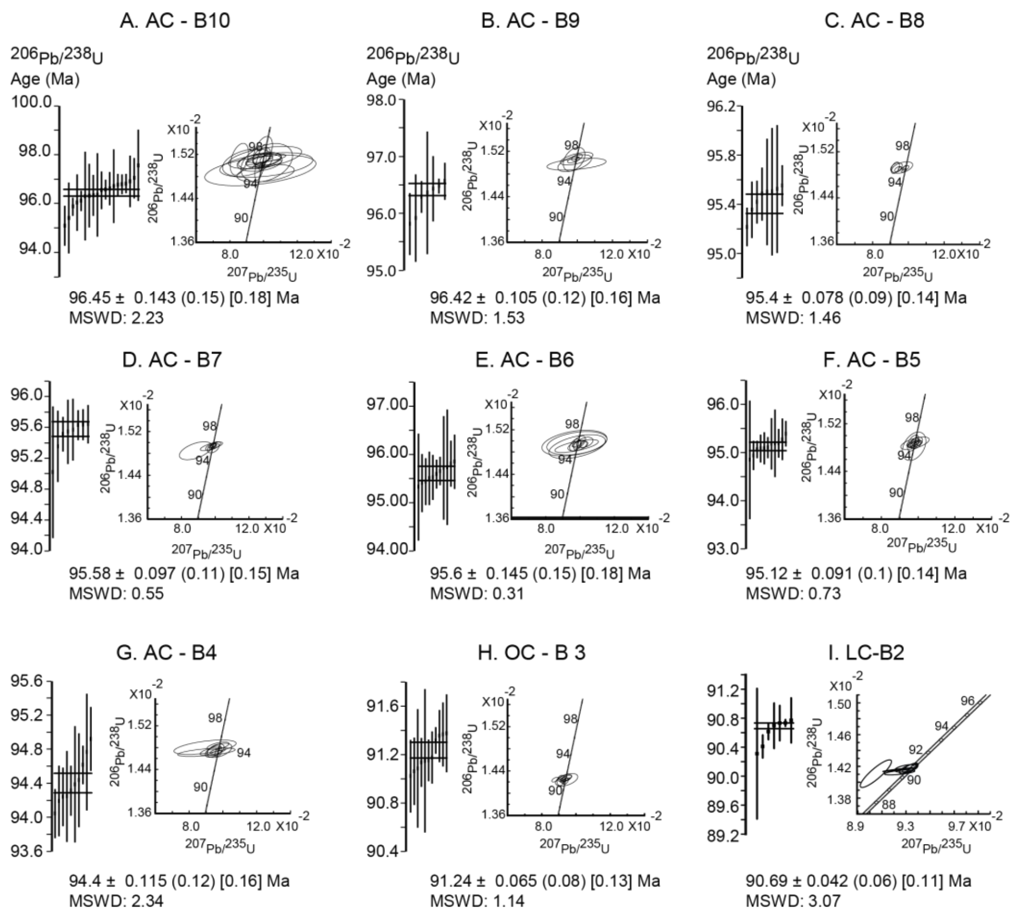

Figure II.4 Age distribution and concordia plots of isotope dilution thermal ionization mass spectrometry (ID-TIMS) $^{206}Pb/^{238}U$ zircon analyses for individual volcanic ash beds. (A) AC-B10 ash bed (Terrell County). (B) AC-B9 ash bed (Terrell County). (C) AC-B8 ash bed (Terrell County). (D) AC-B7 ash bed (Terrell County). (E) AC-B6 ash bed (Terrell County). (F) AC-B5 ash bed (Terrell County). (G) AC-B4 ash bed (Terrell County). (H) OC-B3 ash bed (Terrell County). (I) LC-B2 ash bed (Terrell County). (J) LC-B1 ash bed (Terrell County). (K) S-B2 ash bed (McMullen County). (L) S-B1 ash bed (McMullen County). (M) W2-B4 ash bed (Karnes County). (N) W2-B3 ash bed (Karnes County). (O) W2-B2 ash bed (Karnes County). (P) W2-B1 ash bed (Karnes County). MSWD = mean square of weighted deviates.

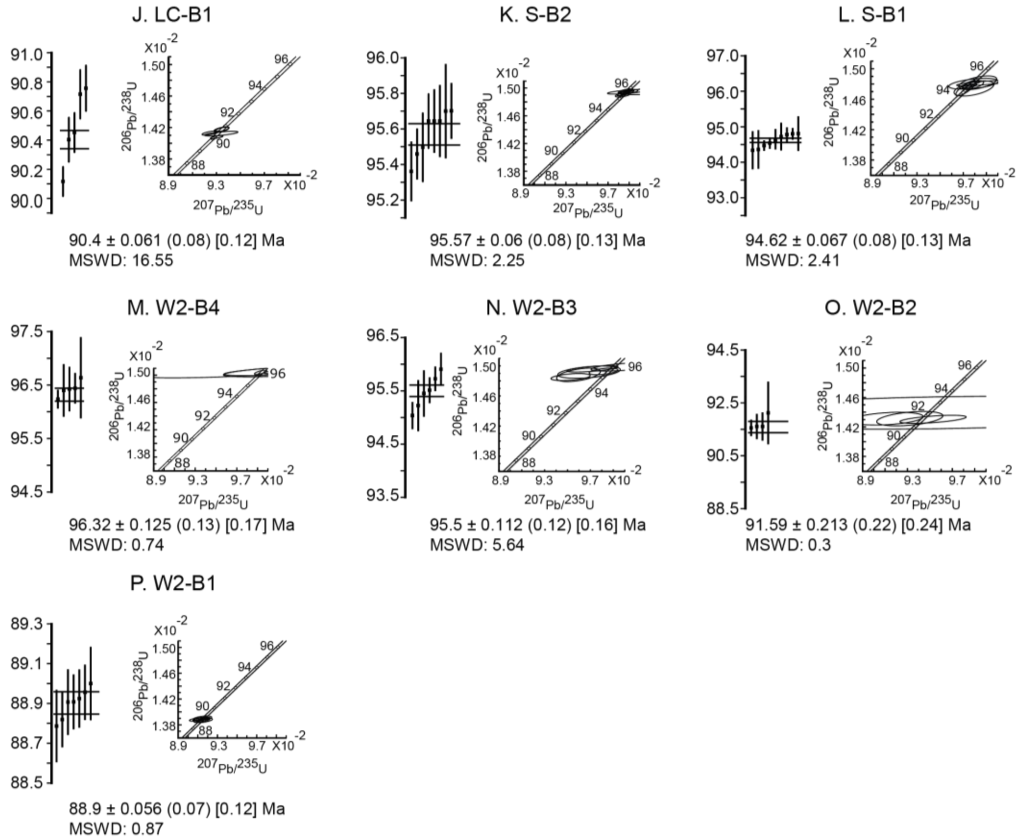

Figure II.4 Continued

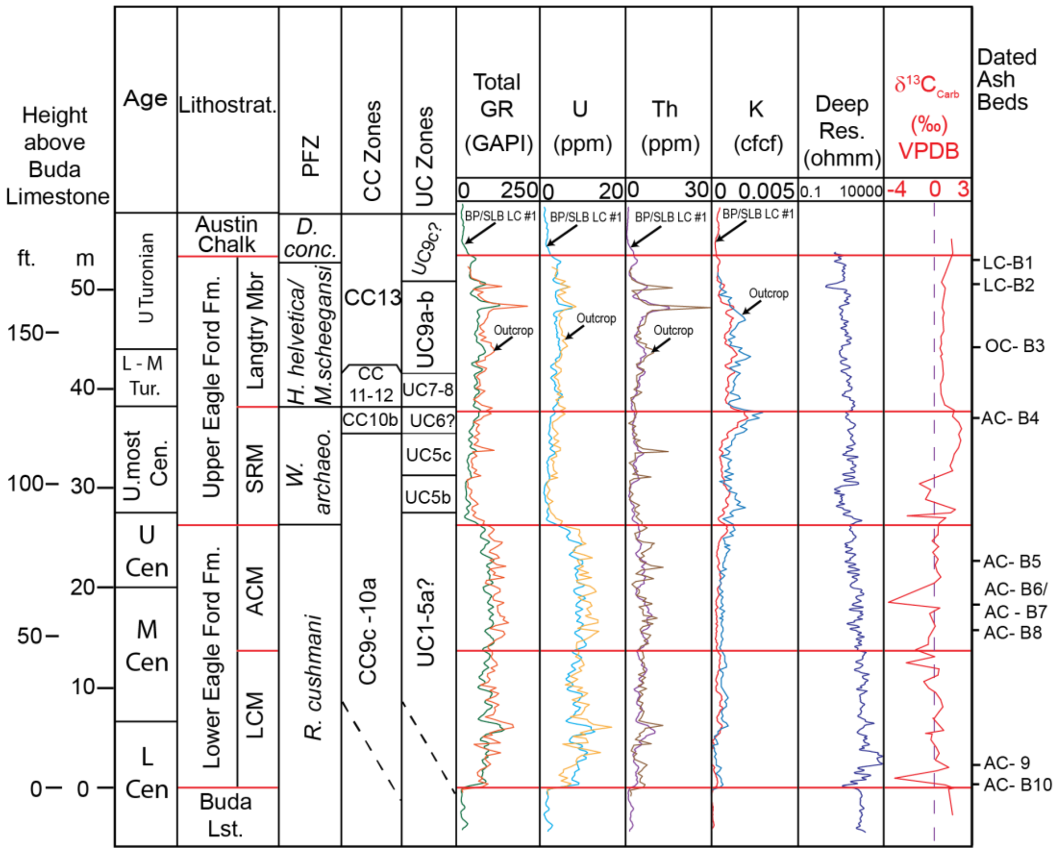

Figure II.5 Composite section for the Lozier Canyon outcrop, Antonio Creek outcrop and BP/SLB Lozier Canyon #1 research well (Terrell County, Texas) with a summary of the biostratigraphic, U-Pb ages, and petrophysical data. The integrated stratigraphic data from this outcrop provides the foundation for correlating outcrop units to subsurface units in oil- and gas-producing wells in south Texas. Planktic foraminifera zonation (PFZ) is from Lowery et al. (2014); CC and UC calcareous nannofossil zones are from Corbett et al. (2014); $\delta^{13}C_{carb}$ is from Donovan et al. (2015); geophysical well logs are from Donovan et al., (2012) and (2015). Geologic stages after Ogg et al. (2016). Fm. = Formation; Mbr. = Member; Cen = Cenomanian; Tur = Turonian; Con = Coniacian; U.most = Uppermost; Res. = Resistivity; Lst. = Limestone; *D. conc.* = *Dicarinella concavata*; *W. archaeo.* = *Whiteinella archaeocretacea*

Three out of the eleven analyzed zircon grains were excluded from the final age interpretation because they were inferred to be xenocrysts. The weighted mean age of 95.4 ± 0.078 (0.09) [0.14] Ma with MSWD of 1.46 for the remaining eight analyses (figure 4.IIC) was taken as the most robust age interpretation. The AC-B7 ash bed is ~ 19.5 m (64 ft.) stratigraphically above the top of the Buda Limestone (figure II.5). Four out of the twelve analyzed zircon grains were excluded from the final age interpretation because they were inferred to be xenocrysts. The weighted age of 95.58 ± 0.097 (0.11) [0.15] with MSWD of 0.55 for the remaining eight analyzed zircon grains (figure 4.IID) was taken as the most robust age interpretation. The AC-B6 ash bed is ~ 19.7 m (64.5 ft.) stratigraphically above the top of the Buda Limestone (figure II.5). Ten out of the twenty-one zircon grains analyzed were excluded from the final age interpretation because they were inferred to be xenocrysts or extreme outliers due to Pb-loss, incorrect Pb_c correction or unusably imprecise analysis. The weighted mean age of 95.6 ± 0.145 (0.15) [0.18] with MSWD of 0.31 for the remaining eleven analyzed zircon grains (figure 4.IIE) was taken as the most robust age interpretation. The AC B5 ash bed is ~ 24.4 m (80 ft.) stratigraphically above the top of the Buda Limestone (figure II.5). Eleven of the fourteen zircon grains analyzed have relatively tight cluster on Concordia plot with a weighted mean age of 95.12 ± 0.091 (0.1) [0.14] Ma and MSWD of 0.73 (figure 4 IIF). This age was taken as the most robust age interpretation due to the minimal effect of Pb loss, xenocrystic inheritance or incorrect Pb_c correction. The AC-B4 ash bed is ~ 41.1 m (135 ft.) stratigraphically above the top of the Buda Limestone (figure II.5). Seven out of the seventeen analyzed zircon grains were excluded from the final age interpretation because they were inferred to be xenocrysts or extreme outliers due to Pb-loss, incorrect Pb_c correction or unusably imprecise analysis. The weighted mean age of 94.4 ± 0.115 (0.12) [0.16] Ma with MSWD of 2.34 for the remaining ten analyzed zircon grains (figure 4.IIG) was taken as the most robust age interpretation. The OC-B3 ash bed is ~ 47.2 m (155 ft.) stratigraphically above the top of the Buda Limestone (figure II.5). Two out of the thirteen analyzed zircon grains were excluded from the final age interpretation because they were inferred to be xenocrysts. The weighted mean age of 91.24 ± 0.065 (0.08) [0.13] Ma with MSWD of 1.14 for the remaining eleven analyzed zircon grains (figure II.4G) was taken as the most robust age interpretation. The LC-B2 ash bed from the road cut outcrop along US Hwy 90 correlates to an ash bed at Lozier Canyon that is ~ 48.5 m (~159 ft.) stratigraphically above the top of the Buda Limestone. This ash bed also is 2.1 m (~ 6.9 ft.) stratigraphically below the Eagle Ford Group – Austin Chalk contact (figure II.5). Fifteen zircon grains were analyzed, and eight were excluded from the final age interpretation because they were inferred to be xenocrysts or extreme outliers due to Pb-loss, incorrect Pb_c or unusably imprecise analysis. The weighted mean age of 90.69 ± 0.042 (0.06) [0.11] Ma with MSWD of 3.07 for the seven remaining zircon grains was taken as the most robust age interpretation (figure II.4I). The LC-B1 ash bed from the road cut outcrop along US Hwy 90 correlates to an ash bed at Lozier Canyon that is ~ 50.5 m (166 ft.) stratigraphically above the top of the Buda Limestone. The stratigraphic position of this ash bed also is coincident with Eagle Ford Group – Austin Chalk contact (figure II.5). Five of the seven zircon grains analyzed have relatively tight cluster on Concordia plot with a weighted mean age of 90.40 ± 0.061 (0.08) [0.12] Ma and MSWD of 16.55

(figure II.4J). This age was taken as the most robust age interpretation due to the minimal effect of Pb loss, xenocrystic inheritance or incorrect Pb_c correction.

The S-B2 ash bed is 32 m (106 ft.) stratigraphically above the top of the Buda Limestone (figure II.6). All eight zircon grains analyzed are relatively tightly clustered on Concordia plot (figure II.4K), and their weighted mean age of 95.57 ± 0.06 (0.08) [0.13] with MSWD of 2.25 was taken as the most robust age interpretation. The S-B1 ash bed is 45 m (148.5 ft.) stratigraphically above the top of the Buda Limestone (figure II.6). Sixteen zircon grains were analyzed, and seven were excluded from the final age interpretation because they were inferred to be xenocrysts or extreme outliers due to incorrect Pb_c correction or unusably imprecise analysis. The weighted mean age of 94.62 ± 0.067 (0.08) [0.13] Ma with MSWD of 2.41 for the remaining nine grains was taken as the most robust age interpretation (figure II.4L).

The W2-B4 ash bed is ~11.5 m (~38 ft.) stratigraphically above the top of the Buda Limestone (figure II.7). Six out of the eleven zircon grains analyzed were excluded from the final age interpretation because they were inferred to be xenocrysts or outliers due to Pb loss or incorrect Pb_c correction. The remaining five grains have a weighted mean age of 96.32 ± 0.125 (0.13) [0.17] Ma with a MSWD of 0.74 (figure II.4M). This age was taken as the most robust age interpretation. The W2-B3 ash bed is ~48 m (~157.1 ft.) stratigraphically above the top of the Buda Limestone (figure II.7). Six out of the twelve analyzed zircon grains were excluded from the final age interpretation because they were inferred to be xenocrysts or unusable outliers due to Pb loss or incorrect Pb_c correction. The weighted mean age of 95.5 ± 0.112 (0.12) [0.16] with MSWD of 5.64 for the six remaining zircon grains was taken as the most robust age interpretation (figure II.4N). The W2-B2 ash bed is ~72.8 m (~ 239 ft.) stratigraphically above the top of the Buda Limestone (figure II.7). Nine out of the thirteen analyzed zircon grains were excluded from the final age interpretation because they were inferred to be xenocrysts or outliers due to Pb-loss or incorrect Pb_c correction. The remaining four analyses have a weighted mean age of 91.59 ± 0.213 (0.22) [0.24] with MSWD of 0.3 and was taken as the most robust age interpretation (figure II.4O). The W2-B1 ash bed is ~ 84 m (~ 270.3 ft.) stratigraphically above the top of the Buda Limestone, and ~ 1.4 m (~ 4.65 ft.) stratigraphically above the Eagle Ford Group – Austin Chalk contact (figure II.7). Seven out of the fourteen analyzed zircon grains are relatively tightly clustered on Concordia plot with a weighted mean age 88.9 ± 0.056 (0.07) [0.12] and MSWD of 0.87 (figure II.4P). This age was taken as the most robust age interpretation due to the minimal effect of Pb-loss, xenocrystic inheritance or incorrect Pb_c correction.

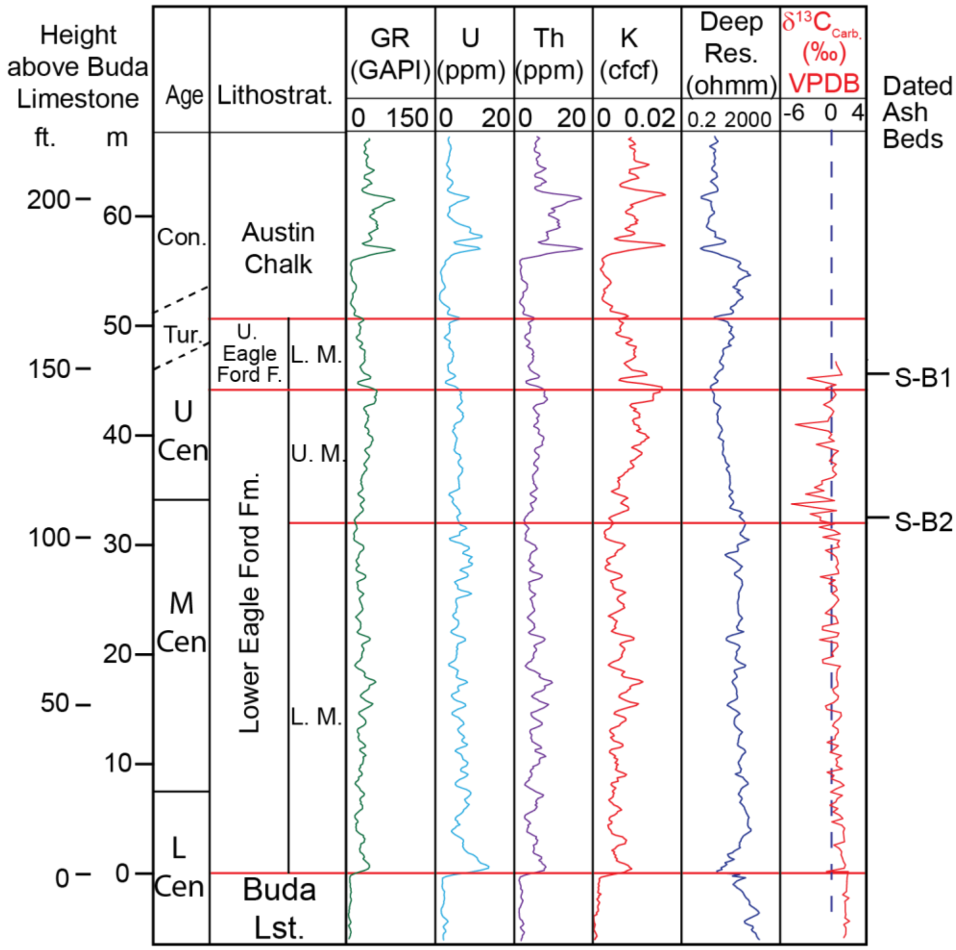

Figure II.6 Summary of Swenson 1H well (McMullen County, Texas) stratigraphy with geophysical logs showing the stratigraphic positions of the dated ash beds. Note that the Upper Member of the Upper Eagle Ford Formation is not present in this well.

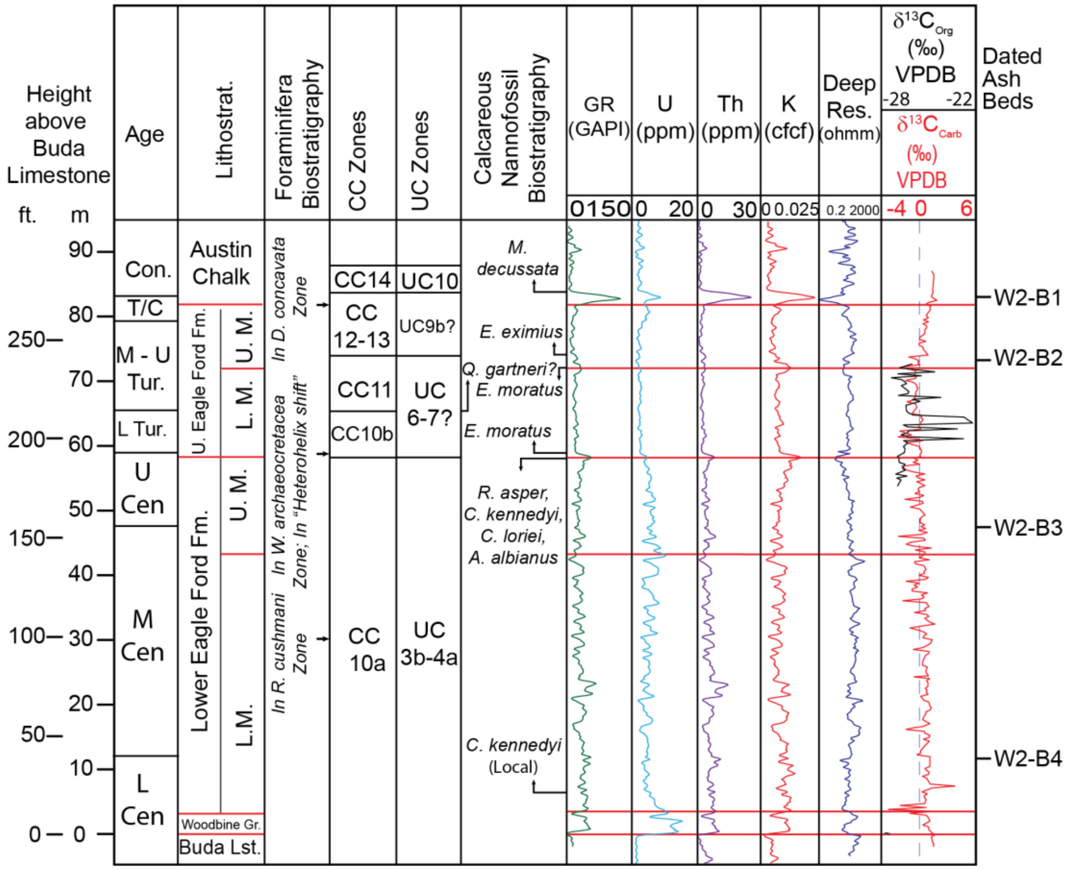

Figure II.7 Summary of well 2 (Karnes County, Texas) stratigraphy and geophysical well logs showing the stratigraphic positions of the dated ash beds. The occurrence of calcareous nannofossil *E. moratus* close to the Lower – Upper Eagle Ford Formation boundary in this well suggests a significant hiatus at this contact. Due to very poor preservation, foraminifera events were observed from only three samples (stratigraphic positions indicated with black arrows in the "foraminifera biostratigraphy" column). Geologic stages after Ogg et al. (2016).

Biostratigraphy and Carbon Stable Isotope Stratigraphy

Calcareous nannofossil preservation generally is very poor in the Lower Eagle Ford Formation (Corbett et al., 2014). Locally, the lowest occurrence (LO) of calcareous nannofossil *C. kennedyi*, a Lower Cenomanian marker for the base of the CC9b and UC1a zones at 100.5 Ma (Ogg et al., 2016), occurs stratigraphically higher in the Eagle Ford

Group and may not be a reliable age marker due to poor preservation (Corbett et al., 2014). The LO of *C. kennedyi* occurs near the base of the Eagle Ford Group within 2 to 10 m (6.6 to 33 ft.) stratigraphically above the top of the Buda Limestone in wells 2 and 1 (figures II.7 and II.8), consistent with observation in the Fasken A 1H well (Corbett et al., 2014). The Lower Eagle Ford Formation interval occurs within the foraminifera *R. cushmani* zone (figure II.9) (Lowery et al., 2014; Lowery and Leckie, 2017b). In wells 1 and 2, the highest occurrence (HO) of *C. Kennedyi*, *A. albianus*, *R. asper* and *C. loreiei* are the common calcareous nannofossil events that mark the Lower – Upper Eagle Ford Formation transition (figures II.7 and II.8), consistent with other Eagle Ford Group biostratigraphic studies (e.g. Corbett et al., 2014). In well 2, the LO of calcareous nannofossil *E. moratus*, a reliable Lower Turonian marker (Corbett et al., 2014; Denne et al., 2014; Denne et al., 2016; Ogg et al., 2016), is nearly coincident with the Lower – Upper Eagle Ford Formation contact and the HO of *C. kennedyi* (figure II.7). The LO of *E. moratus* and the HO *C. kennedyi* are two calcareous nannofossil events that are separated by ~ 900 k.y. (Corbett et al., 2014; Ogg et al., 2016). The LO of calcareous nannofossil *Q. gartneri* occurs at ~ 8 m (~26 ft.) above the Lower – Upper Eagle Ford Formation contact in well 2. Additionally, in well 2, the $\delta^{13}C_{org}$ for the Lower Turonian interval has isolated intervals with positive CIE (figure II.7). Although foraminifera preservation is very poor in well 2, the "*Heterohelix* shift," representing a dramatic shift in the planktic foraminifera assemblages in the uppermost Cenomanian (Leckie, 1985; Lowery and Leckie, 2017b), occurs in a sample from the Lower – Upper Eagle Ford Formation contact, just below a phosphate skeletal debris interval (chapter III). In well 1 (figure II.8), the HO of *H. chiastia*, a calcareous nannofossil event within the OAE 2 interval in the Eagle Ford Group (Corbett et al., 2014), occurs at ~ 2 m (~6.6 ft.) above the Lower - Upper Eagle Ford Formation contact within the positive $\delta^{13}C_{org}$ excursion. While no positive $\delta^{13}C_{carb}$ excursion record is preserved in well 1, the $\delta^{13}C_{org}$ delineates a positive CIE of ~+2 to +4 ‰ (figure II.8). The positive CIE occurs close to the Cenomanian – Turonian (C-T) stage boundary and is used as a global secondary marker for the C-T stage boundary (Schlanger and Jenkyns, 1976; Arthur et al., 1987; Kennedy et al., 2005). The LO of *E. moratus* occurs ~ 9 m (~ 29.5 ft.) above the Lower – Upper Eagle Ford Formation contact in well 1 and is used as a Lower Turonian proxy (Corbett et al., 2014; Ogg et al., 2016).

In wells 1 and 2, the LO of calcareous nannofossil *E. eximius*, a Middle – Upper Turonian marker, occurs within the Upper Member of the Upper Eagle Ford Formation, consistent with other regional studies (e.g. Corbett et al., 2014; Denne et al., 2016; Ogg et al., 2016). The LO of calcareous nannofossil *M. decussata*, a reliable Lower Coniacian marker (Corbett et al., 2014; Ogg et al., 2016), occurs near the base of the Austin Chalk in wells 2 and 1 (figures II.7 and II.8).

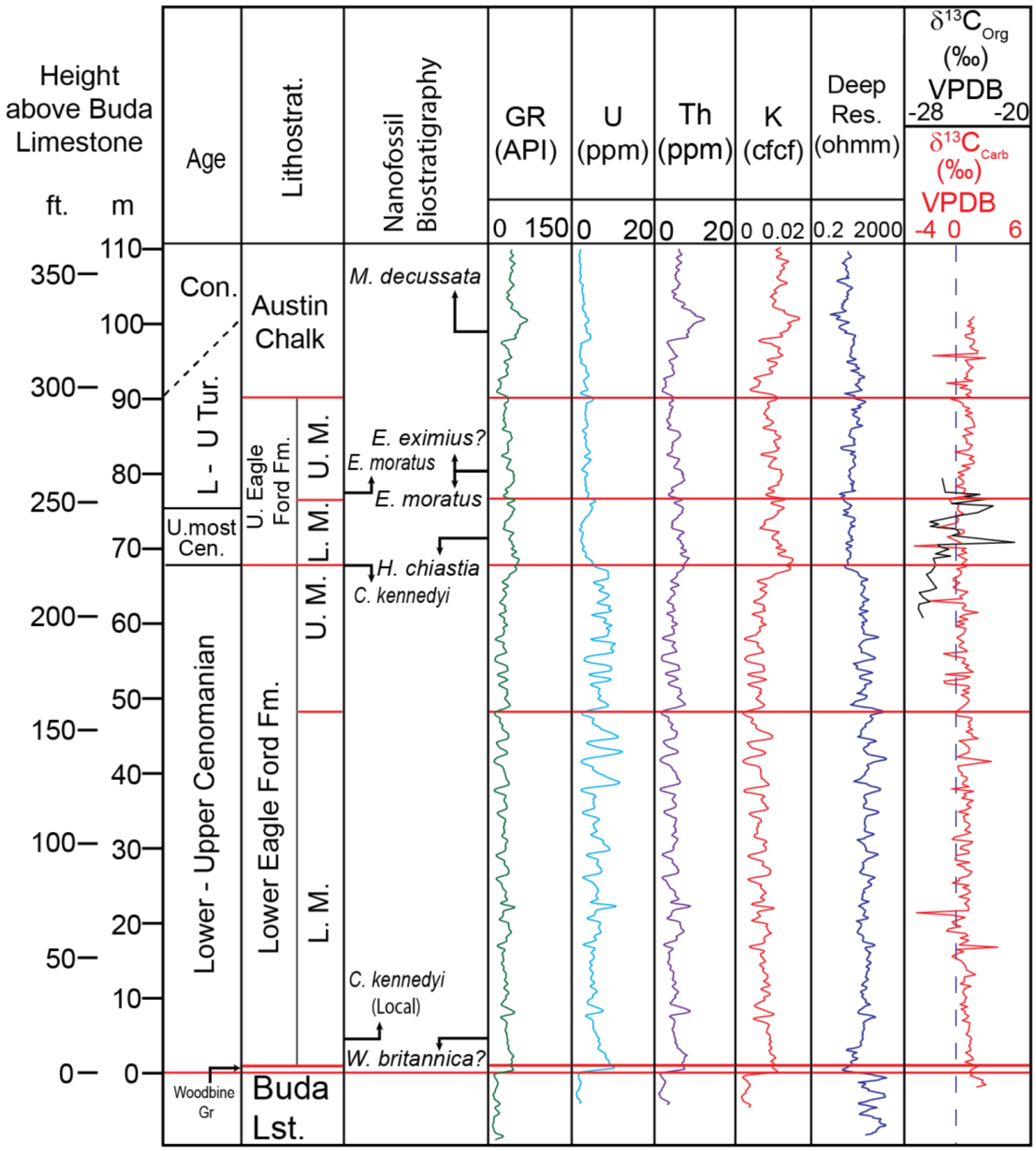

Figure II.8 Summary of well 1 (Live Oak County, Texas) stratigraphy and geophysical well logs. Geologic stages after Ogg et al. (2016). Well 1 has an expanded Lower – Upper Cenomanian interval.

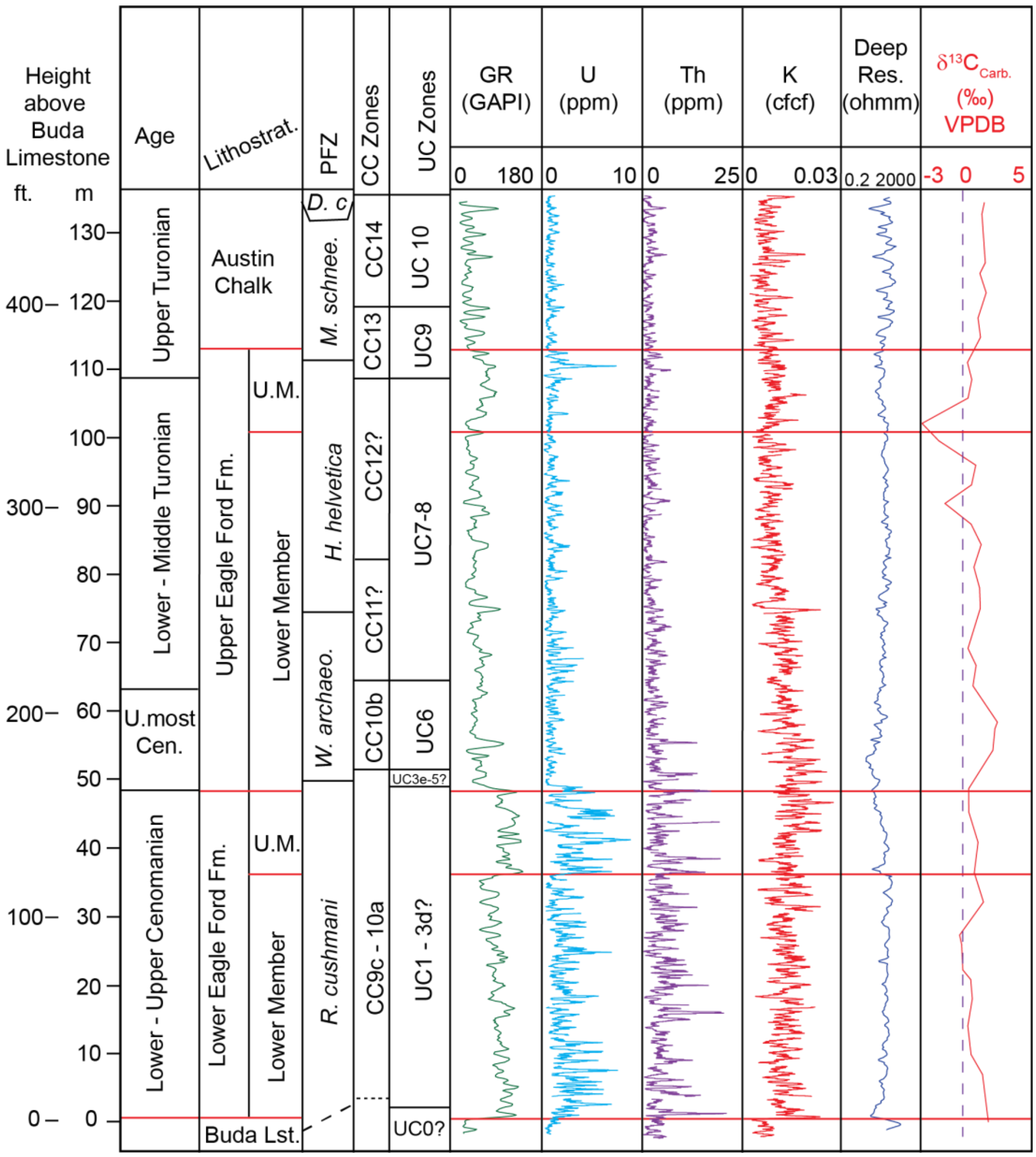

Figure II.9 Summary of Fasken A 1H well (Webb County, Texas) stratigraphy and geophysical well logs. The Fasken A 1H well has an expanded Turonian interval. Geologic stages after Ogg et al. (2016); planktonic foraminifera zonation (PFZ) is from Lowery et al. (2014); CC and UC calcareous nannofossil zones are from Corbett et al. (2014); $\delta^{13}C_{carb}$ from Lowery et al. (2014) and Corbett et al. (2014); TOC and geophysical well logs are from Donovan et al. (2012).

Isochore Thickness Maps

The Eagle Ford Group isochore thickness maps for the study area extend from Lozier Canyon (Terrell County) to southwest of the San Marcos Arch (Wilson and Karnes County; figure II.10). The main paleo-physiographic features that influenced the Eagle Ford Group depositional setting in this area were the San Marcos Arch (to the east), the South Texas Submarine Plateau, the older Edwards and Sligo reef margins, and the Maverick Basin (to the west), a Mesozoic intra-shelf basin inbound of the Edwards reef margin in southwest Texas (figures II.1 and II.2).

In south Texas, the total Eagle Ford Group isochore thickness gradually increases southward across the depositional dip from ~ 14 m (~ 46 ft.) in northern Wilson and Atascosa County to ~ 45 m – 90 m (148 ft. – 295 ft.) close to the Edwards reef margin and in the South Texas Submarine Plateau (figure II.10A). This thickness abruptly increases to ~ 228 m (~ 750 ft.) further south close to the Sligo shelf margin in Live Oak County.

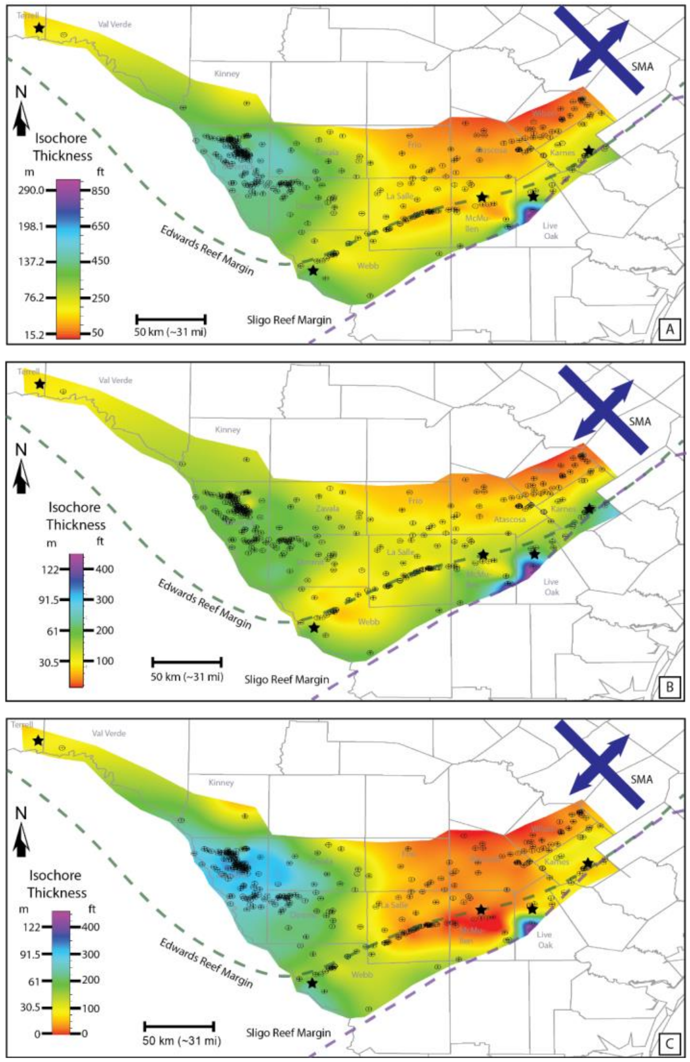

Figure II.10 Eagle Ford Group isochore thickness maps linking outcrop units to subsurface units. (A) Total Eagle Ford Group thickness. The total Eagle Ford Group isochore thickness gradually increases southward across the depositional dip from Wilson and Atascosa County. Note the abrupt increase in thickness close to the Sligo Shelf margin in Live Oak County. In west Texas, the total Eagle Ford Group isochore thickness gradually increases from Lozier Canyon to the Maverick Basin. (B) Lower Eagle Ford Formation isochore. In west Texas, The Lower Eagle Ford Formation thickness gradually increase from the Lozier Canyon outcrop into the Maverick Basin and south Texas Submarine plateau. (C) Upper Eagle Ford Formation isochore thickness. The Upper Eagle Ford Formation significantly thins out close to the San Marcos Arch and in parts of McMullen County. The Upper Eagle Ford Formation also remains relatively thin across the older Edwards reef margin. Black stars are the location of cored control wells shown in figure II.1A.

In west Texas, the total Eagle Ford Group isochore thickness gradually increases from ~ 51 m (167 ft.) at Lozier Canyon to ~ 156 m (~ 512 ft.) in the Maverick Basin (figure II.10A). Isochore thickness map for the Lower Eagle Ford Formation indicates thickness variation from ~14 m (46 ft.) in northern Wilson and Atascosa County to ~ 117 m (384 ft.) close to the Sligo shelf margin in Live Oak County (figure II.10B). In west Texas, the Lower Eagle Ford Formation has greatest isochore thickness of ~ 42 m (~ 138 ft.) in the Maverick Basin and gradually thins up dip to ~ 28 m (92 ft.) at Lozier Canyon. The Upper Eagle Ford Formation isochore thickness map indicates that the Upper Eagle Ford Formation is absent in northern Atascosa and Wilson County and in some parts of McMullen County in south Texas, remaining relatively thin further south of the San Marcos Arch, and abruptly increases to ~ 109 m (~358 ft.) in Live Oak County close to the Sligo shelf margin (figure II.10C). In west Texas, the Upper Eagle Ford Formation isochore thickness gradually increases from ~ 22 m (75 ft.) at Lozier Canyon to ~ 95 m (314 ft.) in the Maverick Basin (figure II.10C).

Discussion

Eagle Ford Group Age Interpretation

The interpreted $^{206}Pb/^{238}U$ zircon ages within the Eagle Ford Group are consistent with the stratigraphic correlation from Lozier Canyon to well 2 (figures II.11 and II.12). In west Texas, the Eagle Ford Group was deposited unconformably on top of the Buda Limestone.

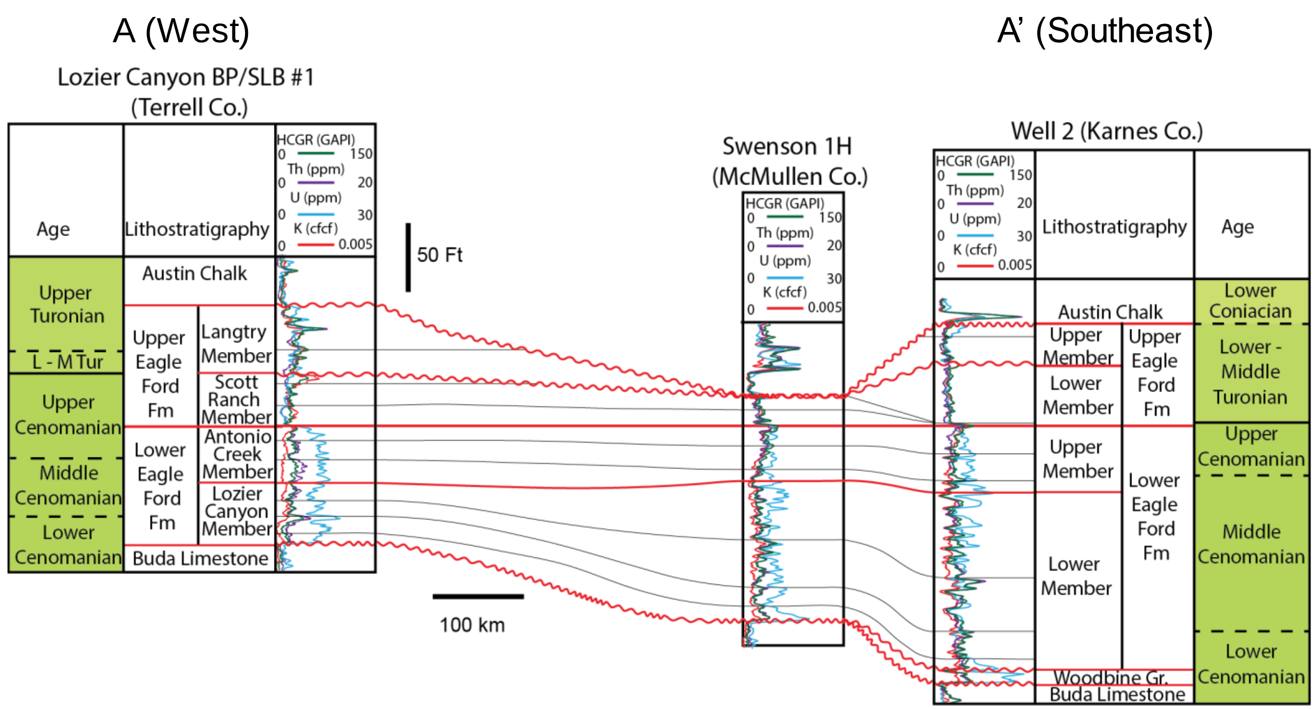

Figure II.11 Stratigraphic correlation (cross-section line A-A' in figure II.1) for Lozier Canyon, Swenson 1H well and well 2 with U-Pb ages. Deposition for the base of the Eagle Ford Group in both west and south Texas is constrained to the uppermost Lower Cenomanian. The Lower Eagle Ford Formation in Karnes County records an expanded Middle Cenomanian interval relative to Lozier Canyon. Deposition for the base of the Austin Chalk at Lozier Canyon (west Texas) is constrained to the Upper Turonian, whereas deposition for the base of the Austin Chalk in well 2 (Karnes County) is constrained to the Lower Coniacian.

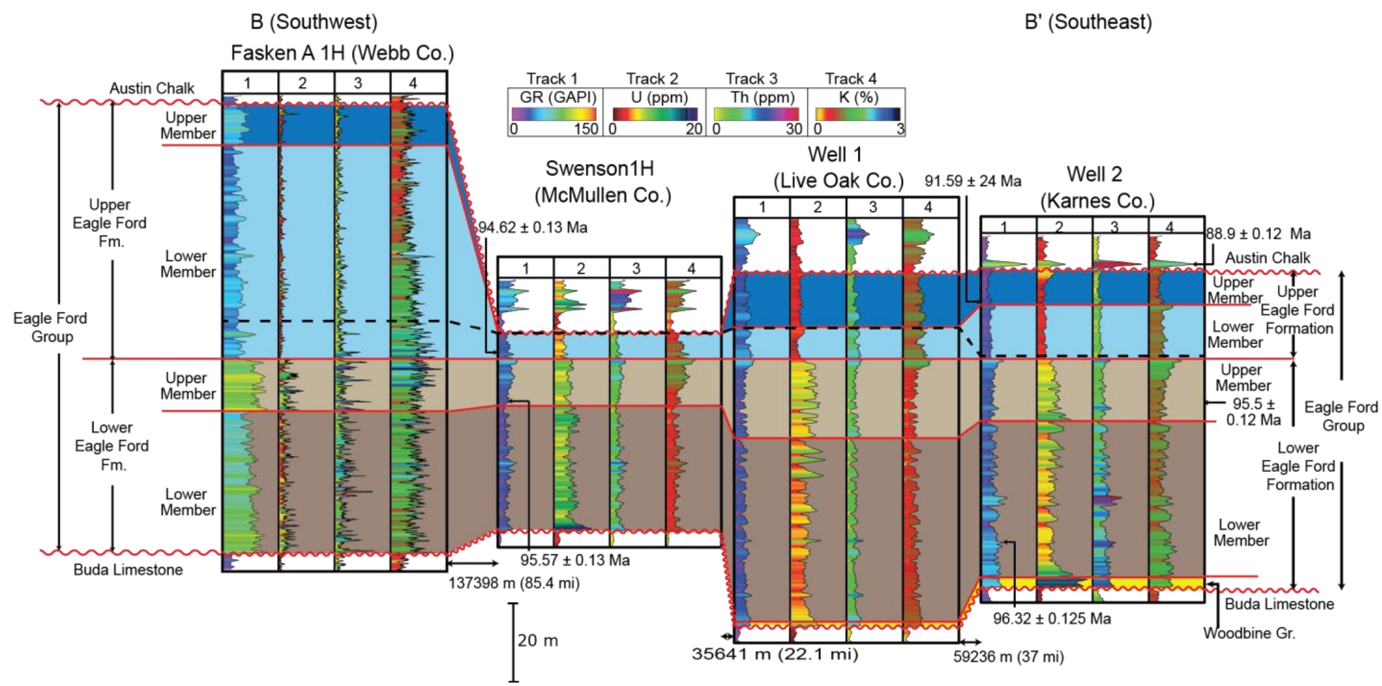

Figure II.12 Southeast to southwest correlation (B-B cross-section line in figure II.1) showing the U-Pb zircon ages and variations in stratigraphic thickness from the Fasken well in Webb County to well 2 in Karnes County. Stratigraphic thickness of the Eagle Ford Group strata varies across the study area and may be related to variation in accommodation and the inherited paleo-topography. The relatively thin Eagle Ford Group section in the Swenson 1H well may be related to decreased accommodation at this locality due to its proximity to the older Edwards reef margin, which produced paleo-topography upon which Upper Cretaceous sediments were deposited. In the south Texas Submarine Plateau, wells 1 and 2 record an expanded Lower – Upper Cenomanian interval relative to the Fasken A 1H well, whereas the latter records an expanded Turonian interval. Black jotted line indicate the top of the OAE 2 interval.

Clasts of the Buda Limestone at the base of the Eagle Ford Group were identified in a core from west Texas (Eldrett et al., 2015), indicating the erosive nature of this contact. The hiatus on top of the Buda Limestone correlates with an Early Cenomanian regional unconformity that is recognized across much of Texas and the US Gulf Coastal Plain (Mancini and Puckett, 2005; Ambrose et al., 2009). In the KWIS, this hiatus was interpreted to be less than 1 Mya in duration (Phelps et al., 2014; Eldrett et al., 2015). Above this unconformity in west Texas, deposition for the base of the Lower Eagle Ford Formation is interpreted to be upper Lower Cenomanian based on the AC-B10 $^{206}Pb/^{238}U$ age, younger than previous $^{206}Pb/^{238}U$ and astronomical age models for a cored well in west Texas (Eldrett et al., 2015). The $^{206}Pb/^{238}U$ age for the AC-B8 ash bed is younger than the ages of the two ash beds (AC-B6 and AC-B7) stratigraphically above it, violating the law of superposition. Therefore, the AC-B8 ash bed is excluded from all stratigraphic age interpretation for the west Texas outcrops. In the same vein, the $^{206}Pb/^{238}U$ age for the AC-B7 ash bed is excluded from the west Texas age interpretation because it is slightly younger than the stratigraphically higher AC-B6 age, albeit they both overlap within uncertainty. In well 2 and well 1, a thin condensed interval of the Woodbine Group is present between the Buda Limestone and the Eagle Ford Group. The basal Lower Member of the Lower Eagle Ford Formation in well 2 is interpreted to be uppermost Lower Cenomanian based on the W2-B4 $^{206}Pb/^{238}U$ age, constraining deposition for the base of the Eagle Ford Group in Karnes County to the upper Lower Cenomanian (> 96.32 ± 0.17 Ma), which is slightly older than previous biostratigraphic age interpretation in this area (Denne et al., 2016). At Lozier Canyon and Antonio Creek, the Middle Cenomanian interval spans the Lozier Canyon Member/Antonio Creek Member stratigraphic boundary, and the Antonio Creek Member is interpreted to be Middle – Upper Cenomanian age (figure II.5). Based on the Lozier Canyon, Swenson well and well 2 correlation, the Lower Member of the Lower Eagle Ford Formation is interpreted to be uppermost Lower Cenomanian – Middle Cenomanian, whereas the Upper Member of the Lower Eagle Ford Formation is interpreted to be Middle – Upper Cenomanian (figures II.4, II.6, II.7, II.11 and II.13).

Although the Swenson 1H well penetrates only the basal section of the Lower Member of the Upper Eagle Ford Formation and does not have $\delta^{13}C_{carb}$ data for the positive CIE in the OAE 2 interval, the S-B1 $^{206}Pb/^{238}U$ age (figure II.4E) and extensive bioturbation in this interval (chapter III) are consistent with age models for OAE 2 interval in the Eagle Ford Group and KWIS (Joo and Sageman, 2014; Eldrett et al., 2015). The S-B1 $^{206}Pb/^{238}U$ age of 94.62 ± 0.08 Ma (figure II.4) is consistent with the $^{206}Pb/^{238}U$ ash bed age (bentonite B4 – 94.45 ± 0.51 Ma) from the coeval interval in the Shell Iona-1 core in west Texas (Eldrett et al., 2015), and should overlap within uncertainty with the base of the OAE 2 positive CIE. The AC-B4 ash bed is in the uppermost interval of the Scott Ranch Member within the positive CIE and is stratigraphically below the base of the Langtry Member. The contact between the Scott Ranch Member and the Langtry Member is marked by clasts at the base of the Langtry Member at Lozier Canyon and Antonio Creek, and was interpreted as a hiatal surface linked to a regional erosive event in the Turonian (Lowery et al., 2014; Eldrett et al., 2015; Minisini et al., 2017; Lowery and Leckie, 2017b). The AC-B4 $^{206}Pb/^{238}U$ age of 94.4 ± 0.16 Ma is consistent with previously estimated $^{206}Pb/^{238}U$ age ages for ash beds within the OAE 2 interval in the KWIS (Barker et al., 2011; Eldrett et al., 2015).

In well 2, the Lower – Upper Eagle Ford Formation contact is marked by the occurrence of randomly oriented clasts and phosphate skeletal debris, indicating a submarine erosion surface (Chapter III). Furthermore, the proximity of the C-T boundary to the Lower-Upper Eagle Ford Formation contact also suggests an erosional surface at this contact with a missing time of ~ 900 k.y. based on the HO of *C. kennedyi* and the LO of *E. moratus* (figures II.7, II.12, II.13 and II.14). Similar observations were made in another Karnes County well where the C-T boundary coincides with the Lower – Upper Eagle Ford Formation contact, indicating an approximately 1 m.y. hiatus at the C-T boundary (Denne et al., 2016). Despite the interpreted hiatal surface at the Lower – Upper Eagle Formation contact in well 2 (figures II.13 and II.14), a small portion of the uppermost Cenomanian is preserved based on the observed "*Heterohelix* shift" at this contact (figure II.7). This hiatus appears to be localized to areas that are close to the San Marcos Arch and it is not associated with the hiatus at the base of the Upper Member of the Upper Eagle Ford Formation (Denne et al., 2016). The interpreted hiatus possibly could explain the lack of bioturbation above the Lower – Upper Eagle Ford Formation contact in well 2 (Chapter III) since much of the uppermost Cenomanian is missing. Also, the $\delta^{13}C_{org}$ values for the Lower Turonian interval in well 2 appears too high for the Lower Turonian, where the average $\delta^{13}C_{org}$ is between -27 to -26 ‰ and the positive CIE averages about +1‰ (Joo and Sageman, 2014).

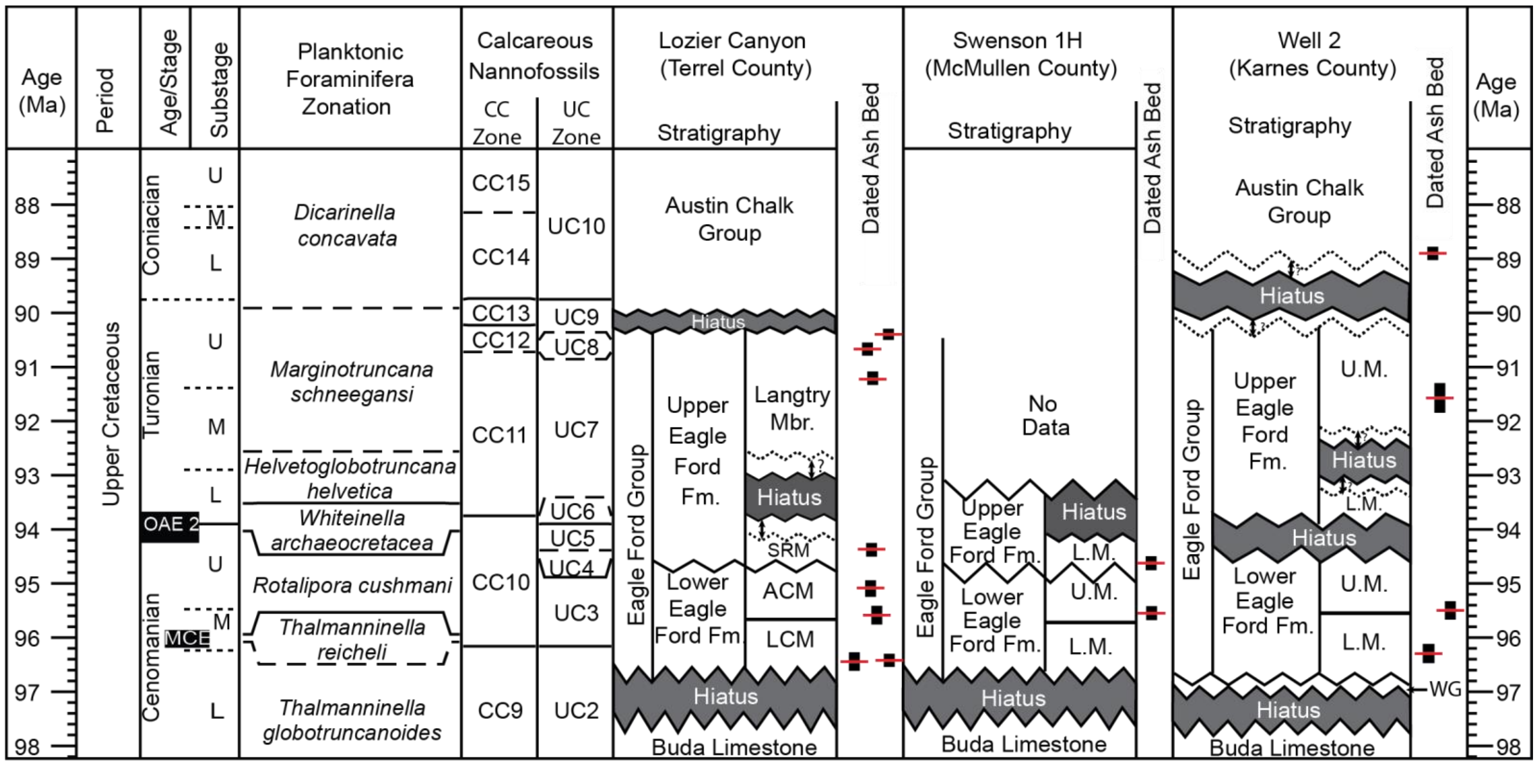

Figure II.13 Chronostratigraphic correlation for Lozier Canyon (Terrell Co.), Swenson 1H well (McMullen Co.), well 1 (Live Oak Co.) and well 2 (Karnes Co.). The amount of hiatuses in the study area vary by location and stratigraphic position. Well 2 in Karnes County records the most significant hiatus between the Lower and Upper Eagle Ford Formation and between the Eagle Ford Group and the Austin Chalk. Geologic timescale after Ogg et. al., (2016).

Given the higher than normal $\delta^{13}C_{org}$ in the Lower Turonian interval, the erosional contact and the interpreted hiatus between the Lower and Upper Eagle Ford Formation (figures II.13 and II.14), the organic carbon in this interval in well 2 is interpreted to be reworked from sediments from the uppermost Cenomanian interval. The W2-B3 bentonite in well 2 is at the base of the Upper Members of the Upper Eagle Ford Formation (figure II.7), constraining deposition for the base of this interval in Karnes County to the uppermost Middle Turonian. The LC-B1 bentonite is at the Eagle Ford Group – Austin Chalk Contact. Based on the W2-B3, OC-B3, LC-B2 and LC-B1 ash beds (figures II.5, II.6, II.11 and II.13), the Upper Member of the Upper Eagle Ford Formation is interpreted to be Middle to Upper Turonian. Although reliable calcareous nannofossil age markers for the uppermost Turonian (e.g. LOs of *M. furcatus*, *L. septenarius* and *B. p. expansa*) are absent in wells 1 and 2, the LO of calcareous nannofossil *M. decussata* (*M. stauropora*) indicates a Lower Coniacian age for deposition at the base of the Austin Chalk in these wells. The Lower Coniacian age for deposition at the base of the Austin Chalk in well 2 is further supported by the W2-B1 $^{206}Pb/^{238}U$ age, constraining deposition for the base of the Austin Chalk in well 2 to the upper Lower Coniacian. This age model is younger than age models for the coeval interval in west Texas and indicates a substantial hiatus of ~ 1 m.y. at the Eagle Ford Group – Austin Chalk contact in Karnes County (figure II.13). The Eagle Ford Group – Austin Chalk transition in well 2 is a composite surface of submarine hardground and submarine erosion or non-deposition (chapter III), and based on the LC-B1 and W2-B1 $^{206}Pb/^{238}U$ ages and the Lozier Canyon to Well 2 correlation, well 2 records a larger hiatus at the Upper Eagle Ford Formation – Austin Chalk contact relative to the Lozier Canyon outcrop (figures II.11 and II.13)

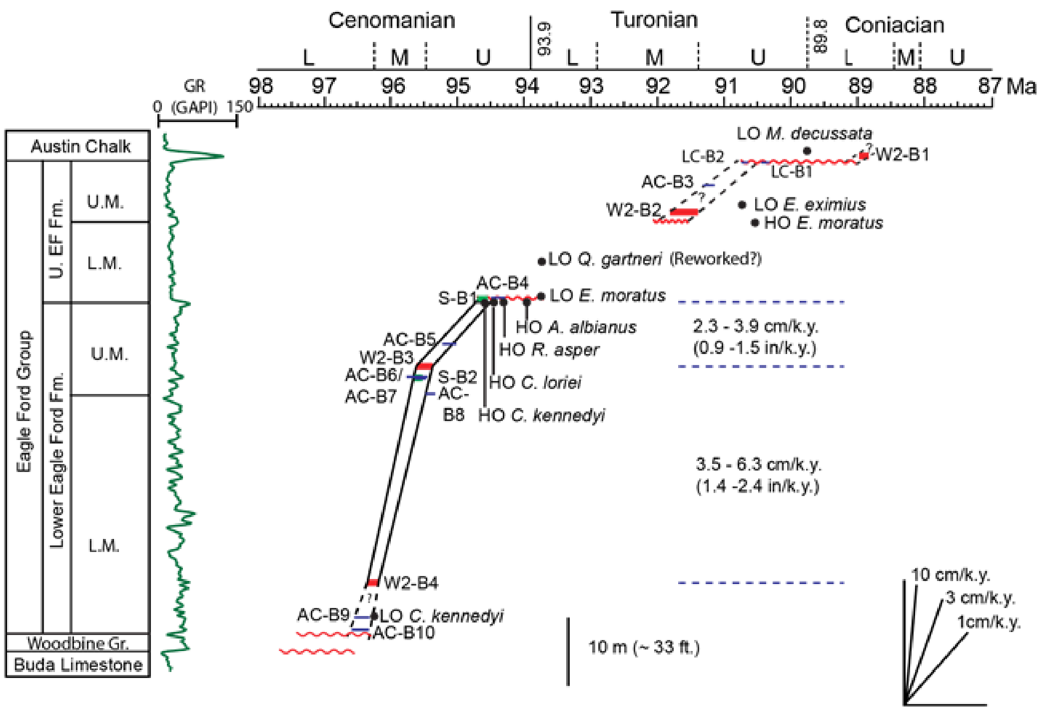

Figure II.14 GR log and age – depth profile for well 2 (Karnes County) showing the ash bed $^{206}Pb/^{238}U$ ages (red lines) and biostratigraphy. Ash bed ages from the Swenson 1H well (green lines) and Lozier Canyon and Osman Canyon outcrops (blue lines) are also projected onto the age – depth profile for comparison. Red zig-zag lines indicate erosional contact. EF = Eagle Ford; LO = lowest occurrence; HO = highest occurrence.

Eagle Ford Group Stratigraphic Variations

South of the Edwards shelf margin, the Lower Eagle Ford Formation isochore trend is largely parallel to the depositional strike, gradually increasing in thickness southward across the depositional dip while recording similar thickness across the depositional strike, suggesting relatively similar accommodation and sediment supply across the shelf margin (figure II.10B). Close to the Edwards shelf margin trend in Atascosa, McMullen and the eastern parts of Webb County, the Lower Eagle Formation strata is relatively thin, indicating that the paleo-relief of the Edwards shelf margin persisted during deposition of the Lower Eagle Ford Formation (figure II.10B). The relatively thin Lower Eagle Ford Formation strata in northern Atascosa and Wilson County likely reflect decreased accommodation related to the paleo-topographic relief in areas that are close to the San Marcos Arch (figure II.15A), over which the Eagle Ford Group significantly thins (Denne and Breyer, 2016; Hammes et al., 2016). In west Texas, the Lower Eagle Ford Formation maintains a gradual increase in thickness from the Lozier Canyon outcrop into the Maverick Basin (figures II.10B and II.15B). The stratigraphic correlations (figures II.11 and II.12) indicate that the Lower Eagle Ford Formation records an expanded Middle Cenomanian section in the southeast (wells 1 and 2) relative to the southwest area (Lozier Canyon, Fasken A 1H and Swenson 1H). The relatively thin Lower Eagle Ford Formation interval in the Swenson well may be related to its proximity to the older Edwards reef margin. The paleo-relief from the Edwards reef margin created a topographic relief that resulted in decreased accommodation along the paleo-reef margin trend. Similarly, the Lozier Canyon location on the shallower Comanche Platform had low accommodation.

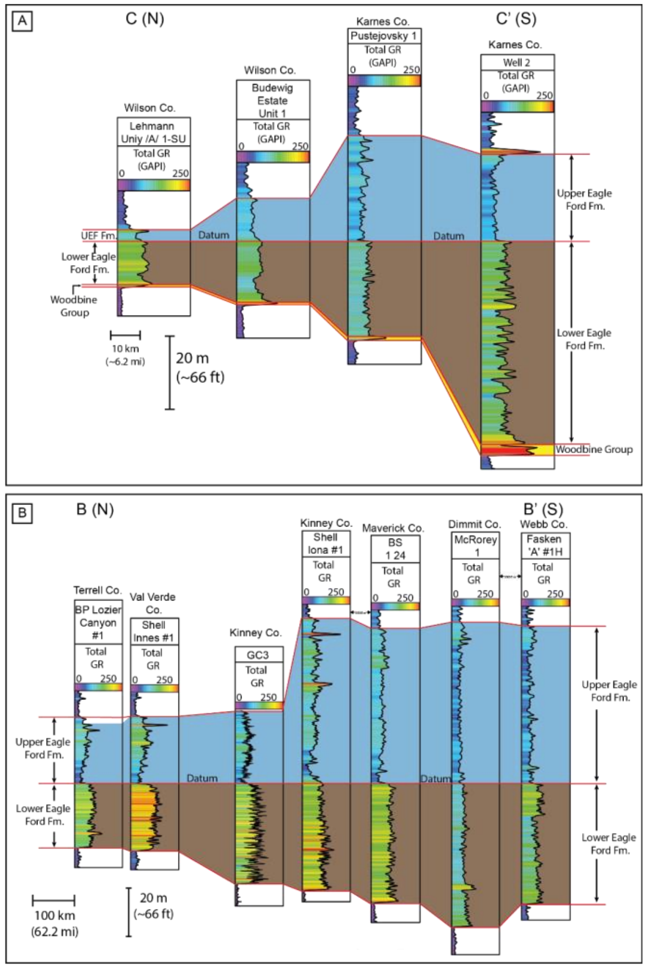

Figure II.15 Cross-sections showing variations in the Lower and Upper Eagle Ford thickness. (A) North-South cross-section from Wilson County to Karnes County (B-B'). Both the Lower and Upper Eagle Ford isochore thickness thins northward going towards the San Marcos Arch. (B) North – south cross-section from Lozier Canyon to Fasken A1 H well (C-C'). The Lower Eagle Ford Formation gradually increase in thickness from Lozier Canyon to the Maverick Basin and south Texas Submarine Plateau. The Upper Eagle Ford Formation recorded an expanded section in the Maverick Basin and in the western part of the south Texas Submarine Plateau. N = north; S = south. Shell Iona #1 and Shell Innes #1 GR logs are from Minisini et al., (2018).

The Upper Eagle Ford Formation thins out in northern Atascosa and Wilson County and in parts of McMullen County (figures II.10C and II.15A). The Upper Eagle Ford Formation strata records an expanded uppermost Cenomanian - Turonian section in west Texas and the Maverick Basin, whereas the coeval interval in south Texas and in areas close to the San Marcos Arch are very thin.

The relatively thin Upper Eagle Ford Formation strata in areas close to the San Marcos Arch may be related to increased uplift of the San Marcos Arch during the Upper Cretaceous (Laubach and Jackson, 1990), resulting in decreased accommodation and increased submarine erosion facilitated by high-energy storm events (Plint et al., 2012; Gardner et al., 2013; Denne and Breyer, 2016; Minisini et al., 2017). The abrupt changes in isochore thickness in both the Lower and Upper Eagle Ford Formation in southern Live Oak County and parts of McMullen County may be related to salt tectonics and their associated faults that variably affected the Eagle Ford Group thickness in this part of the study area (Hammes et al., 2016).

Rock Accumulation Rates

Lozier Canyon

Rock accumulation rates for the Lozier Canyon, Antonio Creek and BP/SLB Lozier Canyon #1 composite section was estimated by linear extrapolation between successive ash beds (figure II.16). Volcanic ash deposits represent instantaneous events in geologic time and their accumulation rates do not reflect the actual rock accumulation rates. Therefore, ~ 103 ash beds were removed from the rock accumulation rate estimation for the Lozier Canyon outcrop. Rock accumulation rate between the AC-B10 and AC-B9 ash beds was not estimated because of the occurrence of multiple deformed beds in this interval (Gardner, 2013).

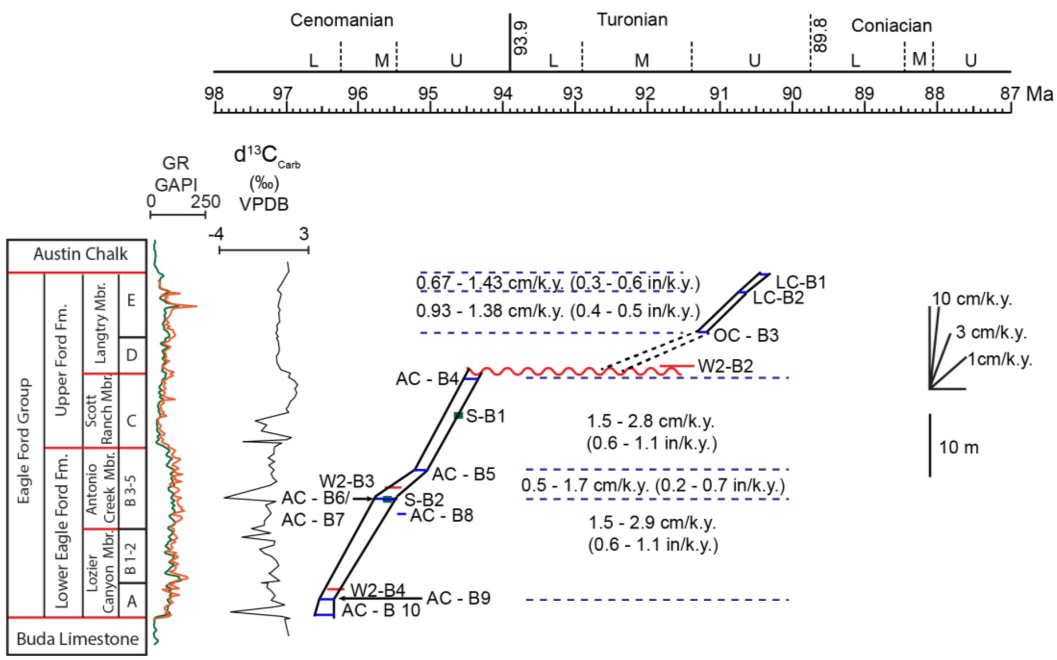

Figure II.16 Age – depth profile with GR log and $\delta^{13}C_{carb}$ for Lozier Canyon showing the ash bed $^{206}Pb/^{238}U$ ages (blue lines). Ash bed ages from the Swenson 1H well (green lines) and the composite Lozier Canyon outcrop data (blue lines) are also projected onto the age – depth profile for comparison. Red zig-zag lines indicate erosional contact

Rock accumulation rates between the AC-B9 and AC-B6 ash beds vary from 1.5 – 2.9 cm/k.y. (0.6 – 1.1 in/k.y.). This range of rock accumulation is consistent with estimated rock accumulation rates for the Lower Eagle Ford Formation in the Shell Iona #1 core in west Texas (Eldrett et al., 2015). The rock accumulation rates decrease slightly in the upper interval of the Lower Eagle Ford Formation between the AC-B6 and AC-B5 ash beds to between 0.5 – 1.7 cm/k.y. (0.2 – 0.7 in/k.y.). Between the AC-B5 and AC-B4 ash beds, the rock accumulation rates range between 1.5 – 2.8 cm/k.y. (0.6 – 1.1 in/k.y.), indicating an increase across the Lower – Upper Eagle Ford Formation boundary into the Upper Eagle Ford Formation. The Langtry Member rock accumulation rates vary from 0.93 – 1.38 cm/k.y (0.4 – 0.5 in/k.y.) between the OC-B3 and LC-B1 ash beds, and between 0.67 – 1.43 cm/k.y (0.3 – 0.6 in/k.y.) between the LC-B2 and LC-B1 ash beds

Well 2

Rock accumulation rates for the Lower Eagle Ford Formation in well 2 were estimated by linear extrapolation between the W2-B4 and W2-B3 ash beds (figure II.14). The age of the Lower – Upper Eagle Ford Formation contact was constrained using age model for the HO of *C. kennedyi* in Eldrett et al., (2015), and the rock accumulation rates between the W2-B3 ash bed and the Lower – Upper Eagle Formation contact were subsequently estimated by linear extrapolation (figure II.14). Rock accumulation rate for the lowermost Lower Eagle Ford Formation between the LO of *C. kennedyi* and the W2-B4 bentonite was not estimated due to poor preservation issues with the LO of *C. kennedyi* in the Eagle Ford Group (Corbett at al., 2014) that makes the LO of *C. kennedyi* an unreliable age marker. Rock accumulation rate for the Upper Eagle Ford Formation was not estimated because of lack of control data in this interval.

The rock accumulation rates (figure II.14) between the W2-B4 and W2-B3 ash beds are estimated to range between ~ 3.5 cm/k.y. (1.4 in/k.y.) and ~ 6 cm/k.y. (2.4 in/k.y.). This range of rock accumulation rates is higher than the estimated rock accumulation rates for the Lozier Canyon composite section and also higher than previous rock accumulation rates estimated for the Lower Eagle Ford Formation in west Texas (Eldrett et al., 2015). The expanded Middle Cenomanian interval in well 2 relative to the west Texas area is consistent with the higher rock accumulation rates between the W2-B4 and W2-B3 ash beds. Furthermore, the higher rock accumulation rates likely precluded accumulation and preservation of large amounts of volcanic ash beds in well 2, consistent with the occurrence of fewer number of volcanic ash beds and volcanic ash deposits mixed with storm-related beds in the Lower Eagle Ford Formation in this well (Chapter III). The rock accumulation rates in well 2 decrease in the uppermost Lower Eagle Formation between the W2-B3 bentonite and the Lower – Upper Eagle Ford Formation contact (HO of *C. kennedyi*) to between ~ 2.3 cm/k.y. (0.9 in/k.y.) and 3.9 cm/k.y. (1.5 in/k.y.) (figure II.14), reflecting a decrease in rock accumulation trend that is similar to the coeval interval in the Lozier Canyon composite section. This decrease in rock accumulation rates in the uppermost Lower Eagle Ford Formation correlates with a decrease in the number and thickness of the storm-related beds as the interval becomes more mudstone-dominated (Chapter III).

Conclusions

Chronostratigraphically tying the Eagle Ford Group outcrop units to subsurface units provides a critical chronostratigraphic framework constraining its timing of deposition and providing better understanding of its three-dimensional stratigraphic architecture. The high precision $^{206}Pb/^{238}U$ age model constrains deposition for the base of the Eagle Ford Group in west Texas to the uppermost Lower Cenomanian. Similarly, deposition for the base of the Eagle Ford Group south of the San Marcos Arch in Karnes County is constrained to the uppermost Lower Cenomanian. The Eagle Ford Group – Austin Chalk contact at Lozier Canyon in west Texas is constrained to the Upper Turonian, whereas deposition for the base of the Austin Chalk in Karnes County is constrained to the upper Lower Coniacian.

This Eagle Ford Group chronostratigraphic correlation indicates regional submarine hiatuses variably affect its stratigraphic thickness, persisting near the Cenomanian – Turonian and Turonian – Coniacian boundaries. Another local submarine hiatus exists between the Lower and Upper Eagle Ford Formation south of the San Marcos Arch in the Karnes County area. The Upper Eagle Ford Formation records an expanded uppermost Cenomanian - Turonian section in west Texas and the Maverick Basin, whereas the coeval interval south of the San Marcos Arch is very thin, indicating the influence of regional tectonics on the Eagle Ford Group deposition.

References

Adkins, W., 1932, The Mesozoic systems in Texas; Part 2 of The geology of Texas, v. 1, Stratigraphy, by EH Sellards et al, University of Texas Bull, v. 3232, p. 1007.

Alnahwi, A., R. G. Loucks, S. C. Ruppel, R. W. Scott, and N. Tribovillard, 2018, Dip-related changes in stratigraphic architecture and associated sedimentological and geochemical variability in the Upper Cretaceous Eagle Ford Group in south Texas, AAPG Bulletin, v. 102, p. 2537-2568.

Ambrose, W. A., T. F. Hentz, F. Bonnaffe, R. G. Loucks, L. F. Brown Jr, F. P. Wang, and E. C. Potter, 2009, Sequence-stratigraphic controls on complex reservoir architecture of highstand fluvial-dominated deltaic and lowstand valley-fill deposits in the Upper Cretaceous (Cenomanian) Woodbine Group, East Texas field: Regional and local perspectives, AAPG bulletin, v. 93, p. 231-269.

Arthur, M., S. t. Schlanger, and H. Jenkyns, 1987, The Cenomanian-Turonian Oceanic Anoxic Event, II. Palaeoceanographic controls on organic-matter production and preservation, Geological Society, London, Special Publications, v. 26, p. 401-420.

Barker, I. R., D. E. Moser, S. L. Kamo, and A. G. Plint, 2011, High-precision U–Pb zircon ID–TIMS dating of two regionally extensive bentonites: Cenomanian Stage, Western Canada Foreland Basin, Canadian Journal of Earth Sciences, v. 48, p. 543-556.

Campbell, C. V., 1967, Lamina, laminaset, bed and bedset, Sedimentology, v. 8, p. 7-26.

Condon, D. J., B. Schoene, N. M. McLean, S. A. Bowring, and R. R. Parrish, 2015, Metrology and traceability of U–Pb isotope dilution geochronology (EARTHTIME Tracer Calibration Part I), Geochimica et Cosmochimica Acta, v. 164, p. 464-480.

Corbett, M., D. Watkins, and J. Pospichal, 2014, A quantitative analysis of calcareous nannofossil bioevents of the Late Cretaceous (Late Cenomanian–Coniacian) Western Interior Seaway and their reliability in established zonation schemes, Marine Micropaleontology, v. 109, p. 30-45.

Cusack, C., J. Beeson, D. Stoneburner, and G. Robertson, 2010, The discovery, reservoir attributes, and significance of the Hawkville Field and Eagle Ford Shale trend, Texas, Gulf Coast Association of Geological Societies, Transactions, v. 60. p. 165-179

Denne, R., J. Breyer, A. Callender, R. Hinote, M. Kariminia, T. Kosanke, Z. Kita, J. Lees, H. Rowe, and J. Spaw, 2016, Biostratigraphic and geochemical constraints on the stratigraphy and depositional environments of the Eagle Ford and Woodbine groups of Texas, *in* J. A. Breyer, ed., The Eagle Ford Shale—A renaissance in US oil production: AAPG Memoir 110, p. 1-86.

Denne, R. A., and J. A. Breyer, 2016, Regional Depositional Episodes of the Cenomanian-Turonian Eagle Ford and Woodbine Groups of Texas and their Relationship to Oceanic Anoxic Event 2 (OAE2), The Eagle Ford Shale—A renaissance in US oil production: AAPG Memoir, v. 110, p. 87-133.

Denne, R. A., R. E. Hinote, J. A. Breyer, T. H. Kosanke, J. A. Lees, N. Engelhardt-Moore, J. M. Spaw, and N. Tur, 2014, The Cenomanian–Turonian Eagle Ford Group of South Texas: Insights on timing and paleoceanographic conditions from geochemistry and micropaleontologic analyses, Palaeogeography, Palaeoclimatology, Palaeoecology, v. 413, p. 2-28.

Donovan, A., R. Gardner, A. Pramudito, T. Staerker, M. Wehner, M. Corbett, J. Lundquist, A. Romero, L. Henry, and J. Rotzien, 2015, Chronostratigraphic relationships of the Woodbine and Eagle Ford Groups across Texas, Gulf Coast Association of Geological Societies, v. 2, p. 67-87.

Donovan, A. D., and T. S. Staerker, 2010, Sequence stratigraphy of the Eagle Ford (Boquillas) Formation in the subsurface of South Texas and outcrops of West Texas, Gulf Coast Association of Geological Societies Transactions, v. 60, p. 861-899.

Donovan, A. D., T. S. Staerker, R. Gardner, M. C. Pope, A. Pramudito, and M. Wehner, 2016, Findings from the Eagle Ford outcrops of west Texas and implications to the subsurface of South Texas, in Breyer, J.A. (Ed.), The Eagle Ford Shale: A renaissance in U.S. oil production, AAPG Memoir v. 110, p. 301-336.

Donovan, A. D., T. S. Staerker, A. Pramudito, W. Li, M. J. Corbett, C. M. Lowery, A. M. Romero, and R. D. Gardner, 2012, The Eagle Ford outcrops of West Texas: A laboratory for understanding heterogeneities within unconventional mudstone reservoirs, Gulf Coast Association of Geological Societies, v. 1, p. 162-185.

Eldrett, J. S., C. Ma, S. C. Bergman, B. Lutz, F. J. Gregory, P. Dodsworth, M. Phipps, P. Hardas, D. Minisini, and A. Ozkan, 2015, An astronomically calibrated stratigraphy of the Cenomanian, Turonian and earliest Coniacian from the Cretaceous Western Interior Seaway, USA: Implications for global chronostratigraphy, Cretaceous Research, v. 56, p. 316-344.

Gardner, R. D., M. C. Pope, M. P. Wehner, and A. D. Donovan, 2013, Comparative Stratigraphy of the Eagle Ford Group Strata in Lozier Canyon and Antonio Creek, Terrell County, Texas, GCAGS Journal, v. 2, p. 42-52.

Hammes, U., R. Eastwood, G. McDaid, E. Vankov, S. A. Gherabati, K. Smye, J. Shultz, E. Potter, S. Ikonnikova, and S. Tinker, 2016, Regional assessment of the Eagle Ford Group of South Texas, USA: Insights from lithology, pore volume, water saturation, organic richness, and productivity correlations, Interpretation, v. 4, p. SC125-SC150.

Joo, Y. J., and B. B. Sageman, 2014, Cenomanian to Campanian carbon isotope chemostratigraphy from the Western Interior Basin, USA, Journal of Sedimentary Research, v. 84, p. 529-542.

Kauffman, E. G., 1984, Paleobiogeography and evolutionary response dynamic in the Cretaceous Western Interior Seaway of North America, *in* G. E. G. Westermann, ed., Jurassic-Cretaceous biochronology and paleogeography of North America, v. 27, Geol. Assoc. Can. Sp. Pap, p. 273-306.

Kennedy, W., I. Walaszczyk, and W. Cobban, 2005, The global boundary stratotype section and point for the base of the Turonian stage of the Cretaceous: Pueblo, Colorado, USA, Episodes-Newsmagazine of the International Union of Geological Sciences, v. 28, p. 93-104.

Laubach, S. E., and M. L. Jackson, 1990, Origin of arches in the northwestern Gulf of Mexico basin, Geology, v. 18, p. 595-598.

Leckie, R. M., 1985, Foraninifera of the Cenomanian-Turonian Boundary Interval, Greenhorn Formation, Rock Canyon Anticline, Pueblo, Colorado, *in* L. Pratt, E. G. Kauffman, and F. B. Zelt, eds., Fine-grained deposits and biofacies of the Cretaceous Western Interior Seaway: evidence of cyclic depositional processes: SEPM Annual Mid-Year Meeting, Field Trip No. 4, p. 139-149.

Lee, C.-T. A., B. Shen, B. S. Slotnick, K. Liao, G. R. Dickens, Y. Yokoyama, A. Lenardic, R. Dasgupta, M. Jellinek, and J. S. Lackey, 2013, Continental arc–island arc fluctuations, growth of crustal carbonates, and long-term climate change, Geosphere, v. 9, p. 21-36.

Lowery, C. M., M. J. Corbett, R. M. Leckie, D. Watkins, A. M. Romero, and A. Pramudito, 2014, Foraminiferal and nannofossil paleoecology and paleoceanography of the Cenomanian–Turonian Eagle Ford Shale of southern Texas, Palaeogeography, Palaeoclimatology, Palaeoecology, v. 413, p. 49-65.

Lowery, C. M., and R. M. Leckie, 2017b, Biostratigraphy of the Cenomanian–turonian Eagle Ford Shale of South Texas, Journal of Foraminiferal Research, v. 47, p. 105-128.

Ludwig, K., 2003, User’s Manual for Isoplot/Ex Version 3.00 e A Geochronology Toolkit for Microsoft Excel, vol. 4, Berkeley Geochronological Center, Special Publication.

Mancini, E. A., and T. M. Puckett, 2005, Jurassic and Cretaceous transgressive-regressive (T-R) cycles, Northern Gulf of Mexico, USA, Stratigraphy, v. 2, p. 31-48.

Mattinson, J. M., 2005, Zircon U–Pb chemical abrasion (“CA-TIMS”) method: combined annealing and multi-step partial dissolution analysis for improved precision and accuracy of zircon ages, Chemical Geology, v. 220, p. 47-66.

Minisini, D., J. Eldrett, S. C. Bergman, and R. Forkner, 2017, Chronostratigraphic framework and depositional environments in the organic-rich, mudstone-dominated Eagle Ford Group, Texas, USA, Sedimentology, p. 1-38.

Ogg, J. G., G. Ogg, and F. M. Gradstein, 2016, The Concise Geologic Time Scale 2016 : 2016: Atlanta, Netherlands, Elsevier.

Phelps, R. M., C. Kerans, R. G. Loucks, R. O. Da Gama, J. Jeremiah, and D. Hull, 2014, Oceanographic and eustatic control of carbonate platform evolution and sequence stratigraphy on the Cretaceous (Valanginian–Campanian) passive margin, northern Gulf of Mexico, Sedimentology, v. 61, p. 461-496.

Plint, A. G., J. H. MacQuaker, and B. L. Varban, 2012, Bedload transport of mud across a wide, storm-influenced ramp: Cenomanian–Turonian Kaskapau Formation, Western Canada Foreland Basin, Journal of Sedimentary Research, v. 82, p. 801-822.

Roberts, L. N. R., and M. A. Kirschbaum, 1995, Paleogeography of the Late Cretaceous of the Western Interior of middle North America-coal distribution and sediment accumulation, United States Geological Survey, Professional Paper 1516, p. 115p.

Schlanger, S. O., and H. Jenkyns, 1976, Cretaceous oceanic anoxic events: causes and consequences, Geologie en mijnbouw, v. 55, p. 179-184.

Schmitz, M. D., and B. Schoene, 2007, Derivation of isotope ratios, errors, and error correlations for U-Pb geochronology using 205Pb-235U-(233U)-spiked isotope dilution thermal ionization mass spectrometric data, Geochemistry, Geophysics, Geosystems, v. 8, No. 8, Q08006, doi:10.1029/2006GC001492

Schoene, B., 2014, 4.10-U–Th–Pb Geochronology, Treatise on geochemistry, v. 4, p. 341-378.

Scholle, P. A., and M. A. Arthur, 1980, Carbon isotope fluctuations in Cretaceous pelagic limestones: potential stratigraphic and petroleum exploration tool, AAPG Bulletin, v. 64, p. 67-87.

CHAPTER III

UNDERSTANDING ORGANIC-RICH MUDSTONE DEPOSITIONAL ENVIRONMENTS: AN EXAMPLE FROM THE CENOMANIAN – TURONIAN EAGLE FORD GROUP IN WEST AND SOUTH TEXAS

Overview

Organic-rich mudstone depositional environments commonly were thought to require low-energy and persistent benthic anoxia for accumulation and preservation of large amounts of organic matter. However, more recent studies indicate that organic-rich mudstone commonly was deposited in environments at least episodically influenced by more energetic bottom currents (e.g. storms, turbidites, debris flows, contourites). Integrated redox-sensitive trace element (RSTE) geochemistry, mineralogy, organic geochemistry, and thin section petrography from outcrops and cores characterizing the Upper Cretaceous (Cenomanian –Turonian) Eagle Ford Group in west and south Texas, USA, indicate that its organic-rich mudstone depositional environments were heterogeneous, having different depositional processes simultaneously affecting coeval deposits in different parts of the same basin.

Enhanced primary productivity resulting from volcanic ash input coupled with variations in basinal water mass restriction promoted widespread anoxia and episodic photic zone euxinia in a stratified water column in the Lower Eagle Ford Formation. The Upper Eagle Ford Formation was deposited mostly under oxic to mildly anoxic conditions, with the down dip section recording lesser degree of benthic oxygenation than the coeval up dip section. Sedimentological data indicate that frequent – episodic interaction of storm waves and currents with the Eagle Ford Group seafloor aided sediment transport and deposition, promoting vertical mixing of the stratified water column, resulting in temporary ventilation of the bottom water masses even during periods of episodic photic zone anoxia. The integrated dataset presented here is the basis for several depositional models during the temporal and spatial evolution of the Eagle Ford Group.

Introduction

Organic-rich mudstone successions like the Upper Cretaceous (Cenomanian – Turonian) Eagle Ford Group generally were described as homogeneous and monotonously uniform sedimentary rocks that formed from continuous mud deposition during suspension settling out of the water column (Ehler and Blatt, 1982; Dawson, 2000; Blatt et al., 2006). This description was predicated on the fact that mud-size particles have low settling velocity and are easily kept in suspension by turbulence (Potter et al., 2005). Thus, organic-rich mudstone commonly was thought to form in low-energy depositional environments with minimum benthic turbulence and persistent anoxia (Blatt et al., 2006). With continued success in the exploration and exploitation of organic-rich mudstone as unconventional source rock reservoirs and improved analytical techniques (e.g. scanning electron microscopy, SEM; and energy dispersive X-ray fluorescence, ED-XRF) used to study mudstone, better understanding is possible of mudstone heterogeneities and complexities in their associated depositional environments under a wide range of hydrodynamic and redox conditions (e.g. Ghadeer and Macquaker, 2012; Lazar et al., 2015; Schieber et al., 2016)

The Upper Cretaceous Eagle Ford Group was deposited during a major third-order sea level rise accompanying global greenhouse conditions (Kauffman, 1984; Lowery et al., 2014; Eldrett et al., 2015; Eldrett et al., 2017; Lowery et al., 2017a; Lowery and Leckie, 2017b). Mudstone deposited in this time interval in marine, continental margins and epicontinental seas record geochemical, biotic and sedimentological signatures that provide insights to better understand depositional processes and environments during a greenhouse period characterized by rapid environmental and biotic changes, elevated tectonic activity and volcanism, eruption of large igneous provinces (LIPs) and widespread burial of large amounts of organic carbon (Schlanger and Jenkyns, 1976; Scholle and Arthur, 1980; Arthur et al., 1987; Lee et al., 2013; McKenzie et al., 2016). The Eagle Ford Group forms several laterally extensive outcrops (e.g. Lozier Canyon) in west Texas that provide excellent exposures and are a natural laboratory to study Upper Cretaceous organic-rich mudstone. The Lozier Canyon outcrop, in particular, is well documented in the literature and was correlated to several other regional and global coeval organic-rich, mudstone-dominated successions (Donovan and Staerker, 2010; Donovan et al., 2012; Gardner et al., 2013; Corbett et al., 2014; Lowery et al., 2014; Romero, 2014; Donovan et al., 2015; Eldrett et al., 2015; Lowery and Leckie, 2017b; Romero et al., 2018).

In this study, the Lozier Canyon outcrop was correlated to four cored oil- and gas-producing wells in south Texas to document the sedimentological and geochemical variations within the Eagle Ford Group depositional setting and provide insights to better understand heterogeneities in organic-rich, mudstone-dominated depositional environments. This correlation is constrained by geochronological age models in chapter II, which is then used to derive depositional models during the temporal and spatial evolution of the Eagle Ford Group as they relate to the development and distribution of organic-rich mudstone.

Geologic Settings

There was a substantial increase in the area of shallow epicontinental seas following the Upper Cretaceous transgression (Arthur et al., 1987; Roberts and Kirschbaum, 1995). During this transgression, the Eagle Ford Group was deposited in the southern aperture (figure III.1) of North America's Cretaceous Western Interior Seaway (KWIS), a shallow, north-south trending epicontinental sea that at peak transgression connected oxygen-rich boreal water masses of the Canadian Arctic and warm, saline, oxygen-poor, northward-migrating Tethyan water masses from the Gulf of Mexico (Sageman and Arthur, 1994; Roberts and Kirschbaum, 1995; Eldrett et al., 2017; Lowery et al., 2017a). The KWIS inundated the Cordilleran orogenic system's foreland basin (figure III.1), which developed via a complex combination of flexural loading and dynamic subsidence, as the Farallon plate collided with North America (Pang and Nummedal, 1995; Liu et al., 2014). In the United States, the Cordilleran orogenic system had a zone of extensive volcanic activity that intermittently produced voluminous amounts of volcanic ash (figure III.1). Interplay among flexural loading, dynamic subsidence and eustatic sea level changes controlled the overall KWIS stratigraphic architecture, accommodation and timing and distribution of its unconformities (Liu et al., 2014). The Eagle Ford Group was deposited at or near the maximum flooding surface of the first-order, unconformity-bounded (Middle Jurassic to Middle Paleocene) Zuni Sequence of North America (Sloss, 1963).

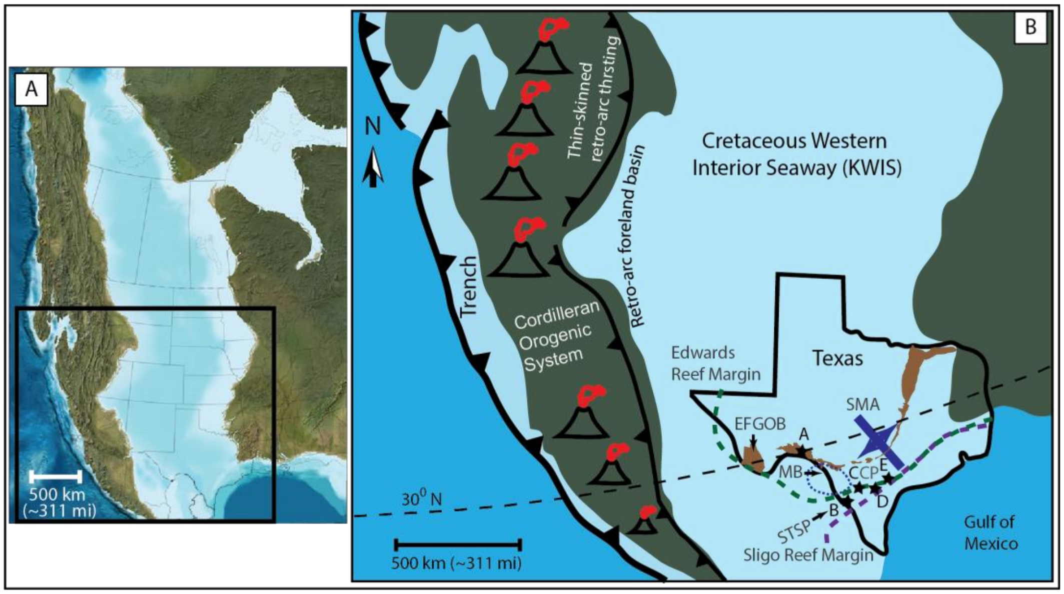

Figure III.1 Upper Cretaceous (92.1 Ma) paleogeographic map of the Cretaceous Western Interior Seaway (KWIS) modified after Blakey (2011). (A) The KWIS extended from the Gulf of Mexico to the Canadian Arctic. Black polygon highlights the zoomed-out section in B. (B) Outline of the Eagle Ford Group outcrop belt and other physiographic elements in the KWIS that affected Eagle Ford Group deposition. The older Edwards and Sligo reef margins produced paleo-topography upon which Upper Cretaceous sediments were deposited. The Cordilleran orogenic system had a zone of extensive volcanic activity the intermittently produced voluminous amounts of ash. CP = Comanche Platform; MB = Maverick Basin; SMA = San Marcos Arch; EFGOB = Eagle Ford Group outcrop belt; STSP = South Texas Submarine Plateau; A = Lozier Canyon Outcrop; B = Fasken 1H well; C = Swenson 1H well; D = Well 1; E = Well 2; black stars are approximate well locations.

The Cretaceous stratigraphy of Texas is sub-divided into two second-order cycles – the Lower Cretaceous, carbonate-prone Comanche Series and the Upper Cretaceous, siliciclastic-prone Gulfian Series (Hill, 1887b; Hill, 1887a). The Comanche series was deposited on the broad

Comanche carbonate platform that developed across much of Texas. The Sligo (Hauterivian to Barremian) and Edwards (Albian) reef margins represent major carbonate reef-building episodes within this series (Hill, 1887b; Hill, 1887a; Donovan et al., 2012; Phelps et al., 2014). The top of the Buda Limestone marks the transition from the Comanche Series to the Gulfian Series (Hill, 1887b; Hill, 1887a; Donovan et al., 2012; Phelps et al., 2014). The Eagle Ford Group was deposited on top of the Comanche Platform during a third-order eustatic sea level rise (Kauffman, 1984; Lowery et al., 2014; Eldrett et al., 2015; Eldrett et al., 2017; Lowery et al., 2017a; Lowery and Leckie, 2017b). The ancestral Sligo and Edwards reef margins created paleo-topographic relief that persisted until Eagle Ford Group deposition and acted as shallow sills which episodically restricted ocean circulation across the platform and inhibited widespread bottom-water circulation, especially during sea level falls (Kauffman, 1984; Arthur and Sageman, 2005; Donovan et al., 2012; Lowery et al., 2014; Lowery et al., 2017a). This restriction allowed episodic development of anoxic and euxinic (containing free H_2S) water columns which facilitated abundant preservation of organic matter (Algeo and Rowe, 2012; Eldrett et al., 2017).

Previous Studies and Eagle Ford Nomenclature

The Eagle Ford Group's nomenclature (Eagle Ford Shale or Boquillas Formation) varies by worker and geographic location (Hill, 1887b; Udden, 1907; Adkins, 1932; Atkins, 1933; Hazzard, 1959; Freeman, 1968; Pessagno, 1969; Lock et al., 2010). See Donovan and Staerker (2010) for details on the different nomenclature schemes. However, based on lithologic similarities among these strata across south and west Texas, Donovan et al. (2012) proposed the Eagle Ford Group nomenclature be used for this stratigraphic unit (figure III.2), since that term predates the use of the name Boquillas Formation (Hill, 1887b; Udden, 1907).

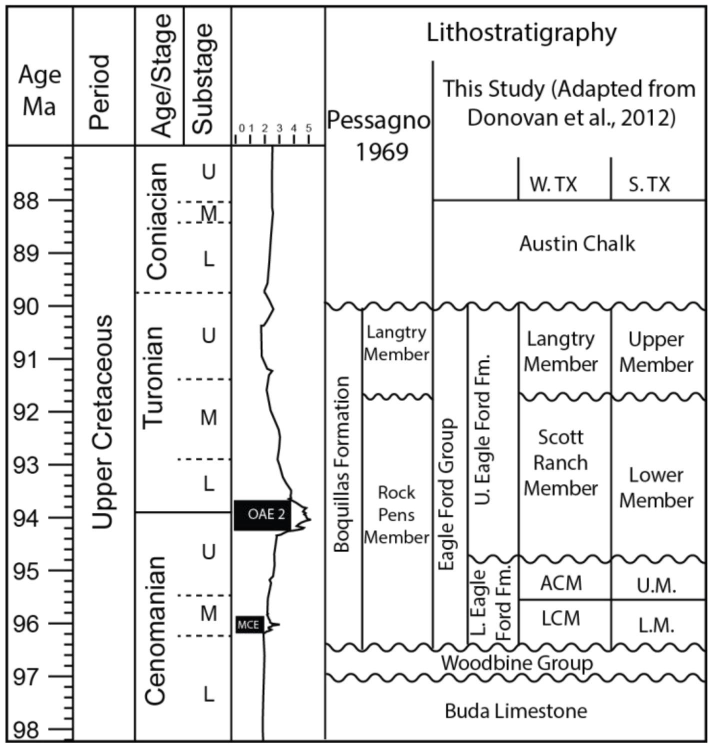

Figure III.2 Chronostratigraphy for the unconformity bounded Cenomanian to Turonian Eagle Ford Group strata. Modified after Donovan et al., 2012. Geologic time scale after Ogg et al. (2016). U.M. = Upper Member; L.M. = Lower Member; LCM = Lozier Canyon Member; ACM = Antonio Creek Member; L = lower; M = middle; U = upper; OAE = oceanic anoxic event; MCE = Middle Cenomanian excursion.

The Eagle Ford Group strata of outcrops in west Texas and in the subsurface of south Texas was elevated to group status and sub-divided into two informal units called the Lower and Upper Eagle Ford Formations (figure III.2), each formation comprising two allostratigraphic members (Donovan et al., 2012). In the west Texas outcrops, these members are designated as the Lozier Canyon (Lower Member) and Antonio Creek (Upper Member) Members of the Lower Eagle Ford

Formation and the Scott Ranch (Lower Member) and Langtry (Upper Member) Members of the Upper Eagle Ford Formation. A similar sub-division also was used for the subsurface in south Texas where the Lower and Upper Eagle Ford Formations were each sub-divided into upper and lower members (Donovan et al., 2015). Each member has chronostratigraphic significance and delineates unique geochemical and petrophysical characteristics. This study follows the stratigraphic nomenclature proposed by Donovan et al. (2012).

Methods and Data

High-resolution outcrop studies of the Eagle Ford Group at Lozier Canyon and Antonio Creek (Gardner, 2013; Gardner et al., 2013) were integrated with petrographic analyses and subsurface core data from Webb, McMullen, Live Oak and Karnes County, Texas, a transect that spans ~ 531 km (~ 329 mi). Redox-sensitive trace element (RSTE) geochemistry, mineralogy, organic geochemistry, and other datasets from unpublished and published M.S. and Ph.D. theses were integrated with Eagle Ford Group age model (chapter II).

Outcrop and core descriptions follow Dunham's (1962) classification scheme for carbonate rocks. However, whereas Dunham's (1962) classification scheme defines mud as < 20 µm, grains as > 20 µm and mudstone as containing < 10% grains, the term mudstone as used here refers to a sedimentary rock where more than fifty percent of the grains are < 62.5 µm. Lamina, lamina set, bed, bed set and bedding geometry were described using Campbell's (1967) classification scheme. Bioturbation index (BI) in this study varies from 1 (no recorded bioturbation, original sedimentary structures preserved) to 6 (burrow-homogenized bedding) (Droser and Bottjer, 1986). The facies associations identified in subsurface cores are designated as units A_s, B_s, C_s and DE_s (table III.1).

Table III.1 Description of Eagle Ford Group subsurface lithologic units

Unit	Lithology	BI	Lamina Geometry/ Sedimentary Structures	Grains	Interpretation
As	Dark to very dark gray siliceous, argillaceous, calcareous mudstone interbedded with centimeter(s) to decimeter(s) thick beds of medium to dark gray bioclastic wackestone. Abundant pyrite.	1	Continuous, planar-parallel laminated; discontinuous, planar-parallel laminated; continuous, curved-nonparallel laminated; continuous to discontinuous, planar-parallel to wavy-parallel. Millimeter to submillimeter thick laminae. Wave ripples laminations, local scours, erosional bed contacts, Thickening and thinning of laminae and pinch-outs.	Winnowed planktic foraminifera grain lags, radiolarians, disarticulated inoceramid bivalve fragments, pelletal grains.	Frequently affected by storm waves and currents that reworked sediments. Deposited within storm wave base Deposited in anoxic, restricted shelf settings.
Bs1	Medium to dark gray calcareous mudstone interbedded with decimeter(s) thick beds of foraminiferal packstone to grainstone.	1 with isolated intervals of 2-3	Continuous, planar-parallel laminated; discontinuous, planar-parallel laminated; continuous, curved-nonparallel laminated. Laminae are millimeter(s) to centimeter(s) thick. Abundant local scours, erosional bed contacts, wave ripple bed sets.	Abundant planktic foraminifera grains, phosphate skeletal debris, pelletal grains.	Episodically affected by storm waves and currents. Deposited in anoxic/euxinic, restricted shelf settings. Episodically within storm wave base.
Bs2	Basal interval comprises medium gray calcareous mudstone. Upper interval comprises dark gray argillaceous, calcareous mudstone interbedded with calcite-cemented, nodular skeletal packstone to grainstone.	1	Continuous, planar-parallel laminated; discontinuous, planar-parallel laminated; continuous, planar-nonparallel, laminated; continuous, curved-parallel laminated; discontinuous curved-parallel laminated. Laminae are millimeter(s) to centimeter(s) thick, may be horizontal or low angle inclined. Abundant Local scours and erosional bed contacts, sharp bed contacts, small basal flame structures, load casts. Occasional HCS, calcite-cemented nodular bedding	Abundant planktic foraminifera grains, pelletal non-skeletal grain lags, occasional disarticulated inoceramid bivalve fragments.	Seafloor was episodically affected by storm waves and currents. Deposited in restricted to open shelf settings. Euxinic/anoxic. Episodically within storm wave base
Cs	Light gray calcareous mudstone interbedded with medium gray argillaceous, calcareous mudstone and skeletal wackestone. Abundant large pyrites.	2-5 (*Chondrites, Planolites and Teichichnus*)	Continuous, planar-parallel; discontinuous, planar-parallel; low-angle, inclined, continuous, planar-nonparallel. Laminae are sub-millimeter to centimeter thick. Occasional HCS, occasional graded bedding.	Abundant planktic foraminifera. Phosphate skeletal grain lags, fish debris	Deposited in oxygenated, open shelf settings. Occasionally within storm wave base.

Table III.1 Continued

Unit	Lithology	BI	Lamina Geometry/ Sedimentary Structures	Grains	Interpretation
DEs	Light to medium gray, stacked bed and bed set of laminated skeletal packstone to grainstone with interbeds of calcareous mudstone	1-4	Continuous, curved-parallel laminated; discontinuous, planar-parallel laminated; continuous, planar-parallel laminated; continuous, planar-nonparallel or continuous, curved-nonparallel. Sharp basal contact, erosional base, local scours and small channels, truncated laminae, small basal rip-up clasts, differential compaction, thickening and thinning of laminae and beds, pinch-out of laminae, abundant HCS, wave ripple lamination, load casts, local subtle grading in laminae	Abundant planktic foraminifera, skeletal debris, phosphate skeletal grains including fish debris.	Deposited in relative shallow waters within storm wave base. Frequently affected by strong waves and currents. Oxygenated environment.

Subsurface datasets from Swenson 1H, Fasken A 1H, wells 1 and 2 were correlated to a composite section of the Lozier Canyon outcrop, Antonio Creek outcrop and the BP/SLB Lozier Canyon #1 well, where the facies association are designated as units A (with subunits A1 – A4), B (with subunits B1 – B5), C (with subunits C1 – C3), D (with subunits D1 -D2) and E (with subunits E1 - E2) (Donovan and Staerker, 2010; Donovan et al., 2012; Gardner et al., 2013). A detailed study of the Lozier Canyon and west Texas Eagle Ford Group outcrops is given in Donovan et al. (2012); Gardner (2013); Gardner et al. (2013); Corbett et al. (2014); Lowery et al. (2014); Donovan et al. (2015) and Lowery and Leckie (2017b). Here, we present only a brief summary (table III.2) of the Lozier Canyon stratigraphic units with main emphasis on the lithologic units (A – E) and their associated sedimentary structures and bed forms. Because of difficulties distinguishing between units D and E in subsurface cores, units D and E are merged into one unit (DE_s) in the core descriptions.

Wells 1 and 2, Swenson 1H well and BP/SLB Lozier Canyon #1 cores were analyzed for elemental composition by ED-XRF analysis using Thermo Scientific Niton XL3t GOLDD+ X-Ray Fluorescence analyzer utilizing the calibration method outlined in Rowe et al. (2012). All the cores were sampled at ~ 15 cm (0.5 ft.) interval, except for the BP/SLB Lozier Canyon #1 core which was sampled at ~ 30.5 cm (1 ft.). The RSTE concentrations obtained by inductively coupled plasma mass spectrometry (ICP-MS) for Swenson 1H well are from Kelly (2016). RSTEs from both XRF (molybdenum, Mo; vanadium, V; and uranium, U) and ICP-MS (Mo, V; and nickel, Ni) analyses were normalized to average upper crust abundance of aluminum (Al) and their enrichment factors calculated following Brumsack (2006).

Aryl isoprenoids ratio (AIR) and pristine/phytane (Pr/Ph) ratios, organic indicators used to assess redox conditions of paleo-water columns during sedimentation (Didyk et al., 1978; Schwark and Frimmel, 2004), for Lozier Canyon outcrop and Swenson 1H well are from Romero (2016) and Maulana (2016), respectively. Pr/Ph ratios less than one indicate deposition under anoxic water column, whereas Pr/Ph ratios greater than one indicate deposition under oxic water column (Didyk et al., 1978). AIR varies between 0.5 and 3.0, with 0.5 indicating persistent photic-zone euxinia (PZE) and 3.0 indicating episodic photic-zone euxinia (Schwark and Frimmel, 2004).

Results

Lithostratigraphy

Lower Member of the Lower Eagle Ford Formation

In west Texas, the transition from the Buda Limestone to the Eagle Ford Group is characterized by a sharp lithological change from very light brown – light gray bioturbated skeletal wackestone and packstone to very dark gray, organic-rich, laminated, siliceous, argillaceous, calcareous mudstone of the Lower Eagle Ford Formation. The lithologic transition at the base of the Eagle Ford Group is marked by a sharp increase in the total clay, TOC and total gamma ray (GR) in the Lower Eagle Ford Formation (figures III.3, III.4, III.5, III.6 and III.7). In wells 1 and 2, a thin condensed interval of the Woodbine Group is present between the Buda Limestone and the Eagle Ford Group (figures III.4, III.5). Close to the Edwards margin and on the south Texas Submarine Plateau, the facies association in the basal section of the Lower Member of the Lower Eagle Ford Formation (Unit A_s) comprises dark to very dark gray, laminated, organic-rich, siliceous, argillaceous, calcareous mudstone with interbeds of laminated bioclastic wackestone (figure III.8A-C; table III.1). Unit A_s grades into an upper interval (unit B_s1) of laminated, organic-rich, calcareous mudstone and interbedded skeletal packstone/grainstone (figure III.9A-C; table III.1). In well 1, unit B_s1 records isolated bioturbated intervals (BI: 2 - 3) on top of laminated beds that were subsequently overlain by organic-rich mudstone (figure III.9C).

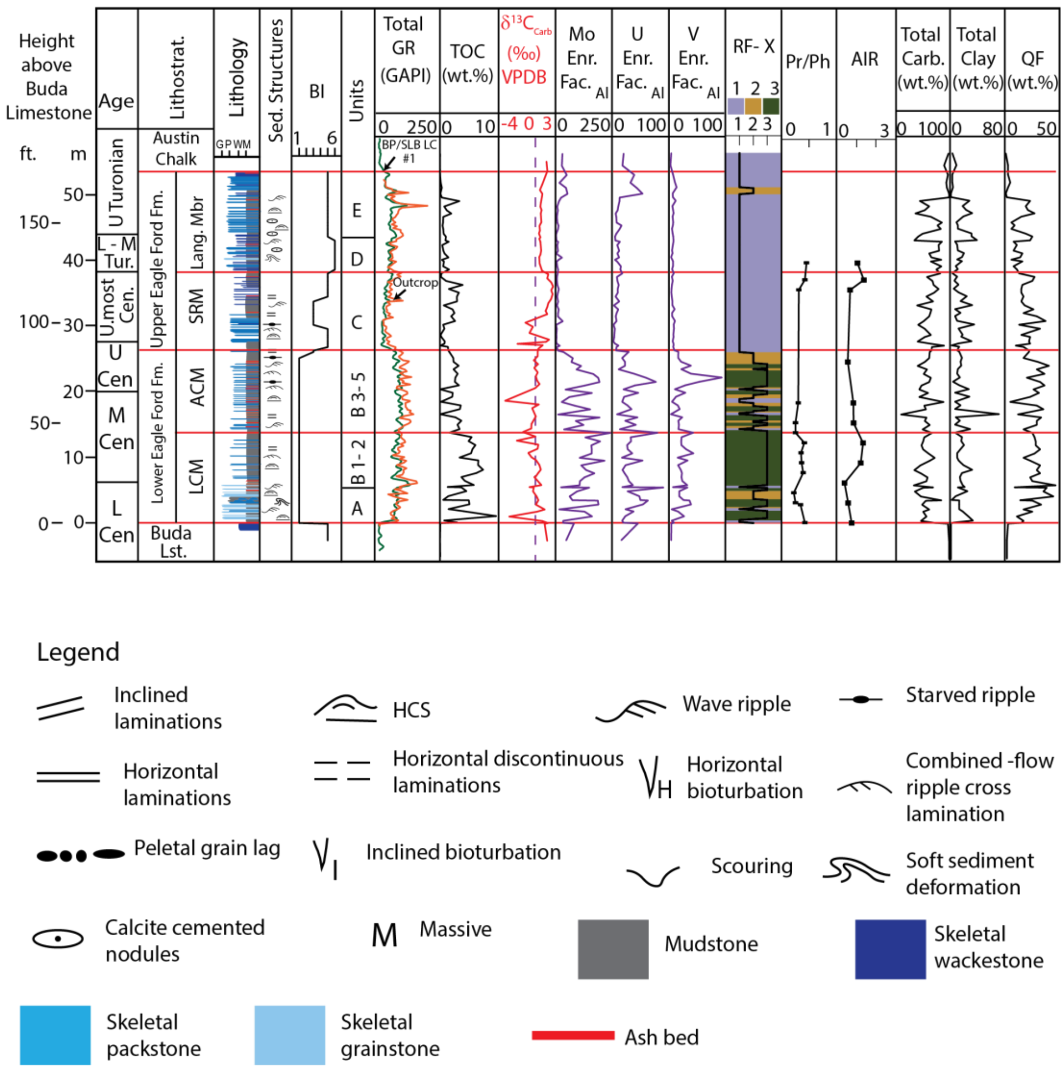

Figure III.3 Integrated composite stratigraphy for the Lozier Canyon outcrop, Antonio Creek outcrop and BP/SLB Lozier Canyon #1 well (Terrell County, Texas) with a summary of the geochemical, mineralogical and petrophysical data. The integrated stratigraphic data from this outcrop provides the foundation for correlating outcrop units to subsurface units in oil- and gas-producing wells in south Texas. Age model is from chapter II, Lowery et al. (2014) and Corbett et al. (2014). Total organic carbon, X-Ray diffraction (XRD) data, GR logs and $\delta^{13}C_{carb}$ are from Donovan et al. (2015); pristane/phytane (Pr/Ph) ratio and aryl isoprenoid ratios (AIR) are from Romero (2014); lithology and division of lithologic units are based on Donovan et al. (2012) and Gardner (2013). Geologic stages after Ogg et al. (2016). Fm. = Formation; Cen. = Cenomanian; Tur. = Turonian; QF = quartz and feldspar; TOC = total organic carbon; Enr.Fac. = enrichment factor; Carb. = carbonate; Lithostrat. = lithostratigraphy; BI = bioturbation index; Mo = molybdenum; V = vanadium; U = uranium; U.most = Uppermost. Mbr = Member; SRM = Scott Ranch Member.

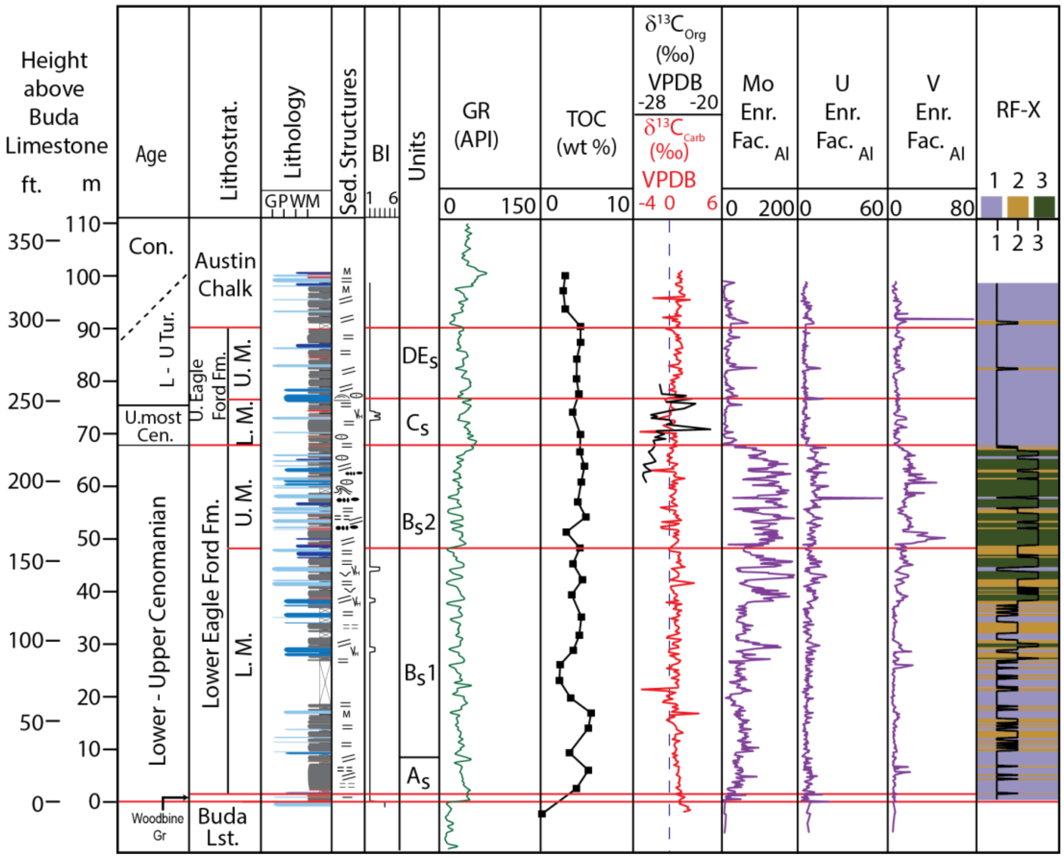

Figure III.4 Summary of lithologic, chemostratigraphic, geochemical and petrophysical data for well 1 (Live Oak County, Texas). Subsurface Eagle Ford Group strata bears similar geochemical and petrophysical characteristics to the outcrop strata. The Lower Eagle Ford Formation is enriched in redox sensitive trace elements (RSTEs) relative to the upper crust. Well 1 has high TOC in both the Lower and Upper Eagle Ford Formations and has isolated bioturbated intervals in the Lower Eagle Ford Formation. A thin (~1.52 m/5 ft) condensed interval of the Woodbine Group is preserved between the Buda Limestone and the Eagle Ford Group. Geologic stages after Ogg et al. (2016); Sed. = Sedimentary.

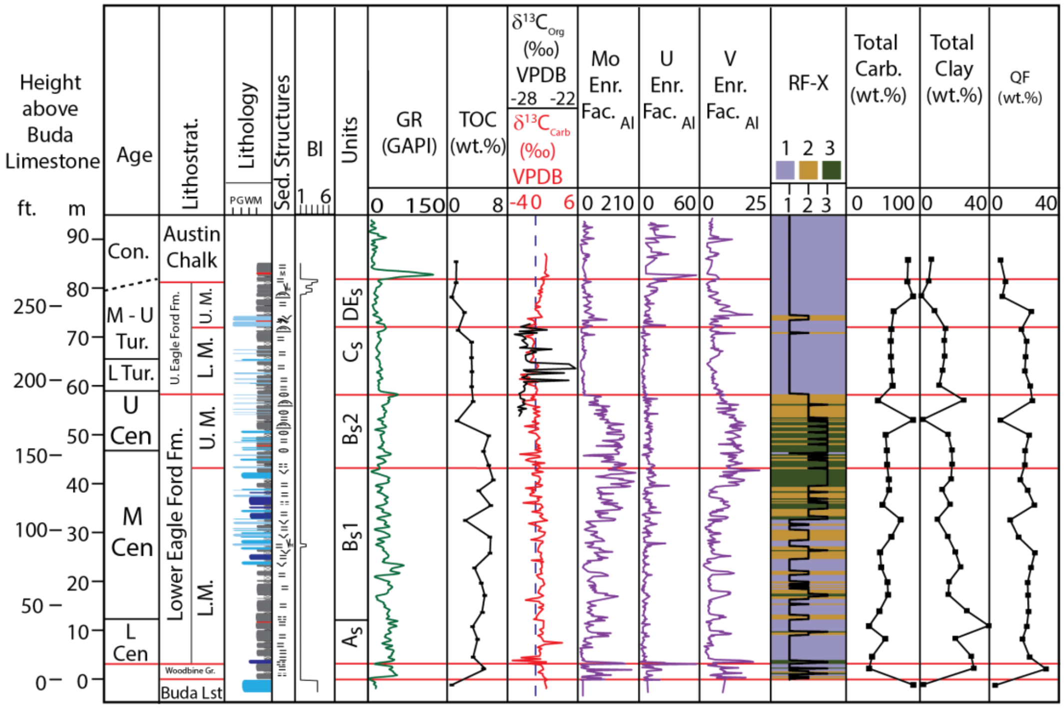

Figure III.5 Summary of lithologic, biostratigraphic, chemostratigraphic, geochemical, mineralogical and petrophysical data for well 2 (Karnes County, Texas). Well 2 also records high TOC in the Upper Eagle Ford Formation. The Lower Member of the Upper Eagle Ford Formation lacks bioturbation. A thin (~ 3 m/10 Ft.) condensed interval of the Woodbine Group is preserved between the Buda Limestone and the Eagle Ford Group. Geologic stages after Ogg et al. (2016).)

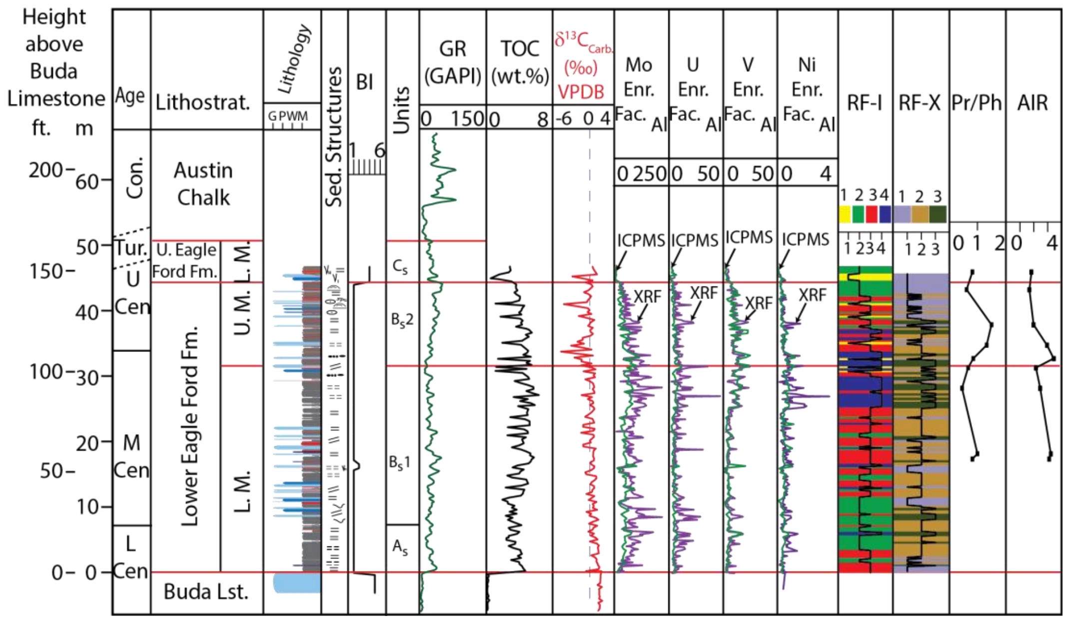

Figure III.6 Summary of lithologic, chemostratigraphic, geochemical and petrophysical data for Swenson 1H well (McMullen County, Texas). High-resolution ICP-MS and TOC data (30.5 cm/1 ft.) provides a detailed insight into the subtle geochemical variations in the Swenson 1H well. Pr/Ph ratio and AIR from Maulana (2016) allows comparison of water column anoxia between the Swenson 1H well and the Lozier Canyon outcrop. Geologic stages after Ogg et al. (2016); ICP-MS data are from Kelly (2016).

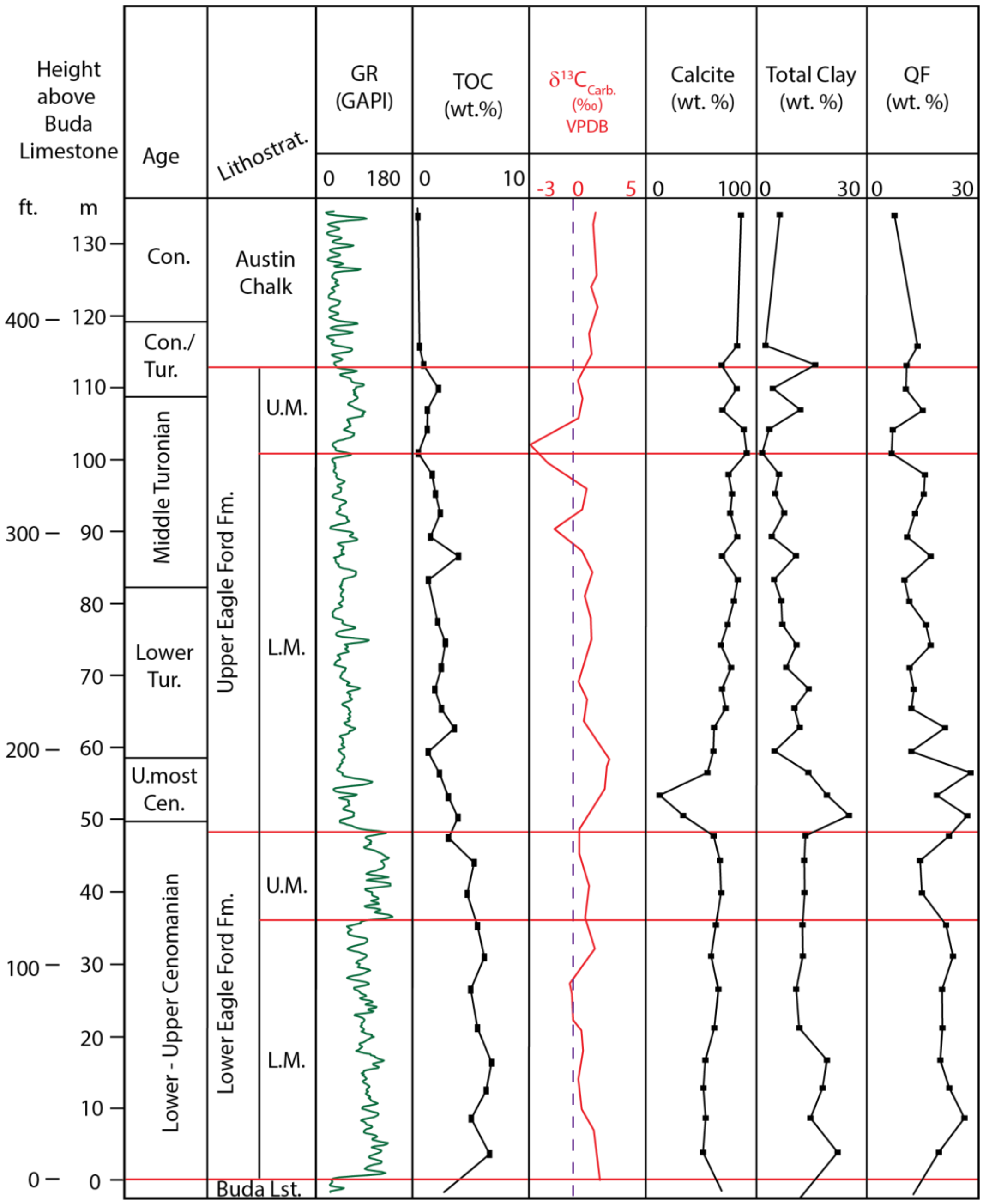

Figure III.7 Summary of biostratigraphic, chemostratigraphic, mineralogical and petrophysical data for Fasken A 1H well (Webb County, Texas). The Fasken A 1H well is in the most distal Eagle Ford Group depositional setting in this study. Geologic stages after Ogg et al. (2016); Age model is from Lowery et al. (2014) and Corbett et al. (2014); $\delta 13C_{carb}$ from Lowery et al. (2014) and Corbett et al. (2014); TOC, well log and XRD are from Donovan et al. (2012).

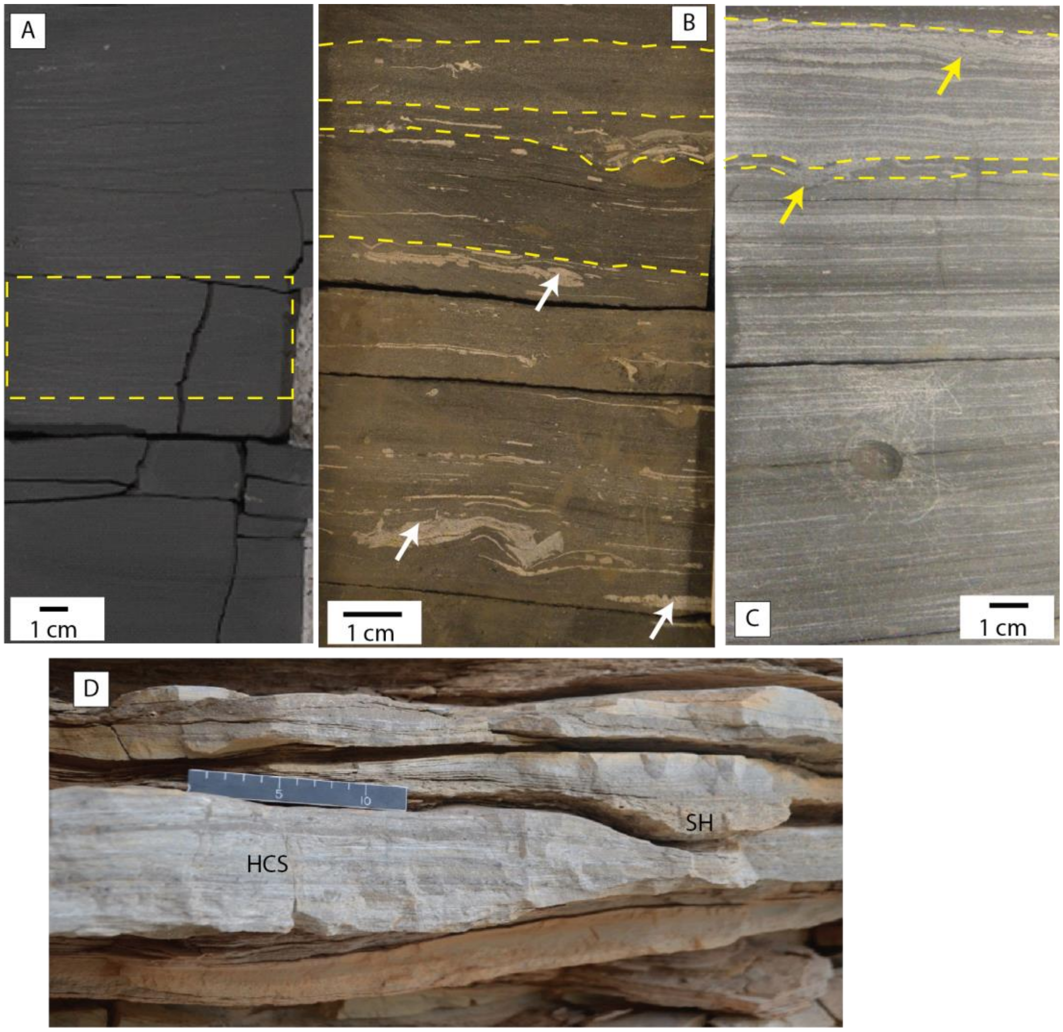

Figure III.8 Images of units A_s from subsurface cores and unit A from Lozier Canyon outcrop. (A) Core image of laminated foraminiferal mudstone (unit A_s). Yellow dotted rectangle highlights wave ripples at the base of the Lower Eagle Ford Formation. (B) Core image of laminated bioclastic wackestone (unit A_s) with abundant inoceramid fragments (white arrows) at the base of the Lower Eagle Ford Formation in well 2 (Karnes County). Yellow dotted lines highlight some of the bed boundaries. (C) Laminated skeletal grainstone/packstone (unit A_s). Yellow arrows point to local scours and yellow dotted lines highlight bedding. (D) Hummocky cross-stratified (HCS) bedding of unit A at Lozier Canyon (SH = shell hash). Scale in centimeters. Scale in centimeters (cm).

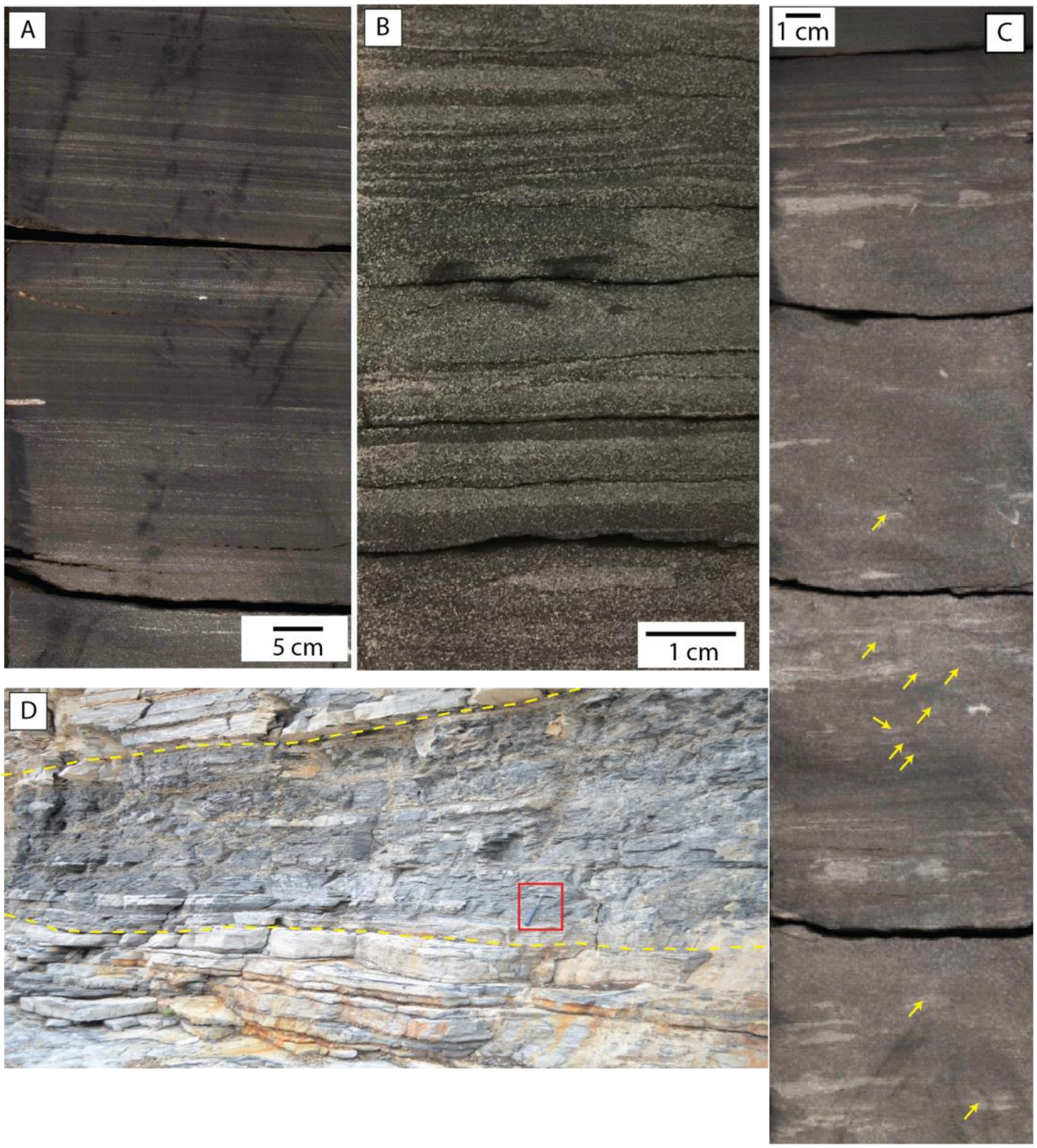

Figure III.9 Images of units B_s1 from subsurface cores and unit B from outcrop. (A) Core image of laminated calcareous mudstone. (B) Core image of laminated foraminiferal packstone/grainstone. (C) Core image of laminated skeletal packstone with disruptions in laminae interpreted to be bioturbation (yellow arrows) in well 1. The bioturbated bed was subsequently overlain by laminated, organic-rich mudstone. (D) Outcrop photo showing the organic-rich laminated mudstone at base of unit B (enclosed between dotted yellow lines). Red square shows hammer (30 cm/~1 ft long) for scale.

Up dip of the Edwards margin (Lozier Canyon and Antonio Creek outcrops), the basal interval comprises unit A of the Lower Member (Lozier Canyon Member) of the Lower Eagle Ford Formation (figure III.8D; table III.2) (Donovan et al., 2012; Gardner et al., 2013). The upper interval of the Lower Member (Lozier Canyon Member) of the Lower Eagle Ford Formation comprises subunits B1 – B2 of unit B (figure III.9D; table III.2) (Donovan et al., 2012; Gardner et al., 2013).

In well 2, Fasken A 1H and Lozier Canyon, the Lower Member of the Lower Eagle Ford Formation has relatively low average total carbonate with relatively high quartz and feldspar and variable total clay (table III.3). The number of volcanic ash beds (table III.4) in the Lower Member of the Lower Eagle Ford Group vary from one in well 2 to thirty six at Lozier Canyon (Gardner, 2013).

Upper Member of the Lower Eagle Ford Formation

Close to the Edwards margin and in the South Texas Submarine Plateau, the facies association comprises dark gray laminated, organic-rich, calcareous mudstone beds interbedded with calcite-cemented, nodular skeletal packstone/grainstone beds (unit B_s2; figure III.10; table III.1). At Lozier Canyon, the interval comprises subunits B3 –B5 of unit B (table III.2) (Donovan et al., 2012; Gardner et al., 2013). The TOC has an overall gradual upward-decreasing trend, except for well 1 where the TOC remains high (> 3%) throughout the interval and records no significant upward decrease.

Table III.2 Summarized comparison between Lozier Canyon outcrop and subsurface units

	Outcrop summary from Gardner (2013) and Donovan et al. (2012)			Subsurface summary		
Formation	Unit	Key sedimentary features	Interpretation	Unit	Key sedimentary features	Interpretation
Upper Member Upper Eagle Ford	E	Light gray, bioturbated grainstone (GS)/packstone (PS) bed sets with abundant wave ripples and hummocky cross stratification (HCS)	Open shelf; deposited within storm wave base	DE_s	Light to medium gray, stacked bed and bed sets of laminated skeletal PS/GS with interbeds of calcareous mudstone; abundant HCS, wave ripple lamination, load casts, local subtle grading in laminae, locally thin bioturbated intervals.	Open shelf, deposited within storm wave base
	D	Light Gray, burrow-homogenized beds of calcareous mudstone (MS) interbedded with skeletal PS; contains basal pebble-sized clasts.	Most oxygenated, open shelf setting; deposited within storm wave base			
Lower Member Upper Eagle Ford	C	Light gray calcareous MS interbedded with skeletal wackestone (WS)/PS bed sets; contains abundant pyrite. Abundant burrows, remnant cross-laminations.	Open shelf, episodically within storm wave base	C_s	Light gray calcareous MS interbedded with medium gray argillaceous, calcareous MS and skeletal WS. Abundant large pyrite. Occasional HCS, rare graded bedding	Open shelf settings, episodically within storm wave base.
Upper Member Lower Eagle Ford	B (Subunits B3-B5)	Carbonate and organic-rich MS interbedded with skeletal GS/PS beds, calcite-cemented, nodular beds of skeletal PS/GS. Occasional horizontal burrows.	Restricted shelf, episodically within storm wave base	B_s2	Medium gray calcareous MS and dark gray argillaceous, calcareous mudstone interbedded with calcite-cemented, nodular skeletal PS/GS. Abundant local scoured bed contacts, basal flame structures, load casts, occasional HCS	Restricted to open shelf settings, episodically within storm wave base
Lower Member Lower Eagle Ford	B (Subunits B1-B2)	Black organic-rich calcareous MS interbedded with skeletal PS/GS bed sets. Stacked HCS/SCS. Upward increase in the frequency and thickness of the skeletal PS/GS beds. Occasional horizontal burrows.	Restricted shelf, episodically within storm wave base	B_s1	Medium to dark gray, argillaceous, calcareous mudstone interbedded with foraminiferal PS/GS. Abundant erosional bed contacts, wave ripple bed sets, thin isolated burrowed intervals	Deposited in restricted shelf settings, episodically within storm wave base.
	A	Bed sets of light gray skeletal PS/GS interbedded with calcareous MS. Abundant pyrite. Abundant HCS, SCS, wave ripples, combined flow structures, local zones of contorted and deformed beds	Restricted shelf, deposited within storm wave base	A_s	Dark to very dark gray siliceous, argillaceous, calcareous MS interbedded with medium to dark gray bioclastic WS; abundant pyrite. Wave ripples, local scoured bed contacts	Restricted shelf setting, deposited within storm wave base

Table III.3 Summarized X-Ray diffraction (XRD) data

Lozier Canyon (Terrell Co.)

	Total Carbonate			Total Clay			QF		
Member	Avg	Min	Max	Avg	Min	Max	Avg	Min	Max
UMUEF	69	35	98	16	0	38	13	1	27
LMUEF	62	40	89	13	1	34	20	10	37
UMLEF	55	11	88	15	3	70	26	5	40
LMLEF	54	34	84	15	1	32	26	9	46

Fasken A 1H (Webb Co.)

	Total Carbonate			Total Clay			QF		
Member	Avg	Min	Max	Avg	Min	Max	Avg	Min	Max
UMUEF	81	70	91	7	1	16	10	7	15
LMUEF	78	69	84	6	4	11	14	10	17
UMLEF	63	35	78	13	5	25	18	12	28
LMLEF	56	52	66	16	11	22	22	20	27

Well 2 (Karnes Co.)

	Total Carbonate			Total Clay			QF		
Member	Avg	Min	Max	Avg	Min	Max	Avg	Min	Max
UMUEF	80	65	91	5	1	8	15	7	23
LMUEF	62	61	63	13	11	15	20	18	23
UMLEF	60	43	91	16	2	25	18	6	24
LMLEF	52	31	74	21	10	40	21	12	25

UMUEF Upper Member Upper Eagle Ford Formation
LMUEF Lower Member Upper Eagle Ford Formation
UMLEF Upper Member Lower Eagle Ford Formation
LMLEF Lower Member Lower Eagle Ford Formation

Table III.4 Number of volcanic ash bed count

Member	Lozier Canyon (Gardner, 2013)	Swenson 1H	Well 1	Well 2
UMUEF	4	-	3	1
LMUEF	21	5	4	0
UMLEF	58	24	7	1
LMLEF	36	19	7	1

In well 2, Fasken A 1H well and Lozier Canyon, the average and maximum total carbonate increase slightly relative to the underlying interval (table III.3). While there is no increase in the number of volcanic ash beds in this interval in wells 1 and 2, the Swenson 1H and Lozier Canyon locations record a significant increase in the number of volcanic ash beds (table III.4). In well 2, although the interval has only one ash bed (table III.4), there are diagenetically altered grainstone/packstone beds mixed with volcanic ash (figure III.10C).

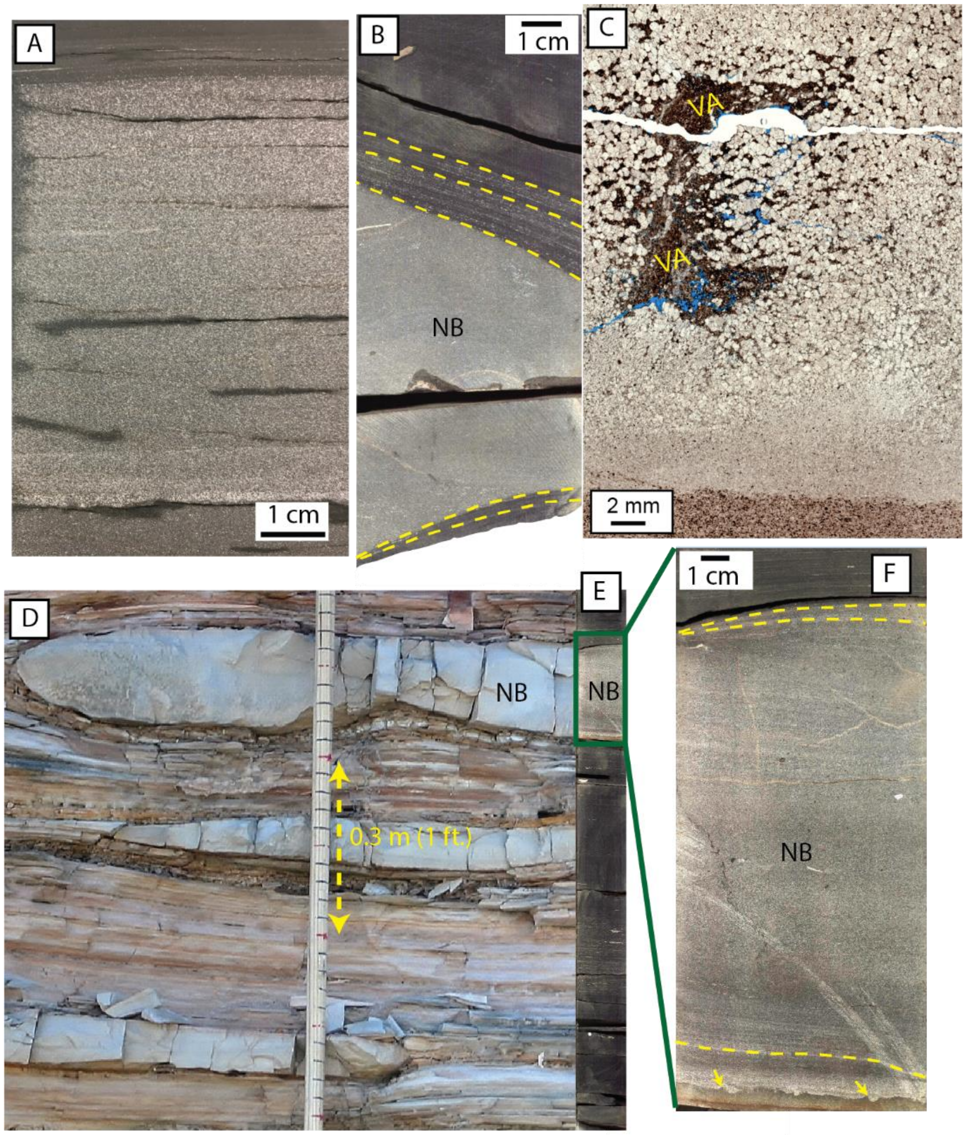

Figure III.10 Images of units B_s2 from subsurface cores and unit B (subunit B3-5) from outcrop. (A) Core image showing interbedded skeletal grainstone and mudstone (B) Core image showing HCS and calcite-cemented nodular bedding (NB) with inclined laminae (basal yellow dotted lines). (C) Scanned thin section showing a storm-related deposit that is mixed with volcanic ash (VA) and phosphate debris and has been diagenetically altered. (D) and (E) comparing calcite-cemented nodular beds from the Upper Member of the Lower Eagle Ford Formation in outcrop (D) to the coeval section in subsurface core (E). Both core and outcrop images have the same scale. (F) Enlarged image of the highlighted section (green rectangle) in E showing curved laminae (yellow dotted lines) and sharp erosional base with small load cast and flame structures (yellow arrows).

Lower Member of the Upper Eagle Ford Formation

Close to the Edwards margin and on the South Texas Submarine Plateau, the facies association comprises very light to medium gray, laminated, bioturbated calcareous mudstone and argillaceous, calcareous mudstone interbedded with skeletal packstone/grainstone (unit C_s; figure III.11A-C & E; table III.1). The interval also contains abundant pyrite. In the Swenson 1H well, the trace fossils in this zone include *Teichichnus*, *Planolites* and *Chondrites* (figure III.11A – C). *Teichichnus* trace fossils occur mostly in calcareous mudstone (figure III.11C) having low TOC (<<1%) with bioturbation index varying from 3 to 5, whereas *Chondrites* and *Planolites* trace fossils occur mostly in argillaceous, calcareous mudstone with moderate TOC values (generally <2%) and bioturbation index varying from 2 to 4 (figure III.11B). The interval has no bioturbation in well 2. At Lozier Canyon, the interval comprises unit C (figure III.11C; table III.2) (Donovan et al., 2012; Gardner et al., 2013). In both the up dip and down dip sections, the TOC generally is low, with the bioturbated intervals recording some of the lowest TOC (< 0.1 wt.%), except for wells 1 and well 2 (figures III.4 & III.5) where the interval persistently records TOC values over 3 wt.% and 4 wt.%, respectively.

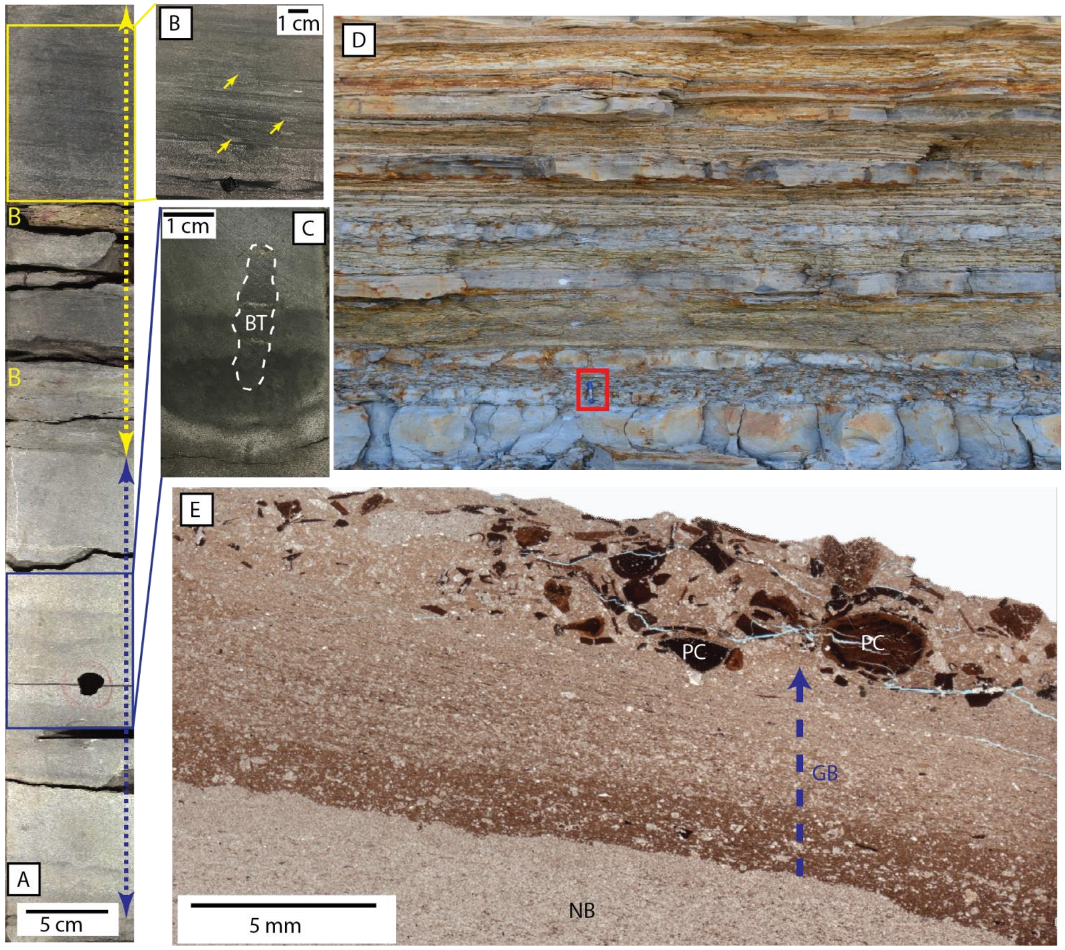

Figure III.11 Units C_s from subsurface core and Unit C from outcrop. (A) Core image showing variation in bioturbated limestone interval (blue dotted double head arrow) and bioturbated argillaceous, calcareous mudstone interval (yellow dotted double head arrow) with bentonite interbeds (B). (B) Core image showing *Chondrites* and *Planolites* bioturbation (yellow arrows). (C) Core image showing centimeter thick *Teichichnus* burrow (white dotted line) surrounded by several smaller vertical to sub-vertical burrows. (D) Unit C in outcrop showing interbedded calcareous mudstone and wackestone with extensive bioturbation and abundant pyrite. Red box shows Sharpie marker (14 cm/~ 0.46 ft. long) for scale. (E) Thin section photomicrograph from the base of the Lower Member of the Upper Eagle Ford Formation (Lower/Upper Eagle Ford Formation contact) in well 2, Karnes County, Texas, showing coarse phosphate skeletal debris overlying a graded bed (dotted blue arrow).

The average total carbonate increases in both the up dip and down dip sections, whereas the total clay decreases (table III.3). The number of ash bed varies from four in well 1 to 21 at Lozier Canyon, whereas well 2 has no ash beds (table III.4). The base of this interval marks the transition from the Lower to the Upper Eagle Ford Formation and is characterized by a decrease in total GR. A thin section from the base of the Lower Member of the Upper Eagle Ford Formation in well 2 contains randomly oriented and scattered phosphate skeletal debris overlying graded bedding (figure III.11E).

Upper Member of the Upper Eagle Ford Formation

Close to the Edwards margin and on the South Texas Submarine Plateau, the facies association in the Upper Member of the Upper Eagle Ford Formation comprises light to medium gray, laminated skeletal packstone to grainstone interbedded with calcareous mudstone, and bioturbated calcareous mudstone (Unit DE_s; figure III.12; table III.1).

In well 2, this interval has abundant lamina with varying thicknesses and geometry, sharp bed contacts, erosional bases separating laminated beds, local scoured surfaces, soft-sediment deformation, local rip-up clasts and differential compaction passing upward to abundant bioturbation and phosphate skeletal debris near the Upper Eagle Ford Formation – Austin Chalk contact. At the Lozier Canyon, the interval is sub-divided into units D and E (figure III13; table III.2) (Donovan et al., 2012; Gardner et al., 2013). In well 2, Lozier Canyon and the Fasken A 1H well, this interval records high average and maximum total carbonate with low average total clay and quartz and feldspar (table III.3).

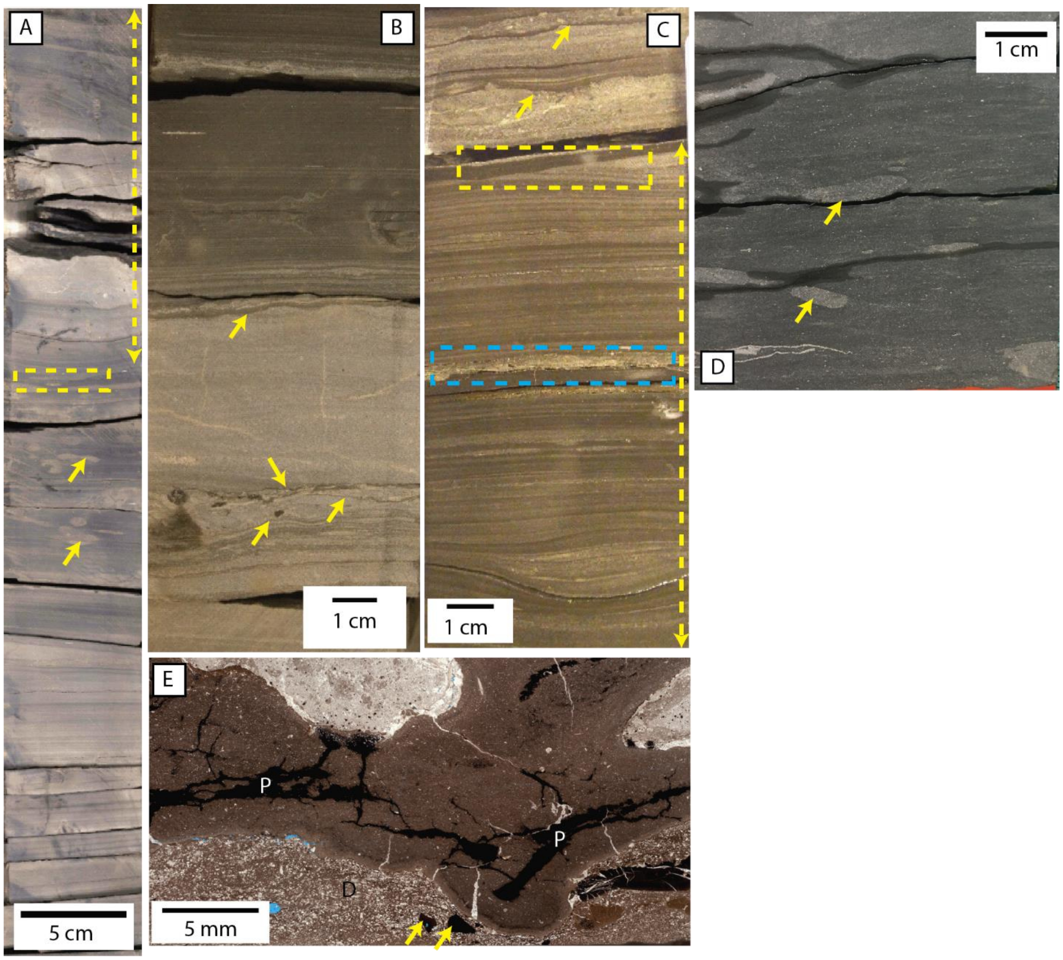

Figure III.12 Unit DE_s from core and scanned thin section. (A) Core image of well laminated calcareous mudstone, calcite-cemented nodular bed (dotted double head arrow) and bioturbation (yellow arrows) from well 1 in Live Oak County, Texas. Yellow rectangle highlights scouring at the base of a calcite-cemented nodule. (B) Core image showing erosional bases and sharp bed contacts (yellow arrows). Note the mudstone bed above the sharp bed contact. (C) Core image showing stacked thin beds with sharp bed contacts, erosional bases (yellow arrows) and differential compaction overlying a HCS bed set (yellow dotted double head arrow). Blue rectangle highlights erosional base with grain lags separating the two HCS beds. Yellow rectangle highlights a thin mudstone bed (< 1 cm) overlying an erosional truncation that cuts out the laminae in the underlying HCS bed. (D) Core image showing bioturbation (yellow arrows) close to the top of the Upper Member of the Upper Eagle Ford Formation in Karnes County, Texas. (E) Thin section photomicrograph showing phosphate interval with skeletal debris (D), phosphate clasts (yellow arrows) and pyrite (P) close to the Eagle Ford Group/Austin Chalk contact in Karnes County, Texas.

The interval has only few ash beds (table III.4). In well 2, Fasken A 1H well, and at the Lozier Canyon, the interval records low TOC values (< 1 to < 2.5 wt.%), whereas well 1 records TOC values above 4 wt.%.

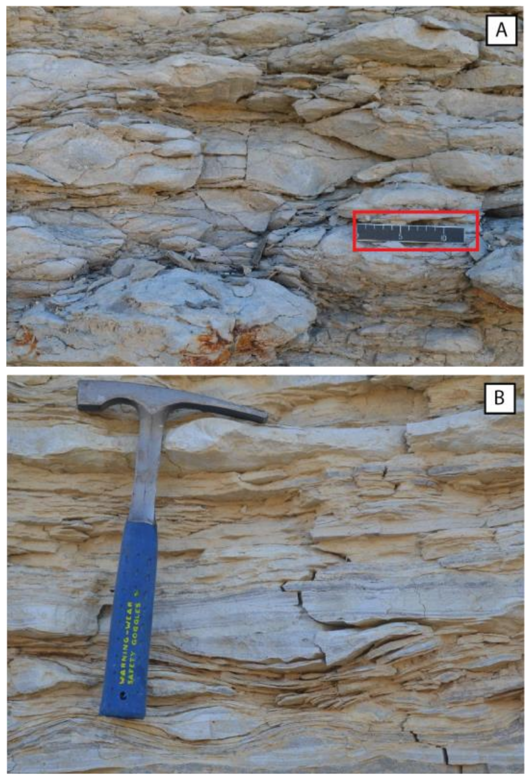

Figure III.13 Units D and E from outcrop. (A). Burrow-homogenized bedding of unit D (Antonio Creek, west Texas). Red rectangle shows centimeter scale. (B) Outcrop image of chaotic bedding and HCS in unit E, very similar to unit DE_s. Hammer for scale (13 cm length)

Geochemistry

In wells 1 and 2, Swenson 1H and the Lozier Canyon outcrop (figures III.3, III.4, III.5 and III.6; table III.5), the Lower Eagle Ford Formation is enriched in RSTEs (Mo, U and V) relative to the upper crust. RSTE enrichment decreases significantly in the Upper

Eagle Ford Formation, with the Lower Member of the Upper Eagle Ford Formation having the lowest average RSTEs enrichment (table III.5).

XRF data for wells 1 and 2, Swenson 1H and the Lozier Canyon outcrop were classified by unsupervised neural network analysis. Three classes of redox facies (RF-X) were identified based on Mo and V enrichment (figure III.14A). RF-X1 is characterized by low Mo (0 – 50) and low V (0 – 20) enrichment, RF-X2 is characterized by moderate Mo (~ 50 – 110) and low V (0 -20) enrichment, and RF-X3 is characterized by high Mo (> 110) and variable V (> 5 – 40) enrichment (figure III.12A). The Swenson 1H well was selected for further geochemical analysis for correlation with organic biomarker records and high-resolution (~30.5 cm; 1 ft) TOC and ICP-MS data (Kelly, 2016; Maulana, 2016).

The ICP-MS (Mo, V and Ni) and TOC data were analyzed by principal component analysis (PCA; table III.6) and an unsupervised neural network analysis to create four redox facies (RF-I; figure III.14C-D). In the unsupervised neural network analysis, only principal component 1 (PC1) and principal component 2 (PC2) were used in the final redox facies generation because PC1 has the most positive correlation with the RSTEs (0.81, 0.91 and 0.94 for V, Ni and Mo, respectively) and PC2 has the most negative correlation (~ - 0.81) with TOC, and both have the most contribution (87%) to the PCA (table III.6). While the RF-X redox facies compares Mo and V enrichment among Wells 1 and 2, Swenson 1H well and Lozier Canyon, RF-I redox facies provides better insights into the subtle geochemical variations at the Swenson 1H well location (figures III.4 and III.14B-D).

Table III.5 Summarized redox-sensitive trace element (RSTE) values

Lozier Canyon (Terrell County)

	Mo(EnrFac)			U (EnrFac)			V (EnrFac)			
Member	Avg	Min	Max	Avg	Min	Max	Avg	Min	Max	XRF Redox Facies
UMUEF	14	2	52	15	5	53	8	4	14	RF-X1
LMUEF	9	2	31	7	2	18	7	4	11	RF-X1
UMLEF	98	11	194	29	7	77	25	4	94	RF-X3, -X2, X1
LMLEF	126	16	242	36	17	90	24	5	44	RF-X3*, -X2

Swenson 1H Well (McMullen County)

	Mo(EnrFac)			U (EnrFac)			V (EnrFac)			
Member	Avg	Min	Max	Avg	Min	Max	Avg	Min	Max	XRF Redox Facies
UMUEF	-	-	-	-	-	-	-	-	-	-
LMUEF	8	1	7	3	1	5	4	2	4	RF-X1
UMLEF	80	26	217	9	2	47	12	3	204	RF-X3*, -X2*, X1
LMLEF	77	13	218	7	2	31	5	1	18	RF-X3*, -X2*, -X1

Well 1 (Live Oak County)

	Mo(EnrFac)			U (EnrFac)			V (EnrFac)			
Member	Avg	Min	Max	Avg	Min	Max	Avg	Min	Max	XRF Redox Facies
UMUEF	17	4	39	5	2	16	7	4	10	RF-X1
LMUEF	14	3	50	4	2	7	8	5	16	RF-X1
UMLEF	118	27	189	11	3	56	17	6	51	RF-X3*, -X2, X1
LMLEF	54	7	177	6	2	16	6	2	18	RF-X3,-X2*, -X1

Well 2 (Karnes County)

	Mo(EnrFac)			U (EnrFac)			V (EnrFac)			
Member	Avg	Min	Max	Avg	Min	Max	Avg	Min	Max	XRF Redox Facies
UMUEF	29	8	97	11	5	27	7	3	19	RF-X1
LMUEF	14	4	53	5	2	2	6	3	12	RF-X1
UMLEF	112	44	200	9	4	30	11	3	21	RF-X3*, -X2
LMLEF	56	2	153	6	2	27	5	2	18	RF-X3, -X2*, -X1

Asterisk indicate the dominant RF-X (redox facies generated using XRF data) facies in the interval

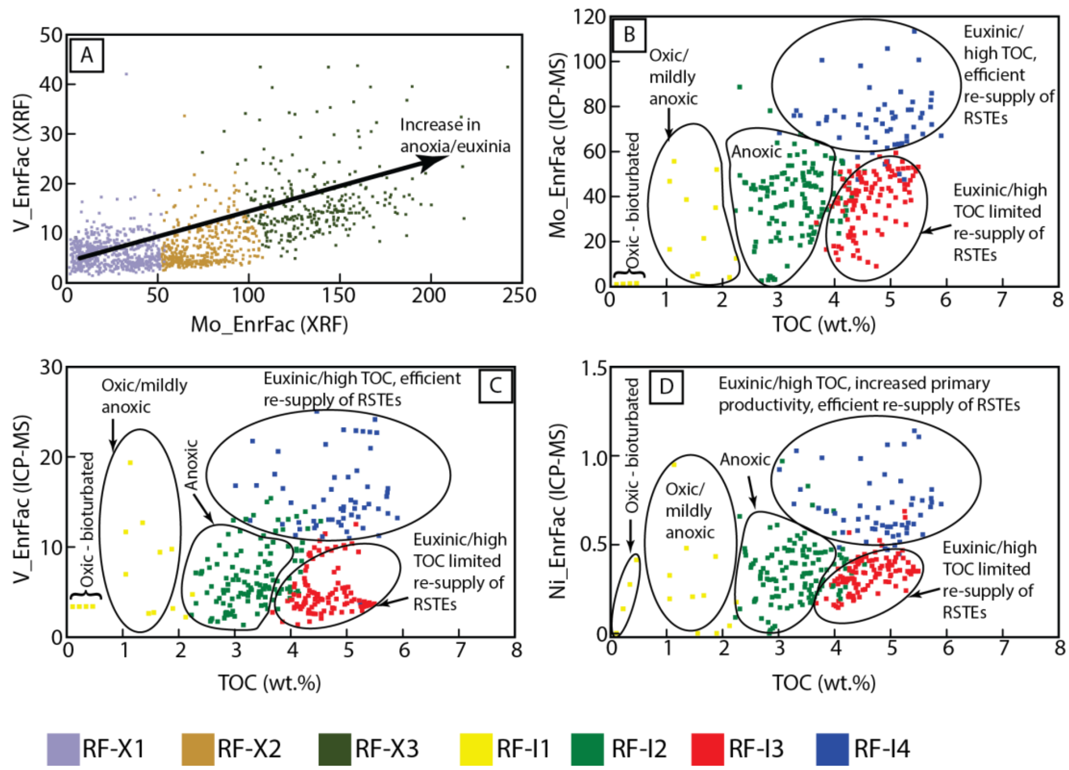

Figure III.14 Redox facies cross plots. XRF data provides comparison of redox sensitive trace elements (Mo and V) for Lozier Canyon, well 1, well 2 and Swenson 1H, whereas corresponding ICP-MS and TOC data at 30.5 cm (1 ft.) interval provides detailed insight into subtle geochemical variations at the Swenson 1H well location. (A) XRF V and Mo enrichment factor cross plot colored by redox facies (RF-X). (B) ICP-MS Mo enrichment factor/TOC cross plot for Swenson 1H colored by redox facies (RF-I). (C) ICP-MS V enrichment factor/TOC cross plot for Swenson 1H colored by redox facies (RF-I). (D) ICP-MS Ni enrichment factor/TOC cross plot for Swenson 1H colored by redox facies (RF-I).

Table III.6 Correlation table and PCA parameters for Swenson 1H well redox facies (RF-I)

Correlation Coefficients	PC1	PC2	PC3	PC4
Mo (EnrFac)	0.94	0.06	0.22	0.27
Ni (EnrFac)	0.91	0.17	0.28	-0.24
V (EnrFac)	0.81	0.31	-0.49	-0.01
TOC (wt.%)	0.57	-0.82	-0.11	-0.04
Eigenvalue	2.69	0.79	0.38	0.13
Contribution (%)	67.22	19.85	9.58	3.36
Cumulative Contribution (%)	67.22	87.07	96.64	100.00

Discussion

Eagle Ford Group Depositional Models

Based on the sedimentology, mineralogy, RSTE geochemistry, organic geochemistry and geochronological age models from chapter II, the Eagle Ford Group depositional setting is sub-divided into five time intervals from the base of the Eagle Ford Group to the Eagle Ford Group – Austin Chalk contact (figure III.15A-E). Each time interval has a depositional model that extends from the Lozier Canyon outcrop on the Comanche Platform to the south Texas Submarine Plateau down dip of the Edwards reef margin.

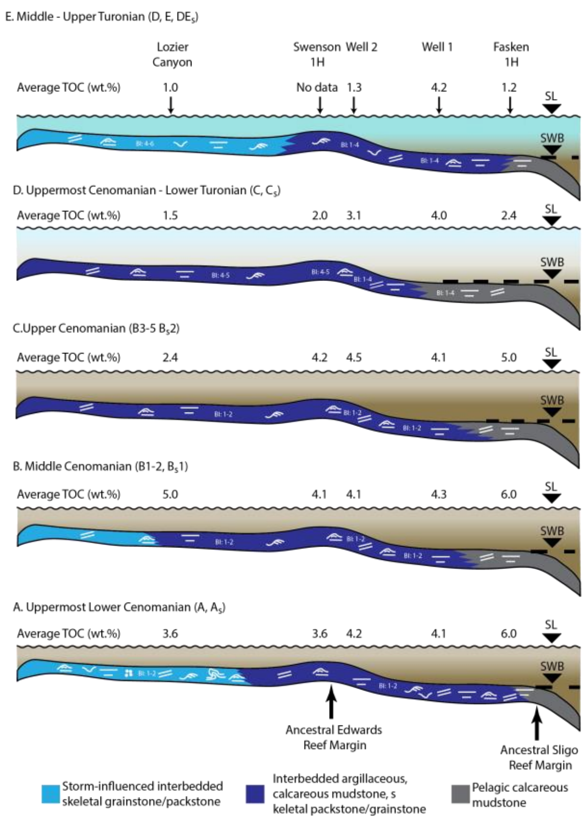

Figure III.15 Proposed depositional profiles for the Eagle Ford Group depositional setting. (A) Uppermost Lower Cenomanian. This time interval is marked by weakly restricted circulation coupled with primary productivity that is enhanced by volcanic ash input, promoting widespread benthic anoxia and episodic photic zone euxinia. (B) Middle Cenomanian. This time interval is marked by weakly restricted bottom water circulation coupled with enhanced primary productivity linked to volcanic ash input resulting in a prolonged drawdown of RSTEs, widespread benthic anoxia and episodic photic zone euxinia (C) Upper Cenomanian. This interval is marked by weakly restricted to open marine circulation, increased volcanic ash input that enhanced primary productivity through iron fertilization, widespread benthic anoxia and episodic photic zone euxinia, and efficient re-supply of RSTEs from the global ocean as the Atlantic Tethyan water masses migrated northward into the KWIS (D) Uppermost Cenomanian – Lower Turonian. This time interval is marked by open marine circulation, improved benthic oxygenation and widespread bioturbation (E) Middle – Upper Turonian. This time interval is marked by open marine circulation with the up dip section recording higher degree benthic oxygenation than the coeval down dip section.

Uppermost Lower Cenomanian

This time interval corresponds to the deposition of units A and A_s (figure III.15A), with storm-influenced interbedded skeletal packstone and grainstone up dip of the Edwards reef margin, passing down dip into interbedded siliceous, argillaceous, calcareous mudstone and bioclastic wackestone, and pelagic calcareous mudstone in the most distal settings. This time interval also is coincident with the initial transgression of warm, normal-saline, oxygen-poor water masses from the Tethyan region into the KWIS (Eldrett, 2017; Kauffman, 1984; Lowery, 2017a). The interval has skeletal grainstone/packstone bed sets containing abundant wave-generated sedimentary structures produced within storm wave base in the base of the Lower Eagle Ford Formation. This interval is interpreted to represent a time of weakly restricted circulation coupled with primary productivity that was enhanced by iron fertilization related to volcanic ash input (Zeng et al., 2018), promoting widespread benthic anoxia and episodic photic zone euxinia.

Middle Cenomanian

This time interval coincides with the deposition of unit B_s1 and subunits B1 – B2 of unit B and records widespread deposition of organic-rich, calcareous mudstone interbedded with skeletal packstone /grainstone in both up dip and down dip sections (figure III.15B). In the Swenson 1H well, the upward increase in TOC without a concomitant increase in RSTE (change from RF-I2 to RF-I3) potentially reflects a prolonged drawdown in RSTEs linked to basinal water mass restriction that limits the re-supply of RSTE from the open ocean. The interval is capped by a significant increase in RSTEs (predominantly RF-I4 in the Swenson 1H well; and RF-X3 in the Swenson 1H well, wells 1 and 2, and Lozier Canyon), indicating an increase in re-supply of RSTEs. In the Swenson 1H well, the increase in Ni enrichment in the uppermost interval relative to the underlying interval suggests increased primary productivity. In this time interval, weakly restricted bottom water circulation coupled with enhanced primary productivity linked to volcanic ash input (Zeng et al., 2018) resulted in widespread benthic anoxia and episodic photic zone euxinia.

Uppermost Middle - Upper Cenomanian

This time interval corresponds to the deposition of unit B_s2 and subunits B3 – B5 of unit B (figure III.15C). The interval records widespread deposition of organic-rich, calcareous mudstone interbedded with skeletal packstone/grainstone and calcite-cemented nodular skeletal packstone/grainstone bed in both the up dip and down dip sections (figure III.10D-F), indicating a laterally extensive depositional environment. In the Swenson 1H well and Lozier Canyon, the interval also records a significant increase in the number of volcanic ash beds relative to the underlying interval. High enrichment of RSTEs (Mo and V) in the basal section of this interval suggests a strongly euxinic environment with efficient re-supply of RSTEs to the basinal water mass from the global ocean. In the Swenson 1H well, high Ni enrichment in the basal interval suggests high primary productivity. This interval is interpreted to represent a time of weakly restricted to open marine circulation, increased volcanic ash input that enhanced primary productivity through iron fertilization, widespread benthic anoxia and episodic photic zone euxinia, and efficient re-supply of RSTEs from the global ocean as Tethyan water masses migrated northward into the KWIS.

Uppermost Cenomanian – Lower Turonian

The uppermost Cenomanian – Lower Turonian interval corresponds to the deposition of units C and C_s, with widespread deposition of interbedded argillaceous, calcareous mudstone and skeletal wackestone/packstone, and pelagic calcareous mudstone (figure III.15D). The interval also encompasses the OAE 2 section. In the Swenson 1H well, wells 1 and 2, and Lozier Canyon, the entire interval consists mostly on RF-X1. The RF-I1 facies in the Swenson 1H well corresponds to a highly bioturbated interval (BI: 5) with very low TOC (< 0.1%) and RSTE enrichment, indicating the presence of a diverse benthic fauna beneath a well oxygenated water column close to the Edwards reef margin. Furthermore, the low Ni enrichment in this interval in the Swenson 1H well suggests a decrease in primary productivity. The relatively high TOC and low BI in wells 1 and 2 indicate that the down dip section did not achieve complete benthic oxygenation, although the water column was more oxygenated. This interval is interpreted to represent a time of open marine circulation and improved benthic oxygenation.

Middle – Upper Turonian

The Middle – Upper Turonian interval corresponds to the deposition of units D, E and DE_s, with deposition of storm-influenced interbedded skeletal packstone/grainstone in both the up dip and down dip sections (figure III.15E). Although the up dip section records extensive bioturbation, the down dip section in wells 1 and 2, records persistently high TOC with isolated intervals of RF-X2, suggesting that this interval experienced occasional benthic anoxia. The widespread occurrence of bed sets containing wave-generated sedimentary structures indicate deposition within storm wave base. This interval is interpreted to represent a time of open marine circulation with the up dip section recording a higher degree of benthic oxygenation than the coeval down dip section.

Outcrop to Subsurface Stratigraphy

Lower Member of the Lower Eagle Ford Formation

The sharp lithological change at the base of the Eagle Ford Group represents a rapid marine transgression at the base of a transgressive systems tract. The Eagle Ford Group strata is equivalent to the third-order Greenhorn Cyclotherm further north that was deposited during the Cenomanian – Turonian marine transgression (Kauffman, 1984). Clasts of the Buda Limestone at the base of the Eagle Ford Group indicate the erosive nature of this contact (Eldrett et al., 2015). The bed forms and sedimentary structures of the basal Eagle Ford Group (Unit A; figure III.8D) were interpreted as storm-related structures (Trevino, 1989; Gardner et al., 2013). Similarly, hummocky cross stratification (HCS) and storm-related deposits were identified in outcrops and cores from west Texas in the Lower Cenomanian section of the Eagle Ford Group, just a few feet above the Buda Limestone (Minisini et al., 2017). Alternatively, these bed forms and sedimentary structures were interpreted as products of deep water processes (e.g. turbidites and contourites) that formed well below storm wave base (Lock and Peschier, 2006; Lock et al., 2010; Ruppel et al., 2012; Alnahwi et al., 2018). Also, based on qualitative planktic and benthic foraminifera abundances from subsurface cores, the Eagle Ford Group in south Texas was interpreted to form below storm wave base in low energy environments (Alnahwi et al., 2018). However, planktic and benthic foraminifera abundance trends in poorly ventilated and anoxic basins are profoundly influenced by oxygen depletion, potentially resulting in unreliable paleo-bathymetric interpretations in the absence of a rigorous quantitative investigation that takes into account foraminifera stress-marker species (Van Hinsbergen et al., 2005). Furthermore, the hummocky bed forms (figure III.8D) of the amalgamated skeletal grainstone/packstone beds and the geometry of the laminae within the beds are consistent with HCS and swaley cross stratification (SCS) of calcareous tempestites (e.g. Aigner, 1982; Tucker, 1990; Molina et al., 1997), indicating that the deposits were transported with the aid of storm waves and currents. HCS and SWS optimally form in a water depth range of about 20 to 50 m (~ 66 to 164 ft.) (Tucker, 1990; Dumas and Arnott, 2006; Plint et al., 2012). Unit A does not occur in the subsurface to the south, but passes down dip into interbedded siliceous, argillaceous, calcareous mudstone and bioclastic wackestone with occasional HCS and wave ripples, frequent scours, erosional bed contacts, and planar laminations (unit A_s). Given the similar ages for deposition at the base of the Lower Eagle Ford Formation in well 2 and at Lozier Canyon (Chapter II), it is plausible that the sedimentological and lithological differences between units A and As represent a facies change related to the inherited paleo-topography. This is consistent with the geochemical variations at the base of the Eagle Ford Group (discussed in later sections). The high total clay and quartz and feldspar in both the up dip and down dip sections suggest high siliciclastic input during deposition of these units.

In the Swenson 1H well, well 1 and well 2, Unit B_s1 has an upward increase in TOC trend, indicating an upward increase in organic-richness, consistent with the upward increase in RSTEs. At Lozier Canyon, subunits B1 and B2 represent the highest TOC interval and is coincident with high Mo and V enrichment (RF-X3). The isolated bioturbated intervals of unit B_s1 in well 1 suggest that bioturbation occurred in laminated storm-related deposits and represent periods of brief benthic ventilation that were subsequently overlain by organic-rich mudstone.

Upper Member of the Lower Eagle Ford Formation

Scoured bed contacts, basal skeletal and pelletal grain lags, occasional HCS and wave-ripple lamination, and abundant skeletal packstone/grainstone bed sets both in the up dip and down dip sections of the Upper Member of the Lower Eagle Ford Formation suggest deposition in an environment where the seafloor was episodically affected by wave agitation and traction currents. Interbedded calcareous mudstone and calcite-cemented nodular packstone/grainstone bed occur in the upper interval both in the up dip and down dip sections (figure III.10D-F). The frequency of the calcite-cemented nodular beds increases upward. Basal detrital skeletal and non-skeletal grain lags, scouring into underlying beds, sharp bed contacts and continuous, curved, nonparallel internal laminae of the calcite-cemented nodular beds indicate that they formed from high-energy storm events. The bi-convex morphology suggests they were differentially compacted with respect to the surrounding mudstone due to early diagenetic cementation just below the sediment-water interface where the pore water was saturated with carbon dioxide produced by sulfate-reducing bacteria during organic matter diagenesis (Irwin and Curtis, 1977). The Upper Member of the Lower Eagle Ford Formation is correlated from the Lozier Canyon Outcrop to the subsurface of south Texas, suggesting a laterally extensive depositional environment created by increased accommodation (figure III.10D-F). At this time, any inherited topography that existed during deposition of the underlying Lower Member of the Lower Eagle Ford Formation may have been filled, creating a relative flat, low-angled slope for the deposition of the Upper Member of the Lower Eagle Ford Formation.

Lower Member of the Upper Eagle Ford Formation

The transition from the Lower to the Upper Eagle Ford Formation is marked by a lithological, geochemical and petrophysical change from unit B to unit C (outcrop) and unit B_s to unit C_s (core), reflecting a change in depositional and oceanographic conditions. The interval also encompasses a positive 2 to 4 ‰ shift in the $\delta^{13}C$ (Carbon Isotope Excursion - CIE) that occurs close to the Cenomanian – Turonian boundary and is associated with oceanic anoxic event 2 (OAE 2). Across the KWIS, the OAE 2 interval is characterized by the appearance of diverse benthic fauna assemblages, and decrease in TOC and RSTEs enrichment (Eldrett et al., 2017; Lowery et al., 2017a). The Lozier Canyon outcrop of this transition records high bioturbation index (3 – 5) and a concomitant decrease in TOC in light gray calcareous mudstone. The extensive bioturbation reflects the existence of a thriving benthic fauna colonizing the seafloor beneath a well oxygenated water column. Variation in the bioturbation index and TOC down dip of the Edwards margin (wells 1 and 2) indicate variation in the degree of benthic oxygenation in the more distal settings. In wells 1 and 2, high TOC, low BI and abundant pyrite suggest that while the water column was more oxygenated, full oxygenation below the sediment – water interface was not completely achieved in down dip sections. Lozier Canyon and the Swenson 1H well also contain abundant pyrite in this interval, suggesting episodic low oxygen conditions in the sediments even during periods of increased water column oxygenation. In the Swenson 1H well, the RF-I1 facies occurs in a highly bioturbated interval, suggesting a well oxygenated benthic interval that precluded organic matter preservation and RSTEs enrichment.

OAEs record extreme perturbations in the global carbon cycle and are marked by widespread burial of organic-rich sediments with a concomitant positive CIE (Schlanger and Jenkyns, 1976; Scholle and Arthur, 1980; Arthur et al., 1987). The OAE 2 interval is well documented in several localities around the world (Arthur et al., 1987; Jarvis et al., 2006; Keller et al., 2008; Eldrett et al., 2015; Eldrett et al., 2017). In some locations, for example Europe and North Africa, the OAE 2 interval is marked by deposition of laminated organic-rich sediments with a concomitant increase in TOC and RSTEs, and low diversity, high stress faunal assemblages (Coccioni and Luciani, 2005; Mort et al., 2007; Keller et al., 2008; Touati, 2017). This is in contrast with observations in the KWIS and Eagle Ford Group depositional setting, where the OAE 2 interval is marked by the presence of increased benthic fauna assemblages, widespread bioturbation, and a decrease in TOC and RSTEs (Lowery et al., 2014; Eldrett et al., 2015; Eldrett et al., 2017; Lowery and Leckie, 2017b). Organic-rich sediment deposition in the Eagle Ford Group occurs prior to the onset of the positive CIE associated with the OAE 2 interval. This diachroneity suggests that local and regional conditions such as primary productivity, water mass restriction, sediment supply and benthic oxygenation may ultimately overwhelm global conditions (Zeng et al., 2018). At Lozier Canyon, the top of the positive CIE was abruptly terminated by a Lower – Middle Turonian unconformity (Lowery et al., 2014). In well 2, the occurrence of randomly oriented and scattered phosphate skeletal debris (figure III.11E) at the base of the Lower Member of the Upper Eagle Ford Formation and the proximity of the C-T boundary to the Lower-Upper Eagle Ford Formation contact suggest a submarine erosional surface with a missing time of ~ 900 k.y. (Chapter II). The hiatus at this contact possibly could explain the lack of bioturbation in this interval since much of the uppermost Cenomanian is missing and the isolated $\delta^{13}C_{org}$ excursions are interpreted to be re-worked sediments from the uppermost Cenomanian interval (Chapter II).

Upper Member of the Upper Eagle Ford Formation

The Upper Cenomanian – Lower Turonian global sea level rise was followed by a global relative sea level drop, resulting in the development of a Lower – Middle Turonian unconformity that can be regionally correlated in west Texas (Lowery et al., 2014; Eldrett et al., 2015; Lowery and Leckie, 2017b). At Lozier Canyon, this hiatus is expressed as an erosional surface containing pebble-sized clasts at the base of the Upper Member (Langtry Member) of the Upper Eagle Ford Formation and truncating the upper interval of the positive CIE associated with the OAE 2 (Lowery et al., 2014; Lowery and Leckie, 2017b). The burrow-homogenized beds of unit D (table III.2; figure III.13A) at Lozier Canyon indicate a well oxygenated benthic environment up dip of the Edwards margin. Unit D (table III.2; figure III.13A) passes upward into unit E (Donovan et al., 2012; Gardner et al., 2013). The bed forms and sedimentary structures of unit E (figure III.13B) indicate an oxic depositional environment where high-energy storm waves and currents frequently influenced the seabed, promoting widespread submarine erosion. Around the Edwards margin and on the South Texas Submarine Plateau, the Upper Member of the Upper Eagle Ford Formation has very similar characteristics to unit E (tables III.1 and III.2). In wells 1 and 2, the abundant HCS, sharp bed contacts, erosional bases separating HCS beds, local scours, soft-sediment deformation and local rip-up clasts (figure III.12), indicate that the down dip section also was deposited in an environment influenced by wave agitation and traction currents that promoted widespread submarine erosion. The occurrence of several thin beds with sharp bed contacts and erosional bases (figure III.12) indicate several cryptic disconformities within this interval. The high TOC, isolated intervals of high Mo and V enrichment (RF-X2) and low bioturbation index recorded in well 1(figure III.4) suggest that the down dip section did not achieve complete oxygenation below the sediment – water interface.

In well 2, the transition from the Upper Eagle Ford Formation to the base of the Austin Chalk is characterized by moderate bioturbation in the uppermost Upper Eagle Ford Formation that passes upward into an intensely bioturbated (figure III.12D) interval that underlies a phosphate interval with pyrite-filled fractures and skeletal debris (including phosphate skeletal debris) near the base of the Austin Chalk (figure III.12E). Similar Upper Eagle Ford Formation – Austin Chalk transition around the San Marcos Arch and north and central Texas areas were previously described (McNulty Jr, 1966; Lundquist, 2001; Lowery et al., 2014; Minisini et al., 2017; Lowery and Leckie, 2017b). Based on biostratigraphic data in the Fasken A 1H well, continuous deposition across the Eagle Ford – Austin Chalk contact was interpreted in the Middle Turonian (Lowery and Leckie, 2017b). This contact is marked by a condensed section in the Lozier Canyon outcrop (Lowery 2014, 2017). The phosphate and pyrite interval in well 2 near the Upper Eagle Ford Formation – Austin Chalk is interpreted to be a composite surface of a submarine hardground and submarine sediment erosion or non-deposition with a hiatus of ~ 1 m.y. (Chapter II).

Geochemistry and Paleo-Redox Variations

The Lower Eagle Ford Formation records significantly higher RSTE (Mo, U and V) enrichment than the Upper Eagle Ford Formation, indicating significant differences in the paleoredox state of their depositional environments (figures III.3 – III.6 and III.16). RSTEs generally are conservative under oxic conditions but have enhanced uptake in oxygen-depleted environments. In the Eagle Ford Group depositional setting, an important contributor to water column oxygen-depletion was increased biological productivity related to volcanic ash input that supplied critical nutrients (e.g. iron) to support phytoplankton bloom (Lee et al., 2018; Zeng et al., 2018). Additionally, in weakly restricted to fully restricted settings (e.g. Saanich Inlet, Black Sea), RSTE enrichment depends not only on the redox state of the environment but also the degree of water mass restriction, where the latter controls the supply of RSTEs from the global ocean to the basinal water mass. Low TOC values (<2%) generally indicate oxic to weakly anoxic conditions (Tribovillard et al., 2006).

The Lower Member of the Lower Eagle Ford Formation in wells 1 and 2, Swenson 1H and Lozier Canyon records an upward increase in enrichment of RSTEs (figures III.3 – III.6). The basal interval of the Upper Member of the Lower Eagle Ford Formation records higher Mo and V enrichment (mostly RF-X3 and -X2) in wells 1 and 2 and Swenson 1H well, whereas the coeval interval at Lozier Canyon records a mix of RF-X1, -X2 and -X3. Both Mo and V are good paleo-redox proxies that are linked to the redox-cycling of manganese (Mn). Mo requires the presence of dissolved H_2S for reduction and subsequent authigenic enrichment in in sediments (Helz et al., 1996). Reduction of V, on the other hand, takes place in two steps depending on the concentration of dissolved H_2S in the system, making V a good indicator for subtle redox variations (Algeo and Maynard, 2004; Tribovillard et al., 2006). In mildly reducing environments that are free of H_2S (non-euxinic), V has relatively limited up take in sediments, whereas in strongly reducing environments where free H_2S is present, V has an increased enrichment in sediments.

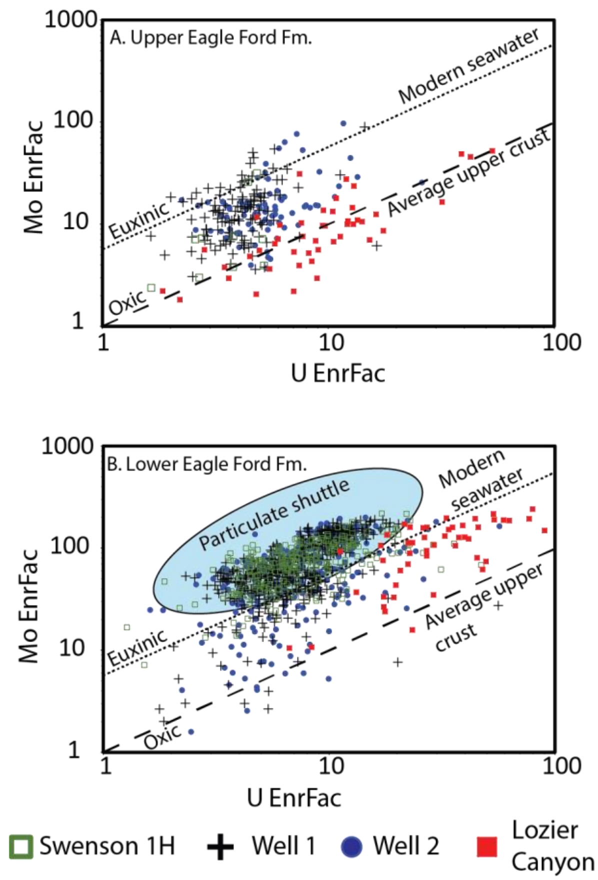

Figure III.16 Mo versus U enrichment factor co-variation plots for the Upper and Lower Eagle Ford Formations. Points close to the average upper crust line are generally associated with oxic depositional environments, whereas points close to the modern sea water line are generally associated with euxinic depositional environments. Points well above the modern sea water line are associated with an efficient particulate pump in a fluctuating redox-cline. (A) The Upper Eagle Ford Formation was deposited predominantly under oxic – mildly anoxic conditions. (B) The Lower Eagle Ford was deposited under predominantly anoxic – euxinic conditions.

Given the high TOC values in the Lower Member of the Lower Eagle Ford Formation, the occurrence of several zones with low Mo and V enrichment (RF-X1) in the basal interval (figures III.3 – III.6) are interpreted to represent moderately reducing anoxic environments. Alternatively, the low Mo and V enrichment intervals could also be interpreted to indicate a drawdown in RSTE due to prolonged anoxia in a weakly restricted setting (Algeo and Rowe, 2012). At Lozier Canyon, the Lower Member of the Lower Eagle Ford Formation has predominantly RF-X3, indicating strongly reducing conditions at that location. The Lozier Canyon outcrop also has higher number of ash beds (table III.4) in the Lower Member of the Lower Eagle Ford Formation than the Swenson 1H well, and wells 1 and 2, suggesting that enhanced primary productivity resulting from volcanic ash input coupled with water mass restriction promoted extreme anoxic conditions at the Lozier Canyon location relative to the other well locations. Local basinal water mass restriction and hypersalinity at the Lozier Canyon location is further supported by the occurrence of authigenic dolomite rhombs, commonly associated with high evaporation in restricted settings, in the basal Lower Eagle Ford Formation above the Buda Limestone unconformity (Lowery et al., 2014). The upward increase in the enrichment of RSTEs in both the up dip and down dip sections of the Lower Member of the Lower Eagle Ford Formation suggests an upward increase in euxinic paleo-redox conditions coupled with a progressive increase in re-supply of RSTEs from the global ocean. The Upper Member of the Lower Eagle Ford Formation in wells 1 and 2, Swenson 1 H well and Lozier Canyon has a mix of predominantly RF-X3 and -X2 with few intervals of RF-X1, indicating a relatively strongly reducing interval that is punctuated by mildly anoxic zones. The Lozier Canyon and Swenson 1H well locations record a significant increase in the number of volcanic ash beds in the Upper Member of the Lower Eagle Ford Formation, indicating that the development of anoxic and euxinic paleo-redox conditional in this interval was likely the result of increased primary productivity linked to volcanic ash input

(Zeng et al., 2018). Although well 2 records only one ash bed in the Upper Member of the Lower Eagle Ford Formation, it has multiple diagenetically altered grainstone/packstone beds that are mixed with volcanic ash, and its Mo and V enrichment trends are very similar to the other study locations, suggesting that increased primary productivity linked to volcanic ash input was not limited only to areas where ash beds are preserved, but was rather a regional phenomenon across the entire Lower Eagle Ford Formation depositional settings. In wells 1 and 2 and at Lozier Canyon, the Upper Eagle Ford Formation is characterized mostly by RF-X1 with isolated intervals of RF-X2 in the Upper Member of the Upper Eagle Ford Formation, indicating a relatively oxygenated depositional setting. While the number of volcanic ash beds significantly decreases in the Lower Member of the Upper Eagle Ford Formation, the Lozier Canyon location still records a significantly higher number of ash beds than the other locations. The occurrence of volcanic ash beds in the Lower Member of the Upper Eagle Ford Formation, however, did not result in increased primary productivity and subsequent increase in TOC and RSTE enrichment as increased benthic oxygenation precluded preservation of large amounts of organic matter in this interval.

In the Swenson 1H well, both the Lower and Upper Members of the Lower Eagle Ford Formation are further sub-divided using RF-I redox facies, which is a more detailed analysis using high-resolution ICPMS (Mo, V and Ni) and TOC data (Kelly, 2016), and provides better insights into the subtle paleoredox variations at the Swenson 1H well location. Furthermore, Ni, a reliable productivity marker (Tribovillard et al., 2006), was used as an additional proxy to constrain the development of euxinia (productivity/water mass restriction) in the RF-I facies. RF-I1 is interpreted to indicate oxic to mildly anoxic depositional settings, whereas RF-I2 (figure III.14B-D) is interpreted to be anoxic (non-sulfidic). While both RF-I3 and RF-I4 are interpreted to be high TOC, euxinic depositional environments, RF-I3 has relatively lower RSTE enrichment than RF-I4 (figure III.12B-D). The basal interval of the Lower Member of the Lower Eagle Ford Formation has predominantly RF-I2, passing upward to predominantly RF-I3, reflecting an upward increase in TOC without a corresponding increase in RSTEs (figures III.6 and III.14B, C, D). The upward increase in TOC without a corresponding increase in RSTE enrichment likely reflects a prolonged drawdown in RSTEs caused by increasing anoxic to euxinic conditions. Such conditions potentially occur where the RSTE sink flux is higher than the source flux as is the case in basins with some degree of basinal water mass restriction (Algeo and Rowe, 2012; Tribovillard et al., 2012). Increased primary productivity linked to volcanic ash input coupled with basinal water mass restriction likely promoted the development of anoxic and euxinic conditions in this interval. AIR and Pr/Ph data from the upper interval of the Lower Member of the Lower Eagle Ford Formation in the Swenson 1H well indicate episodic photic zone euxinia, whereas AIR and Pr/Ph data from the coeval interval at Lozier Canyon indicates conditions closer to persistent photic zone euxinia (figures III.3, III.6 and III.17).

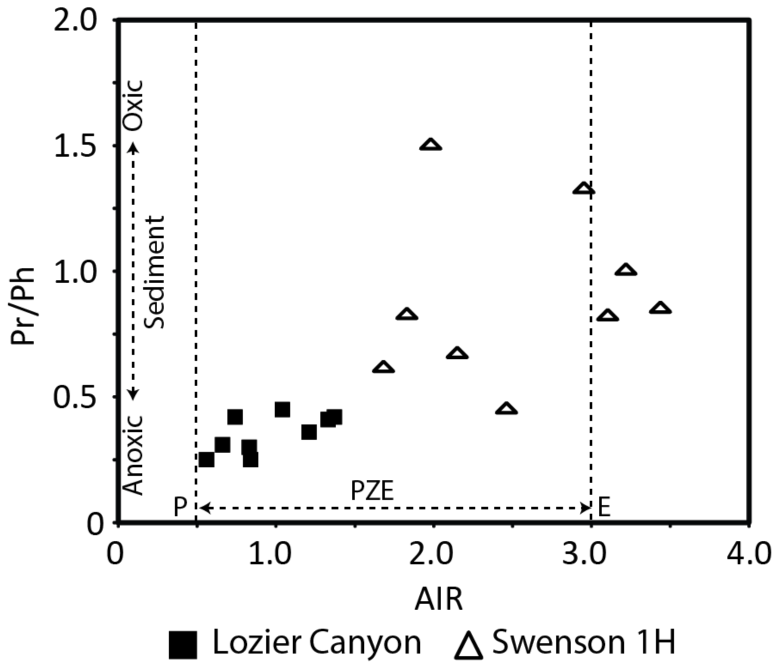

Figure III.17 Aryl isoprenoids ratio (AIR) plotted versus pristine/phytane (Pr/Ph) for Lozier Canyon outcrop and Swenson 1H well. Data are from Romero (2014) and Mualana (2016), respectively. Plot modified from Schwark and Frimmel (2004). The Eagle Ford Group strata at Lozier Canyon records more persistent Photic zone euxinia (PZE) relative to the Swenson 1H well location. P = persistent; E = episodic.

Aryl isoprenoids were identified in the Lower Eagle Ford Formation from several well and outcrop samples across multiple locations in Texas, indicating the existence of photic zone euxinia in the Lower Eagle Ford Formation water column (Romero, 2014; Sun et al., 2016; Romero et al., 2018). The uppermost interval of the Lower Member of the Lower Eagle Ford Formation has predominantly RF-I4, reflecting high TOC and high RSTE enrichment (figures III.6 and III.14B, C, D). The high RSTE enrichment in the uppermost interval of the Lower Member of the Lower Eagle Ford Formation suggests an efficient re-supply of RSTEs to the basinal water mass from the global ocean relative to the underlying interval. Furthermore, the increase in Ni enrichment in this interval suggests that the development of euxinia was the product of enhanced primary productivity. Furthermore, rising eustatic levels facilitated improved connection between the KWIS and the global ocean resulting in increased supply of RSTEs. The basal section of the Upper Member of the Lower Eagle Ford has predominantly RF-I4 and -I3 with high Mo, V and Ni enrichment, and coincides with an increase in the number of volcanic ash beds, suggesting that the development of euxinia in this interval was the product of enhanced primary productivity that was promoted by iron fertilization as more volcanic ash entered the paleo-water column (Zeng et al., 2018). The basal interval in the Upper Member of the Lower Eagle Ford Formation passes upward into a mixed interval of RF-I3, -I2 and -I1, indicating a gradual transition to lower TOC and lower RSTE enrichment, reflecting a long-term trend towards benthic oxygenation. The base of the Lower Member of the Upper Eagle Ford Formation corresponds to RF- I1 and -I2. Whereas the RF-I1 interval has mostly *Teichichnus* trace fossils and TOC values as low as 0.09% in calcareous mudstone, the RF-I2 interval has mostly *Planolites* and *Chondrites* trace fossils in argillaceous, calcareous mudstone mixed with volcanic ash and having TOC up to 3%, indicating variation in the degree of benthic oxygenation within the same stratigraphic interval. Although five volcanic ash beds occur in this short interval in the Swenson 1H well (table III.4), increased benthic oxygenation during this time precluded preservation of large amounts of organic matter. In Wells 1 and 2, although the Mo and V enrichment factor values decrease drastically in the Lower Member of the Upper Eagle Ford Formation, the interval records persistently high TOC and very low bioturbation, suggesting that the down dip section experienced a lesser degree of benthic oxygenation than the coeval up dip section. Given that the down dip section of the Upper Eagle Ford Formation was not completely oxygenated, its low RSTE enrichment may be related to a drawdown in the global ocean's RSTEs during the OAE 2 as a 2-3% areal increase in euxinic seafloor would crash the Mo and V reservoirs in a period of < 500 k.y. and < 40 k.y., respectively (Sahoo et al., 2012).

Water Mass Restriction and Water Column Stratification

Mo versus uranium (U) enrichment factor and Mo versus TOC plots were used to constrain the degree of water mass restriction and development of euxinic conditions in the Eagle Ford Group depositional settings. U is chemically stable under oxic conditions, requiring a chemically reducing environment for the removal of U from the water column to the sediments via formation of organometallic complexes in humic acid (Algeo and Maynard, 2004; Tribovillard et al., 2006). Reduction of U, however, does not require the presence of free H_2S in the water column (Algeo and Maynard, 2004; Tribovillard et al., 2006; Algeo and Tribovillard, 2009). Therefore, the authigenic Mo and U covariation in sedimentary environments can potentially constrain the redox conditions of the bottom water masses, providing insights into the paleo-redox conditions of the depositional environment (Algeo and Tribovillard, 2009; Algeo and Rowe, 2012; Tribovillard et al., 2012). Mo and U covariation plots (figure III.16) indicate that the Lower Eagle Ford Formation was deposited under predominantly anoxic to euxinic conditions, whereas the Upper Eagle Ford Formation was deposited under mostly oxic to mildly anoxic conditions. For the Lower Eagle Ford Formation (figure III.16B), the large cloud of points well above the modern sea water line in the Swenson 1H, and wells 1 and 2 reflect an efficient particulate pump in a redox-cline that periodically moved from the sediment up into the water column and efficient re-supply of Mo from the global ocean to the basinal water mass (Algeo and Tribovillard, 2009). Vertical fluctuation of the redox-cline accelerates transfer of Mo to the sediment relative to U, which is decoupled from the manganese-iron (Mn-Fe) cycling (Algeo and Tribovillard, 2009). AIR and Pr/Ph ratios from the Lower Eagle Ford Formation indicate the development of episodic photic zone euxinia, which supports the formation of a redox-cline in a stratified water column, during deposition of this unit. Furthermore, gammacerane, a specific indicator for water column stratification and hypersalinity in both marine and non-marine environments, occurs in the Eagle Ford Group (Romero, 2014; Romero et al., 2018). The Lozier Canyon location, however, does not have a Mo versus U covariation trend that indicates the existence of an efficient particulate pump (figure III.16B). Rather, the Lozier Canyon location indicates a trend that is characteristic of a highly restricted environment with a shallow and stable redox-cline where the deep water mass has a long residence time and sedimentation promotes decline of aqueous Mo without a corresponding re-supply, resulting in a decline of the authigenic Mo/U ratios (Algeo and Tribovillard, 2009). Sedimentological data from the Lower Eagle Ford Formation indicates that storm waves and currents frequently to intermittently interacted with the seabed, promoting vertical mixing of the water column. Interaction of storm waves with the sea floor disrupted water column stratification and shifted the redox-cline near to, or below, the sediment – water interface, resulting in temporary ventilation of the bottom water mass before returning to a stratified water column. Temporary ventilation of the bottom water mass also is indicated by bioturbation limited to the top of storm beds in the Lower Eagle Ford Formation (figure III.9C).

Increasing water mass restriction potentially limits the enrichment of RSTEs in sediments by hindering the re-supply of the RSTEs to the basinal water mass from the global ocean (Algeo and Tribovillard, 2009; Algeo and Rowe, 2012; Tribovillard et al., 2012). TOC versus Mo concentration co-variation plot provides insights into the degree of water mass restriction of depositional environments (Algeo and Lyons, 2006; Tribovillard et al., 2012). Lower Eagle Ford Formation Mo versus TOC co-variation plot (figure III.18) for the Swenson 1H, well 2 and Lozier Canyon indicates that while the overall Eagle Ford Group depositional setting was only moderately restricted, the Swenson 1H and well 2 locations were less restricted relative to the Lozier Canyon location. This trend is consistent with the Mo versus U co-variation and Pr/Ph versus AIR plots (figures III.16 and III.17), which indicate that the Lozier Canyon Location was relatively more restricted and had close to persistent photic zone euxinia. Also, other organic geochemical data indicate that the Eagle Ford Group depositional environment in west Texas (Lozier Canyon) was more restricted and experienced higher degree of water column stratification and hypersalinity relative to central Texas (Romero, 2014).

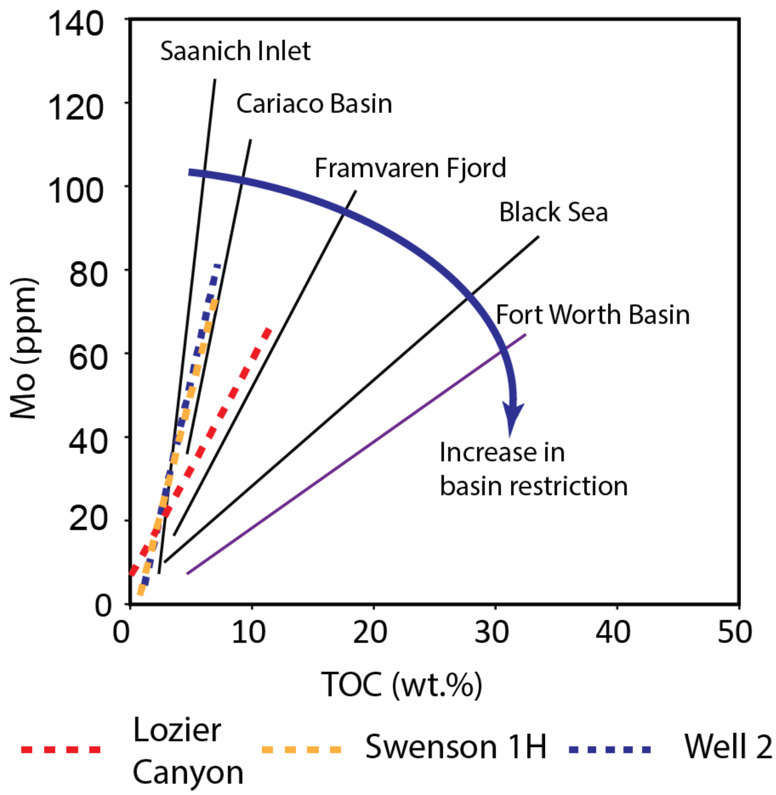

Figure III.18 XRF Mo concentration plotted versus total organic carbon (TOC) for the Lower Eagle Ford Formation compared to modern and ancient anoxic silled-basins. Modified from Algeo and Rowe (2012). While the Lower Eagle Ford Formation depositional setting was only moderately restricted, the Lozier Canyon location was more restricted relative to well 2 and the Swenson 1H well locations.

Conclusions

Sedimentological and geochemical data from the Upper Cretaceous Eagle Ford Group in west and south Texas indicate their organic-rich mudstone-dominated depositional environments were heterogeneous, and had different depositional, sedimentological and geochemical processes simultaneously affecting coeval deposits in different parts of the same basin. The Lower Eagle Ford Formation is enriched in RSTEs relative to the upper crust. RSTE enrichment decreases significantly in the Upper Eagle

Ford Formation, with the Lower Member of the Upper Eagle Ford Formation having the lowest average RSTEs enrichment.

During Lower Eagle Ford Formation deposition, increased primary productivity resulting from volcanic ash input coupled with weak basinal water mass restriction promoted widespread anoxia and episodic photic zone euxinia in a stratified water column. The Upper Eagle Ford Formation was deposited mostly under oxic to mildly anoxic conditions, recording benthic oxygenation with burrow homogenized beds that pass down dip into high TOC laminated facies. While the overall Eagle Ford Group depositional setting was only moderately restricted, the Lozier Canyon location in west Texas experienced a greater degree of water mass restriction, water column stratification and hypersalinity relative to wells in the down dip section.

Frequent to intermittent interaction of storm waves and currents with the Eagle Ford Group's seabed promoted vertical mixing of the water column, disrupted water column stratification and shifted the redox-cline near to, or below, the sediment – water interface, resulting in temporary ventilation of the bottom water masses before returning to a stratified water column.

References

Adkins, W., 1932, The Mesozoic systems in Texas; Part 2 of The geology of Texas, v. 1, Stratigraphy, by EH Sellards et al, Univ. Texas Bull, v. 3232, p. 1007.

Algeo, T. J., and T. W. Lyons, 2006, Mo–total organic carbon covariation in modern anoxic marine environments: Implications for analysis of paleoredox and paleohydrographic conditions, Paleoceanography, v. 21, doi:10.1029/2004PA001-112

Algeo, T. J., and J. B. Maynard, 2004, Trace-element behavior and redox facies in core shales of Upper Pennsylvanian Kansas-type cyclothems, Chemical Geology, v. 206, p. 289-318.

Algeo, T. J., and H. Rowe, 2012, Paleoceanographic applications of trace-metal concentration data, Chemical Geology, v. 324, p. 6-18.

Algeo, T. J., and N. Tribovillard, 2009, Environmental analysis of paleoceanographic systems based on molybdenum–uranium covariation, Chemical Geology, v. 268, p. 211-225.

Alnahwi, A., R. G. Loucks, S. C. Ruppel, R. W. Scott, and N. Tribovillard, 2018, Dip-related changes in stratigraphic architecture and associated sedimentological and geochemical variability in the Upper Cretaceous Eagle Ford Group in south Texas, AAPG Bulletin, v. 102, p. 2537-2568.

Arthur, M., S. t. Schlanger, and H. Jenkyns, 1987, The Cenomanian-Turonian Oceanic Anoxic Event, II. Palaeoceanographic controls on organic-matter production and preservation, Geological Society, London, Special Publications, v. 26, p. 401-420.

Arthur, M. A., and B. B. Sageman, 2005, Sea-level control on source-rock development: perspectives from the Holocene Black Sea, the mid-Cretaceous Western Interior Basin of North America, and the Late Devonian Appalachian Basin, SEPM Special Publication No. 82, p. 35-59.

Atkins, W. S., 1933, The Mesozoic systems in Texas in E. H. Sellards, W. S. Adkins, and F. B. Plummer, eds., The geology of Texas: University of Texas Bulletin 3232, Austin, p. 422-439.

Blatt, H., R. Tracy, and B. Owens, 2006, Petrology: igneous, sedimentary, and metamorphic: New York, 3rd ed., W.H. Freeman and Company, 530 p.

Coccioni, R., and V. Luciani, 2005, Planktonic foraminifers across the Bonarelli Event (OAE2, latest Cenomanian): the Italian record, Palaeogeography, Palaeoclimatology, Palaeoecology, v. 224, p. 167-185.

Corbett, M., D. Watkins, and J. Pospichal, 2014, A quantitative analysis of calcareous nannofossil bioevents of the Late Cretaceous (Late Cenomanian–Coniacian) Western Interior Seaway and their reliability in established zonation schemes, Marine Micropaleontology, v. 109, p. 30-45.

Dawson, W. C., 2000, Shale microfacies: Eagle Ford Group (Cenomanian-Turonian) north-central Texas outcrops and subsurface equivalents, Gulf Coast Association of Geological Societies Transactions, v. 50, p. 607-621.

Didyk, B., B. Simoneit, S. t. Brassell, and G. Eglinton, 1978, Organic geochemical indicators of palaeoenvironmental conditions of sedimentation, Nature, v. 272, p. 216.

Donovan, A., R. Gardner, A. Pramudito, T. Staerker, M. Wehner, M. Corbett, J. Lundquist, A. Romero, L. Henry, and J. Rotzien, 2015, Chronostratigraphic relationships of the Woodbine and Eagle Ford Groups across Texas, Gulf Coast Association of Geological Societies, v. 2, p. 67-87.

Donovan, A. D., and T. S. Staerker, 2010, Sequence stratigraphy of the Eagle Ford (Boquillas) Formation in the subsurface of South Texas and outcrops of West Texas, Gulf Coast Association of Geological Societies Transactions, v. 60, p. 861-899.

Donovan, A. D., T. S. Staerker, A. Pramudito, W. Li, M. J. Corbett, C. M. Lowery, A. M. Romero, and R. D. Gardner, 2012, The Eagle Ford outcrops of West Texas: A laboratory for understanding heterogeneities within unconventional mudstone reservoirs, Gulf Coast Association of Geological Societies, v. 1, p. 162-185.

Droser, M. L., and D. J. Bottjer, 1986, A semiquantitative field classification of ichnofabric, Journal of Sedimentary Research, v. 56.

Dumas, S., and R. Arnott, 2006, Origin of hummocky and swaley cross-stratification—The controlling influence of unidirectional current strength and aggradation rate, Geology, v. 34, p. 1073-1076.

Dunham, R. J., 1962, Classification of carbonate rocks according to depositional textures, in W. E. Ham, ed.. Classification of carbonate rocks—a symposium, American Association of Petroleum Geologists Bulletin Mem. 1, p. 108-121.

Ehler, E., and H. Blatt, 1982, Petrology: Igneous, Sedimentary and Metamorphic, WH Freemanand Company, San Francisco, 732 p.

Eldrett, J. S., P. Dodsworth, S. C. Bergman, M. Wright, and D. Minisini, 2017, Water-mass evolution in the Cretaceous Western Interior Seaway of North America and equatorial Atlantic, Climate of the Past, v. 13, p. 855.

Eldrett, J. S., C. Ma, S. C. Bergman, B. Lutz, F. J. Gregory, P. Dodsworth, M. Phipps, P. Hardas, D. Minisini, and A. Ozkan, 2015, An astronomically calibrated stratigraphy of the Cenomanian, Turonian and earliest Coniacian from the Cretaceous Western Interior Seaway, USA: Implications for global chronostratigraphy, Cretaceous Research, v. 56, p. 316-344.

Freeman, V. L., 1968, Geology of the Comstock-Indian Wells Area, Val Verde, Terrell, and Brewster Counties, Texas, American Association of Petroleum Geologists Bulletin, v. 45, p. 105-107.

Gardner, R. D., 2013, Lateral Continuity of the Eagle Ford Group Strata in Lozier Canyon and Antonio Creek, Terrell County, Texas, M.S. thesis, Texas A&M University, College Station, 118 p.

Gardner, R. D., M. C. Pope, M. P. Wehner, and A. D. Donovan, 2013, Comparative Stratigraphy of the Eagle Ford Group Strata in Lozier Canyon and Antonio Creek, Terrell County, Texas, GCAGS Journal, v. 2, p. 42-52.

Ghadeer, S. G., and J. H. Macquaker, 2012, The role of event beds in the preservation of organic carbon in fine-grained sediments: analyses of the sedimentological processes operating during deposition of the Whitby Mudstone Formation (Toarcian, Lower Jurassic) preserved in northeast England, Marine and Petroleum Geology, v. 35, p. 309-320.

Hazzard, R., 1959, Measured section, in R. L. Cannon, R. T. Hazzard, A. Young, and K. P. Young, eds, Geology of the Val Verde Basin. West Texas Geological Society Guidebook, Midland (November 5–8, 118 p.).

Helz, G., C. Miller, J. Charnock, J. Mosselmans, R. Pattrick, C. Garner, and D. Vaughan, 1996, Mechanism of molybdenum removal from the sea and its concentration in black shales: EXAFS evidence, Geochimica et Cosmochimica Acta, v. 60, p. 3631-3642.

Hill, R. T., 1887a, ART. XXXIV.--The Texas Section of the American Cretaceous, American Journal of Science (1880-1910), v. 34, p. 287.

Hill, R. T., 1887b, The topography and geology of the Cross Timbers and surrounding regions in northern Texas, American Journal of Science, p. 291-303.

Jarvis, I., A. S. Gale, H. C. Jenkyns, and M. A. Pearce, 2006, Secular variation in Late Cretaceous carbon isotopes: a new δ13C carbonate reference curve for the Cenomanian–Campanian (99.6–70.6 Ma), Geological Magazine, v. 143, p. 561-608.

Kauffman, E. G., 1984, Paleobiogeography and evolutionary response dynamic in the Cretaceous Western Interior Seaway of North America, *in* G. E. G. Westermann, ed., Jurassic-Cretaceous biochronology and paleogeography of North America, v. 27, Geol. Assoc. Can. Sp. Pap, p. 273-306.

Keller, G., T. Adatte, Z. Berner, E. Chellai, and D. Stueben, 2008, Oceanic events and biotic effects of the Cenomanian-Turonian anoxic event, Tarfaya Basin, Morocco, Cretaceous Research, v. 29, p. 976-994.

Kelly, C. M., 2016, Molybdenum, Vanadium and Nickel Covariation as an Indicator of Paleo-Redox Conditions and Basin Restriction Within the Eagle Ford Formation-Implications for the Interpretation of Volcanic Ash Fertilization, M.S. thesis, Texas A&M University, College Station, Texas, 203 p.

Lazar, O. R., K. M. Bohacs, J. H. Macquaker, J. Schieber, and T. M. Demko, 2015, Capturing Key Attributes of Fine-Grained Sedimentary Rocks In Outcrops, Cores, and Thin Sections: Nomenclature and Description Guidelines, Journal of Sedimentary Research, v. 85, p. 230-246.

Lee, C.-T. A., H. Jiang, E. Ronay, D. Minisini, J. Stiles, and M. Neal, 2018, Volcanic ash as a driver of enhanced organic carbon burial in the Cretaceous, Scientific reports, v. 8, p. 4197.

Lee, C.-T. A., B. Shen, B. S. Slotnick, K. Liao, G. R. Dickens, Y. Yokoyama, A. Lenardic, R. Dasgupta, M. Jellinek, and J. S. Lackey, 2013, Continental arc–island arc fluctuations, growth of crustal carbonates, and long-term climate change, Geosphere, v. 9, p. 21-36.

Liu, S., D. Nummedal, and M. Gurnis, 2014, Dynamic versus flexural controls of Late Cretaceous Western Interior Basin, USA, Earth and Planetary Science Letters, v. 389, p. 221-229.

Lock, B. E., and L. Peschier, 2006, Boquillas (Eagle Ford) upper slope sediments, west Texas: Outcrop analogs for potential shale reservoirs, GCAGS, v. 56, p. 491-508.

Lock, B. E., L. Peschier, and N. Whitcomb, 2010, The Eagle Ford (Boquillas Formation) of Val Verde County, Texas-A Window on the South Texas Play, Transactions of the Gulf Coast Association of Geological Societies, v. 60, p. 419-434.

Lowery, C. M., M. J. Corbett, R. M. Leckie, D. Watkins, A. M. Romero, and A. Pramudito, 2014, Foraminiferal and nannofossil paleoecology and paleoceanography of the Cenomanian–Turonian Eagle Ford Shale of southern Texas, Palaeogeography, Palaeoclimatology, Palaeoecology, v. 413, p. 49-65.

Lowery, C. M., and R. M. Leckie, 2017b, Biostratigraphy of the Cenomanian–turonian Eagle Ford Shale of South Texas, Journal of Foraminiferal Research, v. 47, p. 105-128.

Lowery, C. M., R. M. Leckie, R. Bryant, K. Elderbak, A. Parker, D. E. Polyak, M. Schmidt, O. Snoeyenbos-West, and E. Sterzinar, 2017a, The Late Cretaceous Western Interior Seaway as a model for oxygenation change in epicontinental restricted basins, Earth-Science Reviews, p. 545-564.

Lundquist, J. J., 2001, Foraminiferal biostratigraphic and paleoceanographic analysis of the Eagle Ford, Austin, and lower Taylor Groups (Middle Cenomanian through Lower Campanian) of central Texas. Ph.D. Thesis, University of Texas at Austin, Austin, Texas, 545 p.

Maulana, I., 2016, Basin Geochemical Evolution of the Eagle Ford and Effects on Trace Element Release, M.S. thesis, Texas A&M University, College Station, Texas, 49 p.

McKenzie, N. R., B. K. Horton, S. E. Loomis, D. F. Stockli, N. J. Planavsky, and C.-T. A. Lee, 2016, Continental arc volcanism as the principal driver of icehouse-greenhouse variability, Science, v. 352, p. 444-447.

McNulty Jr, C., 1966, Nomenclature of uppermost Eagle Ford Formation in northeastern Texas, AAPG Bulletin, v. 50, p. 375-379.

Minisini, D., J. Eldrett, S. C. Bergman, and R. Forkner, 2017, Chronostratigraphic framework and depositional environments in the organic-rich, mudstone-dominated Eagle Ford Group, Texas, USA, Sedimentology, p. 1-38.

Mort, H., O. Jacquat, T. Adatte, P. Steinmann, K. Föllmi, V. Matera, Z. Berner, and D. Stüben, 2007, The Cenomanian/Turonian anoxic event at the Bonarelli Level in Italy and Spain: enhanced productivity and/or better preservation?, Cretaceous Research, v. 28, p. 597-612.

Pang, M., and D. Nummedal, 1995, Flexural subsidence and basement tectonics of the Cretaceous Western Interior basin, United States, Geology, v. 23, p. 173-176.

Pessagno, E. A., 1969, Upper Cretaceous stratigraphy of the western Gulf Coast area of Mexico, Texas, and Arkansas, Geological Society of America Memoirs, v. 111, p. 1-139.

Phelps, R. M., C. Kerans, R. G. Loucks, R. O. Da Gama, J. Jeremiah, and D. Hull, 2014, Oceanographic and eustatic control of carbonate platform evolution and sequence stratigraphy on the Cretaceous (Valanginian–Campanian) passive margin, northern Gulf of Mexico, Sedimentology, v. 61, p. 461-496.

Plint, A. G., J. H. MacQuaker, and B. L. Varban, 2012, Bedload transport of mud across a wide, storm-influenced ramp: Cenomanian–Turonian Kaskapau Formation, Western Canada Foreland Basin, Journal of Sedimentary Research, v. 82, p. 801-822.

Potter, P. E., J. B. Maynard, and P. J. Depetris, 2005, Mud and mudstones: Introduction and overview: Berlin, Germany, Springer Science & Business Media, 304 p.

Roberts, L. N. R., and M. A. Kirschbaum, 1995, Paleogeography of the Late Cretaceous of the Western Interior of middle North America-coal distribution and sediment accumulation, United States Geological Survey, Professional Paper 1516, p. 115p.

Romero, A. A. M., 2014, Subsurface and outcrop organic geochemistry of the Eagle Ford shale (Cenomanian-Coniacian) in west, southwest, central, and east Texas, Doctor of Philosophy thesis, University of Oklahoma, Oklahoma, 289 p.

Romero, A. A. M., T. Nguyen, and R. P. Philp, 2018, Organic geochemistry of the eagle ford group in Texas, AAPG Bulletin, v. 102, p. 1379-1412.

Rowe, H., N. Hughes, and K. Robinson, 2012, The quantification and application of handheld energy-dispersive x-ray fluorescence (ED-XRF) in mudrock chemostratigraphy and geochemistry, Chemical Geology, v. 324, p. 122-131.

Ruppel, S., R. Loucks, and G. Frébourg, 2012, Guide to field exposures of the Eagle Ford-equivalent Boquillas Formation and related Upper Cretaceous Units in southwest Texas, BEG Mudrock Consortium Field Trip, v. 8, p. 12.

Sageman,B. B., and M. A. Arthur, 1994, Early Turonian paleo-geographic/paleo-bathymetric map, western interior, US, *in* M. V. Caputo, J. A. Peterson, and K. J. Franczyk, eds., Mesozoic Systems of the Rocky Mountain Region, USA: SEPM, Rocky Mountain Section, Denver, Colorado, p. 457-469.

Sahoo, S. K., N. J. Planavsky, B. Kendall, X. Wang, X. Shi, C. Scott, A. D. Anbar, T. W. Lyons, and G. Jiang, 2012, Ocean oxygenation in the wake of the Marinoan glaciation, Nature, v. 489, p. 546.

Schieber, J., R. Lazar, K. Bohacs, R. Klimentidis, M. Dumitrescu, and J. Ottmann, 2016, An SEM study of porosity in the Eagle Ford Shale of Texas—Pore types and porosity distribution in a depositional and sequence-stratigraphic Context, *in* J. A. Breyer, ed., The Eagle Ford Shale: A renaissance in U.S. oil production, AAPG Memoir 110, p. 167-186.

Schlanger, S. O., and H. Jenkyns, 1976, Cretaceous oceanic anoxic events: causes and consequences, Geologie en mijnbouw, v. 55, p. 179-184.

Scholle, P. A., and M. A. Arthur, 1980, Carbon isotope fluctuations in Cretaceous pelagic limestones: potential stratigraphic and petroleum exploration tool, AAPG Bulletin, v. 64, p. 67-87.

Schwark, L., and A. Frimmel, 2004, Chemostratigraphy of the Posidonia Black Shale, SW-Germany: II. Assessment of extent and persistence of photic-zone anoxia using aryl isoprenoid distributions, Chemical Geology, v. 206, p. 231-248.

Sloss, L., 1963, Sequences in the cratonic interior of North America, Geological Society of America Bulletin, v. 74, p. 93-114.

Sun, X., T. Zhang, Y. Sun, K. L. Milliken, and D. Sun, 2016, Geochemical evidence of organic matter source input and depositional environments in the lower and upper Eagle Ford Formation, south Texas, Organic Geochemistry, v. 98, p. 66-81.

Touati, Z., 2017, Evidence of bottom-redox conditions during oceanic anoxic event 2 (OAE2) in Wadi Bazina, Northern Tunisia (Southern Tethyan margin), Arabian Journal of Geosciences, v. 10, p. 291.

Trevino, R. H. I., 1989, Facies and depositional environments of the Boquillas Formation, Upper Cretaceous of southwest Texas, M.S. thesis, University of Texas at Arlington, Arlington, Texas, 135 p.

Tribovillard, N., T. Algeo, F. Baudin, and A. Riboulleau, 2012, Analysis of marine environmental conditions based on molybdenum–uranium covariation—Applications to Mesozoic paleoceanography, Chemical Geology, v. 324, p. 46-58.

Tribovillard, N., T. J. Algeo, T. Lyons, and A. Riboulleau, 2006, Trace metals as paleoredox and paleoproductivity proxies: an update, Chemical Geology, v. 232, p. 12-32.

Tucker, M. E., 1990, Carbonate depositional systems I: Marine shallow-water and lacustrine carbonates, *in* M. E. Tucker, and V. P. Wright, eds., Carbonate Sedimentology: Oxford, Blackwell Scientific Publications, p. 1-27.

Udden, J. A., 1907, A Sketch of the Geology of the Chisos Country, Brewster County, Texas Bulletin 93, p. 101p.

Van Hinsbergen, D., T. Kouwenhoven, and G. Van der Zwaan, 2005, Paleobathymetry in the backstripping procedure: Correction for oxygenation effects on depth estimates, Palaeogeography, Palaeoclimatology, Palaeoecology, v. 221, p. 245-265.

Zeng, Z., M. Pike, M. M. Tice, C. Kelly, F. Marcantonio, G. Xu, and I. Maulana, 2018, Iron fertilization of primary productivity by volcanic ash in the Late Cretaceous (Cenomanian) Western Interior Seaway, Geology, v. 46, p. 859-862.

CHAPTER IV

APATITE TRACE-ELEMENT TEPHROCHRONOLOGY OF THE CENOMANIAN - TURONIAN EAGLE FORD GROUP ASH BEDS AT LOZIER CANYON, WEST TEXAS, USA

Overview

The Cenomanian – Turonian Eagle Ford Group outcrops in west Texas, USA, contain several volcanic ash deposits with abundant apatite crystals. Over 230 apatite samples characterizing eight volcanic ash beds in the Eagle Ford Group in west Texas were analyzed for trace element concentrations using laser ablation inductively coupled plasma mass spectrometry (LA-ICP-MS). Rare earth elements (REEs) chondrite-normalized patterns indicate a pronounced negative europium anomaly (Eu/Eu*) in apatite crystals from both the Cenomanian and Turonian ash beds. Apatite crystals from the Cenomanian ash beds have higher chondrite-normalized europium (Eu_{CN}) values and higher Eu/Eu* ratios (10^{th} percentile = 0.49; median = 0.60; 90^{th} percentile = 0.66), whereas apatite crystals from the Turonian ash beds have lower Eu_{CN} values and lower Eu/Eu* ratios (10^{th} percentile = 0.30; median = 0.35; 90^{th} percentile = 0.42). The REE chondrite-normalized plots also indicate enrichment in the lighter REEs over the heavier for apatite crystals from both the Cenomanian and Turonian ash beds. Apatite crystals from the Turonian ash beds, however, are more enriched in lighter REEs than apatite crystals from the Cenomanian ash beds. When the apatite trace element concentrations are integrated with established U-Pb zircon geochronology and outcrop-based stratigraphy,

the Cenomanian and Turonian ash beds in west Texas can be distinguished by their Eu/Eu* and on cross-plots using various combination of chondrite-normalized thorium/uranium $(Th/U)_{CN}$, cerium/ytterbium $(Ce/Yb)_{CN}$, Ce_{CN} and ∑(lanthanum, La; Ce; praseodymium, Pr; and neodymium, $Nd)_{CN}$. This technique provides a potentially rapid, sensitive, cost-effective and viable way to characterize Eagle Ford Group volcanic ashes across west Texas.

Introduction

The stratigraphic record of the Upper Cretaceous (Cenomanian – Turonian) Eagle Ford Group in west Texas contains several volcanic ash deposits bearing abundant apatite, a common accessory mineral in most igneous and metamorphic rocks and commonly occurs in volcanic ashes. Volcanic ash beds are highly susceptible to weathering and diagenetic alteration (e.g. bentonite) that may alter the original ash composition, making characterization ("finger printing") of volcanic ash beds for correlation difficult and potentially unreliable (Sell and Samson, 2011). Most volcanic ashes, however, contain apatite, a robust mineral with strong resistance to diagenetic alteration and weathering processes, offering a viable alternative method to reliably characterize volcanic ashes (Sell and Samson, 2011). An important characteristic of apatite is its ability to accommodate high concentrations of various trace elements in its crystal structure, making it a good mineral for trace element composition analyses (Belousova et al., 2002; Mao et al., 2016). Multiple studies have demonstrated that trace element composition in apatite can be related to the nature of its parent magma (Hoskin et al., 2000; Belousova et al., 2002;

Miles et al., 2014; Takashima et al., 2017). For example, apatite trace element composition was used to characterize Quaternary ignimbrites and co-ignimbrite ashes in Japan (Takashima et al., 2017), and apatite was used as an indicator mineral for mineral exploration because of the relationship of its trace element compositions to host rock type (Belousova et al., 2002). Also, when integrated with robust stratigraphic data, volcanic ash bed apatite trace element geochemistry can provide valuable insights to characterize and compare volcanic ash deposits from coeval or similar stratigraphic intervals (Sell and Samson, 2011; Heintz et al., 2015).

Although several uranium - lead (U-Pb) ash bed age dates were published for the Eagle Ford Group strata in west Texas (Eldrett et al., 2017; Minisini et al., 2017), there has been no study to characterize the ash beds based on apatite trace element geochemistry. Laser ablation inductively coupled plasma mass spectrometry (LA-ICP-MS), an analytical technique commonly used in elemental analyses of geologic samples, provides a quick, reliable, *in situ* determination of trace element concentrations in solid samples (Humayun et al., 2010; Liu et al., 2013), and is applicable to apatite trace element analyses. In this study, LA-ICP-MS apatite trace element geochemistry from multiple stratigraphic intervals in the Eagle Ford Group in west Texas was integrated with stratigraphic and geochronological data to characterize the ash beds and determine the apatite trace element characteristics that might be useful for future ash bed correlations in this area.

Geologic Setting and Stratigraphy

In west Texas, the Cenomanian – Turonian Eagle Ford Group is an unconformity bounded unit between the Buda Limestone and the Austin Chalk Group (figure IV.1). The Eagle Ford Group strata in west Texas was sub-divided into two informal units called the Lower and Upper Eagle Ford Formations, with each formation comprising two allostratigraphic members (Donovan et al., 2012). These members are designated as the Lozier Canyon and Antonio Creek Members of the Lower Eagle Ford Formation and the Scott Ranch and Langtry Members of the Upper Eagle Ford Formation (figure IV.1).

The Eagle Ford Group strata was deposited during a major third-order sea level rise in the southern aperture of North America's Cretaceous Western Interior Seaway (KWIS), a shallow, north-south trending epicontinental sea (figure IV.2) that connected boreal water masses of the Canadian Arctic with equatorial Tethyan water masses from the Gulf of Mexico (Lowery et al., 2014; Eldrett et al., 2015). The KWIS inundated the retro-arc foreland basin of the Cordilleran orogenic system as the Farallon plate collided with North America. In the United States, the Cordilleran orogenic system had a zone of extensive volcanic activity that intermittently produced voluminous amounts of volcanic ash that are well preserved as bentonites in the KWIS rock record. These volcanic ashes provide regional marker beds for stratigraphic correlation and precise age determination (Eldrett et al., 2015).

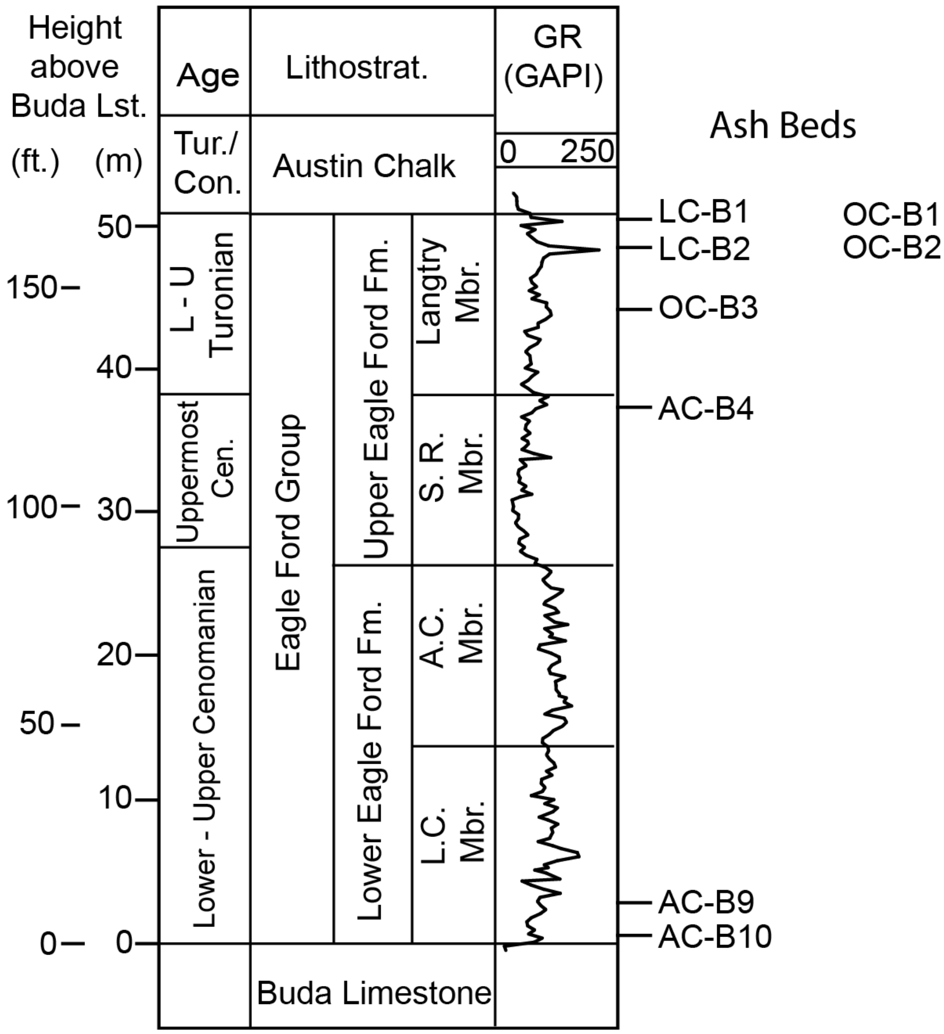

Figure IV.1 Eagle Ford Group stratigraphy at Lozier Canyon, west Texas. Apatite crystals from eight volcanic ash beds were analyzed for trace element concentration. L.C. = Lozier Canyon; A.C. = Antonio Creek; S.R. = Scott Ranch; Mbr. = Member

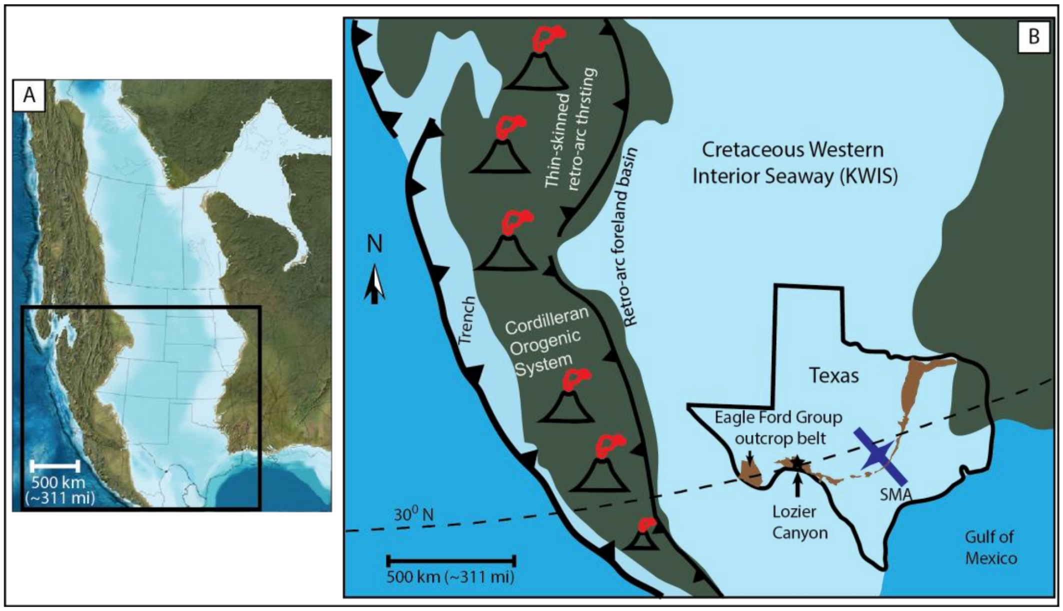

Figure IV.2 Upper Cretaceous (92.1 Ma) paleogeographic map of the Cretaceous Western Interior Seaway. The Cordilleran Orogenic system was a zone of extensive volcanic activity the intermittently produced voluminous amount of ash. Map adapted from Blakey (2011).

Samples and Analytic Methods

A total of thirteen ash bed samples were collected from eleven stratigraphic intervals within the Cenomanian – Turonian Eagle Ford Group succession at Antonio Creek (~ 2.5 mi/4 km south of Lozier Canyon), along a road cut outcrop on US Highway 90 (~ 12 km/7.5mi north of Lozier Canyon) and Osman Canyon (~ 20 km or 12.4 mi NE of Lozier Canyon). Eight out of the thirteen ash beds contained abundant apatite crystals from six stratigraphic intervals (figure IV.1; table IV.1).

Table IV.1 Apatite samples

Ash bed	Age	Location	No. of samples
LC-B1	Turonian	US Hwy 90	32
OC-B1	Turonian	Osman Canyon	27
LC-B2	Turonian	US Hwy 90	12
OC-B2	Turonian	Osman Canyon	29
OC-B3	Turonian	Osman Canyon	28
AC-B4	Cenomanian	Antonio Creek	36
AC-B9	Cenomanian	Antonio Canyon	45
AC-B10	Cenomanian	Antonio Creek	27

Apatite crystals were hand-picked under a binocular microscope and photographed. Trace element concentration analyses were conducted in the R. Ken Williams ’45 Radiogenic Isotope Geosciences Laboratory at Texas A&M University (TAMU) on an ESI/New Wave Research, 193 nm excimer laser ablation system coupled to a ThermoScientific iCAP RQ inductively coupled mass spectrometer. A spot size of 30 µm, repetition rate of 15 Hz, laser wavelength of 193 nm and pulse width of 4 ns were used to analyze each sample. The ablated material was carried from the ablation cell to the ICPMS using helium (He) as the carrier gas. National Institute of Standards and Technolog-612 (NIST-612) was used as the trace element calibration standard and each analysis was normalized to calcium (Ca) to determine the ablation yield. Details of the LA-ICP-MS analytical method, equipment conditions and reference standards are given in table IV.2. Acquisition of the LA-ICP-MS data occurred in a time-resolved mode, displaying element signal for each analysis as a function of time. This allows for easy selection of the time interval of interest to be integrated while avoiding unwanted micro-inclusions. The LA-ICP-MS trace element concentration data were reduced using Iolite® version 3 software.

Table IV.2 LA-ICP-MS system

Laser ablation system	
Make, Model & type	ESI/New Wave Research, 193nm excimer, ns
Ablation cell & volume	NWR TV2 cell
Laser wavelength	193 nm
Pulse width	4 ns
Fluence	3.1 (J.cm-2)
Repetition rate	15 Hz
Spot size (um)	30 um
Sampling mode / pattern	stationary circle
Carrier gas	He 0.6 l/min, Ar make-up gas 0.8 l/min combined 1/4 of way along sample line.
Ablation duration (secs)	30 s
Cell carrier gas flow (l/min)	0.6 l/min
ICP-MS Instrument	
Make, Model & type	ThermoScientific iCAP RQ
Sample introduction	Ablation aerosol directly to injector
RF power (W)	1450W
Make-up gas flow (l/min)	0.8 l/min Ar
Detection system	pulse / analog SEM (analog trigger >2.5M cps)
Masses measured	29Si, 31P, 45Sc, 49Ti, 88Sr, 89Y, 93Nb, 139La, 140Ce, 141Pr, 142Nd, 152Sm, 153Eu, 157Gd, 159Tb, 164Dy, 165Ho, 166Er, 169Tm, 174Yb, 175Lu, 178Hf, 181Ta, 202Hg, 204Pb, 206Pb, 207Pb, 208Pb, 232Th, 235U, 238U, 232Th.16O, 238U.16O
Integration time per peak (ms)	varies, 0.01 to 0.05 sec
Sensitvity / Efficiency (%, element)	7.5E3 to 10E3 CPS/ppm (NIST 612)
IC Dead time (ns)	20 ns
Data Processing	
Gas blank	10 second on-peak zero subtracted
Calibration strategy	NIST 612 (concentrations)
Data processing package used / Correction for LIEF	Iolite V3

The apatite trace element concentrations were integrated with a detailed stratigraphic study (Donovan et al., 2012; Gardner, 2013) and high-precision chemical abrasion isotope dilution thermal ionization mass spectrometry (CA-ID-TIMS) U - Pb geochronology for the Lozier Canyon outcrop (Chapter II).

Results

Apatite's crystal structure and mineral chemistry allow it to accommodate high concentrations of many trace elements, including the rare earth elements (REEs) (Belousova et al., 2002; Mao et al., 2016). Over 230 apatite crystals from Cenomanian and Turonian ash beds in the Eagle Ford Group in west Texas were analyzed for their trace element concentrations (table IV.1). The apatite trace element concentrations were normalized to chondrite values of Anders and Grevesse (1989). The chondrite-normalized trace element patterns indicate variations in the REEs and europium (Eu) anomaly in apatite crystals from the Cenomanian and Turonian ash beds. The Eu anomaly is numerically expressed as Eu_{CN}/Eu^*, where Eu_{CN} is the chondrite-normalized Eu value and $Eu^* = \sqrt{(Sm)_{CN} * (Gd)_{CN}}$ (McLennan, 1989), where Sm_{CN} and Gd_{CN} are the chondrite-normalized samarium (Sm) and gadolinium (Gd) values, respectively. The average Eu_{CN}/Eu^* was calculated for each age group (Cenomanian and Turonian), and apatite crystals with Eu_{CN}/Eu^* ratios outside the 2σ error were excluded from all analyses. Eu/Eu* values < 1 are considered negative, whereas Eu/Eu* values > 1 are considered positive. Apatite crystals from both the Cenomanian and Turonian ash beds of the Eagle Ford Group in west Texas have a negative Eu_{CN}/Eu^* and a negative REEs slope (cerium/ytterbium, Ce_{CN}/Yb_{CN} >5) on chondrite-normalized plots (figures IV.3, IV.4 and IVA), indicating a relative enrichment in lighter REEs over heavier REEs.

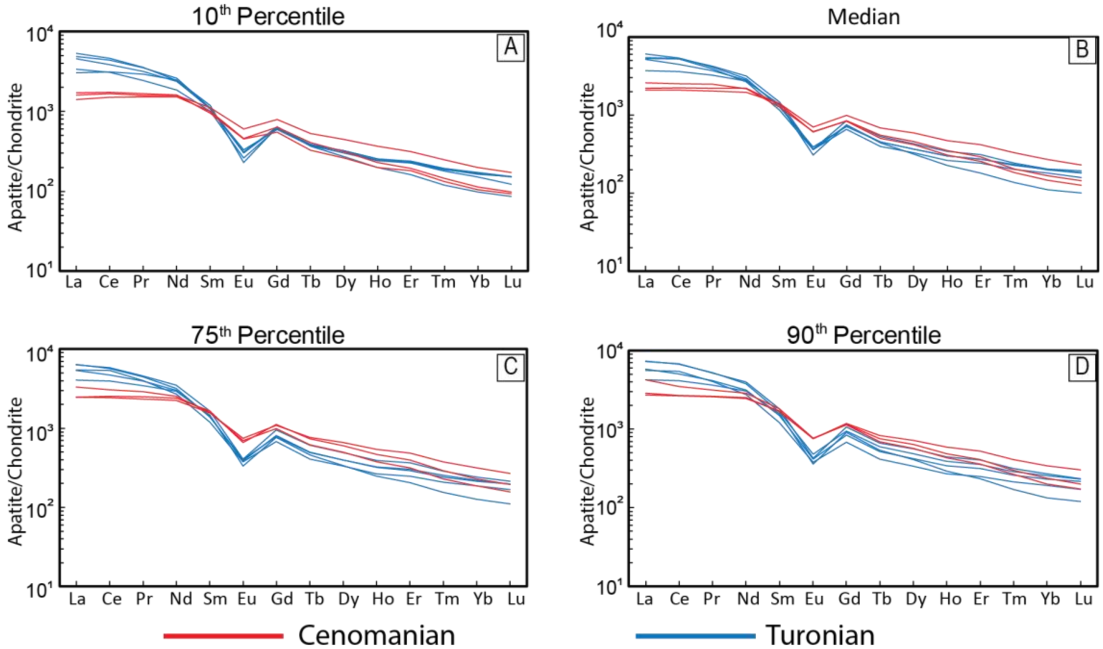

Figure IV.3 Chondrite-normalized rare earth element (REE) plots for apatite trace element concentrations plotted by percentile for individual ash beds. Apatite crystals from the Cenomanian ash beds have higher chondrite-normalized europium (Eu) concentrations and higher Eu/Eu* ratios (weaker Eu anomaly), whereas apatite crystals from the Turonian ash beds have lower chondrite-normalized Eu concentrations and lower Eu/Eu* ratios (stronger Eu anomaly). Both Cenomanian and Turonian apatite crystals have negative REE slope. (A) 10th percentile (B) Median (50th percentile) (C) 75th percentile (D) 90th percentile

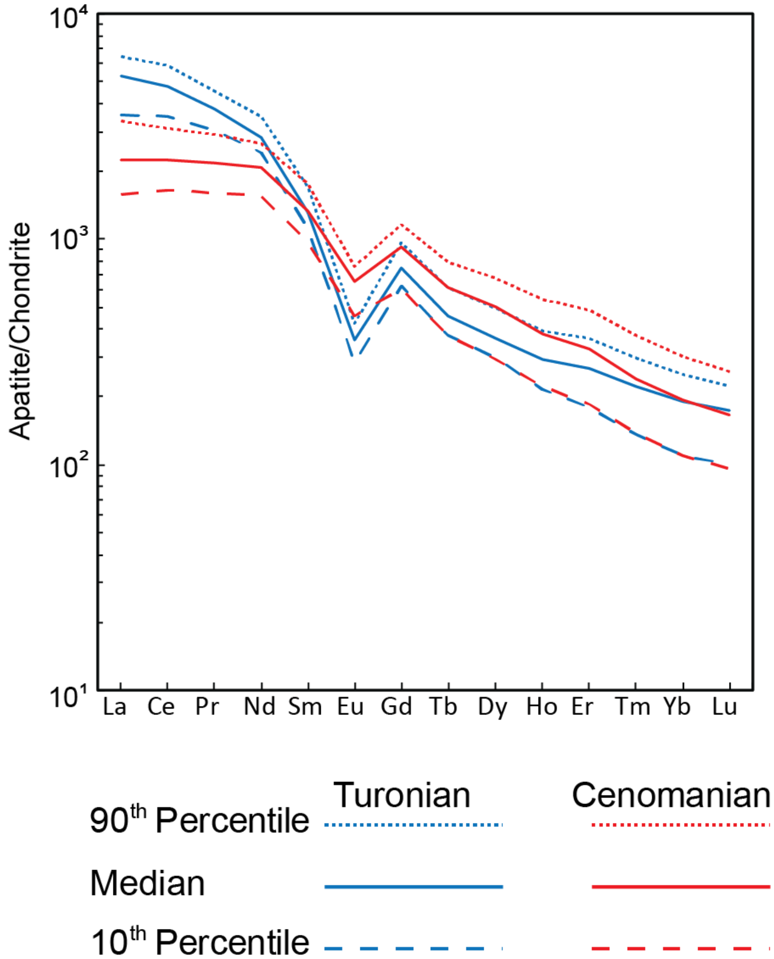

Figure IV.4 Chondrite-normalized REE plots with ash beds grouped by age and plotted by percentiles. The plot is very similar to the plot for individual ash beds (figure IV.3).

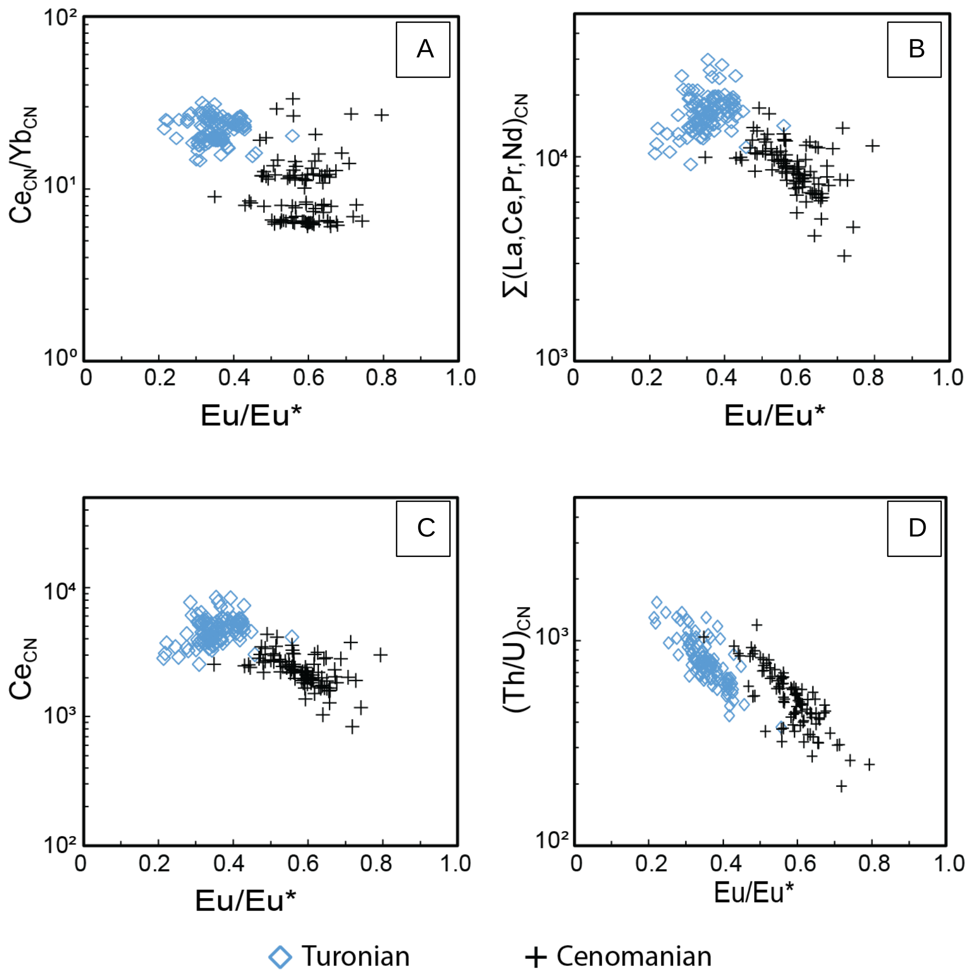

Figure IV.5 Chondrite-normalized apatite trace element concentration cross-plots. When the apatite trace element concentrations are integrated with established U-Pb zircon geochronology and stratigraphy, the Cenomanian and Turonian ash beds in west Texas can be distinguished using various combination of cross-plots (A) Semi-log plot of Ce_{cn}/Yb_{cn} versus Eu/Eu* (B) Semi-log plot of $\sum(La, Ce, Pr, Nd)_{CN}$ versus Eu/Eu* (C) Semi log plot of Ce_{CN} versus Eu/Eu* (D) Semi-log plot of $Thcn/U_{CN}$ versus Eu/Eu*.

REE chondrite-normalized patterns show a general temporal variation in the negative Eu anomaly from the Cenomanian to the Turonian ash beds (figures IV.3 and IV.4). Apatite crystals from the Cenomanian ash beds have higher Eu_{CN} values and weaker Eu anomaly ratios (10^{th} percentile = 0.49; median = 0.60; 90^{th} percentile = 0.66), whereas apatite crystals from the Turonian ash beds have lower Eu_{CN} valuess and stronger Eu anomaly ratios (10th percentile = 0.30; median = 0.35; 90th percentile = 0.42). Similar trends also are indicated in the chondrite-normalized thorium/uranium $(Th/U)_{CN}$ and $(Ce/Yb)_{CN}$ ratios, and $\sum(La, Ce, Pr, Nd)_{CN}$ values (figure IV.5). Apatite crystals from the Turonian ash beds have higher lighter REEs enrichment than apatite crystals from the Cenomanian ash beds, resulting in a relatively higher $\sum(La, Ce, Pr, Nd)_{CN}$ in the Turonian apatite crystals (figure IV.5B). Also, apatite crystals from the Turonian ash beds have relatively higher Th_{cn}/U_{cn} and Ce_{cn}/Yb_{cn} ratios than apatite crystals from the Cenomanian ash beds (figure IV.4). The LC B2 (~ 11.3 km/11 mi north of Lozier Canyon) and OC B2 (Osman Canyon) are from the same stratigraphic interval, and LC B1 (~11.3 km/7 mi northwest of Lozier Canyon) and the OC B1 (Osman Canyon) also are from the same stratigraphic interval (figure IV.1). Stratigraphic age constraints are established by CA-ID-TIMS zircon geochronology (Chapter II) and lithostratigraphy (Donovan et al., 2012; Gardner, 2013). Volcanic ashes from Antonio Creek, Osman Canyon and US HWY 90 are correlated to a composite section of the Lozier Canyon outcrop using high-resolution stratigraphic correlation (Gardner, 2013).

Discussion

Volcanic ash beds generally are susceptible to degradation and compositional alteration when exposed to different weathering, diagenetic and pedogenic processes. Apatite, however, because of its robust nature, resistance to weathering and diagenetic alteration, and ability to accommodate high concentrations of various elements in its crystal structure, presents a viable alternative to characterize volcanic ash beds that are severely altered or weathered (Sell and Samson, 2011). The chondrite-normalized trace element concentration patterns for all the apatite crystals characterizing multiple ash beds from the Cenomanian – Turonian Eagle Ford Group in west Texas have pronounced negative Eu anomalies. Development of negative Eu anomalies in apatites requires a redox transition of Eu^{3+} to Eu^{2+} (Puchelt and Emmermann, 1976). Reduction of Eu^{3+} to Eu^{2+} is accompanied by an increase in the ionic radius and subsequent discrimination of Eu^{2+} from the apatite lattice during crystallization (Puchelt and Emmermann, 1976). Apatite crystals from the Cenomanian ash beds in the Eagle Ford Group in west Texas have higher Eu_{CN} concentration and weak Eu anomalies, whereas apatites from the Turonian ash beds have lower Eu_{CN} concentration and strong Eu anomalies, indicating a temporal change in the Eu_{CN} concentration and Eu anomaly. This temporal change in Eu anomaly from the Cenomanian to Turonian apatites likely reflects a change in the parent magma oxygen fugacity (Puchelt and Emmermann, 1976). The negative slope with high $(Ce/Yb)_{CN}$ in apatite crystals from both the Cenomanian and Turonian ash beds (figure IV.4A) indicate a relative enrichment in the lighter REEs over the heavier. Apatite crystals from the Turonian ash beds, however, have higher $(Ce/Yb)_{CN}$ and higher $\sum(La, Ce, Pr, Nd)_{CN}$

values than apatite crystals from the Cenomanian ash beds, indicating a slight increase in the slope of the chondrite-normalized patterns and a temporal change in the apatite REE trace element concentrations (figure IV.5A). Apatite crystals from the Cenomanian and Turonian ash beds in west Texas can be distinguished on cross plots using various combination of Eu/Eu*, $\sum(La, Ce, Pr, Nd)_{CN}$ $(Th/U)_{CN}$ and $(Ce/Yb)_{CN}$ (figure IV.4).

Conclusions

Volcanic ashes from the Cenomanian – Turonian Eagle Ford Group commonly bear abundant apatite phenocrysts. Trace element concentration analyses by LA-ICP-MS of over 230 apatite crystals characterizing volcanic ashes in the Eagle Ford Group at Lozier Canyon in west Texas indicate that the Cenomanian and Turonian ash beds can be distinguished based on apatite trace element concentrations. This potentially provides a rapid, sensitive, cost-effective and viable way to characterize volcanic ashes from the Eagle Ford Group. When the apatite trace element concentrations are integrated with U-Pb zircon geochronology, the Cenomanian and Turonian ash beds can be distinguished on the basis of the Eu/Eu* on chondrite-normalized REE plots and on cross-plots using a combination of $(Th/U)_{CN}$, $\sum(La, Ce, Pr, Nd)_{CN}$ and $(Ce/Yb)_{CN}$.

References

Anders, E., and N. Grevesse, 1989, Abundances of the elements: Meteoritic and solar, Geochimica et Cosmochimica Acta, v. 53, p. 197-214.

Belousova, E., W. Griffin, S. Y. O'Reilly, and N. Fisher, 2002, Apatite as an indicator mineral for mineral exploration: trace-element compositions and their relationship to host rock type, Journal of Geochemical Exploration, v. 76, p. 45-69.

Deluca, M. J., 2016, Ash Bed Analysis of the Cretaceous Eagle Ford Shale Using ID-TIMS U/Pb Methods: Implications for Biostratigraphic Refinement and Correlations Within the Western Interior Seaway, Geology and Geophysics Department, Texas A&M University, 68 p.

Donovan, A. D., T. S. Staerker, A. Pramudito, W. Li, M. J. Corbett, C. M. Lowery, A. M. Romero, and R. D. Gardner, 2012, The Eagle Ford outcrops of West Texas: A laboratory for understanding heterogeneities within unconventional mudstone reservoirs, Gulf Coast Association of Geological Societies, v. 1, p. 162-185.

Eldrett, J. S., P. Dodsworth, S. C. Bergman, M. Wright, and D. Minisini, 2017, Water-mass evolution in the Cretaceous Western Interior Seaway of North America and equatorial Atlantic, Climate of the Past, v. 13, p. 855.

Eldrett, J. S., C. Ma, S. C. Bergman, B. Lutz, F. J. Gregory, P. Dodsworth, M. Phipps, P. Hardas, D. Minisini, and A. Ozkan, 2015, An astronomically calibrated stratigraphy of the Cenomanian, Turonian and earliest Coniacian from the Cretaceous Western Interior Seaway, USA: Implications for global chronostratigraphy, Cretaceous Research, v. 56, p. 316-344.

Gardner, R. D., 2013, Lateral Continuity of the Eagle Ford Group Strata in Lozier Canyon and Antonio Creek, Terrell County, Texas, M.S. thesis, Geology & Geophysics, Texas A&M University, College Station, 118 p.

Heintz, M. L., T. E. Yancey, B. V. Miller, and M. T. Heizler, 2015, Tephrochronology and geochemistry of Eocene and Oligocene volcanic ashes of east and central Texas, Bulletin, v. 127, p. 770-780.

Hoskin, P. W., P. D. Kinny, D. Wyborn, and B. W. Chappell, 2000, Identifying accessory mineral saturation during differentiation in granitoid magmas: an integrated approach, Journal of Petrology, v. 41, p. 1365-1396.

Humayun, M., F. A. Davis, and M. M. Hirschmann, 2010, Major element analysis of natural silicates by laser ablation ICP-MS, Journal of Analytical Atomic Spectrometry, v. 25, p. 998-1005.

Liu, Y., Z. Hu, M. Li, and S. Gao, 2013, Applications of LA-ICP-MS in the elemental analyses of geological samples, Chinese Science Bulletin, v. 58, p. 3863-3878.

Lowery, C. M., M. J. Corbett, R. M. Leckie, D. Watkins, A. M. Romero, and A. Pramudito, 2014, Foraminiferal and nannofossil paleoecology and paleoceanography of the Cenomanian–Turonian Eagle Ford Shale of southern Texas, Palaeogeography, Palaeoclimatology, Palaeoecology, v. 413, p. 49-65.

Mao, M., A. S. Rukhlov, S. M. Rowins, J. Spence, and L. A. Coogan, 2016, Apatite trace element compositions: A robust new tool for mineral exploration, Economic Geology, v. 111, p. 1187-1222.

McLennan, S. M., 1989, Rare earth elements in sedimentary rocks: influence of provenance and sedimentary processes, Geochemistry and Mineralogy of Rare Earth Elements, Reviews in Mineralogy 21, p. 169-200.

Miles, A., C. Graham, C. Hawkesworth, M. Gillespie, R. Hinton, and G. Bromiley, 2014, Apatite: A new redox proxy for silicic magmas?, Geochimica et Cosmochimica Acta, v. 132, p. 101-119.

Minisini, D., J. Eldrett, S. C. Bergman, and R. Forkner, 2017, Chronostratigraphic framework and depositional environments in the organic-rich, mudstone-dominated Eagle Ford Group, Texas, USA, Sedimentology, p. 1-38.

Puchelt, H., and R. Emmermann, 1976, Bearing of rare earth patterns of apatites from igneous and metamorphic rocks, Earth and Planetary Science Letters, v. 31, p. 279-286.

Sell, B. K., and S. D. Samson, 2011, A tephrochronologic method based on apatite trace-element chemistry, Quaternary Research, v. 76, p. 157-166.

Takashima, R., S. Kuwabara, T. Sato, K. Takemura, and H. Nishi, 2017, Utility of trace elements in apatite for discrimination and correlation of Quaternary ignimbrites and co-ignimbrite ashes, Japan, Quaternary Geochronology, v. 41, p. 151-162.

CHAPTER V

CONCLUSIONS

Chronostratigraphically tying the Eagle Ford Group outcrop units to subsurface units provides a critical chronostratigraphic framework constraining its timing of deposition and providing better understanding of its three-dimensional stratigraphic architecture. The Eagle Ford Group depositional environment was episodically to frequently affected by storm wave agitation and the flow of traction currents across the sea floor, aiding in sediment transport and deposition. When high precision $^{206}Pb/^{238}U$ ages are integrated with biostratigraphy, carbon stable isotope chemostratigraphy, sedimentology, RSTE geochemistry and thin section petrography, the Eagle Ford Group mudstone-dominated depositional environment can be sub-divided into five time intervals: Uppermost Lower Cenomanian, Middle Cenomanian, Upper Cenomanian, uppermost Cenomanian – Lower Turonian and Middle – Upper Turonian.

Sedimentological and geochemical data from the Eagle Ford Group in west and south Texas indicate their organic-rich, mudstone-dominated depositional environments were heterogeneous, and had different depositional, sedimentological and geochemical processes simultaneously affecting coeval deposits in different parts of the same basin. LA-ICP-MS trace element concentrations of apatite crystals characterizing volcanic ashes in the Eagle Ford Group at Lozier Canyon in west Texas indicate that the Cenomanian and Turonian ash beds can be distinguished on the basis of apatite trace element concentrations. This potentially provides a rapid, sensitive, cost-effective and viable way to characterize volcanic ashes from the Eagle Ford Group.

APPENDIX A

U-PB ISOTOPE DATA

W2-B1: Well 2 (Karnes Co.) - 82.3 m (270 ft.) above Buda Limestone

	Compositional Parameters								Radiogenic Isotope Ratios								Isotopic Ages					
Sample	U (ng)	$\frac{Th}{U}$	Pb (pg)	$^{206}Pb^*$ x10^{-13} mol	mol % $^{206}Pb^*$	$\frac{Pb^*}{Pb_c}$	Pb_c (pg)	$\frac{^{206}Pb}{^{204}Pb}$	$\frac{^{208}Pb}{^{206}Pb}$	$\frac{^{207}Pb}{^{206}Pb}$	% err	$\frac{^{207}Pb}{^{235}U}$	% err	$\frac{^{206}Pb}{^{238}U}$	% err	corr. coef.	$\frac{^{207}Pb}{^{206}Pb}$	±	$\frac{^{207}Pb}{^{235}U}$	±	$\frac{^{206}Pb}{^{238}U}$	±
(a)	(b)	(c)	(b)	(d)	(d)	(d)	(d)	(e)	(f)	(f)	(g)	(f)	(g)	(f)	(g)	(f)	(g)	(h)	(g)	(h)	(g)	(h)
(Z74) zirc 1	1.58	0.482	24.2	0.9122	97.85%	14.0	1.62	868	0.15	0.05	0.75	0.09	0.84	0.01	0.20	0.56	93.28	17.67	88.95	0.71	88.79	0.18
(Z77) zirc 2	1.94	0.438	28.9	1.1240	98.49%	19.8	1.39	1236	0.14	0.05	0.55	0.09	0.63	0.01	0.15	0.60	91.49	13.11	88.91	0.54	88.82	0.14
(Z39) zirc 3	1.19	0.447	18.6	0.6891	97.13%	10.3	1.64	651	0.14	0.05	0.85	0.09	0.95	0.01	0.18	0.61	80.76	20.13	88.62	0.80	88.91	0.16
(Z75) zirc 4	1.10	0.469	17.0	0.6368	97.62%	12.5	1.26	783	0.15	0.05	0.70	0.09	0.79	0.01	0.15	0.67	85.27	16.52	88.78	0.67	88.91	0.13
(Z43) zirc 5	0.98	0.466	14.7	0.5681	98.61%	21.6	0.65	1338	0.15	0.05	0.50	0.09	0.59	0.01	0.16	0.64	83.00	11.93	88.71	0.50	88.92	0.14
(Z76) zirc 6	1.91	0.495	29.2	1.1084	98.22%	16.9	1.63	1045	0.16	0.05	0.49	0.09	0.58	0.01	0.15	0.71	82.28	11.57	88.72	0.50	88.96	0.14
(Z78) zirc 7	1.66	0.478	25.1	0.9600	98.29%	17.6	1.35	1092	0.15	0.05	0.77	0.09	0.84	0.01	0.20	0.45	85.59	18.28	88.88	0.72	89.00	0.18
(Z1) zirc 8	1.35	0.457	30.5	0.7764	84.85%	1.7	11.36	123	0.15	0.05	2.07	0.09	2.22	0.01	0.29	0.58	86.20	49.08	88.20	1.88	88.27	0.25
(Z40) zirc 9	2.06	0.446	30.3	1.1867	98.81%	25.3	1.15	1571	0.14	0.05	0.41	0.09	0.50	0.01	0.15	0.69	86.03	9.68	88.40	0.42	88.49	0.13
(Z4) zirc 10	0.83	0.445	24.7	0.4786	75.15%	0.9	12.98	75	0.14	0.05	3.15	0.09	3.35	0.01	0.41	0.54	102.45	74.43	89.13	2.86	88.63	0.36
(Z3) zirc 11	0.50	0.481	19.2	0.2895	66.47%	0.6	11.97	55	0.15	0.05	4.40	0.10	4.65	0.01	0.58	0.48	216.12	101.80	93.90	4.17	89.16	0.51
(Z72) zirc 12	2.33	0.435	34.8	1.3568	98.57%	20.8	1.60	1301	0.14	0.05	0.45	0.09	0.53	0.01	0.14	0.69	88.58	10.57	89.34	0.46	89.37	0.13
(Z2) zirc 13	0.64	0.462	23.9	0.3760	67.90%	0.6	14.57	58	0.15	0.05	4.74	0.10	5.01	0.01	0.59	0.51	218.55	109.67	94.97	4.54	90.12	0.53
(Z44) zirc 14	0.20	0.533	3.9	0.1240	92.39%	3.8	0.83	245	0.17	0.05	3.13	0.10	3.38	0.01	0.75	0.43	68.05	74.51	93.92	3.03	94.94	0.71

W2-B2: Well 2 (Karnes Co.) - 72.2 m (238.5 ft.) above Buda Limestone

Sample	Compositional Parameters								Radiogenic Isotope Ratios								Isotopic Ages					
	U (ng)	Th/U	Pb (pg)	$^{206}Pb^*$ x10^{-13} mol	mol % $^{206}Pb^*$	Pb^*/Pb_c	Pb_c (pg)	$^{206}Pb/^{204}Pb$	$^{208}Pb/^{206}Pb$	$^{207}Pb/^{206}Pb$	% err	$^{207}Pb/^{235}U$	% err	$^{206}Pb/^{238}U$	% err	corr. coef.	$^{207}Pb/^{206}Pb$	±	$^{207}Pb/^{235}U$	±	$^{206}Pb/^{238}U$	±
(a)	(b)	(c)	(b)	(d)	(d)	(d)	(d)	(e)	(f)	(f)	(g)	(f)	(g)	(f)	(g)	(f)	(g)	(h)	(g)	(h)	(g)	(h)
(Z26a) zirc 1	0.25	0.494	4.8	0.1471	91.53%	3.3	1.10	220	0.16	0.05	2.37	0.10	2.54	0.01	0.31	0.58	114.59	55.87	92.41	2.24	91.55	0.28
(Z28b) zirc 2	0.26	0.556	4.5	0.1553	95.72%	7.0	0.56	436	0.18	0.05	2.76	0.09	2.88	0.01	0.49	0.33	8.61	66.46	88.61	2.45	91.61	0.45
(Z25a) zirc 3	0.21	0.606	3.9	0.1278	94.18%	5.1	0.64	321	0.19	0.05	2.41	0.09	2.59	0.01	0.56	0.40	61.08	57.51	90.49	2.24	91.61	0.51
(Z28a) zirc 4	0.05	0.560	1.2	0.0271	80.49%	1.3	0.53	96	0.18	0.05	18.49	0.10	18.75	0.01	1.26	0.24	117.95	435.81	93.09	16.68	92.12	1.16
(Z23a) zirc 5	0.15	0.616	3.7	0.0901	83.58%	1.6	1.43	114	0.20	0.05	5.11	0.09	5.40	0.01	0.52	0.58	120.12	120.49	90.64	4.68	89.53	0.46
(Z30a) zirc 6	0.11	0.669	3.0	0.0639	79.63%	1.3	1.32	92	0.21	0.05	8.25	0.09	8.64	0.01	0.90	0.48	2.58	198.57	86.97	7.20	90.07	0.80
(Z26b) zirc 7	0.12	0.625	3.0	0.0738	84.71%	1.8	1.08	122	0.20	0.05	5.42	0.09	5.71	0.01	0.58	0.53	-10.51	130.90	89.56	4.90	93.36	0.54
(Z27b) zirc 8	0.27	0.601	5.5	0.1656	91.14%	3.3	1.30	211	0.19	0.05	2.92	0.09	3.11	0.01	0.42	0.51	47.14	69.80	92.09	2.74	93.83	0.39
(Z29a) zirc 9	0.30	0.517	6.0	0.2014	94.49%	5.3	0.95	339	0.17	0.05	1.55	0.11	1.94	0.02	0.95	0.62	64.37	36.84	102.15	1.88	103.78	0.97
(Z27a) zirc 10	0.09	0.556	2.4	0.0601	85.42%	1.8	0.83	128	0.18	0.05	5.89	0.11	6.14	0.02	0.47	0.55	99.37	139.31	104.71	6.11	104.94	0.49
(Z31b) zirc 11	0.38	0.430	9.3	0.2966	92.36%	3.7	1.98	244	0.14	0.05	2.04	0.13	2.19	0.02	0.26	0.64	226.24	47.05	126.18	2.60	120.93	0.31
(Z29b) zirc 12	0.10	0.423	2.5	0.0811	92.40%	3.7	0.54	245	0.13	0.06	2.78	0.16	3.07	0.02	0.85	0.46	599.22	60.28	150.77	4.30	123.79	1.04
(Z30b) zirc 13	0.26	0.219	11.9	0.4788	98.01%	14.1	0.79	935	0.07	0.06	0.90	0.35	1.03	0.04	0.36	0.53	467.79	19.88	302.69	2.71	281.70	0.98

W2-B3: Well 2 (Karnes Co.) - 48 m (157.3 ft.) above Buda Limestone

	Compositional Parameters								Radiogenic Isotope Ratios								Isotopic Ages					
Sample	U (ng)	$\frac{Th}{U}$	Pb (pg)	$^{206}Pb^*$ x10^{-13} mol	mol % $^{206}Pb^*$	$\frac{Pb^*}{Pb_c}$	Pb_c (pg)	$\frac{^{206}Pb}{^{204}Pb}$	$\frac{^{208}Pb}{^{206}Pb}$	$\frac{^{207}Pb}{^{206}Pb}$	% err	$\frac{^{207}Pb}{^{235}U}$	% err	$\frac{^{206}Pb}{^{238}U}$	% err	corr. coef.	$\frac{^{207}Pb}{^{206}Pb}$	±	$\frac{^{207}Pb}{^{235}U}$	±	$\frac{^{206}Pb}{^{238}U}$	±
(a)	(b)	(c)	(b)	(d)	(d)	(d)	(d)	(e)	(f)	(f)	(g)	(f)	(g)	(f)	(g)	(f)	(g)	(h)	(g)	(h)	(g)	(h)
(Z34) zirc 1	0.57	0.409	9.4	0.3515	97.03%	9.8	0.87	628	0.131	0.046525	1.387	0.095271	1.476	0.014852	0.256	0.424	24.92	33.25	92.40	1.30	95.04	0.24
(Z46) zirc 2	0.29	0.371	5.0	0.1795	95.50%	6.3	0.68	415	0.119	0.046770	1.454	0.095962	1.635	0.014881	0.493	0.498	37.48	34.78	93.04	1.45	95.22	0.47
(Z36) zirc 3	0.26	0.474	4.6	0.1620	95.65%	6.7	0.60	429	0.152	0.047105	2.158	0.096883	2.306	0.014917	0.445	0.418	54.54	51.46	93.89	2.07	95.45	0.42
(Z69) zirc 4	0.65	0.505	10.9	0.4044	97.69%	13.1	0.77	809	0.162	0.047689	0.959	0.098148	1.046	0.014927	0.242	0.460	83.88	22.75	95.07	0.95	95.51	0.23
(Z37) zirc 5	0.37	0.397	6.4	0.2278	95.26%	6.0	0.92	393	0.127	0.047112	1.739	0.097180	1.877	0.014960	0.229	0.644	54.93	41.46	94.17	1.69	95.73	0.22
(Z6) zirc 6	1.18	0.510	31.7	0.7396	82.09%	1.4	13.23	104	0.163	0.048432	2.306	0.100092	2.477	0.014989	0.311	0.593	120.45	54.32	96.86	2.29	95.91	0.30
(Z51) zirc 7	0.26	0.285	9.8	0.1532	67.00%	0.6	6.16	56	0.091	0.045534	11.061	0.089099	11.491	0.014192	0.810	0.556	-27.00	267.87	86.66	9.55	90.84	0.73
(Z32) zirc 8	0.36	0.352	6.2	0.2176	94.51%	5.1	1.02	340	0.113	0.048981	6.666	0.099132	7.004	0.014679	0.448	0.768	146.91	156.25	95.98	6.41	93.94	0.42
(Z35) zirc 9	0.31	0.513	5.4	0.1958	96.74%	9.2	0.53	573	0.164	0.046848	1.721	0.096556	1.824	0.014948	0.350	0.383	41.49	41.14	93.59	1.63	95.65	0.33
(Z45) zirc 10	3.74	0.474	60.3	2.3656	99.12%	34.4	1.70	2118	0.152	0.048187	0.290	0.100865	0.391	0.015181	0.143	0.796	108.45	6.84	97.57	0.36	97.13	0.14
(Z5) zirc 11	0.35	0.458	21.1	0.2285	54.81%	0.4	15.45	41	0.146	0.052444	6.605	0.113483	6.917	0.015694	0.942	0.391	304.82	150.46	109.15	7.16	100.38	0.94
(Z47) zirc 12	2.98	0.462	48.9	1.9532	99.57%	69.9	0.69	4292	0.148	0.048527	0.215	0.105074	0.338	0.015704	0.176	0.832	125.02	5.06	101.45	0.33	100.45	0.18

W2-B4: Well 2 (Karnes Co.) - 12 m (39 ft.) above Buda Limestone

Sample	Compositional Parameters								Radiogenic Isotope Ratios								Isotopic Ages					
	U (ng)	Th/U	Pb (pg)	$^{206}Pb^{*}$ x10^{-13} mol	mol % $^{206}Pb^{*}$	Pb^{*}/Pb_c	Pb_c (pg)	$^{206}Pb/^{204}Pb$	$^{208}Pb/^{206}Pb$	$^{207}Pb/^{206}Pb$	% err	$^{207}Pb/^{235}U$	% err	$^{206}Pb/^{238}U$	% err	corr. coef.	$^{207}Pb/^{206}Pb$	±	$^{207}Pb/^{235}U$	±	$^{206}Pb/^{238}U$	±
(a)	(b)	(c)	(b)	(d)	(d)	(d)	(d)	(e)	(f)	(f)	(g)	(f)	(g)	(f)	(g)	(f)	(g)	(h)	(g)	(h)	(g)	(h)
(Z20) zirc 1	1.03	0.698	18.7	0.6410	96.51%	9.0	1.88	534	0.22	0.05	0.85	0.10	0.95	0.01	0.15	0.70	104.39	19.99	95.84	0.87	95.49	0.15
(Z21) zirc 2	0.27	0.692	9.8	0.1672	71.55%	0.8	5.38	66	0.22	0.05	13.50	0.10	13.85	0.01	0.53	0.66	145.40	316.62	97.56	12.88	95.61	0.50
(Z70) zirc 3	0.35	0.880	6.5	0.2195	97.49%	13.2	0.46	743	0.28	0.05	1.50	0.10	1.58	0.01	0.34	0.35	47.30	35.81	93.85	1.42	95.69	0.32
(Z73) zirc 4	0.50	0.499	9.9	0.3106	92.19%	3.6	2.13	239	0.16	0.05	1.79	0.10	1.92	0.01	0.22	0.63	88.53	42.36	95.43	1.75	95.71	0.21
(Z72) zirc 5	0.70	0.558	11.7	0.4381	98.17%	16.8	0.66	1019	0.18	0.05	0.67	0.10	0.76	0.01	0.19	0.55	84.69	15.95	95.37	0.69	95.80	0.18
(Z75) zirc 6	0.88	0.471	14.1	0.5495	98.79%	25.0	0.54	1545	0.15	0.05	0.39	0.10	0.49	0.02	0.17	0.71	93.43	9.18	96.13	0.45	96.24	0.16
(Z14) zirc 7	0.61	0.493	24.2	0.3851	68.25%	0.7	14.56	59	0.16	0.05	5.53	0.10	5.86	0.02	0.50	0.67	177.55	129.00	99.63	5.56	96.40	0.48
(Z17) zirc 8	0.72	0.572	28.6	0.4514	68.20%	0.7	17.14	59	0.18	0.05	5.01	0.10	5.30	0.02	0.42	0.72	161.47	117.02	99.00	5.00	96.43	0.40
(Z19) zirc 9	0.73	0.500	19.3	0.4585	82.58%	1.5	7.82	107	0.16	0.05	3.39	0.10	3.60	0.02	0.28	0.78	200.76	78.57	100.62	3.45	96.44	0.27
(Z15) zirc 10	0.51	0.414	28.4	0.3187	55.75%	0.4	20.63	42	0.13	0.05	9.46	0.10	9.94	0.02	0.78	0.64	62.35	225.32	95.32	9.04	96.64	0.75
(Z74) zirc 11	0.63	0.454	11.8	0.4427	97.72%	13.1	0.83	819	0.15	0.05	0.62	0.12	0.84	0.02	0.43	0.71	248.46	14.18	114.77	0.91	108.42	0.46

S-B1: Swenson 1H well (McMullen Co.) - 45 m (148.5 ft.) above Buda Limestone

	Compositional Parameters								Radiogenic Isotope Ratios								Isotopic Ages					
Sample	U (ng)	Th/U	Pb (pg)	^{206}Pb* x10^{-13} mol	mol % ^{206}Pb*	Pb*/Pb$_c$	Pb$_c$ (pg)	^{206}Pb/^{204}Pb	^{208}Pb/^{206}Pb	^{207}Pb/^{206}Pb	% err	^{207}Pb/^{235}U	% err	^{206}Pb/^{238}U	% err	corr. coef.	^{207}Pb/^{206}Pb	±	^{207}Pb/^{235}U	±	^{206}Pb/^{238}U	±
(a)	(b)	(c)	(b)	(d)	(d)	(d)	(d)	(e)	(f)	(f)	(g)	(f)	(g)	(f)	(g)	(f)	(g)	(h)	(g)	(h)	(g)	(h)
(Z51) zirc 1	0.68	0.719	12.3	0.4157	96.07%	8.0	1.38	474	0.23	0.05	1.24	0.10	1.44	0.01	0.55	0.52	108.01	29.28	94.86	1.30	94.34	0.52
(Z55) zirc 2	1.29	0.425	20.0	0.7904	98.93%	28.0	0.69	1747	0.14	0.05	0.43	0.10	0.75	0.01	0.56	0.82	90.90	10.30	94.23	0.67	94.36	0.52
(Z56) zirc 3	1.27	0.470	19.8	0.7796	99.20%	37.9	0.51	2332	0.15	0.05	0.25	0.10	0.37	0.01	0.13	0.92	92.07	5.96	94.38	0.33	94.47	0.13
(Z63) zirc 4	1.47	0.479	23.0	0.9029	99.18%	36.9	0.61	2265	0.15	0.05	0.43	0.10	0.51	0.01	0.15	0.64	94.30	10.14	94.53	0.46	94.54	0.14
(Z52) zirc 5	0.62	0.431	9.9	0.3849	98.49%	19.8	0.48	1237	0.14	0.05	0.64	0.10	0.77	0.01	0.32	0.60	98.74	15.05	94.78	0.70	94.62	0.30
(Z15) zirc 6	0.35	0.803	6.5	0.2139	96.13%	8.3	0.70	482	0.26	0.05	1.63	0.10	1.78	0.01	0.39	0.47	97.45	38.66	94.83	1.61	94.72	0.37
(Z57) zirc 7	0.81	0.474	15.9	0.5001	91.97%	3.5	3.55	232	0.15	0.05	1.74	0.10	1.89	0.01	0.20	0.76	115.56	41.03	95.58	1.72	94.78	0.19
(Z12) zirc 8	0.91	0.493	14.5	0.5607	98.72%	23.8	0.59	1463	0.16	0.05	0.47	0.10	0.56	0.01	0.15	0.65	93.08	11.19	94.74	0.50	94.80	0.14
(Z11) zirc 9	0.59	0.334	9.8	0.3622	96.04%	7.1	1.21	472	0.11	0.05	1.18	0.10	1.37	0.01	0.50	0.53	104.21	27.92	95.17	1.24	94.81	0.47
(Z59) zirc 10	1.07	0.490	16.8	0.6538	98.94%	28.8	0.56	1765	0.16	0.05	0.78	0.10	1.14	0.01	0.79	0.73	84.19	18.54	93.07	1.01	93.41	0.73
(Z16) zirc 11	0.27	0.715	5.7	0.1706	91.76%	3.6	1.24	226	0.23	0.05	2.39	0.10	2.59	0.01	0.48	0.48	122.88	56.28	96.77	2.39	95.72	0.46
(Z62) zirc 12	0.67	0.446	11.1	0.4190	97.77%	13.3	0.77	836	0.14	0.05	1.83	0.10	2.53	0.02	1.74	0.69	81.06	43.38	95.64	2.31	96.22	1.66
(Z14) zirc 13	0.37	0.768	8.0	0.2340	91.65%	3.6	1.72	223	0.25	0.05	2.33	0.10	2.50	0.02	0.27	0.67	100.04	55.11	96.54	2.31	96.40	0.26
(Z58) zirc 14	0.63	0.438	11.2	0.4327	98.29%	17.5	0.61	1094	0.14	0.05	0.53	0.11	0.68	0.02	0.29	0.66	103.02	12.52	104.59	0.67	104.66	0.30
(Z53) zirc 15	0.06	0.304	9.5	0.3785	98.56%	20.3	0.45	1295	0.09	0.07	0.49	1.59	1.09	0.16	0.94	0.89	971.83	9.94	968.03	6.78	966.35	8.45
(Z13) zirc 16	0.39	0.609	144.6	5.3593	99.55%	72.5	1.97	4128	0.18	0.11	0.14	5.08	0.33	0.33	0.23	0.93	1839.28	2.52	1833.16	2.78	1827.76	3.73

S-B2: Swenson 1H well (McMullen Co.) - 32 m (106 ft.) above Buda Limestone

	Compositional Parameters								Radiogenic Isotope Ratios								Isotopic Ages					
Sample	U (ng)	$\frac{Th}{U}$	Pb (pg)	$^{206}Pb^*$ x10^{-13} mol	mol % $^{206}Pb^*$	$\frac{Pb^*}{Pb_c}$	Pb_c (pg)	$\frac{^{206}Pb}{^{204}Pb}$	$\frac{^{208}Pb}{^{206}Pb}$	$\frac{^{207}Pb}{^{206}Pb}$	% err	$\frac{^{207}Pb}{^{235}U}$	% err	$\frac{^{206}Pb}{^{238}U}$	% err	corr. coef.	$\frac{^{207}Pb}{^{206}Pb}$	±	$\frac{^{207}Pb}{^{235}U}$	±	$\frac{^{206}Pb}{^{238}U}$	±
(a)	(b)	(c)	(b)	(d)	(d)	(d)	(d)	(e)	(f)	(f)	(g)	(f)	(g)	(f)	(g)	(f)	(g)	(h)	(g)	(h)	(g)	(h)
(Z41) zirc 1	2.80	0.517	45.5	1.7380	98.59%	21.6	2.02	1320	0.17	0.05	0.52	0.10	0.61	0.01	0.17	0.58	94.09	12.41	95.31	0.55	95.36	0.16
(Z27) zirc 2	1.31	0.644	22.1	0.8163	98.54%	21.6	0.98	1277	0.21	0.05	0.38	0.10	0.49	0.01	0.15	0.83	92.16	9.01	95.33	0.45	95.46	0.14
(Z42) zirc 3	5.12	0.504	82.0	3.1825	98.98%	29.8	2.67	1821	0.16	0.05	0.39	0.10	0.49	0.01	0.20	0.66	92.27	9.23	95.37	0.45	95.50	0.19
(Z61) zirc 4	1.74	0.524	28.9	1.0868	98.18%	16.7	1.63	1025	0.17	0.05	0.70	0.10	0.78	0.01	0.16	0.57	98.34	16.67	95.75	0.72	95.64	0.15
(Z46) zirc 5	0.84	0.663	16.0	0.5255	94.86%	5.9	2.30	363	0.21	0.05	1.48	0.10	1.60	0.01	0.18	0.71	98.02	34.98	95.74	1.46	95.64	0.17
(Z43) zirc 6	3.29	0.423	51.1	2.0499	99.37%	47.4	1.05	2952	0.14	0.05	0.51	0.10	0.59	0.01	0.21	0.52	95.35	12.06	95.63	0.54	95.64	0.20
(Z47) zirc 7	1.24	0.522	25.3	0.7698	91.25%	3.2	6.03	212	0.17	0.05	1.93	0.10	2.07	0.01	0.27	0.58	145.93	45.20	97.67	1.93	95.70	0.26
(Z30) zirc 8	1.32	0.691	22.4	0.8199	98.54%	21.9	0.98	1280	0.22	0.05	0.51	0.10	0.59	0.01	0.16	0.61	92.41	11.98	95.57	0.54	95.70	0.15

LC-B1: Lozier Canyon (Terrell Co.) - 50.5 m (165.7 ft.) above Buda Limestone

	Compositional Parameters								Radiogenic Isotope Ratios								Isotopic Ages					
Sample	U (ng)	$\frac{Th}{U}$	Pb (pg)	$^{206}Pb^*$ x10^{-13} mol	mol % $^{206}Pb^*$	$\frac{Pb^*}{Pb_c}$	Pb_c (pg)	$\frac{^{206}Pb}{^{204}Pb}$	$\frac{^{208}Pb}{^{206}Pb}$	$\frac{^{207}Pb}{^{206}Pb}$	% err	$\frac{^{207}Pb}{^{235}U}$	% err	$\frac{^{206}Pb}{^{238}U}$	% err	corr. coef.	$\frac{^{207}Pb}{^{206}Pb}$	±	$\frac{^{207}Pb}{^{235}U}$	±	$\frac{^{206}Pb}{^{238}U}$	±
(a)	(b)	(c)	(b)	(d)	(d)	(d)	(d)	(e)	(f)	(f)	(g)	(f)	(g)	(f)	(g)	(f)	(g)	(h)	(g)	(h)	(g)	(h)
(Z7) zirc 1	1.16	0.554	18.3	0.6823	98.17%	16.7	1.03	1018	0.18	0.05	0.32	0.09	0.46	0.01	0.11	1.18	95.51	7.56	90.31	0.40	90.12	0.10
(Z4) zirc 2	1.14	0.551	19.6	0.6735	95.48%	6.6	2.58	413	0.18	0.05	1.11	0.09	1.21	0.01	0.17	0.68	97.62	26.16	90.67	1.05	90.40	0.15
(Z2) zirc 3	2.95	0.546	46.5	1.7345	98.06%	15.7	2.79	959	0.17	0.05	0.53	0.09	0.62	0.01	0.15	0.69	73.24	12.55	89.83	0.53	90.45	0.14
(Z78) zirc 4	1.08	0.479	16.4	0.6384	98.85%	26.4	0.60	1628	0.15	0.05	0.43	0.09	0.53	0.01	0.19	0.65	90.00	10.26	90.69	0.46	90.72	0.17
(Z3) zirc 5	1.68	0.562	26.3	0.9929	98.62%	22.4	1.12	1354	0.18	0.05	0.46	0.09	0.55	0.01	0.17	0.64	88.99	10.82	90.69	0.48	90.76	0.16
(Z8) zirc 6	0.25	0.561	3.9	0.1435	97.76%	13.6	0.27	831	0.18	0.05	0.34	0.09	0.52	0.01	0.15	1.11	85.46	8.04	89.11	0.44	89.24	0.14
(Z1) zirc 7	6.54	0.569	100.4	3.8030	98.77%	25.1	3.85	1516	0.18	0.05	0.44	0.09	1.45	0.01	1.36	0.95	93.06	10.51	89.42	1.24	89.28	1.21

LC-B2: Lozier Canyon (Terrell Co.) - 48.5 m (159.1 ft.) above Buda Limestone

	Compositional Parameters								Radiogenic Isotope Ratios								Isotopic Ages					
Sample	U (ng)	Th/U	Pb (pg)	$^{206}Pb^*$ x10^{-13} mol	mol % $^{206}Pb^*$	Pb^*/Pb_c	Pb_c (pg)	$^{206}Pb/^{204}Pb$	$^{208}Pb/^{206}Pb$	$^{207}Pb/^{206}Pb$	% err	$^{207}Pb/^{235}U$	% err	$^{206}Pb/^{238}U$	% err	corr. coef.	$^{207}Pb/^{206}Pb$	±	$^{207}Pb/^{235}U$	±	$^{206}Pb/^{238}U$	±
(a)	(b)	(c)	(b)	(d)	(d)	(d)	(d)	(e)	(f)	(f)	(g)	(f)	(g)	(f)	(g)	(f)	(g)	(h)	(g)	(h)	(g)	(h)
(15) zirc 1	1.37	0.569	21.7	0.8039	97.94%	14.9	1.37	907	0.18	0.05	0.57	0.09	1.17	0.01	1.01	0.88	24.75	13.56	87.96	0.99	90.31	0.90
(16) zirc 2	0.89	0.455	14.4	0.5259	96.68%	8.8	1.46	561	0.15	0.05	1.01	0.09	1.11	0.01	0.18	0.62	73.71	24.08	89.80	0.96	90.41	0.16
(18) zirc 3	0.85	0.694	14.5	0.5021	96.73%	9.6	1.37	571	0.22	0.05	0.80	0.09	0.91	0.01	0.12	0.96	58.72	18.98	89.46	0.78	90.61	0.11
(Z79) zirc 4	2.59	1.022	45.6	1.5314	98.31%	20.5	2.13	1106	0.33	0.05	0.51	0.09	0.68	0.01	0.35	0.67	85.34	12.13	90.50	0.59	90.70	0.32
(Z81) zirc 5	1.44	0.629	22.9	0.8487	98.55%	21.7	1.01	1290	0.20	0.05	0.74	0.09	0.83	0.01	0.27	0.49	78.84	17.47	90.30	0.72	90.73	0.24
(13) zirc 6	1.25	0.509	19.6	0.7378	98.03%	15.3	1.20	945	0.16	0.05	0.05	0.09	0.37	0.01	0.05	3.53	84.70	1.11	90.51	0.32	90.73	0.05
(Z80) zirc 7	2.33	0.471	35.0	1.3748	99.06%	32.4	1.05	1994	0.15	0.05	0.39	0.09	0.57	0.01	0.35	0.73	86.71	9.27	90.62	0.49	90.77	0.31
(9) zirc 8	1.27	0.560	19.8	0.7254	97.53%	12.4	1.49	756	0.18	0.05	#NUM!	0.09	0.90	0.01	0.84	#NUM!	70.61	#NUM!	87.09	0.75	87.70	0.74
(17) zirc 9	1.53	0.524	26.1	0.8776	94.58%	5.4	4.09	344	0.17	0.05	1.08	0.09	1.25	0.01	0.38	0.55	58.51	25.85	86.91	1.04	87.95	0.33
(Z82) zirc 10	0.44	0.477	23.5	0.2574	55.20%	0.4	17.14	41	0.15	0.05	7.37	0.09	7.70	0.01	1.00	0.39	101.28	174.26	89.57	6.60	89.13	0.88
(14) zirc 11	1.54	0.555	23.4	0.8982	99.12%	35.2	0.65	2117	0.18	0.05	#NUM!	0.09	0.30	0.01	0.27	#NUM!	80.46	#NUM!	89.44	0.26	89.77	0.24
(11) zirc 12	2.98	0.525	46.2	1.7450	98.32%	18.1	2.41	1110	0.17	0.05	0.14	0.09	0.38	0.01	0.18	1.14	93.11	3.38	90.00	0.33	89.88	0.16
(12) zirc 13	2.72	0.789	44.6	1.5926	98.57%	22.8	1.87	1302	0.25	0.05	#NUM!	0.09	0.26	0.01	0.13	#NUM!	74.50	#NUM!	89.39	0.23	89.95	0.11
(Z83) zirc 14	1.02	0.520	18.1	0.6052	94.38%	5.2	2.92	332	0.17	0.05	1.47	0.09	1.59	0.01	0.26	0.55	81.56	34.76	90.98	1.39	91.34	0.23
(10) zirc 15	1.42	0.548	23.2	0.8464	97.35%	11.5	1.86	705	0.18	0.05	0.32	0.09	1.26	0.01	1.19	0.97	62.68	7.69	90.67	1.10	91.74	1.09

(a) Z1, Z2 etc. are internal laboratory labels for fractions composed of single zircon grain aliquots; all fractions were annealed and chemically abraded after Mattinson (2005).

(b) U and total Pb content of zircon remnants after chemical abrasion.

(c) Model Th/U ratio calculated from radiogenic 208Pb/206Pb ratio and 207Pb/235U age.

(d) Pb* and Pbc represent radiogenic and common Pb, respectively; mol % 206Pb* with respect to radiogenic, blank and initial common Pb.

(e) Measured ratio corrected for spike and fractionation only.
Daly Pb analyses corrected for 0.22%/AMU mass bias based on repeat analysis of NBS-981.Faraday U analyses corrected for mass bias based on measured 233U/235U ratio.

(f) Corrected for fractionation, spike, and common Pb; up to 1 pg of common Pb was assumed to be procedural blank: 206Pb/204Pb = 18.66 ± 0.60%; 207Pb/204Pb = 15.54 ± 0.25%;
208Pb/204Pb = 37.62 ± 0.55% (all uncertainties 1-sigma). Excess over blank was assigned to initial common Pb.

(g) Errors are 2-sigma, propagated using the algorithms of Schmitz and Schoene (2007) and Crowley et al. (2007).

(h) Calculate ages are based on the decay constants of Jaffey et al. (1971).

(x) Analysis excluded from age calculation due to inferred: (1) xenocryst or anticryst component, (2) excessive Pb-loss, or (3) unusably imprecise analysis.

AC-B10 ~ 0.5 m (1.5 ft) above Buda Limestone

		Compositional Parameters								Radiogenic Isotope Ratios								Isotopic Ages					
Sample (a)	n= (b)	U (ng) (c)	Pb (pg) (c)	Th/U (d)	$^{206}Pb^*$ x10^{-13} mol (e)	mol % $^{206}Pb^*$ (e)	Pb^*/Pb_c (e)	Pb_c (pg) (e)	$^{206}Pb/^{204}Pb$ (f)	$^{208}Pb/^{206}Pb$ (g)	$^{207}Pb/^{206}Pb$ (g)	% err (h)	$^{207}Pb/^{235}U$ (g)	% err (h)	$^{206}Pb/^{238}U$ (g)	% err (h)	corr. coef. (g)	$^{207}Pb/^{206}Pb$ (h)	± (i)	$^{207}Pb/^{235}U$ (h)	± (i)	$^{206}Pb/^{238}U$ (h)	± (i)
(Z6)	1	0.09	2.5	0.731	0.0540	80.55%	1.4	1.05	96	0.23	0.05	13.45	0.10	13.73	0.01	0.87	0.36	165.32	314.14	97.84	12.81	95.09	0.82
(Z9)	1	0.08	6.2	0.613	0.0507	45.93%	0.3	4.88	34	0.20	0.05	26.84	0.10	27.49	0.01	1.52	0.45	84.44	636.53	94.99	24.93	95.41	1.44
(Z41)	2	0.41	7.4	0.677	0.2531	96.17%	8.1	0.82	487	0.22	0.05	1.13	0.10	1.27	0.01	0.39	0.50	88.89	26.68	95.60	1.16	95.87	0.37
(Z55)	1	0.10	4.6	0.762	0.0608	62.44%	0.5	2.97	50	0.24	0.05	21.78	0.10	22.25	0.02	1.22	0.41	152.13	509.98	98.25	20.83	96.04	1.16
(Z5)	1	0.18	4.7	0.647	0.1128	83.81%	1.7	1.76	115	0.21	0.05	6.69	0.10	7.01	0.02	0.44	0.74	160.59	156.45	98.65	6.59	96.11	0.42
(Z81)	1	0.06	2.1	0.863	0.0403	77.30%	1.2	0.96	82	0.28	0.05	11.76	0.10	12.28	0.02	1.90	0.35	151.60	275.36	98.48	11.52	96.30	1.82
(Z2)	1	0.09	3.3	1.061	0.0553	72.81%	0.9	1.67	69	0.34	0.04	12.99	0.09	13.42	0.02	1.37	0.36	-134.49	321.13	87.92	11.30	96.32	1.31
(Z43)	2	0.29	8.2	0.631	0.1830	81.05%	1.4	3.48	98	0.20	0.05	10.97	0.10	11.19	0.02	0.87	0.29	49.35	261.92	94.54	10.10	96.34	0.83
(Z3)	3	0.76	13.5	0.295	0.4746	94.34%	4.8	2.31	330	0.09	0.05	2.20	0.10	2.96	0.02	1.78	0.67	66.43	52.43	95.20	2.69	96.35	1.70
(Z26)	1	0.08	2.4	0.490	0.0476	76.55%	1.0	1.18	80	0.16	0.05	10.36	0.10	10.71	0.02	0.80	0.46	48.90	247.39	94.72	9.68	96.54	0.77
(Z27)	1	0.17	4.3	0.760	0.1066	85.27%	1.9	1.49	127	0.24	0.05	6.19	0.10	6.51	0.02	0.42	0.78	39.10	147.95	94.38	5.86	96.58	0.40
(Z10)	1	0.24	5.6	0.901	0.1531	90.31%	3.2	1.33	192	0.29	0.05	8.18	0.10	8.50	0.02	0.71	0.48	96.16	193.54	96.60	7.83	96.61	0.68
(Z52)	1	0.23	4.5	0.629	0.1449	93.68%	4.7	0.79	295	0.20	0.04	4.69	0.09	5.14	0.02	1.57	0.42	-283.71	119.54	83.37	4.11	96.71	1.51
(Z30)	1	0.22	4.7	0.469	0.1372	89.11%	2.5	1.36	171	0.15	0.05	4.20	0.10	4.46	0.02	0.47	0.59	67.79	99.93	95.64	4.07	96.77	0.45
(ZR1)	2	0.32	7.0	0.863	0.2040	91.93%	3.9	1.45	231	0.28	0.05	2.33	0.10	2.54	0.02	0.42	0.56	119.24	54.79	97.67	2.36	96.79	0.40
(Z9)	1	0.11	3.0	0.577	0.0689	81.63%	1.4	1.25	102	0.18	0.05	8.79	0.10	9.07	0.02	0.41	0.67	139.23	206.41	98.49	8.51	96.81	0.40
(Z6)	1	0.09	5.4	1.023	0.0579	55.79%	0.4	3.74	42	0.33	0.05	17.05	0.10	17.59	0.02	1.10	0.52	112.19	402.23	97.51	16.35	96.91	1.06
(Z19)	1	0.16	3.4	0.698	0.0987	90.65%	3.1	0.82	199	0.22	0.05	4.05	0.10	4.32	0.02	0.85	0.41	63.52	96.33	95.74	3.95	97.04	0.82
(Z53)	1	0.15	3.8	0.683	0.0984	87.07%	2.2	1.18	144	0.22	0.05	4.18	0.10	4.65	0.02	1.51	0.46	66.33	99.36	96.34	4.27	97.56	1.46
(Z10)	1	0.09	6.5	1.053	0.0578	49.14%	0.3	4.89	37	0.34	0.05	35.62	0.10	36.46	0.01	4.28	0.25	142.58	835.59	96.58	33.59	94.72	4.03
(Z87)	1	0.05	2.3	0.629	0.0297	61.68%	0.5	1.49	49	0.20	0.04	61.69	0.09	62.04	0.01	2.71	0.15	-60.75	1503.84	89.91	53.39	95.68	2.57
(Z40)	1	0.05	4.4	0.584	0.0328	42.80%	0.2	3.57	33	0.19	0.05	52.46	0.10	53.11	0.01	2.82	0.26	73.94	1246.57	95.05	48.19	95.89	2.68
(Z55)	1	0.04	1.6	0.611	0.0257	69.66%	0.7	0.90	61	0.20	0.04	48.93	0.08	49.29	0.01	3.16	0.15	-311.27	1252.86	81.90	38.79	95.97	3.01
(Z26)	1	0.11	4.4	0.676	0.0721	69.65%	0.7	2.55	61	0.22	0.04	11.40	0.09	14.47	0.02	8.32	0.62	-111.84	280.53	88.78	12.30	96.41	7.96
(Z8)	1	0.10	5.7	0.783	0.0609	55.08%	0.4	4.05	41	0.25	0.05	36.55	0.10	36.97	0.02	1.57	0.28	45.19	873.25	94.48	33.35	96.45	1.50
(Z25)	1	0.09	2.9	0.819	0.0576	77.08%	1.1	1.39	81	0.26	0.04	12.91	0.09	13.97	0.02	4.44	0.39	-169.53	321.51	86.91	11.64	96.52	4.26
(Z36)	1	0.06	2.9	0.638	0.0361	59.13%	0.5	2.02	46	0.20	0.05	43.64	0.10	44.59	0.02	5.59	0.23	64.57	1038.78	95.39	40.60	96.62	5.36
(Z59)	1	0.09	3.1	0.622	0.0559	73.09%	0.9	1.66	69	0.20	0.04	45.66	0.09	46.49	0.02	2.85	0.32	-182.57	1139.59	86.88	38.71	96.98	2.74
(Z31)	1	0.11	3.1	0.589	0.0708	81.79%	1.4	1.27	102	0.19	0.04	10.69	0.09	11.21	0.02	2.04	0.34	-286.68	272.44	84.36	9.08	98.00	1.98
(BT)	1	0.04	1.6	0.700	0.0233	65.73%	0.6	0.98	54	0.22	0.03	163.45	0.07	164.57	0.02	15.27	0.12	-884.54	4721.00	69.96	111.26	100.60	15.24
(Z20)	1	0.21	4.6	0.382	0.1395	90.64%	2.9	1.17	199	0.12	0.06	2.34	0.13	2.52	0.02	0.29	0.67	568.75	50.90	122.86	2.92	101.05	0.29
(Z65)	1	0.17	3.9	0.783	0.1157	92.28%	4.0	0.78	242	0.25	0.05	3.67	0.10	5.61	0.02	4.07	0.76	48.41	87.70	99.37	5.31	101.50	4.09
(Z21)	1	0.07	3.1	0.817	0.0541	72.87%	0.9	1.63	69	0.26	0.05	11.97	0.13	13.73	0.02	6.03	0.49	117.47	282.06	126.71	16.35	127.20	7.60
(BB)	1	0.32	8.1	0.756	0.2753	96.69%	9.6	0.76	563	0.24	0.05	1.18	0.14	1.34	0.02	0.44	0.49	112.01	27.91	129.32	1.62	130.27	0.57
(BC)	1	0.34	26.8	0.389	1.0605	99.28%	41.9	0.63	2575	0.12	0.08	0.18	0.78	0.57	0.07	0.50	0.95	1105.26	3.59	583.66	2.54	458.73	2.23
(Z23)	1	0.32	30.3	0.374	1.1925	99.20%	37.8	0.78	2322	0.12	0.08	0.19	1.04	2.13	0.09	2.11	1.00	1280.42	3.61	726.11	11.05	559.91	11.33

AC-9 ~2.9 m (9.5 ft) above Buda Limestone

					Compositional Parameters					Radiogenic Isotope Ratios								Isotopic Ages					
Sample (a)	n= (b)	U (ng) (c)	Pb (pg) (c)	Th/U (d)	$^{206}Pb^*$ x10^{-13} mol (e)	mol % $^{206}Pb^*$ (e)	Pb^*/Pb_c (e)	Pb_c (pg) (e)	$^{206}Pb/^{204}Pb$ (f)	$^{208}Pb/^{206}Pb$ (g)	$^{207}Pb/^{206}Pb$ (g)	% err (h)	$^{207}Pb/^{235}U$ (g)	% err (h)	$^{206}Pb/^{238}U$ (g)	% err (h)	corr. coef. (g)	$^{207}Pb/^{206}Pb$ (h)	± (i)	$^{207}Pb/^{235}U$ (h)	± (i)	$^{206}Pb/^{238}U$ (h)	± (i)
(Z10)	2	0.49	9.5	1.053	0.3080	97.29%	12.7	0.69	688	0.34	0.05	0.74	0.10	0.86	0.02	0.14	0.92	99.79	17.42	96.61	0.79	96.48	0.13
(Z11)	1	0.36	7.3	0.555	0.2274	92.00%	3.6	1.60	233	0.18	0.05	2.30	0.10	2.45	0.02	0.34	0.52	97.65	54.36	96.61	2.26	96.56	0.32
(Z12)	1	0.10	2.7	0.685	0.0627	82.62%	1.5	1.07	107	0.22	0.05	7.23	0.10	7.57	0.02	0.60	0.60	96.57	171.12	96.44	6.97	96.43	0.57
(Z13)	1	0.06	1.6	0.392	0.0352	78.95%	1.1	0.76	89	0.13	0.05	13.64	0.10	13.88	0.01	0.57	0.44	109.79	321.97	96.35	12.76	95.81	0.55
(Z15)	1	0.12	2.3	0.445	0.0739	92.10%	3.5	0.51	236	0.14	0.05	2.82	0.10	2.98	0.02	0.29	0.57	60.39	67.22	94.91	2.70	96.29	0.28
(Z33)	1	0.10	2.2	0.759	0.0599	88.54%	2.5	0.63	163	0.24	0.05	4.79	0.10	5.13	0.02	1.13	0.40	65.09	113.94	95.16	4.66	96.36	1.08
(Z3)	1	0.20	7.8	0.672	0.1238	68.90%	0.7	4.56	60	0.22	0.05	7.59	0.10	8.00	0.01	0.80	0.54	83.01	180.06	95.42	7.28	95.92	0.77
(Z61)	1	0.36	12.1	0.690	0.2281	75.34%	1.0	6.10	75	0.22	0.05	5.94	0.10	6.77	0.02	2.63	0.49	55.46	141.61	95.56	6.18	97.17	2.53

AC-B8 ~18 m (59 ft) above Buda Limestone

					Compositional Parameters					Radiogenic Isotope Ratios								Isotopic Ages					
Sample (a)	n= (b)	U (ng) (c)	Pb (pg) (c)	Th/U (d)	$^{206}Pb^*$ x10^{-13} mol (e)	mol % $^{206}Pb^*$ (e)	Pb^*/Pb_c (e)	Pb_c (pg) (e)	$^{206}Pb/^{204}Pb$ (f)	$^{208}Pb/^{206}Pb$ (g)	$^{207}Pb/^{206}Pb$ (g)	% err (h)	$^{207}Pb/^{235}U$ (g)	% err (h)	$^{206}Pb/^{238}U$ (g)	% err (h)	corr. coef. (g)	$^{207}Pb/^{206}Pb$ (h)	± (i)	$^{207}Pb/^{235}U$ (h)	± (i)	$^{206}Pb/^{238}U$ (h)	± (i)
(Z3)	4	1.46	25.7	0.488	0.9057	95.79%	7.0	3.23	443	0.16	0.05	1.09	0.10	1.20	0.01	0.17	0.67	77.63	25.97	94.54	1.08	95.21	0.16
(Z12)	2	0.56	9.6	0.402	0.3466	95.94%	7.1	1.19	459	0.13	0.05	1.52	0.09	1.63	0.01	0.24	0.52	-10.66	36.61	91.40	1.42	95.35	0.23
(Z10)	3	1.25	19.7	0.413	0.7771	98.75%	23.7	0.80	1492	0.13	0.05	0.53	0.10	0.62	0.01	0.18	0.58	13.48	12.85	92.34	0.55	95.42	0.17
(Z1)	3	0.87	15.5	0.449	0.5420	95.34%	6.2	2.14	400	0.14	0.05	1.45	0.10	1.56	0.01	0.23	0.54	92.87	34.44	95.38	1.42	95.48	0.21
(Z7)	1	0.29	5.0	0.395	0.1781	95.59%	6.5	0.66	423	0.13	0.05	2.82	0.09	2.95	0.01	0.46	0.35	-35.34	68.46	90.65	2.56	95.50	0.43
(Z11)	1	0.50	8.9	0.399	0.3136	95.22%	6.0	1.27	390	0.13	0.05	1.91	0.09	2.09	0.01	0.55	0.44	-53.76	46.58	89.99	1.80	95.50	0.52
(Z5)	1	0.21	4.4	0.591	0.1318	91.18%	3.3	1.03	211	0.19	0.05	4.71	0.10	4.94	0.01	0.55	0.46	43.97	112.66	93.57	4.42	95.52	0.52
(Z6)	1	0.55	9.7	0.778	0.3417	98.09%	17.0	0.54	975	0.25	0.05	0.67	0.10	0.78	0.01	0.18	0.67	81.58	15.94	95.01	0.70	95.55	0.17
(Z4)	1	0.40	8.5	0.579	0.2528	90.64%	3.0	2.11	199	0.19	0.05	2.47	0.10	2.64	0.02	0.25	0.70	92.89	58.46	95.89	2.41	96.01	0.24
(Z2)	1	0.36	7.2	0.530	0.2240	92.01%	3.6	1.57	234	0.17	0.05	2.29	0.10	2.46	0.02	0.28	0.63	87.09	54.28	95.99	2.25	96.34	0.27
(Z8)	2	0.98	16.6	0.395	0.6501	98.40%	18.4	0.86	1163	0.13	0.05	0.60	0.11	0.71	0.02	0.23	0.59	219.89	13.99	107.13	0.72	102.12	0.23

AC-B7 ~ 19.5m (64 ft) above Buda Limestone

Compositional Parameters										Radiogenic Isotope Ratios								Isotopic Ages					
Sample (a)	n= (b)	U (ng) (c)	Pb (pg) (c)	$\frac{Th}{U}$ (d)	$^{206}Pb^*$ x10^{-13} mol (e)	mol % $^{206}Pb^*$ (e)	$\frac{Pb^*}{Pb_c}$ (e)	Pb_c (pg) (e)	$\frac{^{206}Pb}{^{204}Pb}$ (f)	$\frac{^{208}Pb}{^{206}Pb}$ (g)	$\frac{^{207}Pb}{^{206}Pb}$ (g)	% err (h)	$\frac{^{207}Pb}{^{235}U}$ (g)	% err (h)	$\frac{^{206}Pb}{^{238}U}$ (g)	% err (h)	corr. coef. (g)	$\frac{^{207}Pb}{^{206}Pb}$ (h)	± (i)	$\frac{^{207}Pb}{^{235}U}$ (h)	± (i)	$\frac{^{206}Pb}{^{238}U}$ (h)	± (i)
(Z44)	1	0.30	10.4	0.373	0.1840	71.53%	0.7	5.98	65	0.12	0.04	8.42	0.09	8.86	0.01	0.90	0.52	-156.82	209.16	86.03	7.31	95.02	0.85
(Z42)	1	0.89	15.9	0.540	0.5509	95.69%	6.9	2.01	433	0.17	0.05	2.65	0.10	2.82	0.01	0.49	0.42	103.47	62.58	95.67	2.57	95.35	0.46
(Z31)	1	0.88	17.8	0.453	0.5491	91.33%	3.2	4.25	215	0.15	0.05	1.70	0.10	1.84	0.01	0.23	0.65	97.69	40.25	95.59	1.68	95.51	0.22
(Z57)	1	0.43	13.1	0.448	0.2692	77.22%	1.0	6.49	82	0.14	0.05	5.27	0.10	5.58	0.01	0.44	0.73	73.50	125.28	94.70	5.05	95.54	0.41
(Z46)	1	0.46	8.5	0.509	0.2838	94.39%	5.2	1.36	333	0.16	0.05	3.43	0.10	3.70	0.01	0.42	0.66	95.34	81.20	95.56	3.37	95.57	0.40
(Z20)	1	0.78	16.8	0.530	0.4876	89.70%	2.7	4.56	181	0.17	0.05	1.76	0.10	1.90	0.01	0.21	0.74	86.85	41.62	95.29	1.73	95.63	0.20
(Z30)	1	0.59	10.5	0.423	0.3673	95.06%	5.8	1.55	377	0.14	0.05	1.36	0.10	1.47	0.01	0.21	0.58	95.27	32.09	95.62	1.34	95.63	0.20
(Z32)	1	0.59	10.4	0.446	0.3669	95.42%	6.3	1.42	408	0.14	0.05	1.22	0.10	1.36	0.01	0.26	0.58	99.16	28.96	95.78	1.24	95.64	0.25
(Z59)	1	0.17	4.1	0.464	0.1047	85.20%	1.8	1.47	126	0.15	0.05	4.44	0.10	4.70	0.02	0.36	0.73	95.40	105.00	96.34	4.32	96.38	0.35
(Z58)	1	0.20	4.4	0.572	0.1268	89.57%	2.7	1.19	179	0.18	0.05	3.19	0.10	3.48	0.02	0.87	0.45	69.05	75.89	95.61	3.18	96.68	0.84
(Z54)	1	0.51	9.5	0.389	0.3328	94.90%	5.6	1.45	366	0.12	0.05	3.31	0.11	3.51	0.02	0.43	0.52	180.31	77.00	102.57	3.42	99.25	0.42
(Z56)	1	0.25	14.4	0.704	0.1600	56.24%	0.4	10.20	42	0.23	0.05	7.27	0.11	7.62	0.02	0.84	0.46	200.31	168.78	104.12	7.54	99.96	0.83

AC-B7 ~ 19.5m (64 ft) above Buda Limestone

		Compositional Parameters								Radiogenic Isotope Ratios								Isotopic Ages					
Sample (a)	n= (b)	U (ng) (c)	Pb (pg) (c)	Th/U (d)	$^{206}Pb^*$ x10^{-13} mol (e)	mol % $^{206}Pb^*$ (e)	Pb^*/Pb_c (e)	Pb_c (pg) (e)	$^{206}Pb/^{204}Pb$ (f)	$^{208}Pb/^{206}Pb$ (g)	$^{207}Pb/^{206}Pb$ (g)	% err (h)	$^{207}Pb/^{235}U$ (g)	% err (h)	$^{206}Pb/^{238}U$ (g)	% err (h)	corr. coef. (g)	$^{207}Pb/^{206}Pb$ (h)	± (i)	$^{207}Pb/^{235}U$ (h)	± (i)	$^{206}Pb/^{238}U$ (h)	± (i)
(Z44)	1	0.30	10.4	0.373	0.1840	71.53%	0.7	5.98	65	0.12	0.04	8.42	0.09	8.86	0.01	0.90	0.52	-156.82	209.16	86.03	7.31	95.02	0.85
(Z42)	1	0.89	15.9	0.540	0.5509	95.69%	6.9	2.01	433	0.17	0.05	2.65	0.10	2.82	0.01	0.49	0.42	103.47	62.58	95.67	2.57	95.35	0.46
(Z31)	1	0.88	17.8	0.453	0.5491	91.33%	3.2	4.25	215	0.15	0.05	1.70	0.10	1.84	0.01	0.23	0.65	97.69	40.25	95.59	1.68	95.51	0.22
(Z57)	1	0.43	13.1	0.448	0.2692	77.22%	1.0	6.49	82	0.14	0.05	5.27	0.10	5.58	0.01	0.44	0.73	73.50	125.28	94.70	5.05	95.54	0.41
(Z46)	1	0.46	8.5	0.509	0.2838	94.39%	5.2	1.36	333	0.16	0.05	3.43	0.10	3.70	0.01	0.42	0.66	95.34	81.20	95.56	3.37	95.57	0.40
(Z20)	1	0.78	16.8	0.530	0.4876	89.70%	2.7	4.56	181	0.17	0.05	1.76	0.10	1.90	0.01	0.21	0.74	86.85	41.62	95.29	1.73	95.63	0.20
(Z30)	1	0.59	10.5	0.423	0.3673	95.06%	5.8	1.55	377	0.14	0.05	1.36	0.10	1.47	0.01	0.21	0.58	95.27	32.09	95.62	1.34	95.63	0.20
(Z32)	1	0.59	10.4	0.446	0.3669	95.42%	6.3	1.42	408	0.14	0.05	1.22	0.10	1.36	0.01	0.26	0.58	99.16	28.96	95.78	1.24	95.64	0.25
(Z59)	1	0.17	4.1	0.464	0.1047	85.20%	1.8	1.47	126	0.15	0.05	4.44	0.10	4.70	0.02	0.36	0.73	95.40	105.00	96.34	4.32	96.38	0.35
(Z58)	1	0.20	4.4	0.572	0.1268	89.57%	2.7	1.19	179	0.18	0.05	3.19	0.10	3.48	0.02	0.87	0.45	69.05	75.89	95.61	3.18	96.68	0.84
(Z54)	1	0.51	9.5	0.389	0.3328	94.90%	5.6	1.45	366	0.12	0.05	3.31	0.11	3.51	0.02	0.43	0.52	180.31	77.00	102.57	3.42	99.25	0.42
(Z56)	1	0.25	14.4	0.704	0.1600	56.24%	0.4	10.20	42	0.23	0.05	7.27	0.11	7.62	0.02	0.84	0.46	200.31	168.78	104.12	7.54	99.96	0.83

AC-B6 ~19.7 m (64.5 ft) above Buda Limestone

		Compositional Parameters								Radiogenic Isotope Ratios								Isotopic Ages					
Sample (a)	n= (b)	U (ng) (c)	Pb (pg) (c)	Th/U (d)	$^{206}Pb^*$ x10^{-13} mol (e)	mol % $^{206}Pb^*$ (e)	Pb^*/Pb_c (e)	Pb_c (pg) (e)	$^{206}Pb/^{204}Pb$ (f)	$^{208}Pb/^{206}Pb$ (g)	$^{207}Pb/^{206}Pb$ (g)	% err (h)	$^{207}Pb/^{235}U$ (g)	% err (h)	$^{206}Pb/^{238}U$ (g)	% err (h)	corr. coef. (g)	$^{207}Pb/^{206}Pb$ (h)	± (i)	$^{207}Pb/^{235}U$ (h)	± (i)	$^{206}Pb/^{238}U$ (h)	± (i)
(Z82)	1	0.15	6.3	0.372	0.0960	65.96%	0.6	4.03	55	0.12	0.05	13.14	0.10	13.66	0.01	1.17	0.48	91.66	311.12	95.18	12.41	95.32	1.11
(Z53)	1	0.17	6.8	0.356	0.1026	65.68%	0.6	4.37	54	0.11	0.05	10.19	0.10	10.61	0.01	0.63	0.68	82.98	241.62	94.93	9.61	95.40	0.60
(Z30)	1	0.32	6.6	0.366	0.1974	89.63%	2.6	1.85	180	0.12	0.05	4.53	0.10	4.75	0.01	0.51	0.48	99.65	107.18	95.60	4.34	95.43	0.48
(Z81)	1	0.37	7.3	0.422	0.2322	91.94%	3.4	1.65	231	0.14	0.05	2.42	0.10	2.62	0.01	0.58	0.45	58.25	57.57	94.08	2.36	95.50	0.55
(Z41)	2	0.80	14.9	0.490	0.5008	94.20%	5.0	2.49	322	0.16	0.05	1.75	0.10	1.93	0.01	0.49	0.47	92.55	41.52	95.41	1.76	95.52	0.46
(Z34)	3	1.01	16.4	0.380	0.6259	97.51%	11.7	1.29	749	0.12	0.05	1.49	0.10	1.54	0.01	0.32	0.25	171.49	34.74	98.58	1.44	95.59	0.30
(Z49)	1	1.42	26.4	0.446	0.8866	94.01%	4.7	4.61	310	0.14	0.05	2.65	0.10	2.89	0.01	0.31	0.78	96.31	62.74	95.68	2.63	95.65	0.29
(Z33)	1	0.14	4.5	0.575	0.0879	75.84%	1.0	2.27	77	0.18	0.05	14.24	0.10	14.58	0.01	1.13	0.34	78.41	338.04	95.05	13.23	95.72	1.08
(Z37)	1	0.06	2.0	0.413	0.0378	73.30%	0.8	1.11	70	0.13	0.05	15.59	0.10	16.00	0.01	1.26	0.36	42.28	372.75	93.70	14.32	95.73	1.19
(Z33)	1	0.19	3.6	0.376	0.1162	91.73%	3.3	0.85	226	0.12	0.05	3.64	0.10	3.80	0.01	0.50	0.39	183.58	84.76	99.28	3.60	95.80	0.47
(Z40)	1	0.35	6.8	0.425	0.2158	91.86%	3.4	1.55	229	0.14	0.05	2.77	0.10	3.02	0.01	0.59	0.50	106.26	65.45	96.25	2.77	95.85	0.56
(Z61)	1	0.22	6.4	0.376	0.1356	78.06%	1.1	3.09	85	0.12	0.05	5.99	0.10	6.33	0.01	0.44	0.79	36.75	143.39	92.78	5.61	94.97	0.41
(Z1)	3	0.92	18.7	0.381	0.5762	90.73%	2.9	4.80	201	0.12	0.05	1.54	0.10	1.68	0.02	0.20	0.71	110.50	36.36	96.59	1.55	96.03	0.19
(Z2)	1	0.29	6.2	0.561	0.1840	90.44%	3.0	1.57	195	0.18	0.05	2.60	0.10	2.78	0.02	0.22	0.84	84.67	61.70	95.65	2.54	96.09	0.21
(Z31)	2	0.55	10.2	0.563	0.3448	95.08%	6.1	1.44	379	0.18	0.05	1.58	0.10	1.68	0.02	0.24	0.48	165.48	37.00	98.84	1.59	96.10	0.22
(Z2)	1	0.09	3.2	1.067	0.0552	72.79%	0.9	1.67	69	0.34	0.05	14.70	0.09	15.07	0.02	1.32	0.32	-52.72	357.69	90.58	13.06	96.11	1.26
(Z3)	2	0.52	10.3	0.486	0.3245	92.08%	3.6	2.26	236	0.16	0.05	2.07	0.10	2.23	0.02	0.18	0.90	92.29	49.11	96.03	2.04	96.18	0.17
(Z51)	1	0.15	4.3	0.393	0.0960	79.65%	1.2	1.98	92	0.13	0.05	7.26	0.10	7.63	0.02	0.50	0.75	16.52	174.41	93.21	6.79	96.24	0.48
(Z4)	1	0.31	6.3	0.414	0.1918	90.74%	2.9	1.58	201	0.13	0.05	2.68	0.10	2.86	0.02	0.22	0.85	91.11	63.39	96.14	2.62	96.34	0.21
(Z52)	1	0.28	6.1	0.481	0.1753	88.77%	2.4	1.79	166	0.15	0.05	3.12	0.10	3.33	0.02	0.22	0.91	44.50	74.66	94.38	3.00	96.36	0.21
(Z61)	4	0.70	24.2	0.360	0.7221	90.66%	3.0	6.08	199	0.11	0.10	0.82	0.34	0.98	0.02	0.23	0.71	1618.71	15.34	296.40	2.51	157.02	0.36

AC-B5 ~ 24.4 m (80 ft) above Buda Limestone

		Compositional Parameters								Radiogenic Isotope Ratios								Isotopic Ages					
Sample (a)	n= (b)	U (ng) (c)	Pb (pg) (c)	Th/U (d)	$^{206}Pb^*$ x10^{-13} mol (e)	mol % $^{206}Pb^*$ (e)	Pb^*/Pb_c (e)	Pb_c (pg) (e)	$^{206}Pb/^{204}Pb$ (f)	$^{208}Pb/^{206}Pb$ (g)	$^{207}Pb/^{206}Pb$ (g)	% err (h)	$^{207}Pb/^{235}U$ (g)	% err (h)	$^{206}Pb/^{238}U$ (g)	% err (h)	corr. coef. (g)	$^{207}Pb/^{206}Pb$ (h)	± (i)	$^{207}Pb/^{235}U$ (h)	± (i)	$^{206}Pb/^{238}U$ (h)	± (i)
(Z8)	3	0.60	10.9	0.513	0.3725	95.09%	6.0	1.56	380	0.16	0.05	5.01	0.10	5.34	0.01	1.31	0.37	92.64	118.68	94.76	4.83	94.84	1.23
(Z9)	1	0.23	4.5	0.639	0.1402	92.83%	4.1	0.88	260	0.20	0.05	2.07	0.10	2.23	0.01	0.32	0.55	115.79	48.85	95.74	2.04	94.93	0.30
(Z5)	3	0.85	13.8	0.462	0.5236	97.94%	14.5	0.89	904	0.15	0.05	0.68	0.10	0.77	0.01	0.19	0.55	96.02	16.14	95.10	0.70	95.06	0.18
(Z7)	1	0.15	3.0	0.440	0.0933	91.29%	3.2	0.72	214	0.14	0.05	2.98	0.10	3.16	0.01	0.31	0.61	100.67	70.40	95.29	2.87	95.08	0.29
(Z58)	1	0.30	6.7	0.799	0.1888	90.27%	3.1	1.65	192	0.26	0.05	3.01	0.10	3.20	0.01	0.35	0.58	93.02	71.32	95.00	2.90	95.08	0.33
(Z52)	1	0.35	6.7	0.585	0.2152	93.51%	4.5	1.21	287	0.19	0.05	1.77	0.10	1.91	0.01	0.23	0.64	93.13	41.90	95.02	1.73	95.10	0.22
(91)	1	0.12	3.5	0.745	0.0774	80.98%	1.4	1.47	98	0.24	0.05	6.10	0.10	6.42	0.01	0.57	0.60	96.28	144.29	95.22	5.84	95.18	0.54
(Z51)	1	0.36	7.5	0.606	0.2210	90.86%	3.1	1.80	204	0.19	0.05	2.38	0.10	2.65	0.01	0.75	0.48	71.04	56.57	94.27	2.39	95.19	0.70
(Z57)	1	0.23	5.1	0.549	0.1447	89.27%	2.6	1.41	174	0.18	0.05	2.96	0.10	3.16	0.01	0.32	0.66	73.45	70.25	94.36	2.84	95.19	0.30
(Z55)	1	0.29	6.0	0.630	0.1821	91.66%	3.5	1.34	224	0.20	0.05	2.81	0.10	3.00	0.01	0.45	0.48	106.24	66.42	95.69	2.74	95.27	0.43
(Z10)	1	0.31	5.8	0.551	0.1954	95.00%	5.9	0.83	373	0.18	0.05	1.49	0.10	1.62	0.01	0.28	0.53	89.26	35.23	95.15	1.47	95.39	0.26
(14)	1	0.10	3.7	0.591	0.0582	67.89%	0.7	2.23	58	0.19	0.05	12.56	0.10	13.25	0.01	2.20	0.39	169.36	293.17	96.52	12.20	93.60	2.05
(Z56)	3	0.66	17.3	0.569	0.4074	82.67%	1.5	6.98	107	0.18	0.05	2.76	0.10	3.29	0.01	1.48	0.55	130.52	64.89	95.55	3.00	94.16	1.38
(Z6)	2	0.46	9.4	0.495	0.2851	90.93%	3.1	2.30	206	0.16	0.05	3.18	0.10	4.70	0.01	3.30	0.74	87.55	75.29	95.45	4.28	95.77	3.14

AC-B4 ~ 41.1 m (135 ft) above Buda Limestone

		Compositional Parameters								Radiogenic Isotope Ratios								Isotopic Ages					
Sample (a)	n= (b)	U (ng) (c)	Pb (pg) (c)	$\frac{Th}{U}$ (d)	$^{206}Pb^*$ x10^{-13} mol (e)	mol % $^{206}Pb^*$ (e)	$\frac{Pb^*}{Pb_c}$ (e)	Pb_c (pg) (e)	$\frac{^{206}Pb}{^{204}Pb}$ (f)	$\frac{^{208}Pb}{^{206}Pb}$ (g)	$\frac{^{207}Pb}{^{206}Pb}$ (g)	% err (h)	$\frac{^{207}Pb}{^{235}U}$ (g)	% err (h)	$\frac{^{206}Pb}{^{238}U}$ (g)	% err (h)	corr. coef. (g)	$\frac{^{207}Pb}{^{206}Pb}$ (h)	± (i)	$\frac{^{207}Pb}{^{235}U}$ (h)	± (i)	$\frac{^{206}Pb}{^{238}U}$ (h)	± (i)
(Z81)	2	0.62	11.0	0.719	0.3770	96.69%	9.5	1.04	563	0.23	0.05	1.60	0.10	1.71	0.01	0.31	0.41	94.64	37.97	94.07	1.53	94.05	0.29
Z(4)	1	0.07	1.9	0.812	0.0425	82.79%	1.6	0.72	108	0.26	0.04	15.13	0.09	15.39	0.01	0.44	0.58	-85.78	370.68	87.69	12.93	94.19	0.42
(Z37)	1	0.19	4.1	0.589	0.1141	88.70%	2.5	1.18	165	0.19	0.04	4.17	0.09	4.40	0.01	0.37	0.65	-56.18	101.64	88.76	3.74	94.24	0.35
(Z39)	1	0.20	4.5	0.792	0.1200	88.19%	2.5	1.30	158	0.25	0.05	4.13	0.09	4.39	0.01	0.57	0.49	25.17	99.15	91.67	3.85	94.25	0.53
Z(3)	1	0.17	3.6	0.788	0.1056	91.78%	3.7	0.76	227	0.25	0.05	3.78	0.10	3.99	0.01	0.32	0.68	85.72	89.61	93.99	3.58	94.31	0.29
(Z76)	2	0.32	13.2	0.540	0.1990	66.45%	0.6	8.22	55	0.17	0.05	5.93	0.10	6.25	0.01	0.73	0.48	104.15	140.14	94.76	5.65	94.39	0.68
(Z39)	1	0.20	4.5	0.798	0.1201	88.28%	2.5	1.29	159	0.26	0.05	3.96	0.10	4.21	0.01	0.59	0.49	53.46	94.39	92.90	3.74	94.44	0.55
(Z31)	1	0.67	10.8	0.446	0.4148	98.19%	16.4	0.62	1029	0.14	0.05	0.75	0.10	0.85	0.01	0.24	0.53	98.89	17.80	94.78	0.77	94.61	0.23
Z(12)	1	0.07	2.3	0.649	0.0415	73.18%	0.9	1.23	70	0.21	0.04	16.43	0.09	16.82	0.01	0.73	0.54	-122.59	405.40	86.95	14.01	94.77	0.69
Z(11)	1	0.11	2.5	0.642	0.0696	88.36%	2.4	0.74	160	0.21	0.05	5.23	0.10	5.46	0.01	0.40	0.60	72.78	124.37	94.08	4.91	94.92	0.37
Z(2)	1	0.06	2.8	0.638	0.0368	61.15%	0.5	1.89	48	0.20	0.05	39.46	0.10	39.88	0.01	1.15	0.38	64.96	939.17	92.93	35.41	94.02	1.08
(Z34)	1	0.89	18.3	0.630	0.5283	90.12%	2.9	4.72	188	0.20	0.05	2.76	0.09	3.74	0.01	2.33	0.68	69.31	65.69	90.06	3.22	90.84	2.10
(Z35)	1	0.60	10.4	0.637	0.3723	97.56%	12.8	0.75	765	0.20	0.05	0.77	0.10	0.87	0.01	0.20	0.59	92.38	18.26	95.46	0.79	95.58	0.19
(Z37)	1	0.26	5.1	0.501	0.1655	93.11%	4.2	0.99	271	0.16	0.05	2.11	0.10	2.27	0.02	0.33	0.53	128.26	49.74	97.85	2.12	96.61	0.31
(Z36)	1	0.37	21.7	0.490	0.6604	91.18%	3.2	5.21	211	0.16	0.06	1.38	0.33	1.58	0.04	0.54	0.53	477.77	30.46	291.74	4.02	269.04	1.42
(Z29)	4	0.31	36.6	0.737	0.6757	74.69%	1.0	18.78	73	0.23	0.05	2.97	0.36	3.16	0.05	0.44	0.48	126.58	69.93	308.55	8.40	333.15	1.43
(Z84)	1	0.04	4.9	0.741	0.1536	93.63%	4.8	0.84	293	0.23	0.06	1.90	0.70	4.75	0.09	4.30	0.92	506.21	41.76	537.16	19.82	544.48	22.44

OC-B3 ~ 47.2 m (155 ft) above Buda Limestone

		Compositional Parameters								Radiogenic Isotope Ratios								Isotopic Ages					
Sample (a)	n= (b)	U (ng) (c)	Pb (pg) (c)	Th/U (d)	$^{206}Pb^*$ x10^{-13} mol (e)	mol % $^{206}Pb^*$ (e)	Pb^*/Pb_c (e)	Pb_c (pg) (e)	$^{206}Pb/^{204}Pb$ (f)	$^{208}Pb/^{206}Pb$ (g)	$^{207}Pb/^{206}Pb$ (g)	% err (h)	$^{207}Pb/^{235}U$ (g)	% err (h)	$^{206}Pb/^{238}U$ (g)	% err (h)	corr. coef. (g)	$^{207}Pb/^{206}Pb$ (h)	± (i)	$^{207}Pb/^{235}U$ (h)	± (i)	$^{206}Pb/^{238}U$ (h)	± (i)
(Z5)	3	1.38	22.6	0.313	0.8179	95.39%	6.0	3.21	404	0.10	0.05	1.30	0.09	1.44	0.01	0.33	0.51	95.39	30.80	91.18	1.25	91.02	0.30
(Z9)	1	0.43	6.9	0.446	0.2555	96.83%	9.3	0.68	589	0.14	0.05	0.95	0.09	1.08	0.01	0.31	0.54	60.01	22.59	89.93	0.93	91.06	0.28
(Z62)	3	1.75	26.2	0.320	1.0397	98.18%	15.8	1.56	1025	0.10	0.05	2.04	0.09	2.10	0.01	0.54	0.25	23.02	48.95	88.63	1.79	91.08	0.49
(Z3)	1	0.42	8.2	0.375	0.2498	90.33%	2.8	2.16	193	0.12	0.05	2.50	0.09	2.67	0.01	0.22	0.79	85.14	59.27	90.91	2.32	91.13	0.20
(Z50)	2	0.44	18.3	0.285	0.2628	63.90%	0.5	12.17	51	0.09	0.05	5.41	0.09	5.69	0.01	0.65	0.48	106.60	127.75	91.72	4.99	91.15	0.59
(Z44)	1	0.45	6.9	0.308	0.2655	97.01%	9.5	0.66	625	0.10	0.05	1.18	0.09	1.30	0.01	0.19	0.68	89.60	27.93	91.09	1.13	91.15	0.17
(Z45)	1	0.34	5.5	0.240	0.2030	95.46%	6.0	0.78	411	0.08	0.04	1.72	0.09	1.84	0.01	0.24	0.58	-70.54	41.88	85.49	1.51	91.17	0.22
(Z46)	2	0.94	14.4	0.301	0.5599	97.42%	11.0	1.20	724	0.10	0.05	0.89	0.09	1.01	0.01	0.12	0.95	27.45	21.39	89.00	0.86	91.32	0.11
(Z47)	2	0.80	12.3	0.347	0.4744	97.51%	11.6	0.98	750	0.11	0.05	1.88	0.09	2.00	0.01	0.24	0.53	44.50	44.97	89.65	1.71	91.35	0.22
(Z29)	1	0.53	9.9	0.314	0.3125	91.13%	3.0	2.46	210	0.10	0.05	2.64	0.09	2.81	0.01	0.29	0.63	95.16	62.48	91.50	2.46	91.36	0.26
(Z48)	2	0.66	14.5	0.237	0.3931	85.56%	1.7	5.41	129	0.08	0.05	3.32	0.09	3.52	0.01	0.35	0.60	72.68	78.83	90.69	3.05	91.37	0.32
(Z60)	4	1.18	22.8	0.335	0.9138	98.95%	28.1	0.78	1782	0.11	0.06	0.20	0.16	0.39	0.02	0.23	0.94	647.40	4.19	147.42	0.53	118.22	0.26
(Z8)	4	1.19	29.2	0.191	1.2200	99.20%	35.9	0.79	2345	0.06	0.07	0.18	0.23	0.31	0.02	0.14	0.99	874.40	3.64	210.59	0.60	156.11	0.22

(a) Z1, Z2 etc. are internal laboratory labels for fractions composed of single zircon grain aliquots; all fractions were annealed and chemically abraded after Mattinson (2005).

Brackets indicate inferred reason for excluding analysis from age calcuations; inheritance = inh, Pb-loss = Pbl, or imprecise = imp. Imprecise defined as >2% 206Pb/238U age or >30% 207Pb/235U age

(b) Number of zircon grains dissolved together.

(c) U and total Pb content of zircon remnants after chemical abrasion.

(d) Model Th/U ratio calculated from radiogenic 208Pb/206Pb ratio and 207Pb/235U age.

(e) Pb* and Pbc represent radiogenic and common Pb, respectively; mol % 206Pb* with respect to radiogenic, blank and initial common Pb.

(f) Measured ratio corrected for spike and fractionation only.

Daly Pb analyses corrected for 0.22%/AMU mass bias based on repeat analysis of NBS-981.Faraday U analyses corrected for mass bias based on measured 233U/235U ratio.

(g) Corrected for fractionation, spike, and common Pb; up to 1 pg of common Pb was assumed to be procedural blank: 206Pb/204Pb = 18.66 ± 0.60%; 207Pb/204Pb = 15.54 ± 0.25%;

208Pb/204Pb = 37.62 ± 0.55% (all uncertainties 1-sigma). Excess over blank was assigned to initial common Pb.

(h) Errors are 2-sigma, propagated using the algorithms of Schmitz and Schoene (2007) and Crowley et al. (2007).

(i) Calculate ages are based on the decay constants of Jaffey et al. (1971).

APPENDIX B

GEOCHEMICAL DATA

Well 1 XRF Data

Height above Buda Limestone		Mo	U	V	Al
ft		ppm	ppm	ppm	ppm
323.5	98.6028	23.48	8.01	363.14	40100.54
321.5	97.9932	4.05	6.42	160.54	33486.92
320.5	97.6884	3.29	4.14	205.66	29709.92
320	97.536	3.16	3.88	261.37	29216.54
319.1	97.26168	2.51	4.61	179.7	39606.64
317	96.6216	2.53	2.41	294.12	36799.65
315	96.012	2.76	5.13	316.71	33921.27
314.5	95.8596	2.18	3.72	259.86	37195.91
312	95.0976	16.57	6.21	412.68	30484.7
311.5	94.9452	13.08	7.34	432.77	29048.56
311	94.7928	14.3	4.9	531.46	35746.75
310.5	94.6404	5.9	3.66	433.98	30721.63
310	94.488	8.61	5.24	342.85	28956.46
309.5	94.3356	5.72	7.99	316.14	26297.71
309	94.1832	4.63	5.53	339.62	31906.48
308.2	93.93936	4.5	5.82	323.24	31990.8
307.5	93.726	9.92	6.81	253.88	23393.39
307	93.5736	10.05	6.77	266.01	28444.11
305	92.964	10	4.51	237.37	25737.6
304.5	92.8116	8.12	3.97	211.36	25828.48
304	92.6592	10.55	5.68	199.93	26783.31
303.5	92.5068	8.17	3.1	163.14	17632.05
303.2	92.41536	6.17	5.61	259.4	37190.19
302.5	92.202	8.71	5.47	200.2	25691.88
302	92.0496	9.97	3.58	310.5	33131.58
301.5	91.8972	14.53	7.09	189.01	23981.16
301	91.7448	14.12	6.91	2996.6	29266.88
298.5	90.9828	43.75	12.24	474.53	34959.01
298	90.8304	13.91	5.91	474.17	34465.54

297.5	90.678	12.71	5.11	345.62	32366.58
294.5	89.7636	10.23	4.23	240.45	25179.26
294	89.6112	6.94	3.51	216.57	22204.51
293.5	89.4588	12.15	2.97	373.42	28979
293	89.3064	10.81	3.6	320.91	25304.97
292.5	89.154	9.76	5.88	263.76	22925.86
292.2	89.06256	10	4.2	264.38	28952.76
291.5	88.8492	9.11	4.71	315.82	33009.27
291	88.6968	8.25	4.6	201.46	26145.54
290.5	88.5444	7.21	3.2	174.76	21951.42
290	88.392	11.31	3.36	228.85	22614.74
289.5	88.2396	20.88	4.06	383.71	24943.26
288.5	87.9348	8.76	3.5	496.87	26745.4
287	87.4776	5.75	5.21	393.95	29907.47
286.5	87.3252	9.09	4.73	386.28	28932.92
286	87.1728	13.18	3.58	453.56	30884.28
285.5	87.0204	11.59	5.39	454.16	32832.55
285	86.868	13.72	3.28	561.38	36146.82
284.5	86.7156	11.51	6.79	489.67	31818.15
281.8	85.89264	11.64	2.98	327.88	37693.47
281.5	85.8012	9.69	4.87	425.96	40845.28
281	85.6488	9.33	5.52	322.34	38053.38
280.5	85.4964	8.28	3.6	321.86	32582.84
280	85.344	6.03	4.2	283.64	29888.86
279	85.0392	6.78	4.07	312.17	40630.74
278.5	84.8868	8.88	5.92	522.75	42536.92
278	84.7344	6.1	5.07	252.74	39780.96
277	84.4296	13.64	3.57	305.77	41212.2
276.5	84.2772	11.74	3.75	276.55	32502.06
275.8	84.06384	10.45	7.07	352.73	40988.89
275.5	83.9724	6.76	4.13	399.06	41028.75
275	83.82	9.26	4.56	443.31	33016.2
274.5	83.6676	7.32	4.73	299.77	36342.09
274	83.5152	16.52	5.29	481.82	55132.75
273.5	83.3628	8.96	5.78	324.23	43364.12
273	83.2104	20.57	6.56	348.81	36031.17
272.5	83.058	19.53	5.88	408.13	29640.52
271	82.6008	23.76	16.49	378.58	41909.69
270.5	82.4484	43.05	13.01	443.25	25766.36
270	82.296	27.74	5.51	513.05	27328.42

269.5	82.1436	21.15	7.44	560.04	32542.99
268.8	81.93024	6.85	2.86	441.69	33092.62
268.5	81.8388	7.52	3.43	423.3	34699.53
268	81.6864	4.56	3.48	389.9	35168.47
267.5	81.534	7.64	5.92	367.82	36871.88
267	81.3816	3.39	3.43	171	29596.87
265	80.772	3.09	5.24	207.36	40659.33
264.2	80.52816	7.04	4.85	319.63	42867.54
263.5	80.3148	6.4	7.83	341.52	45601.73
263	80.1624	8.02	6.06	382.31	38404.43
262	79.8576	6.68	5.45	350.85	43050.48
261.5	79.7052	5.37	6.98	325.56	44047.35
261	79.5528	8.98	4.79	404.1	42410.8
260.5	79.4004	10.28	5.57	371.92	41215.16
260	79.248	5.09	4.91	345.38	38083.17
259.5	79.0956	13.34	5.7	387.65	46703.35
259.1	78.97368	14.15	6.25	363.81	38217.09
258.5	78.7908	12.88	2.62	353.44	37455.99
258	78.6384	18.4	7.88	385.12	36155
257.5	78.486	18.6	4.77	366.57	33040.37
257	78.3336	6.94	3.9	251.06	26178.45
256	78.0288	11.44	5.32	338.92	46930.8
255.5	77.8764	14.19	8.01	348.34	39557.5
255	77.724	18.78	5.62	413.69	38836.74
254.5	77.5716	13.41	4.2	359.3	32763.04
253.8	77.35824	18.9	7.69	483.69	37252.56
253.5	77.2668	14.29	4.15	233.52	25924.19
253	77.1144	19.92	4.26	303.58	27042.1
252.5	76.962	9.59	5.31	370.85	34625.06
251.5	76.6572	2.98	14.87	354.51	26025.79
251	76.5048	14.63	8.42	689.43	53542.85
250.5	76.3524	12.83	5.75	433.14	50109.46
249.5	76.0476	10.53	8.1	430.69	49128.75
249	75.8952	14.68	7.77	414.12	43052.94
248.6	75.77328	11.19	6.17	422.64	38808.7
248.2	75.65136	14.63	7.09	419.02	38910.06
247.5	75.438	45.25	7.78	421.51	48201.06
247	75.2856	10.52	5.26	412.17	32268.26
246.5	75.1332	9.66	7.26	511.26	38551.56
246	74.9808	8.18	5.03	443.16	41276.45

245.5	74.8284	7.89	7.24	411.89	38776.44
244	74.3712	4.23	4.49	399.35	40874.62
243.5	74.2188	5.37	3.33	422.66	38335.24
241.5	73.6092	3.17	4.76	199.22	25637.75
240	73.152	2.78	2.8	367.6	19415.45
238	72.5424	5.97	4.26	432.79	41951.94
234.5	71.4756	6.63	6.5	537.78	32574.03
234	71.3232	10.23	4.41	606.51	40893.56
233.5	71.1708	5.27	4.53	748.5	34587.99
233	71.0184	3.92	5.36	380.04	36230.69
232.5	70.866	7.19	2.87	490.61	50318.46
232	70.7136	4.2	5.78	512.28	43925.61
231.8	70.65264	4.98	3.52	592.85	53509.92
231.5	70.5612	5.37	5.53	284.98	45070.38
231	70.4088	4.27	3.65	367.37	42306.06
230	70.104	12.04	6.82	376.12	41917.18
229.5	69.9516	7.94	7	367.21	60581.3
229.1	69.82968	2.65	3.31	498.17	53596.39
228.5	69.6468	1.98	2.82	233.71	35074.4
227.5	69.342	3.98	3.06	266.15	40757.7
227	69.1896	5.29	9.32	273.54	36801.58
226.5	69.0372	34.27	8.21	587.56	60586.45
226	68.8848	22.77	8.63	482.3	38331.55
225.5	68.7324	25.16	7.75	505.62	37133.87
225	68.58	22.97	9.78	566	44591.25
224.5	68.4276	23.73	9.17	612.9	53697.72
224.2	68.33616	25.63	8.56	580.38	50267.13
223	67.9704	2.38	8.95	365.82	47818.27
222.5	67.818	22.98	6.62	412.91	41690.21
222	67.6656	22.82	12.44	404.38	38617.97
221.5	67.5132	53.47	17.04	600.33	47417.14
221	67.3608	28.97	30.72	613.97	48309.31
220.5	67.2084	56.63	12.37	540.14	34138.14
220	67.056	59.09	9.55	634.8	35735.3
219.5	66.9036	59.27	11.52	639.91	40319.13
218.5	66.5988	51.17	7.85	541.46	24238.64
218	66.4464	61.23	13.39	682.41	29513.71
217.5	66.294	69.48	12.66	819.79	33117.37
217	66.1416	54.13	11.64	783.4	29498.65
216.5	65.9892	58.03	11.82	682.81	30853.43

215.5	65.6844	31.13	6.72	445.88	18027.82
215	65.532	52.08	11.57	614.21	31643.59
214.5	65.3796	44.44	6.9	681.98	33238.05
213.8	65.16624	65.41	11.54	608.93	32319.88
213.5	65.0748	57.9	9.42	666.99	26328.37
213	64.9224	47.5	10.32	543.02	23513.4
212	64.6176	61.62	8.97	566.8	22575.71
211.5	64.4652	63.84	13.79	649.92	25205.4
211	64.3128	72.88	16.25	804.32	31874.1
210.7	64.22136	78.19	17.16	697.08	24310.95
210.5	64.1604	78.34	13.85	711.58	27080.05
210	64.008	67.66	12.2	688.01	30030.07
209.5	63.8556	94.52	18.56	944.24	35885.18
209.2	63.76416	71.77	12.14	821.56	28345.75
208.5	63.5508	72.19	10	724.99	29836.11
208	63.3984	52.1	11.28	796.57	25011.54
207.6	63.27648	60.85	10.96	832.97	47787.49
207.5	63.246	75.35	8.94	708.89	33994.56
207	63.0936	22.04	4.68	394.77	15126.38
206.5	62.9412	16.04	2.35	326.06	12705.32
206	62.7888	70.07	12.13	888.87	46366.83
205.5	62.6364	70.34	15.11	613.53	23419.27
205	62.484	64.47	9.22	658.52	26757.9
204.5	62.3316	79.84	10.88	597.22	23773.34
204.2	62.24016	63.19	8.89	822.53	20316.97
203.5	62.0268	75.25	12.26	690.4	28841.52
203	61.8744	71.99	9.57	1073.82	32914.39
202.5	61.722	104.31	16.45	1277.03	39684.01
201.5	61.4172	14.6	3.65	543.73	12172.66
200.5	61.1124	71.71	11.09	767.66	32197.24
199.5	60.8076	79.78	11.37	927.3	28679.02
199	60.6552	70.77	9.72	1529.21	26476.79
198.5	60.5028	69.19	8.5	588.75	30219.27
198	60.3504	67.94	8.65	664.25	26630.74
197.2	60.10656	83.27	27.37	809.24	40126.39
197	60.0456	102.58	26.27	798.61	38176.43
196.5	59.8932	105.8	21.55	829.21	36532.59
196	59.7408	77.99	11.65	620.48	27836.78
195	59.436	87.48	14.8	565.56	30342.03
194.5	59.2836	102.23	12.76	728.33	34138.04

194.2	59.19216	97.27	11.28	664.36	29858.75
193.5	58.9788	90.14	10.53	733.28	33836.21
193	58.8264	81.22	10.44	609.29	29686.87
192.5	58.674	98.15	11.77	1329.87	31010.26
192	58.5216	78.72	10.06	582.29	28007.22
191.5	58.3692	97.47	15.03	697.28	35436.25
191	58.2168	23.21	5.04	422.62	13318.35
190	57.912	22.78	5.49	320.81	13323.89
189.5	57.7596	8.25	31.54	360.65	16138.27
189	57.6072	91.95	15.38	627.14	31763.37
188.5	57.4548	75.91	13.95	553.09	26876.95
188	57.3024	88.54	10.01	655.36	35623.97
187.5	57.15	72.07	11.88	580.47	33956.17
187	56.9976	77.76	11.67	596.31	36203.5
186.5	56.8452	83.45	11.36	627.43	31163.21
185.8	56.63184	84.36	13.51	605.31	32357.1
185.5	56.5404	82.82	11.64	586.84	32700.1
185	56.388	87.76	12.99	562.69	30158.03
184.5	56.2356	93.67	10.96	641.1	33905.69
184	56.0832	103.8	16.59	699.99	32679.92
183.5	55.9308	95.34	11.33	555.1	34921.52
183	55.7784	18.49	4.88	308.56	22117.34
182	55.4736	37.85	5.54	284.85	21425.72
180	54.864	67.33	9.86	425.65	36405.21
179.5	54.7116	55.8	8.76	452.07	28450.68
179	54.5592	99.72	12.49	706.45	36406.78
178.5	54.4068	99.01	11.57	763.98	34760.87
178	54.2544	99.53	13.19	781.66	39527.35
177.6	54.13248	85.58	13.03	705	30434.41
176.8	53.88864	100.46	15.79	791.63	28441.98
176.5	53.7972	93.43	15.24	803.4	35010.02
176	53.6448	98.46	12.26	773.73	35365.67
174.5	53.1876	18.06	3.7	338.8	12858.35
174	53.0352	31.17	3.53	474.18	18250.14
173.5	52.8828	92.54	13.81	932.56	34729.41
173	52.7304	85.76	12.47	919.89	37298.83
172.5	52.578	66.35	14.77	759.86	28967.24
171.8	52.36464	70.68	12.99	716.43	30733.85
171.5	52.2732	32.42	6.39	437.41	14954.82
171	52.1208	32.31	4.62	414.81	17539.93

170.5	51.9684	25.43	4.56	412.2	16714.38
170	51.816	29.58	4.56	375.15	15372.92
169.5	51.6636	74.32	8.07	523.81	30910.66
169	51.5112	82.46	11.5	567.65	30324.17
168.5	51.3588	65.16	8.45	461.19	26160.32
168	51.2064	45.47	7.68	807.82	22595.63
167.6	51.08448	77.64	8.19	1353.42	28850.45
166.8	50.84064	41.88	5.41	1057.62	26078.93
166.5	50.7492	80.77	7.68	1172.27	29588.34
166	50.5968	78.44	9.78	1165.72	34048.7
165.5	50.4444	60.99	8.94	1223.08	26852.21
165	50.292	71.36	9.35	1179.04	24345.07
164.5	50.1396	75.21	7.15	1735.25	25391.09
164	49.9872	45.87	4.76	1342.46	23227.89
163.5	49.8348	56.25	9.71	1398.71	30852.22
163	49.6824	82.39	12.73	1476.54	32242.65
162.5	49.53	76.7	12.98	1484.58	32917.25
161.8	49.31664	78.82	13.76	1250.4	37387.34
161.5	49.2252	75.86	13.89	1365.9	41560.04
161	49.0728	69.72	12.33	834.79	30711.52
160	48.768	51.54	8.58	465.03	25686.58
159.5	48.6156	45.73	7.26	473.63	31684.06
159	48.4632	24.9	5.39	465.51	22546.56
156	47.5488	21.33	5.1	301.28	18746.08
155.5	47.3964	37.8	7.06	414.59	27847.23
155	47.244	30.55	5.27	324.67	22447
154.5	47.0916	29.84	4.85	335.71	21390.63
154	46.9392	28.06	4.09	300.37	19661.03
153.5	46.7868	48.94	7.36	378.02	24355.13
153.2	46.69536	32.54	6.76	394.73	19071.12
152.5	46.482	40.41	5.89	495.62	24444.15
152	46.3296	76.35	7.6	506.41	37247.77
151.5	46.1772	61.41	9.54	337.33	23759.64
151	46.0248	71.16	8.72	544.94	30841.97
150.8	45.96384	50.54	7.12	490.21	27312.98
150.5	45.8724	94.79	12.45	642.8	33670.8
150	45.72	87.03	13.48	582.13	25250.89
149.5	45.5676	101.82	15.97	611.6	30349.91
149	45.4152	81.33	10.63	699.14	39693.16
148.5	45.2628	56.58	8.13	679.13	30057.66

148	45.1104	83.93	14.07	830.3	30690.35
147.6	44.98848	92.84	14.12	931.23	32115.6
146.8	44.74464	96.86	18.69	643.7	37624.97
146.5	44.6532	85.03	15.69	671.46	42786.46
145.5	44.3484	11.92	2.83	248.71	17506.35
144.5	44.0436	15.53	4.37	183.85	17607.4
143.5	43.7388	41.53	9.98	324.52	42620.02
143	43.5864	48.05	5.63	263.64	21182.86
142.5	43.434	48.23	5.7	278.06	21291
141.5	43.1292	97.47	16.62	617.32	27574.9
141	42.9768	98.53	18.89	730.34	30292.24
140.5	42.8244	89.58	17.52	636.28	27044.9
140	42.672	109.77	15.05	737.52	31370
139.5	42.5196	90.08	10.49	581.39	33036.41
139	42.3672	60.15	12.66	473.46	28828.93
138.5	42.2148	44.31	10.52	291.47	30863.3
138	42.0624	14.8	3.79	201.36	13567.25
134.5	40.9956	32.31	2.93	178.76	24137.47
134	40.8432	40.99	6.13	247.07	27634.99
133.5	40.6908	51.77	7.64	239.46	27152.02
133	40.5384	43.6	6.17	208.73	21454.74
132.5	40.386	40.03	5.19	249.95	27250.3
131.8	40.17264	67.31	9.7	243.84	24485.56
131.5	40.0812	37.55	5.24	248.84	25979.17
131	39.9288	63.16	10.31	314.87	27269.37
130.5	39.7764	49.22	10.62	301.93	30072.4
130	39.624	97.32	12.24	459.94	31051.11
129.6	39.50208	63.82	10.82	436.72	33241.89
129.5	39.4716	56.22	10.12	390.64	29684.64
129	39.3192	83.27	9.97	454.5	29516.72
128.5	39.1668	91.25	11.21	617.18	32305.73
128.1	39.04488	112.48	12.34	778.06	34043.55
127.5	38.862	85.38	15.78	719.57	35145.18
127	38.7096	85.79	14.69	668.63	42403.26
126.5	38.5572	70.07	12.22	518.11	29229.86
126	38.4048	79.81	13.05	607.27	34201.89
125.5	38.2524	77.16	9.7	512.46	30850.5
125	38.1	39.33	6.83	239.5	25097.21
122.5	37.338	20.97	5.74	206.13	19448.71
122	37.1856	17.44	6.05	260.24	22158.07

121.5	37.0332	33.05	9.19	193.08	31826.14
121	36.8808	39.62	11.44	219.05	34000.23
120.5	36.7284	35.09	3.97	223.28	33392.44
120	36.576	26.95	4.54	174.31	40099.31
119.5	36.4236	27.18	5.27	163.55	25463.25
119.3	36.36264	36.28	4.18	186.68	31643.95
118.5	36.1188	36.8	7.68	217.53	32258.74
118	35.9664	26.95	4.77	174.39	33152.01
117.5	35.814	27.41	6.7	224.06	29348.55
117	35.6616	39.57	4.92	224.17	33798.46
116.5	35.5092	37.23	5.52	178.67	32982.43
116	35.3568	30.37	5.78	263.38	28360.54
115.5	35.2044	26.8	6.09	219.76	35081.18
115	35.052	39.93	8.48	211.21	44946.22
112	34.1376	17.74	2.33	201.16	20278.28
111.5	33.9852	33.65	7.21	203.59	31711.8
111	33.8328	30.7	6.94	240.08	31329.54
110.5	33.6804	39.1	11.04	221.04	31819.28
110	33.528	49.83	4.92	262.43	33651.97
109.5	33.3756	37.45	5.72	259.87	37518.71
109	33.2232	39.62	4.03	268.72	36644.27
108.5	33.0708	32.65	6.2	218.59	32213.56
108	32.9184	35.76	6.33	192.91	31264.99
107.5	32.766	45.02	8.71	194.08	33069.04
106.8	32.55264	34.97	6.77	211.65	35005.14
106.5	32.4612	37.75	5.53	213.95	34808.39
106	32.3088	37.37	4.04	198.69	34972.68
105.5	32.1564	47.78	9.24	209.26	41861.57
105	32.004	37.27	6.17	232.8	36128.59
104.5	31.8516	23.21	6.39	164.78	28565.21
104	31.6992	17.41	7.51	123.11	25479.24
103.5	31.5468	13.36	5.32	124	18863.55
102.5	31.242	14.95	5.29	129.2	18773
101.8	31.02864	25.05	8.5	185.68	37016.15
101.5	30.9372	26.31	7.22	196.2	35232.07
101	30.7848	34.54	9.94	216.68	47539.71
100.5	30.6324	53.44	8.71	234.15	41653.5
100	30.48	41.98	6.3	307.89	38089.78
99.5	30.3276	61.19	9.61	359.66	39518.88
99	30.1752	68.42	11.88	450.78	37888.45

98.5	30.0228	53.24	11.26	435.15	35834.56
98.2	29.93136	56.46	12.62	394.33	32098.16
97.5	29.718	80.6	14.44	459.21	29512.6
97	29.5656	71.34	13.08	476.08	34064.47
96.7	29.47416	69.49	11.11	432.86	34191.71
96.5	29.4132	95.38	9.27	418.62	33166.72
96	29.2608	68.5	6.98	442.6	35389.14
95.5	29.1084	39.98	5.75	393.37	26288.64
94	28.6512	11.62	6.67	292.87	16979.93
92.5	28.194	30.8	9.89	267.46	31259.11
92	28.0416	54.45	10.99	196.29	33711.91
91.5	27.8892	34.44	6.98	187.16	30730.62
91	27.7368	37.4	6.99	233.24	38083.5
90.5	27.5844	38.99	7.41	280.34	39016.47
90	27.432	33.56	5.76	265.58	30084.9
89.5	27.2796	53.34	6.61	373.63	39183.77
89.2	27.18816	83.35	12.81	432.13	35654.22
88.5	26.9748	35.3	4.87	271.13	25099.12
88	26.8224	28.44	5.24	287.25	25390.43
87.8	26.76144	13.14	7.6	243.12	42218.16
87.5	26.67	14.14	11.25	290.67	37178.01
87	26.5176	16.6	9.42	247.37	47194.16
86.5	26.3652	35.9	8.35	267.68	33511.45
86	26.2128	30.08	9.44	317.68	36945.4
85.5	26.0604	25.48	9.16	224.24	29340.14
83.5	25.4508	17.56	4.66	390.88	27292.07
83	25.2984	34.54	7.8	215.25	30950.43
82.5	25.146	27.71	6.68	197.31	37287.27
82	24.9936	25.59	5.24	165.94	30407.56
81.5	24.8412	18.83	9.3	197.28	29330.07
81	24.6888	20.6	7.56	222.92	29768.95
80.5	24.5364	19.53	7.16	152.37	26212.46
80	24.384	31.78	7.17	168.34	34654.88
79.5	24.2316	28.57	9.11	183.64	40406.08
79.2	24.14016	24.17	6.98	178.4	41108.75
78.5	23.9268	26.06	9.41	190.7	30716.97
78	23.7744	40.06	7.92	251.8	36655.49
77.5	23.622	36.14	6.43	269.69	38886.2
77	23.4696	25.88	6.62	202.43	29716.86
76.5	23.3172	43.15	8.17	216.65	36760.81

76	23.1648	24.72	4.82	201.4	34112.92
75.5	23.0124	31.99	8.26	249.11	36364.91
73.5	22.4028	37.04	10.37	197.45	43262.92
73	22.2504	34.79	8.88	247.73	40697.42
72.5	22.098	29.61	7.02	285.95	40260.68
72	21.9456	35.63	14.38	246.91	49238.23
71.5	21.7932	41	18.83	311.78	58837.99
71	21.6408	46.11	9	252.85	41236.71
70.5	21.4884	34.42	4.62	227.34	36934.31
70	21.336	43.85	7.61	179.83	34237.48
69.5	21.1836	52.99	7.54	245.67	37686.04
69	21.0312	37.22	5.57	192.2	37088.76
68.5	20.8788	37.96	3.52	179.84	39796.29
68	20.7264	36.87	5.73	193.01	39123.88
65	19.812	10.18	10.66	211.67	70362.86
64.5	19.6596	16.24	12.93	173.66	38115.81
64	19.5072	19.73	10.83	193.86	43451.7
63.5	19.3548	19.2	9.16	226.04	46609.63
63	19.2024	27.63	10.06	242.35	44352.55
62.5	19.05	24.3	8.62	199.83	43835.79
62	18.8976	25.25	8.87	191.55	48463.79
61.5	18.7452	29.55	8.95	203.47	47735.89
61	18.5928	24.16	9.16	253.89	50372.98
60.5	18.4404	24.55	10.82	265.47	57651.74
60	18.288	30.24	7.09	212.15	35931.75
59.5	18.1356	34.08	4.74	242.43	38523.25
59	17.9832	35.1	6.69	288.24	34602.66
58.5	17.8308	31.12	5.37	274.46	35852.67
57.5	17.526	32.52	7.65	239.24	42151.13
57	17.3736	41.73	7.85	246.3	37459.12
56.5	17.2212	18.1	5.82	159.27	28267.54
56	17.0688	19.71	4.21	154.41	27602.41
54.5	16.6116	17.76	5.41	389.57	30016.72
54.2	16.52016	45.55	6.75	441.01	45447.34
53.5	16.3068	25.23	5.58	396.41	37702.03
53	16.1544	25.15	6.43	378.2	33437.54
52	15.8496	26.22	6.29	330.58	32754.68
51.5	15.6972	22.55	4.35	273.48	24056.34
51	15.5448	43.19	5.88	330.44	33285.47
50.5	15.3924	31.27	5.06	223.38	32431.49

50	15.24	37.85	5.13	245.26	31477.59
49.5	15.0876	41.42	8.95	243.81	35238.85
49.2	14.99616	32.57	6.52	218.62	31092.77
48.5	14.7828	24.93	3.36	171.8	30901.69
48	14.6304	39.65	4.44	237.75	39623.61
47.5	14.478	19.74	2.78	168.05	19817.16
47	14.3256	26.85	4.28	269.04	31096.6
46.5	14.1732	29.36	4.59	328.4	34358.24
46	14.0208	46.56	5.63	237.24	43035.37
45.5	13.8684	48.51	5.58	211.75	34815.68
45	13.716	28.69	3.72	224.51	31504.86
44.5	13.5636	25.5	4.3	211.11	30284.33
44.2	13.47216	25.61	3.19	244.83	31799.06
43.5	13.2588	38.41	7.56	201.41	38718.81
43	13.1064	45.35	7.46	216.61	36868.74
42.5	12.954	43.57	6.19	223.02	38793.21
42	12.8016	44.48	8.52	288.31	41316.89
41.5	12.6492	39.19	4.58	194.46	35300.27
41	12.4968	49.17	6.87	275.91	38808.97
40.5	12.3444	37.25	6.06	179.78	31817.66
40	12.192	21.54	3.83	129.01	22037.79
39.5	12.0396	37.23	5.8	184.22	32624.65
39	11.8872	40.81	5.5	270.47	43008.58
38.5	11.7348	30.08	7.61	258.98	40573.98
38	11.5824	35.5	8.38	288.33	42188.47
37.5	11.43	60.8	9.46	315.39	43845.86
37	11.2776	39.55	5.74	208.18	36051.97
36.5	11.1252	18.45	4.3	131	19158.43
35.9	10.94232	31.2	4.06	234.79	33074.86
35.5	10.8204	41.45	5.06	285.67	37107.2
35	10.668	50.02	7.91	354.36	42669.95
34.5	10.5156	40.39	7.21	318.79	42284.39
34	10.3632	68.98	7.45	345.9	38838.24
33.5	10.2108	49.39	6.95	299.68	44622.57
33	10.0584	22.72	2.93	178.8	24299.49
32	9.7536	45.91	7.57	281.47	30483.53
30.5	9.2964	21.63	5.61	185.28	33979.53
29.5	8.9916	14.4	3.25	149.85	24439.01
28.4	8.65632	42.34	3.45	235.61	42743.38
28	8.5344	28.04	5.89	174.37	38799.44

26.5	8.0772	38.01	7.48	322.06	46486.48
26	7.9248	28.39	9.8	408.89	53449.67
25.5	7.7724	24.93	10.79	294.57	49486.13
25	7.62	19.2	4.17	124.65	24600.33
23	7.0104	22.64	4.92	156.71	31133.84
22.5	6.858	25	5.85	216.58	40679.75
22	6.7056	24.77	5.22	237.23	41168.14
21.5	6.5532	27.78	8.65	694.28	29641.4
21	6.4008	36.82	5.63	264.06	41861.02
20	6.096	32.27	4.96	292.5	44334.36
18.5	5.6388	26.92	8.7	229.26	29090.08
17.6	5.36448	19.06	8.16	395.16	26372.83
16.5	5.0292	28.92	8.18	232.65	30738.06
16	4.8768	38.81	9.9	164.75	23058.23
15.5	4.7244	30.37	8.55	247.97	45395.45
14	4.2672	27.83	8.79	241.18	29641.34
13.5	4.1148	37.45	8.74	224.93	34903.31
12.8	3.90144	25.43	7.21	259.03	49161.62
12.5	3.81	20.85	6.32	256.25	44210.13
11.5	3.5052	18.44	8.47	218.66	29605.18
10.5	3.2004	28.69	9.86	297.33	43303.11
10	3.048	23.66	8.81	328.42	40544.22
9.5	2.8956	31.88	6.22	245.03	34150.61
8.5	2.5908	13.81	11.73	350.23	59791.26
8	2.4384	12.48	8.79	251.97	49641.39
7.5	2.286	18.5	6.86	341.18	58583.41
7	2.1336	33.98	5.68	319.31	56730.7
6.5	1.9812	23.56	10.9	244.05	40505.42
6	1.8288	28.21	16.67	285.2	45576.44
5.5	1.6764	13.56	14.85	268.96	53754
5	1.524	12.78	6.21	366.89	45838.02
4.5	1.3716	45.73	22.26	399.19	40448.81
4.2	1.28016	20.17	9.27	521.46	68623.63
3.5	1.0668	7.04	8.84	281.78	50706.96
3.1	0.94488	22.92	12.07	353.92	59606.61
2.9	0.88392	15.61	5.49	345.29	76977.59
2.5	0.762	13.99	8.49	620.86	79811.16
2	0.6096	36.74	9.59	261.76	41003.74
1.5	0.4572	3.55	9.31	387.53	63245.23
0.8	0.24384	2.73	4.71	539.17	73000.32

Well 2 XRF Data

Height above Buda Limestone		Mo	U	V	Al
ft	m	ppm	ppm	ppm	ppm
312.5	95.25	6.07	7.65	38.3	5736.4
311.5	94.9452	4.36	3.79	130.86	15076.75
309.5	94.3356	5.18	4.45	106.37	18192.9
303.5	92.5068	6.4	9.61	116.61	24895.88
297	90.5256	5.42	11.02	203.76	46540.37
294	89.6112	2.48	10	160.77	42984.3
288	87.7824	3.09	6	71.46	14339.76
287	87.4776	11.82	11.56	162.58	18187.38
273.5	83.3628	4.28	2.62	39.22	10855.68
270	82.296	2.41	4.53	89.08	9760.15
269.5	82.1436	5.36	7.14	87.58	12751.62
269	81.9912	6.12	5.27	47.68	8035.22
268.5	81.8388	4.75	7.55	60.01	7945.57
268.2	81.74736	4.53	7.91	57.8	11621.92
266.5	81.2292	3.44	7.99	77.06	22827.36
265.5	80.9244	3.72	4.3	48.72	11639.49
264.5	80.6196	4.7	8.4	82.76	17044.52
264	80.4672	5.7	10.48	66.73	16828.26
262	79.8576	5.01	8.73	87.25	21555.92
260.5	79.4004	12.09	8.8	155.05	17696.35
260	79.248	7.99	5.62	107.74	13162.39
259.5	79.0956	8.61	6.12	119.69	15925.67
258.5	78.7908	3.98	3.66	82.02	17090.04
256.5	78.1812	9.74	5.93	136.88	19191.54
256	78.0288	10.27	4.2	140.07	17791.74
255.5	77.8764	7.67	3.87	101.14	10255.11
253	77.1144	4.33	3.19	132.51	15421.17
252.5	76.962	8.1	4.68	232.59	19582.97
251.5	76.6572	5.7	2.36	105.42	7424.31
250.5	76.3524	7.69	4.74	139.93	12280.51
249	75.8952	4.22	4.52	121.16	12885.37
248.5	75.7428	5.24	3.53	147.01	13860.2
248.2	75.65136	6.1	2.65	163.52	11835.64
246.3	75.07224	14.6	3.42	278.35	15200.97
246	74.9808	7.8	3.16	217.82	8798.18
245.5	74.8284	18.65	4.71	365.3	25565.18

243.5	74.2188	21.92	4.92	166.47	12102.72
242	73.7616	20.09	6.12	261.76	33460.15
241	73.4568	8.23	5.73	211.69	34652.11
240.5	73.3044	6.07	5.36	162.79	29304.12
239	72.8472	5.54	10.49	91.69	11585.45
238.5	72.6948	13.66	4.36	268.78	25711.44
238	72.5424	6.98	3.64	233.33	31116.04
237.5	72.39	3.11	4.43	182.18	26824.81
235.8	71.87184	3.95	5	174.43	35602.54
235.5	71.7804	3.17	5.92	167.8	31678.12
235	71.628	3.84	5.85	156.38	28330
234.5	71.4756	16.5	6.01	290.35	31845.59
234	71.3232	12.14	2.95	290.06	37758.84
233.5	71.1708	27.35	7.39	458.2	27550.73
232	70.7136	3.34	3.24	119.97	20182.35
231.5	70.5612	4.79	2.63	172.48	29172.97
230.5	70.2564	7.37	3.42	193.51	26969.7
229	69.7992	3.24	4.17	119.49	18753.61
228.5	69.6468	4.45	4.87	129.06	23093.07
226	68.8848	5.03	5.11	182.26	26507.63
225.5	68.7324	6.6	3.51	143.54	22576.66
225	68.58	5.62	5.54	138.18	20271.24
224.5	68.4276	4.94	4.31	156.54	21731.23
224	68.2752	3.85	4.4	154.65	23401.1
223.5	68.1228	4.53	4.2	130.19	23861.09
222.5	67.818	5.46	2.64	146.68	20716.9
222	67.6656	6.53	3.16	155.16	18270.34
221.5	67.5132	5.72	3.67	188.15	17176.71
221	67.3608	7.87	4.11	190.25	19851.88
220	67.056	6.37	6.19	208.95	22283.16
219.5	66.9036	7.06	4.75	201.43	21948.94
219	66.7512	5.26	5.81	170.42	18526.07
218.5	66.5988	5.16	4.5	194.96	22872.06
218.2	66.50736	8.93	4.45	241.39	29256.38
216	65.8368	2.03	4.61	123.37	23863.04
214.5	65.3796	1.8	4.81	133.42	25971.03
213	64.9224	1.92	4.09	79.17	21705.65
212.2	64.67856	1.7	3.63	93.81	22927.43
209.5	63.8556	4.15	2.71	161.94	25811.94
209	63.7032	9.74	5.97	191.1	34821.63

208.5	63.5508	7.69	4.8	183.66	26307.39
207.5	63.246	7.39	2.41	211.21	26116.06
206.5	62.9412	6.6	2.2	138.76	21586.06
205.5	62.6364	6.22	3.52	173.79	28463.5
205	62.484	5.84	5.06	161.59	24963.3
204.5	62.3316	4.1	3.02	173.66	25875.3
204	62.1792	5.29	4.75	198.98	34663.53
203	61.8744	5.54	4.58	217.71	29640.51
202.5	61.722	4.27	3.87	175.89	27667.12
202	61.5696	7.42	4.81	193.45	32602.62
201.5	61.4172	4.46	3.39	172.6	26543.43
200.5	61.1124	6.03	2.3	125.4	19394.49
200	60.96	5.56	4.04	143.23	23742.69
199.5	60.8076	6.42	4.43	190.85	23983.63
199	60.6552	5.54	4.03	173.89	19908.4
198.5	60.5028	6.35	3.65	199.84	24157.2
198.2	60.41136	6.89	2.95	191.8	24123.46
197.5	60.198	5.14	5.16	169.67	21390.97
197	60.0456	4.79	3.49	150.42	21212.77
196.5	59.8932	6.45	3.26	153.52	22341.38
195.5	59.5884	8.71	4.51	224.26	23534.94
195	59.436	5.22	5.14	209.99	23856.31
194.5	59.2836	6.3	2.9	220.71	20297.73
194	59.1312	7.85	5.06	235.61	22696.71
193.5	58.9788	6	3.9	200.41	22509.82
193	58.8264	6.56	7	195.11	24174.26
192.5	58.674	51.95	9.77	491.66	43727.4
192	58.5216	59.99	10.6	491.14	41986.58
191.5	58.3692	53.34	10.87	519.75	51566.12
191	58.2168	51.49	7.34	503.04	52199.72
190.5	58.0644	49.29	9.53	493.46	49792.6
189.5	57.7596	49.73	10.79	442.98	40560.56
189	57.6072	61.66	7.77	564.97	50480.8
187.5	57.15	38.06	7.34	442.53	34482.85
187	56.9976	50.1	10.63	477.59	40236.07
185.5	56.5404	43.07	8.79	395.93	21736.22
185	56.388	53.47	8.21	499.37	36044.09
184.5	56.2356	66.67	12.97	625.76	43778.09
184	56.0832	56.28	10.47	491.34	34723.29
183.5	55.9308	53.42	10.2	446.05	30249.29

182.5	55.626	58.91	10.23	552.01	32096.95
182	55.4736	58.76	6.99	534.65	32467.44
181.5	55.3212	47.67	6.2	455.55	32833.4
181	55.1688	61.13	11.21	468.86	39586.06
180.5	55.0164	48.96	9.15	438.48	49989.99
180	54.864	48.25	17.68	340.87	27448.8
179.5	54.7116	40.14	8.68	360.95	33079.66
179	54.5592	53.55	11.25	472.63	35219.22
178.5	54.4068	41.35	8.57	413.56	25042.42
178	54.2544	53.31	9.56	550.52	34589.53
177.5	54.102	48.53	9.08	476.31	30754.59
177	53.9496	47.27	7.08	485.99	34783.79
176.5	53.7972	39.68	6.5	355.63	20998.55
176.4	53.76672	43.19	6.74	384.18	23619.29
175.4	53.46192	48.23	7.05	454.6	26414.75
175.1	53.37048	43.62	4.65	365.84	22134.69
174.5	53.1876	41.88	8.84	432.13	24653.73
174	53.0352	67.92	9.38	533.04	27495
173.5	52.8828	74.3	11.27	519.16	25335.43
173	52.7304	70.86	10.39	550.41	31500.22
172.5	52.578	56.7	8.96	491.25	29671.06
172	52.4256	68.45	9.87	496.81	34013.71
171.5	52.2732	32.59	7.15	341.36	15825.83
171	52.1208	69.71	9.83	534.54	37671.2
170.5	51.9684	71.64	11.43	564.38	32112.52
170	51.816	56.33	10.51	409.25	26542.32
169.5	51.6636	67.34	11.36	480.76	24608.35
168.5	51.3588	61.9	7.9	430.32	22369.54
167	50.9016	49.67	5.73	330.27	27256.1
166.5	50.7492	88.11	10.56	471.79	30017.7
164.5	50.1396	66.62	8.49	421.39	22558.11
164	49.9872	68.43	10	492.47	25708.17
163.5	49.8348	69.53	9.88	409.42	24307.83
163	49.6824	83.18	8.35	526.47	32545.74
162.5	49.53	11.89	2.98	100.66	7758.88
161.5	49.2252	81.13	13.44	525.05	33759.37
161	49.0728	86.9	13.27	536.21	33962.45
160.5	48.9204	83.88	11.49	515.71	31630.67
160	48.768	71.18	10.52	462.1	30621.2
159.5	48.6156	90.04	9.58	556.04	33033.42

159	48.4632	75.49	11.27	613.73	67630.97
158.5	48.3108	84.31	11.19	582.3	29838.4
158	48.1584	85	8.41	581.67	30423.87
157.5	48.006	58.05	3.73	366.79	22789.26
157	47.8536	60.76	9.79	435.55	24054.3
156.5	47.7012	55.57	11.52	426.12	23474.97
156.35	47.65548	56.12	7.65	410.82	23859.27
154.5	47.0916	65.18	10.88	509.44	24763.75
154	46.9392	63.28	8.47	470.88	24625.64
153.5	46.7868	58.68	6.87	426.87	22566.72
153	46.6344	11.28	1.94	135.79	13662.84
152	46.3296	71.31	12.06	540.96	34163.02
151.5	46.1772	83.27	12.74	652	37067.78
151	46.0248	79.55	12.38	665.2	48142.91
150.5	45.8724	63.84	9.42	471.52	34579.71
150	45.72	81.68	10.34	607.68	35830.97
148.5	45.2628	17.13	3.76	175.54	11743.1
148	45.1104	85.96	11.72	456.63	33438.35
147.5	44.958	69.49	8.92	388.72	25877.46
147	44.8056	80.67	8.99	467.55	26069.25
146.5	44.6532	76.82	10.62	556.48	33165.07
146.3	44.59224	76.07	11.68	500.19	25079.51
145.3	44.28744	86.82	17.78	546.35	32674.16
144.5	44.0436	82.7	15.76	477.01	37725.19
143.5	43.7388	103.32	17.16	607.66	42010.33
143	43.5864	76.9	10.66	531.13	40060.96
142.5	43.434	67.29	10.21	410.19	23681.57
142	43.2816	94.46	12.7	611.68	31236.06
141.5	43.1292	28.37	2.95	243.46	8675.02
141	42.9768	91.68	12.42	512.19	24607.11
140.5	42.8244	78.52	7.87	270.28	24552.69
137.5	41.91	77.48	10.32	356.95	37612.4
137	41.7576	87.2	9.39	431.94	30155.17
136.5	41.6052	71.72	8.52	356.76	27411.23
136.3	41.54424	79.63	8.89	440.28	28886.68
135.2	41.20896	110.4	11.85	639	30498.78
134.5	40.9956	94.92	13.39	605.31	29231.99
134	40.8432	67	12.24	413.66	21850.14
133.5	40.6908	80.6	13.81	529.45	38696.26
133	40.5384	70.91	9.32	428.26	25653.64

132.5	40.386	82.69	11.05	517.34	29794.99
132	40.2336	78.67	24.16	430.21	23283.58
131.5	40.0812	75.97	12.57	436.4	25053.93
131	39.9288	29.65	8.94	242.87	21859.8
130.5	39.7764	28.95	5.45	192.48	24894.9
128.5	39.1668	28.46	3.84	123.77	21476.13
128.2	39.07536	47.65	9.74	155.84	32342.66
127.5	38.862	30.16	6.04	154.92	25626.57
127	38.7096	47.27	9.59	174.75	20994.51
126.5	38.5572	43.48	4.34	153.79	31829.54
126.3	38.49624	39.05	8.45	135.02	28110.35
124.5	37.9476	56.46	9.07	177.18	39299.1
124	37.7952	53.88	8.52	206.33	42513.69
123.5	37.6428	56.31	6.23	232.79	40842.15
123	37.4904	54.13	7.06	260.95	31109.86
122.5	37.338	53.7	9.58	263.58	24747.19
122	37.1856	66.88	12.29	379.42	35064.46
121.5	37.0332	57.89	12.2	378.99	33581.34
121	36.8808	46.51	7.46	313.76	32089.85
120.5	36.7284	50.79	8.61	269.56	20063.49
120	36.576	42.08	11.5	293.32	26012.48
119.5	36.4236	59.85	9.73	312.5	27314.37
119	36.2712	69.01	12.42	343.3	30606.85
118.5	36.1188	75.56	11.73	367.23	30032.53
118.3	36.05784	72.2	11.56	396.33	30295.9
117.5	35.814	68.86	14.2	343.31	24130.42
117	35.6616	76.95	10.41	402.16	29831.21
116.5	35.5092	78.97	10.14	394.14	29380.38
116.3	35.44824	76.68	11.36	385.77	30704.17
115.3	35.14344	9.94	3.11	91.88	9531.47
113.5	34.5948	38.03	5.76	204.88	25051.98
113	34.4424	44.43	5.42	189.37	36103.48
112.5	34.29	42.91	4.29	176.12	36239.56
112	34.1376	35.37	5.53	137.65	25415
111.5	33.9852	32.36	5.97	129.75	25256.39
111	33.8328	27.25	4.54	109.98	19862.57
110.5	33.6804	85.05	15.52	497.1	41612.48
110	33.528	86.67	13.53	485.61	36250.14
109	33.2232	86.29	13.15	466.93	37768.86
108.5	33.0708	30.24	8.04	196.18	39370.63

108.2	32.97936	18.95	9.53	181.25	43179.12
107	32.6136	9.76	5.2	84.79	13282.74
105	32.004	44.96	10.17	190.19	41826.07
103.5	31.5468	25.31	8.73	168.97	55512.79
103	31.3944	13.67	10.63	116.69	42033.13
102.5	31.242	18.9	13.12	141.08	43031.28
102	31.0896	33.8	13.25	162.2	50120.58
101.5	30.9372	34.32	10.84	153.99	29452.47
100.7	30.69336	57.72	6.19	222.43	50373.2
100.5	30.6324	26.72	11.96	162.17	27083.83
100	30.48	35.1	10.33	159.54	35811.8
98	29.8704	30.06	7.92	147.01	28560.36
97.5	29.718	43.25	6.51	178.01	35516.78
97	29.5656	49.09	5.41	188.01	34102.96
95.25	29.0322	71.92	8.76	324.29	43563
95	28.956	42.81	8.91	263.43	43077.53
94.5	28.8036	53.57	10.42	244.58	62395.66
92.5	28.194	36.94	11.71	186.41	44142.21
91.5	27.8892	7.18	5.02	85.78	13657.42
91	27.7368	13.46	4.34	94.96	19627.6
90.5	27.5844	57.95	11.26	210.93	42609.84
90	27.432	58.6	8.8	222.02	41389.11
89.5	27.2796	44.46	6.84	193.22	33940.29
89	27.1272	60.63	6.95	231.6	38582.28
88.5	26.9748	55.93	9.03	233.04	34517.4
88	26.8224	81.56	9.63	263.94	37246.49
87.5	26.67	35.5	5.35	200.53	36354.67
85.8	26.15184	46.49	6.39	226.48	37018.68
85.5	26.0604	57.14	6.89	315.1	44368.54
85.3	25.99944	47.6	7.36	293.3	40796.09
85	25.908	55.12	12.99	378.54	41084.44
84.5	25.7556	61.09	8.14	429.78	41216.2
84	25.6032	64.6	9.13	506.49	34591.32
83.5	25.4508	49.34	8.08	383.49	40201.63
83	25.2984	61.84	7.36	335.72	41026.64
82.5	25.146	48.73	5.1	254.02	34684.25
82	24.9936	23.41	6.2	176.02	45107.63
81	24.6888	34.87	9.71	167.58	47458.96
79	24.0792	11.01	7.48	110.12	36922.68
78	23.7744	13.09	11.56	131.35	58494.87

74.8	22.79904	23.63	7.08	213.47	42179.96
74.5	22.7076	29.13	4.96	214.22	39832.67
74	22.5552	47.17	8.85	262.34	33023.28
73.5	22.4028	50.63	7.38	428.64	31855.25
73	22.2504	60.99	8.53	517.68	35466.95
72.5	22.098	67.82	16.16	593.58	36564.97
72	21.9456	74.78	11.53	570.4	39320.73
71.5	21.7932	47.12	13.66	312.86	52269.2
68.5	20.8788	17.48	4.9	139.59	33878.75
68	20.7264	18.77	4.49	126.92	24947.62
67.5	20.574	32.75	8.49	150.04	35249.91
65.8	20.05584	35.94	6.2	160.33	33782.01
65.5	19.9644	22.3	5.02	176.87	35501.56
65	19.812	33.78	6.38	170.57	31269.92
64.5	19.6596	32.24	4.61	189.46	37255.86
64	19.5072	31.07	7.69	178.37	42639.13
63.5	19.3548	46.2	5.51	190.22	44149.96
63	19.2024	42.96	3.91	208.86	42444.81
62.5	19.05	36.69	7.92	201.69	43146.83
62.3	18.98904	43.15	4.93	234.41	46152.88
62	18.8976	47.17	4.92	234.69	42501.93
61.5	18.7452	55.52	8.76	293.49	54930.08
61	18.5928	53.37	9.13	292.25	54024.15
60.5	18.4404	51.83	7.51	372.65	42997.48
60	18.288	73.68	10.71	554.42	40058.12
59.5	18.1356	64.93	10.51	513.19	35177.27
59	17.9832	57.17	8.52	453.04	33889.42
58.5	17.8308	73.89	11.1	457.95	31886.19
58.2	17.73936	68.09	9.81	367.22	26658.1
55	16.764	18.34	2.38	117.32	20005.78
54.5	16.6116	15.69	3.97	116.2	23203.09
54	16.4592	11.16	3.7	99.19	22238.26
53	16.1544	20.82	6.91	140.78	29803.83
52.5	16.002	32.99	8.09	178.53	39608.15
52	15.8496	31.81	6.55	147.27	29331.55
51.5	15.6972	27.38	5.05	172.43	36323.12
51	15.5448	24.73	5.63	172.06	40224.58
50.5	15.3924	23.58	9.43	173.19	42193.39
50	15.24	23.83	7.6	164.91	39140.92
49.5	15.0876	29.31	8.53	178.74	39101.54

49	14.9352	30.65	7.87	175.36	37455.99
48.5	14.7828	24.69	5.63	151.56	34183.12
48	14.6304	25.21	6.61	167.32	37053.48
47.5	14.478	21.33	7.21	177.27	42606.51
45.8	13.95984	36.44	6.43	184.98	39630.84
45.5	13.8684	36.11	5.5	211.07	46271.48
45	13.716	36.13	7.78	233.54	42697.44
44.5	13.5636	55.31	7.75	270.71	36305.71
44	13.4112	63.04	7	381.48	33861.72
43.5	13.2588	47.15	8.09	356.81	38687.47
43	13.1064	49.35	9.18	421.8	33818.62
42.5	12.954	35.58	5.75	311.35	33409.84
42	12.8016	57.06	7	326.3	33946.22
41.5	12.6492	36.97	8.48	273.51	41919.48
41	12.4968	18.8	4.53	202.5	34870.28
40.5	12.3444	18.02	4.58	155.49	28632.78
40	12.192	16.55	4.66	166.21	49851.32
39.5	12.0396	31.03	19.05	170.11	50421.65
39	11.8872	30.52	7.83	189.67	33256.69
38.5	11.7348	18.12	5.75	141.49	27703.06
38	11.5824	23.4	5.62	182.17	35874.33
37.5	11.43	18.8	5.72	185.69	42600.43
34.9	10.63752	21.96	5.46	190.19	38347.14
34.5	10.5156	27.48	5.81	190.23	39996.63
34	10.3632	35.43	3.87	233.89	43115.75
33.5	10.2108	46.91	6.07	251.61	22549.2
33	10.0584	52.3	8.25	424.68	44211.97
32.5	9.906	57.51	8.07	509	41538.77
32	9.7536	70.22	9.44	553.55	37138.06
31.5	9.6012	66.32	11.91	476.74	34431.95
31	9.4488	35.85	7.22	270.04	48923.98
30.5	9.2964	36.57	6.15	308.93	44252.73
30	9.144	13.11	5.53	196.03	39806.81
29.5	8.9916	13.57	5.93	168.71	35971.83
29	8.8392	14.1	6.93	155.38	36648.29
28.5	8.6868	11.76	6.75	208.82	41384.1
28.2	8.59536	10.17	5.6	171.84	39698.42
26.5	8.0772	40.13	6.19	299.33	52342.26
26	7.9248	18.8	2.62	223.76	40928.05
25.5	7.7724	10.81	4.66	181.78	48947.2

25	7.62	5.46	3.49	159.15	27125.81
24	7.3152	27.31	7.67	205.7	31672.42
23.5	7.1628	2.78	8	219.18	93838.69
23	7.0104	5.85	6	226.09	77219.36
22	6.7056	6.56	5.46	171.75	39189.15
21.5	6.5532	4.91	5.7	180.68	43748.85
21	6.4008	2.66	8.43	169.43	55885.5
20.5	6.2484	6.65	9.98	225.53	67560.69
20	6.096	9.9	10.1	145.82	48117.76
19.5	5.9436	5.29	10.84	184.73	65095.9
19	5.7912	8.2	10.1	198.53	56438.34
18.5	5.6388	6.45	6.16	181.14	51293.78
18	5.4864	4.84	11.69	167.6	43523.27
17.5	5.334	6.33	9.01	196.34	46553.58
15.8	4.81584	15.71	8.13	223.44	50750.78
15.5	4.7244	9.71	13.95	247.02	59404.15
14.5	4.4196	26.09	3.17	419.21	56432.5
14	4.2672	36.21	17.54	405.55	20824.74
13.5	4.1148	70.95	23.77	587.64	24909.33
13	3.9624	81.33	52.66	670.13	26641.05
12	3.6576	3.08	6.22	176.88	27926.37
11	3.3528	10.85	8.76	143.34	17808.57
10.5	3.2004	3.82	13.54	202.49	39068.11
9.5	2.8956	21.11	33.89	499.88	44104.26
9	2.7432	93.9	21	494.82	27096.8
8.5	2.5908	44.43	21.78	534.43	53329.44
8.2	2.49936	29.98	16.47	595.38	61727.76
6.5	1.9812	100.66	16.87	816.92	66370.19
6	1.8288	60.53	17.01	635.36	56252.46
5.5	1.6764	93.24	20.6	879.38	44447.9
5	1.524	39.7	18.43	575.48	51481.07
4.5	1.3716	11.13	17.09	393.8	61112.75
4	1.2192	11.66	14.16	417.64	81846.67
3.5	1.0668	92.69	19.78	675.24	64388.41
3	0.9144	28.8	14.53	488.66	57295.8
2.5	0.762	49.32	20.77	625.92	28901.88
2.3	0.70104	4.02	8.81	424.91	52730.63
0	0	2.73	2.44	64.16	18176.33

Swenson 1H XRF Data

Height above Buda Limestone		Mo	U	V	Al
ft	m	ppm	ppm	ppm	ppm
148.5	45.2628	4.94	6.56	119.16	36919.79
146.5	44.6532	1.74	4.26	135.02	23585.59
145.7	44.40936	1.82	2.32	329.21	81251.64
145.5	44.3484	3.27	4.21	404.19	73464.04
145.1	44.22648	10.7	7.57	374.57	78919.26
144.3	43.98264	29.02	9.22	361.23	60016.66
144	43.8912	36.61	10.43	476.89	61959.63
143.5	43.7388	28.31	10.18	396.18	39518.21
143	43.5864	30.85	10.19	447.48	50965.18
142.5	43.434	18.45	3.13	257.17	35288.31
142	43.2816	37.55	7.4	495.95	62628.11
141.5	43.1292	37.65	10.14	509.63	51592.37
141	42.9768	34.01	6.7	499.44	50956.87
140	42.672	40.19	9.9	595.2	45006.66
139.5	42.5196	33.07	5.43	534.6	39169.78
138.9	42.33672	32.51	6.97	419.76	42474.53
138	42.0624	31.84	9.55	431.35	28037.54
137.5	41.91	31.81	6.67	435.5	47998.73
137	41.7576	39.02	14.75	374.48	38432.38
136.3	41.54424	27.1	6.05	431.34	41968.5
136	41.4528	44.28	10.7	473.03	33078.31
135.7	41.36136	32.39	7.51	419.25	42194.73
135.4	41.26992	35.93	6.53	311.76	36136.25
135	41.148	27.12	7.78	272.29	40805.28
134.5	40.9956	38.01	7.38	482.75	52405.41
132.5	40.386	30.26	7.51	389.67	34406.49
132	40.2336	40.16	6.76	430.25	40378.7
131.5	40.0812	28.84	7.85	315.99	34618.34
131	39.9288	49.07	10.82	610.78	39340.75
130.5	39.7764	34.75	6.97	477.86	41186.11
130	39.624	21.94	7.52	283.35	36971.93
129.5	39.4716	38.49	7.39	434.83	34978.7
129	39.3192	43.78	11.19	443.51	32778.15
128.3	39.10584	23.25	6.04	337.65	38275.19
127.5	38.862	30.42	6.61	408.68	38063.19

126.5	38.5572	27.6	6.87	365.9	32755.54
126	38.4048	35.56	5.53	362.49	25775.15
124.5	37.9476	33.6	12.04	477.77	15764.67
124	37.7952	31.91	12.39	395.87	15633.74
123	37.4904	21.2	6.7	272.38	30156.53
122.5	37.338	45.14	10.03	503.72	54842.75
122	37.1856	45.5	9.24	401.91	19749.01
121.2	36.94176	28.62	6.72	336.73	39292.57
120.5	36.7284	59.84	10.06	546.53	26794.33
120	36.576	41.05	9.05	471.05	20336.05
119	36.2712	55.82	8.3	643.45	29231.41
118.5	36.1188	30.24	7.8	414.94	23095.1
118	35.9664	36.41	6.71	676.55	33376.91
117.5	35.814	34.97	6.32	427.2	29384.12
117	35.6616	29.89	6.08	366.91	26583.76
116.5	35.5092	38	7.02	394.54	28223.16
116	35.3568	34.26	7	332.21	19001.94
115.5	35.2044	38.94	8.03	380.57	41859.5
115	35.052	22.32	5.43	250.5	21757.14
114.5	34.8996	30.6	7.68	224.65	25204.6
114	34.7472	9.49	2.67	122.7	12813.55
113	34.4424	35.5	7.59	292.43	33643.81
112	34.1376	39.04	6.46	352.62	29749.69
111.8	34.07664	34.27	4.05	288.66	25205.71
110.5	33.6804	26.42	3.73	251.81	24155.33
110	33.528	35.37	7.53	284.74	21381.81
109.5	33.3756	38.34	6.12	279.84	28130.83
109	33.2232	42.26	5.94	280.6	25108.72
108.5	33.0708	36.51	8	322.1	18450.27
108	32.9184	64.32	8.64	535.72	21029.38
107.5	32.766	35.56	8.18	348.91	19538.34
107	32.6136	51.29	7.28	471.81	29504.6
106	32.3088	9.9	3.06	197.2	13162.48
105.5	32.1564	38.64	5.69	275.02	17280.7
105	32.004	60.81	7.41	389.66	24284.17
104.5	31.8516	39.1	6.51	294.2	17351.31
104	31.6992	55.01	6.78	351.5	25780.05
103.3	31.48584	48.86	9.08	378.59	22170.66
103	31.3944	61.59	7.85	473.18	20646.7
102	31.0896	11.38	4.57	131.56	6903.65

101	30.7848	40.29	7.49	467.57	20953.9
100.5	30.6324	60.22	10.57	438.65	45292.99
100.1	30.51048	30.52	17.23	570.78	41381.81
99.5	30.3276	62.88	7.92	341.51	30787.45
98.5	30.0228	47.82	8.55	312.62	23519.27
98	29.8704	51.64	17.23	454.6	49711.36
97.5	29.718	44.96	10.94	410.76	15745.38
97	29.5656	51.8	10.27	381.9	16576.52
96.5	29.4132	81.56	11.51	657.01	33394.7
96	29.2608	69.39	12.12	523.67	30271.85
95.5	29.1084	42	7.18	139.75	29521.66
95	28.956	38.49	6.04	288.28	79580.36
94.5	28.8036	36.99	8.24	239.3	20169.84
94	28.6512	27.15	5.46	243.99	19554.36
93.5	28.4988	42.21	7.12	320.27	20661.86
92.5	28.194	43.48	8.33	402.29	22515.06
92	28.0416	69.76	13.22	535.54	17239.55
91.5	27.8892	80.62	11.27	503.94	26991.82
91	27.7368	62.73	17.5	424.1	24823.79
90.5	27.5844	48.63	6.86	328.72	30832.32
90	27.432	55.69	4.59	323.71	36959.38
89.5	27.2796	59.26	7.96	341.51	51122.46
89	27.1272	73.3	9.44	404.49	32343.44
88	26.8224	96.96	12.7	543.53	28877.84
87.8	26.76144	23.89	30.76	5071.52	18719.41
87.5	26.67	32.61	9.51	280.53	18822.8
87	26.5176	25.74	3.36	191.35	11677.42
86.4	26.33472	48.54	9.22	338.1	18002.54
86	26.2128	58.03	6.47	294.37	29032.01
85.5	26.0604	49.25	6.55	283.02	21619.37
85	25.908	38.59	5.98	231.95	23229.62
84	25.6032	72.73	9.78	440.13	28502.98
83.4	25.42032	73.31	12.38	526.06	28015.9
83	25.2984	69.15	15.3	569.63	25544
82.4	25.11552	63.57	10.27	452.46	25786.4
81.3	24.78024	40.72	5.61	188.96	27530.33
81	24.6888	49.68	5.39	185.26	25907.6
80	24.384	40	6	173.72	23700.17
79.1	24.10968	40.69	5.81	189.42	21922.11
77.5	23.622	32.9	4.88	159.18	28333.62

77	23.4696	32.37	6.56	186.75	46638.54
76.5	23.3172	40.44	3.78	141.58	22501.55
76.3	23.25624	24.3	10	124.91	18893.16
76	23.1648	34.99	4.03	130.46	24775.22
75.5	23.0124	34.54	6.93	128.78	22510.8
75	22.86	40.05	5.35	153.37	25042.53
74.5	22.7076	42.49	4.03	155.95	25099.7
74	22.5552	45.29	6.63	146.04	29190.16
72.7	22.15896	49.39	8.74	226.2	30095.36
72.5	22.098	23.43	4.77	139.95	19567.87
72	21.9456	13.54	3.67	71.39	9870.44
71	21.6408	40.74	6.37	140.31	40639.67
70.5	21.4884	49.78	7.87	166.98	50495.98
70	21.336	48.23	7.52	180.13	31135.04
69.5	21.1836	61.23	7.68	235.84	49311.01
69	21.0312	32.27	10.79	172.86	19996.51
68.5	20.8788	45.98	5.45	222.82	32051.18
68	20.7264	26.29	5.41	195.12	21939.55
67.5	20.574	56.65	6.12	273.58	24838.29
67	20.4216	53.07	8.92	257.15	21823.11
66.5	20.2692	11.59	2.31	83.6	10020.28
66	20.1168	26.49	5.58	130.92	40922.75
65.5	19.9644	29.2	6.12	116.76	34884.35
65	19.812	36.97	7.03	122.17	30977.9
64.7	19.72056	33.5	3.94	117.58	29093.93
64	19.5072	33.28	4.97	126.94	25120.46
63.5	19.3548	49.45	6.02	169.7	30682.17
63	19.2024	28.8	5.51	112.77	24374.77
62.5	19.05	21.38	3.18	103.97	18472.8
62	18.8976	11.28	2.62	91.01	14601.79
61.3	18.68424	13.54	12.83	93.36	11772.86
61	18.5928	31.13	4.29	143.19	30190.99
60.5	18.4404	36.39	7.49	140.28	24845.05
60	18.288	41.73	6.19	178.89	44069.5
59.5	18.1356	44.94	5.6	204.91	30360.62
59	17.9832	34.84	5.84	164.66	30775.11
58.1	17.70888	46.15	7.87	195.19	36736.6
57.3	17.46504	94.18	10.67	250.38	52817.73
57	17.3736	80.52	9.78	209.64	49994.2
56.5	17.2212	58.73	6.62	164.53	31571.64

56	17.0688	63.51	5.08	188.18	34055.5
55.5	16.9164	82.52	8.88	227.87	35394.67
55	16.764	82.44	6.6	277.2	41240.15
54.5	16.6116	51.35	7.44	175.1	31041.08
54	16.4592	58.38	5.42	183.67	34421.9
53.5	16.3068	49.9	6.38	166.83	39133.43
53	16.1544	39.14	2.9	140.31	44572.09
52	15.8496	15.87	8.3	113.66	61357.17
51.5	15.6972	15.54	3.78	86.39	24851.87
51	15.5448	32.87	6.46	118.95	42468.75
50.5	15.3924	34.8	6.36	133.31	49418.41
50	15.24	32.92	9.64	145.79	62310.17
49.3	15.02664	32.36	3.9	141.31	26083.08
49	14.9352	29.41	3.09	132.65	25505.54
48.5	14.7828	34.62	5.24	140.01	28039.89
48	14.6304	20.15	8	104.03	19815.19
47	14.3256	25.23	5.93	96.21	20469.59
46.5	14.1732	45.32	5.49	145.77	31907.52
46	14.0208	54.94	5.84	161.49	40162.61
45.5	13.8684	42.77	5.2	158.32	31782.97
45	13.716	45.02	4.65	161.76	30437.83
44.5	13.5636	51.52	3.94	173.27	30977.33
44	13.4112	50.31	9.66	207.02	35072.42
43	13.1064	51.22	6.55	196.76	37545.21
42.5	12.954	35.96	7.22	162.36	43885.03
41.3	12.58824	50.25	5.1	176.7	32442.54
41	12.4968	51.27	6.24	178.46	29741.89
40.5	12.3444	46.56	4.2	165.95	32980.86
40	12.192	67.24	7.14	251.87	46231.04
39	11.8872	52.53	9.1	194.12	32246.43
38.5	11.7348	61.85	9.71	225.12	31677.59
37.1	11.30808	53.07	11.69	362.35	27564.81
37	11.2776	45.3	14.94	223.79	48058.83
34.5	10.5156	17.43	7.13	107.44	37267.42
34	10.3632	11.34	6.31	83.4	17375.38
33	10.0584	33.02	5.46	132.94	32571.72
32.5	9.906	53.4	8.27	290.88	37192.99
31.5	9.6012	52.45	12.02	189.49	15099.39
31	9.4488	48.3	6.27	174.63	24867.74
30.5	9.2964	33.89	4.29	127.98	18098.58

30	9.144	29.51	4.98	120.57	16382.19
29.5	8.9916	39.63	9.07	184.53	20213.74
29	8.8392	69.18	9.59	260.16	29573.7
28.5	8.6868	26.64	6.72	198.85	10503.81
27.5	8.382	86.11	12.64	364.16	21208.88
26	7.9248	20.6	3.31	93.22	17075.21
25.5	7.7724	33.08	8.07	134.2	26358.73
25	7.62	26.42	6.54	125.71	25296.7
24.5	7.4676	63.69	7.46	186.34	35902.54
24.3	7.40664	46.58	8.04	163.47	38150.14
23.3	7.10184	55.82	9.07	218.53	36510.22
22.5	6.858	47.5	6.87	209.51	24221.65
21	6.4008	38.14	5.96	149.16	33508.26
20.5	6.2484	45.4	7.87	158.81	28781.85
20	6.096	70.67	10.49	454.76	21422.13
19.5	5.9436	50.21	11.74	405.68	17157.15
19	5.7912	59.61	7.12	449.18	27566.55
18.5	5.6388	37.58	10.44	268.69	15674.4
18	5.4864	41.53	8.25	236.4	21151.33
17.5	5.334	52.12	7.59	227.41	43457.81
17	5.1816	22.16	4.38	109.74	18096.43
16.5	5.0292	44.61	4.21	169.93	31974.15
15	4.572	38.46	5.88	160.33	17430.81
14	4.2672	25.28	4.67	122.08	14820.62
13.5	4.1148	29.48	6.08	134.25	20001.56
13	3.9624	22.55	3.75	113.49	22918.78
11	3.3528	36.01	7.45	186.75	25503.65
10.5	3.2004	47.22	6.71	165.1	30942.17
10	3.048	46.46	7.78	180.69	35219.84
9.5	2.8956	47.87	6.97	155.49	36584.28
9	2.7432	56.99	7.13	233.72	40419.23
8.5	2.5908	45.65	9.89	234.29	27564.49
8	2.4384	29.28	6.07	129.95	24086.76
7.5	2.286	37.2	5.28	140.9	39308.23
7	2.1336	43.25	4.05	157.84	37968.72
6	1.8288	17.99	4.37	105.98	25371.94
5.5	1.6764	26.79	5.22	168.46	40946.61
5	1.524	66.02	10.23	323.86	42839.99
4.5	1.3716	22.7	10.21	157.45	70616.12
4	1.2192	22.75	8.65	177.94	65715.23

3.5	1.0668	62.63	11.35	387.37	26543.61
3	0.9144	32.79	12.19	156.65	40819.26
2.9	0.88392	36.31	9.95	162.3	53426.39
2.5	0.762	26.54	14.2	164.09	46495.54
2	0.6096	28.7	14.45	163.59	47442.19
1.5	0.4572	34.66	12.31	202.52	52581.18
1	0.3048	28.01	15.58	230.48	74816.98
0.5	0.1524	40.67	12.64	242.91	50109.34
0.1	0.03048	47.39	18.86	755.7	124248.14
0	0	13.36	5.32	692.57	53980.55
-8	-2.4384	2.1	2.75	33.98	11406.21

Lozier Canyon XRF Data

Height above Buda Limestone		Mo	U	V	Al
ft	m	ppm	ppm	ppm	ppm
185.16	56.44	1.19	1.48	11.95	2128.61
179.17	54.61	1.5	1.85	10.95	2959.94
174.53	53.20	2.36	3.5	25.42	2587.82
170.59	52.00	1.4	5.06	65.38	4547.33
168.10	51.24	2.76	4.81	59.4	3238.4
165.10	50.32	2.1	4	19.87	2156.06
163.17	49.73	1.35	1.38	29.13	3051.39
161.40	49.19	5.12	8.37	305.16	18811.68
158.72	48.38	1.63	4.78	109.14	12981.07
156.80	47.79	3.35	6.08	184.04	18474.45
155.17	47.30	3.09	4.82	259.32	23098.56
153.50	46.79	1.58	3.88	141.06	15813.39
150.60	45.90	1	1.89	72.24	7046.37
149.16	45.46	2.64	6.42	109.51	11329.87
147.39	44.92	1.57	3.78	62.54	8401.41
145.02	44.20	1	5.94	219.19	24293.29
143.60	43.77	1	4.34	267.84	25962.28
141.66	43.18	1.89	5.3	303.16	27670.68
141.04	42.99	2.21	5.07	118.16	10810.69
139.39	42.49	1.58	3.76	118.62	12286.77
136.52	41.61	2.46	5.55	98.9	13138.93
135.16	41.20	1	5.64	160.21	18136.95
133.17	40.59	10.79	8.74	109.24	20888.67
132.00	40.23	1.63	1.25	58.93	7434.6
131.15	39.97	1.31	4.76	160.41	16161.18
128.70	39.23	1	4.06	75.34	7648.78
127.15	38.76	2.67	6.61	103.54	13451.68
125.16	38.15	1.08	4.09	78.18	6687.23
123.41	37.62	1.45	4.24	105.78	14853.07
121.39	37.00	1	2.99	87.38	9511.49
119.41	36.40	1.58	4.4	82.69	11184.65
117.38	35.78	1.48	1.92	36.74	5785.23
115.55	35.22	1.79	3.36	58.25	9968.55
113.60	34.63	1.85	3.11	104.99	15404.98

111.16	33.88	2	4.24	83.43	9964.62
109.16	33.27	2.85	2.67	224.13	27140.79
107.16	32.66	1.52	2.22	83.59	6086.1
105.30	32.10	1.94	2.67	77.26	10090.17
103.70	31.61	1.61	1.87	66.93	8788
101.30	30.88	2.9	1.3	71.69	4997.11
99.48	30.32	1	2.25	337.59	29305.06
97.48	29.71	1	1.73	133.72	11054.49
94.38	28.77	1	2.29	192.77	18154.26
93.38	28.46	1	1.71	157.32	14128.47
91.10	27.77	1.09	1.7	240.47	26396.49
90.01	27.44	1.19	1.98	125.69	11487.94
89.03	27.14	1	1.13	33.38	2990.76
88.37	26.94	1	3.52	138.41	13573.74
86.60	26.40	1.95	2.31	129.85	9949.37
85.91	26.19	9.46	14.72	326.35	14585.02
82.82	25.24	22.9	9.76	359.62	16186.15
80.90	24.66	14.13	8.46	313.94	10865.9
78.92	24.05	26.91	10	670.91	12827.83
77.15	23.52	22.96	5.21	394.12	13355.17
74.90	22.83	25.51	11.17	431.09	8221.18
72.99	22.25	21.01	12.33	750.17	5983.32
70.85	21.60	19.04	14.09	381.12	5266.47
69.10	21.06	27.26	15.84	444.73	11410.84
67.13	20.46	21.9	18.52	384.25	26949.13
65.38	19.93	19.78	10.54	258.93	6620.33
63.37	19.32	22.87	14.62	341.73	20300.6
60.87	18.55	4.45	5.44	66.63	8949.46
59.04	18.00	23.95	14.39	323.76	15266.8
57.19	17.43	25.55	10.58	231.19	8980.59
54.64	16.65	12.97	18.9	314.53	64903.8
53.10	16.18	25.57	10.91	223.3	7056.15
51.39	15.66	23.7	11.32	322.03	14293.37
49.38	15.05	16.92	10.65	175.96	7366.03
47.15	14.37	18.15	12.08	600.52	26260.78
45.40	13.84	8.8	5.42	112.8	1951.81
43.17	13.16	27.7	12.8	341.66	11295.63
41.16	12.55	41.06	12.91	327.64	11195.29
39.18	11.94	45.22	13.94	456.07	15347.92
37.15	11.32	31.84	10.11	435.16	10699.08

35.07	10.69	22.36	9.22	437.37	7523.45
32.93	10.04	23.71	7.07	250.33	11978.4
31.50	9.60	30.01	13.84	330.3	7444.52
29.16	8.89	27.25	10.52	281.3	12927.3
26.80	8.17	38.93	9.71	438.97	15469.52
25.17	7.67	33.93	7.97	330.23	10614.16
23.15	7.06	24.09	9.33	302.93	10133.31
21.23	6.47	24.87	12.59	396.92	12419.58
19.16	5.84	20.89	13.4	462.62	10614.77
18.17	5.54	10.58	14.59	230.47	23678.67
18.00	5.49	22.12	25.05	351.8	7996.35
16.10	4.91	44.3	23.71	619.04	25204.31
13.60	4.15	12.68	18.33	272.5	11021.09
11.70	3.57	5.99	7.48	151.15	4332.67
11.50	3.51	46.09	28.98	647.91	13259.39
9.50	2.90	56.79	30.17	845.69	16088.55
7.10	2.16	2.7	7.45	61.43	9170.2
6.00	1.83	52.49	28.84	479.76	22068.08
3.60	1.10	71.12	18.87	857.04	23728
1.40	0.43	21.78	21.29	239.14	35075.24
0.38	0.12	5.19	5.69	102.37	8457.89
0.00	0.00	3.09	3.24	12.11	2057.88

Well 1 $\delta^{13}C_{carb}$

Depth above Buda Limestone		d13C
ft	m	VPDB
330.5	100.7364	1.4102275
329.5	100.4316	1.2824199
328.5	100.1268	1.0024605
327.5	99.822	1.2489465
326.5	99.5172	0.8959542
325.5	99.2124	1.4335574
324.5	98.9076	1.209387
323.5	98.6028	1.3919692
322.5	98.298	0.7154006
321.5	97.9932	0.7924909
320.5	97.6884	1.4193566
319.5	97.3836	1.449787
318.5	97.0788	1.3402376
317.5	96.774	1.0856368
316.5	96.4692	1.2722765
315.5	96.1644	1.7206173
314.5	95.8596	1.6861295
313.5	95.5548	- 1.8143776
312.5	95.25	2.3231386
311.5	94.9452	0.7336589
310.5	94.6404	0.9182698
309.5	94.3356	0.9710158
308.5	94.0308	1.344295
307.5	93.726	1.0917229
306.5	93.4212	0.9740588
305.5	93.1164	0.8188639
304.5	92.8116	0.9202985
303.5	92.5068	0.6474395
302.5	92.202	1.3138646
301.5	91.8972	- 0.7148268
300.5	91.5924	0.907112
299.5	91.2876	0.3187915
298.5	90.9828	1.176928
297.5	90.678	1.1546123

296.5	90.3732	0.7935053
295.5	90.0684	1.1434545
294.5	89.7636	-0.3689349
293.5	89.4588	0.2843037
292.5	89.154	0.5510766
291.5	88.8492	0.5693349
290.5	88.5444	1.0843356
289.5	88.2396	0.7465585
288.5	87.9348	1.2811186
287.5	87.63	0.7496015
286.5	87.3252	1.170555
285.5	87.0204	1.3044486
284.5	86.7156	1.3744385
282.5	86.106	1.4768874
281.5	85.8012	0.6694682
280.5	85.4964	0.9311694
279.5	85.1916	1.3206781
278.5	84.8868	0.5386176
277.5	84.582	0.7800319
276.5	84.2772	0.8784234
275.5	83.9724	0.8104622
274.5	83.6676	1.285176
273.5	83.3628	1.1451963
272.5	83.058	1.0315896
271.5	82.7532	-0.0568034
270.5	82.4484	0.7191711
269.5	82.1436	1.390668
268.5	81.8388	1.0447761
267.5	81.534	1.4251557
266.5	81.2292	1.4150123
265.5	80.9244	0.463556
264.5	80.6196	1.0934647
263.5	80.3148	0.7262715
262.5	80.01	0.1551949
261.5	79.7052	0.62788
260.5	79.4004	0.1764962
259.5	79.0956	0.43414
258.5	78.7908	0.6268657
257.5	78.486	0.5467323

256.5	78.1812	-0.0385451
255.5	77.8764	0.7445298
254.5	77.5716	0.7080133
253.5	77.2668	0.5031155
252.5	76.962	1.1198377
251.5	76.6572	-0.1257789
250.5	76.3524	-0.4889146
249.5	76.0476	-0.3641501
248.5	75.7428	0.2160556
247.5	75.438	0.1693957
246.5	75.1332	0.1125924
245.5	74.8284	0.2799594
244.5	74.5236	0.6177365
243.5	74.2188	-0.1207071
242.5	73.914	0.190697
241.5	73.6092	0.1704101
240.5	73.3044	0.052746
239.5	72.9996	-0.7343863
238.5	72.6948	-1.4312418
237.5	72.39	0.5933922
236.5	72.0852	0.6552673
235.5	71.7804	0.3398058
234.5	71.4756	-0.6775829
233.5	71.1708	-0.2535864
232.5	70.866	0.1511375
231.5	70.5612	0.4889146
230.5	70.2564	-3.26
229.5	69.9516	0.7871323
228.5	69.6468	0.4422547
227.5	69.342	0.8550934
226.5	69.0372	0.1399797
225.5	68.7324	0.4757281
224.5	68.4276	0.8753804
222.5	67.818	0.4442834
221.5	67.5132	0.8145196

220.5	67.2084	0.0608607
219.5	66.9036	0.4067526
218.5	66.5988	0.4168961
217.5	66.294	0.2596725
216.5	65.9892	-0.1693957
215.5	65.6844	-0.2251848
214.5	65.3796	0.2982176
212.5	64.77	-0.2251848
211.5	64.4652	0.0659325
210.5	64.1604	0.9305854
209.5	63.8556	0.6546834
208.5	63.5508	0.2935763
207.5	63.246	0.5076032
206.5	62.9412	-2.1743269
205.5	62.6364	0.6222243
204.5	62.3316	0.7814766
203.5	62.0268	0.4984741
202.5	61.722	0.6364251
201.5	61.4172	1.7217751
200.5	61.1124	0.6556977
199.5	60.8076	0.2895189
198.5	60.5028	0.9376858
197.5	60.198	0.137367
196.5	59.8932	0.6617838
195.5	59.5884	-0.0147848
194.5	59.2836	0.7713331
193.5	58.9788	0.7226445
192.5	58.674	0.6354108
191.5	58.3692	0.3990682
190.5	58.0644	0.0683915
189.5	57.7596	0.351394
188.5	57.4548	0.6394682
187.5	57.15	0.295605
186.5	56.8452	0.2732894
185.5	56.5404	0.6688842
184.5	56.2356	0.8960976
183.5	55.9308	-0.9662411

182.5	55.626	-0.2896725
181.5	55.3212	0.7155441
180.5	55.0164	0.6901855
179.5	54.7116	0.4731155
178.5	54.4068	1.0117331
177.5	54.102	0.7307593
176.5	53.7972	1.0401347
175.5	53.4924	1.3515389
174.5	53.1876	-0.8201753
173.5	52.8828	1.0989668
172.5	52.578	0.5968657
171.5	52.2732	-0.9398681
170.5	51.9684	-0.831907
169.5	51.6636	0.9715997
168.5	51.3588	1.07202
167.5	51.054	0.5415172
166.5	50.7492	1.0233314
165.5	50.4444	0.4197957
164.5	50.1396	0.8224909
163.5	49.8348	1.0334748
162.5	49.53	0.9847862
161.5	49.2252	0.7930749
158.5	48.3108	0.1073772
157.5	48.006	-0.0326025
156.5	47.7012	0.0749181
155.5	47.3964	1.2282292
154.5	47.0916	1.2231575
153.5	46.7868	0.9655137
152.5	46.482	1.1237516
151.5	46.1772	0.9939154
150.5	45.8724	1.3073482
149.5	45.5676	0.8032184
148.5	45.2628	1.2617026
147.5	44.958	1.2830039
146.5	44.6532	1.7374308
145.5	44.3484	0.2503999
144.5	44.0436	0.6175931
142.5	43.434	1.0659339

140.5	42.8244	1.0071018
138.5	42.2148	0.1246211
136.5	41.6052	2.7740921
134.5	40.9956	0.1570801
132.5	40.386	0.2361991
131.5	40.0812	0.4889146
130.5	39.7764	0.4361687
129.5	39.4716	0.8561078
128.5	39.1668	0.8652369
127.5	38.862	0.5873062
126.5	38.5572	0.5294885
125.5	38.2524	1.0255035
124.5	37.9476	-0.3418345
123.5	37.6428	1.3855963
122.5	37.338	0.6390378
121.5	37.0332	0.792204
120.5	36.7284	0.4584843
119.5	36.4236	1.3622663
118.5	36.1188	0.982901
117.5	35.814	0.8439356
116.5	35.5092	1.1725837
115.5	35.2044	0.8429213
114.5	34.8996	0.2018548
113.5	34.5948	0.9910158
112.5	34.29	0.5761484
111.5	33.9852	0.6664251
110.5	33.6804	0.6654108
109.5	33.3756	1.0255035
108.5	33.0708	1.0985364
106.5	32.4612	0.6981568
105.5	32.1564	1.1546123
104.5	31.8516	0.6585973
103.5	31.5468	-0.0940472
102.5	31.242	-0.2969164
101.5	30.9372	1.3158933
100.5	30.6324	1.1140385
99.5	30.3276	0.4526851
98.5	30.0228	0.3370497
97.5	29.718	0.9994175

96.5	29.4132	1.0349196
95.5	29.1084	0.0317316
93.5	28.4988	-0.0656456
92.5	28.194	1.0846225
91.5	27.8892	0.0763628
90.5	27.5844	0.6322243
89.5	27.2796	0.7285871
88.5	26.9748	1.2438748
87.5	26.67	1.1404115
86.5	26.3652	0.8918968
85.5	26.0604	0.255902
84.5	25.7556	0.2538733
83.5	25.4508	-0.2867729
82.5	25.146	1.0207187
81.5	24.8412	0.5399188
80.5	24.5364	1.0247761
79.5	24.2316	1.1333111
78.5	23.9268	0.8077061
77.5	23.622	0.2467729
76.5	23.3172	1.0552065
75.5	23.0124	0.9233415
74.5	22.7076	0.6940994
73.5	22.4028	0.9466715
72.5	22.098	1.0044892
71.5	21.7932	0.9760875
70.5	21.4884	-3.0894102
69.5	21.1836	-0.3060455
68.5	20.8788	0.713085
67.5	20.574	0.2261991
66.5	20.2692	-0.302275
65.5	19.9644	-0.111578
64.5	19.6596	0.3874801
63.5	19.3548	-0.562675
62.5	19.05	-0.7252572
61.5	18.7452	0.7201855
60.5	18.4404	0.9443559
59.5	18.1356	0.3387915
58.5	17.8308	1.006231

56.5	17.2212	0.2586582
55.5	16.9164	3.2854658
54.5	16.6116	0.0770903
53.5	16.3068	0.6136792
52.5	16.002	0.0172439
51.5	15.6972	-0.302275
49.5	15.0876	0.417183
47.5	14.478	0.7326445
45.5	13.8684	0.851323
43.5	13.2588	1.5329633
42.5	12.954	0.6819272
41.5	12.6492	0.6454108
40.5	12.3444	0.6798985
39.5	12.0396	0.3390784
38.5	11.7348	1.1779423
37.5	11.43	0.7062715
36.5	11.1252	0.5896218
35.5	10.8204	0.5561484
33.5	10.2108	0.8320504
32.5	9.906	0.7001855
31.5	9.6012	0.7022142
30.5	9.2964	0.3329923
29.5	8.9916	0.9020403
28.5	8.6868	0.4212404
27.5	8.382	0.7275728
26.5	8.0772	0.7032285
25.5	7.7724	1.0085466
24.5	7.4676	0.8553804
23.5	7.1628	0.5115172
22.5	6.858	1.0825938
21.5	6.5532	1.0694073
20.5	6.2484	1.0105753
19.5	5.9436	1.0328909
18.5	5.6388	0.9497145
17.5	5.334	0.7945196
16.5	5.0292	1.1038951
15.5	4.7244	1.2286596
14.5	4.4196	1.0988233
13.5	4.1148	1.1614259
12.5	3.81	1.0115896

11.5	3.5052	1.1543254
10.5	3.2004	1.1637415
9.5	2.8956	0.762788
8.5	2.5908	1.04202
7.5	2.286	1.2932908
6.5	1.9812	1.3584958
5.5	1.6764	0.7171424
4.5	1.3716	1.2276452
3.5	1.0668	1.7325025
2.5	0.762	1.340965
1.5	0.4572	1.1198377
0.5	0.1524	1.320965
-0.5	-0.1524	1.1299811
-1.5	-0.4572	1.6249818
-2.5	-0.762	2.1243269
-3.5	-1.0668	2.0299927
-4.5	-1.3716	2.3495116
-5.5	-1.6764	1.6303405

Well 2 $\delta^{13}C_{carb}$

Height above Buda		d13C
ft	m	PDB
330.5	100.7364	1.92
328.5	100.1268	1.92
326.5	99.5172	1.85
324.5	98.9076	1.84
322.5	98.298	1.88
320.5	97.6884	1.9
318.5	97.0788	1.76
316.5	96.4692	1.83
314.5	95.8596	1.73
312.5	95.25	1.73
310.5	94.6404	1.59
308.5	94.0308	1.7
306.5	93.4212	1.75
304.5	92.8116	1.82
302.5	92.202	1.74
300.5	91.5924	1.6
298.5	90.9828	1.78
296.5	90.3732	1.73
294.5	89.7636	1.5
292.5	89.154	1.48
290.5	88.5444	1.65
288.5	87.9348	1.35
286.5	87.3252	1.57
284.5	86.7156	1.54
278.5	84.8868	1.42
277.5	84.582	1.49
276.5	84.2772	1.36
275.5	83.9724	1.29
274.5	83.6676	1.53
273.5	83.3628	1.88
272.5	83.058	1.02
271.5	82.7532	0.69
270.5	82.4484	1.21
269.5	82.1436	1.13
268.5	81.8388	1.17

266.5	81.2292	0.83
265.5	80.9244	0.76
264.5	80.6196	0.97
263.5	80.3148	0.44
262.5	80.01	0.98
261.5	79.7052	0.38
260.5	79.4004	0.76
259.5	79.0956	0.79
258.5	78.7908	0.6
256.5	78.1812	0.58
255.5	77.8764	0.35
254.5	77.5716	0.03
253.5	77.2668	0.04
252.5	76.962	0.68
251.5	76.6572	-0.04
250.5	76.3524	-0.03
249.5	76.0476	0.4
248.5	75.7428	0.42
245.5	74.8284	0.93
244.5	74.5236	-1.13
243.5	74.2188	-0.41
242.5	73.914	-0.07
241.5	73.6092	-0.16
240.5	73.3044	0.07
239.5	72.9996	-1.65
238.5	72.6948	-1.48
237.5	72.39	-0.37
235.5	71.7804	-0.52
234.5	71.4756	-0.32
233.5	71.1708	-0.41
232.5	70.866	-1.45
231.5	70.5612	-0.67
230.5	70.2564	-0.34
229.5	69.9516	-0.29
228.5	69.6468	-0.15
225.5	68.7324	-0.44
224.5	68.4276	-0.27
223.5	68.1228	-0.52
222.5	67.818	-0.57
221.5	67.5132	-1.32

220.5	67.2084	-0.42
219.5	66.9036	-0.32
218.5	66.5988	-0.28
215.5	65.6844	-0.77
214.5	65.3796	0.28
213.5	65.0748	0.17
212.5	64.77	0.41
209.5	63.8556	-0.02
208.5	63.5508	-0.02
207.5	63.246	0.16
206.5	62.9412	-2.09
204.5	62.3316	-0.84
203.5	62.0268	-2.27
202.5	61.722	-0.21
201.5	61.4172	0.33
200.5	61.1124	-1.39
199.5	60.8076	-0.67
198.5	60.5028	0.03
197.5	60.198	0.1
196.5	59.8932	0.23
195.5	59.5884	0.23
194.5	59.2836	0.06
193.5	58.9788	0.14
192.5	58.674	-0.53
191.5	58.3692	-0.16
190.5	58.0644	-0.65
189.5	57.7596	0.04
188.5	57.4548	-1.88
186.5	56.8452	-1.35
185.5	56.5404	-0.58
184.5	56.2356	0.59
183.5	55.9308	-0.35
182.5	55.626	-0.15
181.5	55.3212	0.6
180.5	55.0164	-0.27
179.5	54.7116	0.19
178.5	54.4068	0.6
177.5	54.102	-0.03
176.5	53.7972	-0.13
175.5	53.4924	0.03

174.5	53.1876	-0.46
173.5	52.8828	0.46
172.5	52.578	0.05
171.5	52.2732	-1.54
170.5	51.9684	0.31
169.5	51.6636	0.42
167.5	51.054	-0.96
166.5	50.7492	0.05
163.5	49.8348	0.61
162.5	49.53	0.26
161.5	49.2252	0.12
160.5	48.9204	0.08
159.5	48.6156	0.1
158.5	48.3108	0.58
157.5	48.006	0.19
156.5	47.7012	0.68
155.5	47.3964	-0.06
154.5	47.0916	0.85
153.5	46.7868	0.16
152.5	46.482	-2.22
151.5	46.1772	0.49
150.5	45.8724	0.64
149.5	45.5676	-0.92
148.5	45.2628	-1.39
147.5	44.958	-0.62
146.5	44.6532	1.29
145.5	44.3484	-0.42
144.5	44.0436	0.59
143.5	43.7388	0.61
142.5	43.434	0.33
141.5	43.1292	-0.02
140.5	42.8244	1.07
139.5	42.5196	-0.49
138.5	42.2148	-0.44
137.5	41.91	0.49
135.5	41.3004	0.72
134.5	40.9956	0.5
133.5	40.6908	0.55
132.5	40.386	-0.03
131.5	40.0812	0.97

130.5	39.7764	0.67
129.5	39.4716	-1.41
128.5	39.1668	-0.02
127.5	38.862	-0.56
126.5	38.5572	-0.18
125.5	38.2524	-0.77
124.5	37.9476	-0.77
123.5	37.6428	0.88
122.5	37.338	0.23
121.5	37.0332	0.51
120.5	36.7284	0.3
119.5	36.4236	-1.76
118.5	36.1188	0.75
117.5	35.814	0.89
116.5	35.5092	1.04
115.5	35.2044	0.58
114.5	34.8996	0.68
113.5	34.5948	-0.5
112.5	34.29	0.8
111.5	33.9852	1.02
110.5	33.6804	0.59
109.5	33.3756	0.84
108.5	33.0708	1.14
107.5	32.766	1.67
106.5	32.4612	0.21
105.5	32.1564	-0.98
104.5	31.8516	-0.14
103.5	31.5468	0.46
102.5	31.242	0.8
101.5	30.9372	0.49
100.5	30.6324	0.4
99.5	30.3276	1.37
97.5	29.718	1.19
95.5	29.1084	0.39
94.5	28.8036	-0.64
93.5	28.4988	1.03
92.5	28.194	1.02
91.5	27.8892	0.67
88.5	26.9748	0.37
86.5	26.3652	0.33

85.5	26.0604	0.86
83.5	25.4508	0.69
82.5	25.146	0.77
81	24.6888	0.97
80.5	24.5364	-0.56
79.5	24.2316	1.11
78.5	23.9268	0.78
77.5	23.622	0.92
75.5	23.0124	0.91
74.5	22.7076	0.64
73.5	22.4028	0.84
72.5	22.098	0.73
71.5	21.7932	0.94
70.5	21.4884	0.15
68.5	20.8788	0.48
67.5	20.574	1.03
65.5	19.9644	1.14
64.5	19.6596	1.29
63.5	19.3548	1.14
62.5	19.05	0.71
61.5	18.7452	0.7
60.5	18.4404	0.54
59.5	18.1356	0.44
58.5	17.8308	0.36
56.5	17.2212	1.12
55	16.764	0.37
54.5	16.6116	-0.48
53.5	16.3068	-1.42
52.5	16.002	0.55
51.5	15.6972	0.61
50.5	15.3924	1.12
49.5	15.0876	1.09
48.5	14.7828	0.44
47.5	14.478	1.07
45.5	13.8684	0.66
44.5	13.5636	0.46
43.5	13.2588	0.32
42.5	12.954	0.12
41.5	12.6492	0.16
40.5	12.3444	-0.26

39.5	12.0396	1.15
34.5	10.5156	1.12
33.5	10.2108	0.6
32.5	9.906	0.8
31.5	9.6012	1.06
30.5	9.2964	0.99
29.5	8.9916	0.34
28.5	8.6868	0.77
26.5	8.0772	1.04
25.5	7.7724	1.16
24.5	7.4676	3.8
23.5	7.1628	1.35
21.5	6.5532	0.28
20.5	6.2484	0.87
19.5	5.9436	0.51
18.5	5.6388	0.58
17.5	5.334	0.72
15.5	4.7244	0.57
14.5	4.4196	-2.03
13.5	4.1148	0.72
12.5	3.81	-3.3
11.5	3.5052	1.52
10.5	3.2004	-1.01
9.5	2.8956	0.73
8.5	2.5908	0.94
6.5	1.9812	1.13
5.5	1.6764	0.75
4.5	1.3716	0.37
3.5	1.0668	1.02
2.5	0.762	0.99
1.5	0.4572	1.16
0.5	0.1524	1.33
-0.5	-0.1524	1.7
-1.5	-0.4572	1.29
-2.5	-0.762	1.34
-3.5	-1.0668	1.39
-4.5	-1.3716	1.45
-5.5	-1.6764	1.56
-6.5	-1.9812	1.5

Swenson 1H $\delta^{13}C_{carb}$

Height above Buda Limestone		$d^{13}C$ VPDB
ft	m	VPDB
152.5	46.482	0.46
151.5	46.1772	0.56
149.5	45.5676	0.98
148.5	45.2628	1.18
147.5	44.958	-2.87
145.5	44.3484	0.48
144.5	44.0436	-0.70
143.5	43.7388	0.24
142.5	43.434	0.48
141.5	43.1292	0.16
140.5	42.8244	-0.20
139.5	42.5196	-0.95
138.5	42.2148	-0.16
137.5	41.91	0.22
136.5	41.6052	0.02
135.5	41.3004	-0.30
134.5	40.9956	-0.45
133.5	40.6908	-10.17
131.5	40.0812	-0.36
130.5	39.7764	-0.01
129.5	39.4716	-0.36
128.5	39.1668	0.28
127.5	38.862	-1.81
126.5	38.5572	-0.44
125.5	38.2524	0.76
124.5	37.9476	0.24
123.5	37.6428	0.00
122.5	37.338	-0.27
121.5	37.0332	0.51
120.5	36.7284	0.10
119.5	36.4236	0.12
118.5	36.1188	0.54
117.5	35.814	0.11
116.5	35.5092	-1.16

115.5	35.2044	-1.13
114.5	34.8996	-2.02
113.5	34.5948	-0.92
112.5	34.29	-3.06
111.5	33.9852	-1.13
110.5	33.6804	0.31
109.5	33.3756	-4.71
108.5	33.0708	-2.13
107.5	32.766	0.54
106.5	32.4612	-2.52
105.5	32.1564	-1.31
104.5	31.8516	-1.37
103.5	31.5468	0.30
102.5	31.242	-1.46
101.5	30.9372	0.27
100.5	30.6324	0.96
99.5	30.3276	-1.03
98.5	30.0228	0.88
97.5	29.718	0.62
96.5	29.4132	0.86
95.5	29.1084	-0.73
94.5	28.8036	0.03
93.5	28.4988	0.52
92.5	28.194	0.64
91.5	27.8892	0.74
90.5	27.5844	0.47
89.5	27.2796	0.72
88.5	26.9748	0.79
87.5	26.67	-1.34
86.5	26.3652	0.38
85.5	26.0604	-0.33
84.5	25.7556	0.46
83.5	25.4508	0.61
82.5	25.146	0.03
81.5	24.8412	0.59
80.5	24.5364	0.80
78.5	23.9268	0.18
76.5	23.3172	-0.76
75.5	23.0124	0.44
74.5	22.7076	0.60

73.5	22.4028	0.73
72.5	22.098	-1.07
71.5	21.7932	-1.10
70.5	21.4884	0.81
69.5	21.1836	0.62
68.5	20.8788	-1.43
67.5	20.574	0.61
66.5	20.2692	0.71
64.5	19.6596	0.01
63.5	19.3548	0.18
62.5	19.05	-1.08
61.5	18.7452	-1.04
60.5	18.4404	1.00
59.5	18.1356	0.66
58.5	17.8308	0.58
56.5	17.2212	0.56
55.5	16.9164	0.70
54.5	16.6116	0.68
53.5	16.3068	0.10
52.5	16.002	0.26
51.5	15.6972	0.77
50.5	15.3924	0.67
49.5	15.0876	0.19
48.5	14.7828	-0.73
47.5	14.478	-0.58
46.5	14.1732	1.04
45.5	13.8684	1.10
44.5	13.5636	0.80
43.5	13.2588	0.32
42.5	12.954	0.09
41.5	12.6492	0.70
40.5	12.3444	0.74
39.5	12.0396	0.41
38.5	11.7348	0.36
37.5	11.43	-0.55
36.5	11.1252	0.76
35.5	10.8204	0.31
34.5	10.5156	-0.20
33.5	10.2108	1.12
32.5	9.906	0.47

31.5	9.6012	0.66
30.5	9.2964	0.50
29.5	8.9916	1.22
28.5	8.6868	-0.55
27.5	8.382	0.25
26.5	8.0772	-0.06
25.5	7.7724	0.95
24.5	7.4676	1.43
23.5	7.1628	0.53
22.5	6.858	-0.14
21.5	6.5532	1.23
20.5	6.2484	0.63
19.5	5.9436	0.46
18.5	5.6388	-0.24
17.5	5.334	0.70
16.5	5.0292	0.15
15.5	4.7244	0.92
14.5	4.4196	1.28
13.5	4.1148	0.00
12.5	3.81	1.15
11.5	3.5052	1.49
10.5	3.2004	1.33
7.5	2.286	1.47
6.5	1.9812	0.24
5.5	1.6764	0.85
4.5	1.3716	1.14
3.5	1.0668	1.08
2.5	0.762	1.24
1.5	0.4572	1.36
0.5	0.1524	1.59
-0.5	-0.1524	1.44
-1.5	-0.4572	-0.63
-1.5	-0.4572	1.91
-3.5	-1.0668	1.77
-4.5	-1.3716	1.76
-7.5	-2.286	1.71
-8.5	-2.5908	1.26
-9.5	-2.8956	1.99
-10.5	-3.2004	1.52
-11.5	-3.5052	1.57

-12.5	-3.81	1.56
-13.5	-4.1148	1.56
-14.5	-4.4196	1.63
-15.5	-4.7244	1.53
-16.5	-5.0292	2.06
-17.5	-5.334	1.39
-18.5	-5.6388	1.64
-19.5	-5.9436	1.64
-20.5	-6.2484	1.61
-21.5	-6.5532	1.38

Well 1 $\delta^{13}C_{org}$

Deth above Buda Limestone		d13C vs. VPDB
ft	m	
266.5	81.2292	-25.58
260.5	79.4004	-25.39
259.5	79.0956	-23.20
258.5	78.7908	-24.17
257.5	78.486	-22.64
255.5	77.8764	-24.99
254.5	77.5716	-22.35
251.5	76.6572	-23.35
250.5	76.3524	-24.29
247.5	75.438	-26.38
246.5	75.1332	-25.81
245.5	74.8284	-26.34
244.5	74.5236	-24.77
243.5	74.2188	-24.58
242.5	73.914	-24.49
241.5	73.6092	-24.96
239.5	72.9996	-22.36
238.5	72.6948	-21.00
237.5	72.39	-25.88
236.5	72.0852	-25.70
235.5	71.7804	-25.17
233.5	71.1708	-26.01
232.5	70.866	-25.05
231.5	70.5612	-26.15
228.5	69.6468	-25.99
226.5	69.0372	-26.19
225.5	68.7324	-26.30
224.5	68.4276	-26.58
218.5	66.5988	-25.94
217.5	66.294	-26.33
216.5	65.9892	-27.04
214.5	65.3796	-26.80
212.5	64.77	-26.37
211.5	64.4652	-27.04
209.5	63.8556	-27.10
205.5	62.6364	-26.80
204.5	62.3316	-26.79
203.5	62.0268	-25.53
202.5	61.722	-26.98
201.5	61.4172	-25.66
200.5	61.1124	-25.80

Well 2 $\delta^{13}C_{carb}$

Depth above Buda Limestone		d13C vs. VPDB
ft	m	
239.5	72.9996	-26.10
237.5	72.39	-26.91
235.5	71.7804	-24.68
234.5	71.4756	-27.00
233.5	71.1708	-25.52
232.5	70.866	-27.41
231.5	70.5612	-26.76
230.5	70.2564	-26.56
229.5	69.9516	-26.45
228.5	69.6468	-26.78
225.5	68.7324	-26.31
224.5	68.4276	-26.35
223.5	68.1228	-26.96
222.5	67.818	-24.29
221.5	67.5132	-26.08
220.5	67.2084	-25.59
218.5	66.5988	-26.49
215.5	65.6844	-26.45
214.5	65.3796	-26.31
213.5	65.0748	-26.02
212.5	64.77	-22.84
209.5	63.8556	-22.28
208.5	63.5508	-26.65
207.5	63.246	-26.38
206.5	62.9412	-23.24
205.5	62.6364	-26.36
204.5	62.3316	-26.37
203.5	62.0268	-26.79
202.5	61.722	-26.37
201.5	61.4172	-22.86
200.5	61.1124	-26.64
199.5	60.8076	-26.36
197.5	60.198	-26.65
196.5	59.8932	-26.55
194.5	59.2836	-26.58
192.5	58.674	-27.03
191.5	58.3692	-26.93
189.5	57.7596	-26.92

188.5	57.4548	-26.55
186.5	56.8452	-26.71
185.5	56.5404	-26.53
183.5	55.9308	-27.13
182.5	55.626	-26.42
181.5	55.3212	-27.07
180.5	55.0164	-26.80
179.5	54.7116	-26.88
177.5	54.102	-27.02